Hydrodynamics of Micro-swimmers in Complex Fluids and Environments

Arnold J. T. M. Mathijssen
New College
University of Oxford

A thesis submitted for the degree of
Doctor of Philosophy
Supervised by Prof. Julia M. Yeomans FRS

Trinity Term 2016

Hydrodynamics of Micro-swimmers in Complex Fluids and Environments

Arnold J. T. M. Mathijssen, New College, University of Oxford

A thesis submitted for the degree of *Doctor of Philosophy*, Trinity Term 2016

Abstract

Both biological micro-organisms and synthetic micro-robots propel through viscous liquids to achieve their goal, be it to invade new territories or to deliver drugs to infected regions. Considerable attention is devoted to learning how to prevent or encourage these processes, and understanding the interactions between micro-swimmers and their complex environments is an essential part of this. *In vivo* conditions provide a challenge to model, although novel experimental, computational and theoretical techniques have provided clear insights into the continuous interplay between the effects of strong confinement, hydrodynamic interactions, and local activity that drives living systems out of equilibrium.

To analyse the underlying mechanisms of micro-swimmer processes, we develop a hydrodynamic framework based on the fundamental solutions of the Stokes equations to compute swimmer-generated flow fields. These flows affect the motion of swimmers via reflections in surfaces, mix and enhance the uptake of nutrients, and enable cells to sense one another's presence.

Hence, we study the accumulation of microbes on surfaces, which could be relevant for the initial stages of biofilm formation, and compute the strength required for externally imposed flows to detach them. Moreover, we evaluate the ability to swim upstream and uncover that viscoelasticity can provide a natural sorting mechanism for sperm cells. Other ecological effects are considered, including the transport of nutrients by micro-flows, the interaction with water-air interfaces, and the impact of thermal noise and biological fluctuations.

To verify our results, we compare our theory to extensive simulations using a 'Raspberry' swimmer model in combination with the Lattice-Boltzmann fluid solver algorithm. This allows us to determine previously unknown model parameters and hence make suggestions to improve micro-organism treatment and micro-robot design.

This thesis is dedicated to my parents,
Jan and Astrid Mathijssen-Vergouwe.

To both of you I give an incredible hug for you ever-lasting motivation, support, energy and interest. From the very beginning you have taught me how to reason, to analyse and to wonder.

Mamma, your intelligence and social skills are beyond those of many. With the many difficulties that Life has thrown at you there is no better phrase that characterises you than *Luctor et Emergo*.

Pappa, you are mamma's perfect counterpart. An imperishable column of support and hope. Always there with interesting articles that we discussed during many evenings of debate, never without good coffee and Latin expressions.

Pap en Mam, I am ever grateful for the stable, safe, balanced, challenging and exciting environment you have provided for Ralph, Lucas, Jan and myself. We continue to thrive and enjoy Life together.

Publications Related to this Thesis

This thesis has used material from the following publications:

Chapter 2 uses material from A. J. T. M. Mathijssen, D. O. Pushkin, and J. M. Yeomans. Tracer trajectories and displacement due to a micro-swimmer near a surface. J. Fluid Mech., 773:498 – 519, June 2015. doi:10.1017/jfm.2015.269.

Chapter 3 uses material from A. J. T. M. Mathijssen, T. N. Shendruk, J. M. Yeomans, and A. Doostmohammadi. Upstream swimming in microbiological flows. Phys. Rev. Lett., 116:028104, Jan 2016. doi:10.1103/PhysRevLett.116.028104.

Chapter 4 uses material from A. J. T. M. Mathijssen, A. Doostmohammadi, J. M. Yeomans, and T. N. Shendruk. Hydrodynamics of microswimmers in films. J. Fluid Mech. accepted; preprint arXiv:1511.01859, 2015. URL http://arxiv.org/abs/1511.01859.

Chapter 5 uses material from A. J. T. M. Mathijssen, A. Doostmohammadi, J. M. Yeomans, and T. N. Shendruk. Hotspots of boundary accumulation: dynamics and statistics of microswimmers in flowing films. J. R. Soc. Interface, 13:20150936, 2016. doi:10.1098/rsif.2015.0936.

Chapter 6 uses material from J. de Graaf, H. Menke, A. J. T. M. Mathijssen, M. Fabritius, C. Holm, and T. Shendruk. Lattice-boltzmann hydrodynamics of anisotropic active matter. J. Chem. Phys., 144:134106, 2016. doi:10.1063/1.4944962.

Chapter 7 uses material from J. de Graaf, A. J. T. M. Mathijssen, M. Fabritius, H. Menke, C. Holm, and T. N. Shendruk. Understanding the onset of oscillatory swimming in microchannels. Soft Matter, 12:4704–4708, 2016. doi:10.1039/C6SM00939E.

Please note that all LB simulations in Chapters 6 and 7 have been performed by Joost de Graaf at the University of Stuttgart and the University of Edinburgh.

Acknowledgements

In the first place, I would like to thank my supervisor Julia Yeomans for welcoming me to her vibrant research group, and for guiding me throughout the four years I was given to spend here. Julia, with your experience you continually reshape your group to include new characters and research interests. I believe this stimulating environment is key to productivity, and you are always there to lead the many projects taking place, next to your many journeys to tell the world about our work. The privilege to have gotten to know you better and better will sprout often in the fountain of memory.

The work presented in this thesis would also not have been possible without Dr. Mitya Pushkin, Tyler Shendruk and Amin Doostmohammadi, who I am now grateful to consider my mentors. Mitya, you are extraordinary at mathematics, but you also showed me which ice cream shops to explore, and which to ignore. Tyler, your forte is public outreach and news-room-style writing without dropping any scientific accuracy. I hope there is a progressive correlation in the 816 e-mails addressed to you in the @physics outbox. Amin, you are informed of many scientific topics and you also know the people associate with them. This often lead to particularly interesting conversations, also in the Lamb and Flag.

Special thanks go to my office mates Matthew Andrew, Andrew Balin, Rachel Bennett, Anatolij Gelimson and Luuk Metselaar. The whiteboard was never completely white, and blackboard was never black. More curiously though, those seven crates of beer that have been sitting in Room 4.10 for three years are still not finished, in spite of the World Cup and that super hot summer day when we had to work bare-chested, completely in fear Julia wouldn't walk in. Still, we never had to vacate the "Wykeham Chairs".

Warmest thanks and admiration also goes to my brothers Ralph, Lucas and Jan.

A heartfelt thank you I would like to express to my friends Lorenzo Rossi & Benedetta Pacini, Gianluca Lagezza & Giada Nuzzo, Mira Zorkot, & Hamad Fahes, Lisa Brusius, Kirsten Koolstra, Diana di Paolo, Andreas Zöttl and many others in and around the Rudolf Peierls Centre. We surely had the best BBQs and punting trips that Oxford could ever offer. At New College I truly enjoyed working with Chris de L'isle, Elle McDonald and my fellow presidents Lauren Burton, Genevieve Woods and Alex Lucas. For the many beautiful concerts and political discussions I would also like to thank Dr. Nathalie Berny.

I have no words how to describe Bruno Bertini, Mattia Sormani & Viviana Ponta with whom we established the most incredible household at 14 Harley Road. You have become my very best friends, together with my old friends Jeff Rowley and Otto Meij. After your many lessons I truly believe my cooking has improved – even if you think it hasn't – as a result of "harsh condemnation" and "delirious glorification". Not a single day in the house was without laughter.

Philomena, brave and always joyful, with your energy to overturn the Royal Albert Hall you are more inspiring than you could imagine. You keep giving your love, jokes and support; even when a car crashed into the apartment you perfectly handled the estate agents and police. I would like to return my love tenfold, because without you Life would not be as smooth, rich and brilliant as silk.

Contents

List of Figures

List of Tables

CHAPTER 1

Introduction

> "Scientists have a responsibility, or at least I feel I have a responsibility, to ensure that what I do is for the benefit of the human race. It is important that we try to point out facts to help those in power to make decisions. Unfortunately, this is not often the case. Although knowledge cannot guarantee good decisions, common sense suggests that wisdom is an unlikely consequence of ignorance."
>
> Sir Harold Kroto FRS (1939–2016)

The title of this thesis reads 'Hydrodynamics of micro-swimmers in complex fluids and environments'. Before immersing oneself into any details, one might want to ask what is meant by these hydrodynamics, micro-swimmers, complex fluids and complex environments. This chapter introduces the foundations of these concepts and how they are connected to each other, both in the natural world and in the design of new technologies. §1.1 summarises the types of micro-swimmers that exist and why they are studied. §1.2 lays out a mathematical framework to study the hydrodynamic interactions between swimmers and their environment. §1.3 then describes what complexities lie within these environments, and it introduces the equations of motion that are used to model these features in the remaining chapters of the thesis. §1.4 provides an overview of these chapters.

In the spirit of discussing science in a wider context, each chapter of this thesis starts with a quotation. The first one is by Prof Sir Harold Kroto FRS, with whom I had to honour to chat during the 2012 Nobel Laureate Meeting in Lindau. He gave the best powerpoint presentation I have ever seen, frequently going over 10 slides per minute, at least 2 of which being jokes, but keeping perfect coherence. Using memorisation and improvisation, a computer and a

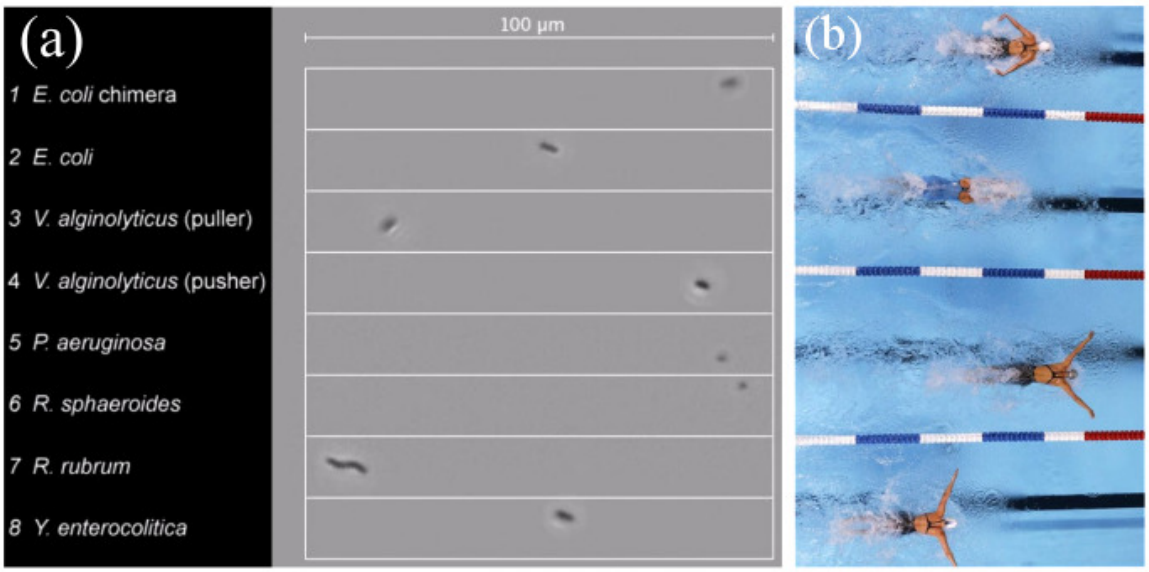

Figure 1.1: (a) Video still of Microbial Olympic swimming, at a low Reynolds number, $\mathrm{Re} \sim 10^{-5}$, organised by the extraordinary committee Youle et al.[7]. (b) Olympic swimming, at a high Reynolds number, $\mathrm{Re} \sim 10^{4}$. Photo: AP/Mark Humphrey. Note the differences in flows, turbulence and interactions with the walls.

piano, graphical design and natural objects, he sparked my imagination and established connections between science and the world we live in. Sadly, just as I was writing this thesis, Harold Kroto died on the 30th of April 2016. I hope his knowledge and enthusiasm for open discussion will be passed on for many future generations to come.

1.1 Micro-swimmers

First of all, one should ask: What is meant by a 'micro-swimmer'? I will define the word, or its abbreviation 'swimmer', as referring to a large group of entities that share two properties: they are small (say $<$ 1mm) and move autonomously through a liquid[8–10]. Because of their small size, the liquid motion is completely different compared to large-scale flows because the associated Reynolds number is very small (**Fig. 1.1**). Consequently, they must use special swimming strategies in order to move forwards at all, since viscosity dominates over inertial effects[11]. Moreover, because of the energy that swimmers produce continually at the smallest length scales, their motion cannot be described by classical thermodynamics since their nature is driven inherently out of equilibrium[12,13]. As a result, many unexpected phenomena can occur in swimmer systems, including giant number fluctuations, rectification, and collective motion[9,14,15]. We will consider two separate classes: biological and synthetic

micro-swimmers.

Prevalent examples of biological micro-swimmers are motile cells, such as swimming bacteria or spermatozoa, and many other unicellular organisms such as archaea, protozoa, algae and fungi. The study of unicellular organisms is interesting by itself, as they are thought to be the oldest form of life on Earth[16]. Another reason to study them is to prevent infections, such as malaria caused by the plasmodium parasite[17], sleeping sickness disease carried by trypanosomes[18], or many other bacterial, tropical or sexually transmitted diseases[19,20]. Multi-cellular swimmer examples are parasitic flatworms called schistosomes, responsible for Schistosomiasis, which is considered "the second most socioeconomically devastating parasitic disease" by the World Health Organisation[21–23], with "hundreds of millions infected worldwide".

On the other hand, during the last decades researchers have achieved technological breakthroughs that enable fabrication on colloidal (1 nm - 1 μm) length scales, developing techniques to create a new type of micro-machine: the 'active colloid' or self-motile particle[24,25]. Different designs have been proposed and realised, with direct applicability in nano-technology, medicine and soil remediation[26–28]. Active colloids, for instance, could be used to transport precious drugs through the bloodstream for tumour-directed local delivery[29,30]. Moreover, some of these ideas could be extended to systems beyond the micro-scale, as countless macroscopic self-propelled 'particles' that occur naturally have been identified, including fish[31], birds[32], insects[33] and humans[34].

Both for biological and synthetic micro-swimmers it is important to understand how they move through a liquid and how they interact with their environments, e.g. how they do or don't get stuck to surfaces. In order to achieve this, theoretical biophysicists can study 'model swimmers' that exhibit certain physical features of real organisms or micro-machines, without unnecessary complexity. Likewise, experimental biophysicists can study 'model organisms' that are easy to cultivate but represent a much larger class of species. The remainder of this section describes a number of the most-often studied theoretical, biological and synthetic model swimmers, following the latest developments in the literature.

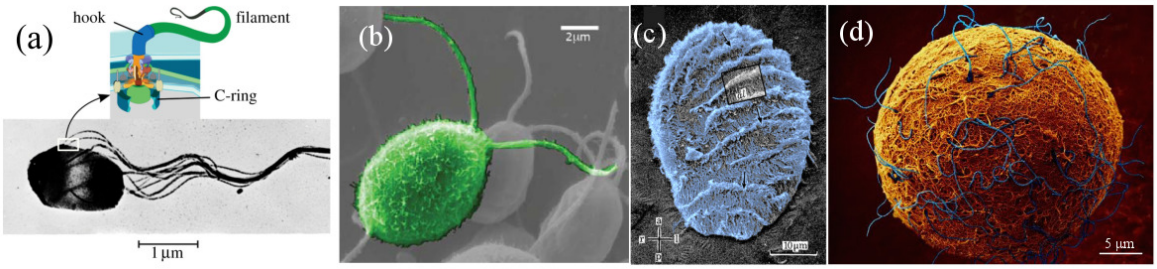

Figure 1.2: Biological model micro-swimmers: (a) Bright field image of a Peritrichous *Salmonella* bacterium with bundled flagella. Inset: the flagellar motor embedded in the cell membrane. Reproduced from Namdeo et al.[46]. (b) SEM image of a *Chlamydomonas reinhardtii* alga with two beating eukaryotic flagella. Reproduced from Elgeti et al.[8]. (c) SEM image of an *Opalina ranarum* ciliated protozoon with metachronal waves travelling along the black arrows (top to bottom). Adapted from Tamm and Horridge[47]. (d) SEM image of human spermatozoa (blue) attempting to fertilise an egg cell (orange). Photo: Yorgos Nikas/Getty Images.

1.1.1 Biological micro-swimmers

1.1.1.1 Bacteria

Bacteria are all around us. On the surfaces we touch, and even in the atmosphere the concentration of cells typically exceeds 10^4 m^{-3} over land[35]. A group of actinobacteria called *actinomycetes* is thought to give rain its 'argillaceous' or earthy smell[36,37], and there are suggestions that bacteria can even 'make rain' themselves by actively producing proteins that help ice crystals nucleate[38]. But bacteria are not just in the air around us. The adult human body is made up of approximately 10^{23} human cells[39] but the intestine hosts a factor of ten times more microorganisms, including archaea, eukarya and bacteria[40,41]. Moreover, compared to any other ecosystem, intestinal bacteria can reach the highest cell densities[42]. Gut microbes can even change the appetite, regulating food intake by releasing proteins that activate anorexigenic neurons in the brain[43]. It is therefore not surprising that understanding micro-organisms was already deemed of the greatest importance by early microbiologists such as Louis Pasteur[44,45].

Of all model micro-swimmers, bacteria are considered to be evolutionary lower as they are prokaryotes without a cell nucleus, mitochondria, or any other membrane-bound organelle. This makes it easy to change features like the swimming speed using genetic modifications, allowing interference with the swimming behaviour in a well-defined and controlled way[48,49]. If it has not been subjected to this 'genetic toolbox', the organism is said to be a member of

the 'wild type'. The typical wild-type bacterial cell body is cigar-shaped, about $\sim 1-2\mu$m long and $\sim 0.2-1\mu$m wide. The propulsion mechanism usually consists of one or more external helical flagella, ranging between $\sim 5-20\mu$m in length, rotated through a flagellar hook by a motor complex anchored to the cell wall[50]. The helix filament width is $\sim$ 6nm, the radius $\sim 0.25\mu$m and wavelength $\sim 2.5\mu$m[51]. Often-studied bacteria with a single flagellum located at the cell pole are *Vibrio cholerae* and *Pseudomonas aeruginosa*, while common 'peritrichous' species with multiple flagella, located at random positions on the cell, are *Escherichia coli* and *Salmonella* (**Fig. 1.2**a). In the latter case, when the different helices turn in the same direction they combine into flagellar bundles[52]. In both cases, the rotation of the flagella (with rotation rate $\sim$ 50Hz) generates a thrust force and torque, causing the cell body to counter-rotate (with rotation rate $\sim$ 10Hz) as it moves forwards (with speed $\sim 25\mu$m/s)[51,53,54].

Bacteria manifest a special swimming strategy called 'run-and-tumble' motion. During the *run* phase the cell moves along a straight line for $\sim$ 1s, and during the *tumble* phase it spontaneously reorientates within a short interval of $\sim$ 0.1s, only to run again[55]. This mechanism is not just meant to randomise the swimming direction, but to help organisms to optimise their search for nutrients or chemicals, a process called chemotaxis[11,56]. When the cell senses that it swims into a preferable region it tumbles less, and if it swims into a region with toxins or less nutrients it can tumble more. Uni-flagellated bacteria can initiate a tumble by reversing the flagellar rotation direction, and hence their motion, which triggers a buckling instability of the flagellar hook that abruptly changes the swimming direction[57]. Peritrichous bacteria can also tumble by making a few of the helical filaments rotate in different directions so that they unbundle, perturbing the linear motion[58]. Because the bundling process depends strongly on hydrodynamic interactions between the helices, these interactions are affected in the presence of walls. The tumbling efficiency of *E. coli* has been observed to decrease near surfaces[59].

1.1.1.2 Chlamydomonas

One of the model micro-organisms we shall consider frequently in this thesis is the unicellular green alga *Chlamydomonas reinhardtii*. The story of investigating 'Chlamy' started in a potato field in the vicinity of Amherst Massachusetts. In that field, in December 1945, G.M. Smith isolated the first strain that is still sold today[60]. Since then this species has received special

attention in several areas of cell and molecular biology, as it became a model organism to study organelle biogenesis, photosynthesis, intercellular recognition and growth of eukaryotic flagella[61]. Also physicists became interested in examining its swimming behaviour because it is a relatively uncomplicated organism with a few non-trivial features like self-synchronising flagella and an eyespot that can detect light intensity and direction[62,63]. Like for *E. coli*, a substantial genetic toolbox has been developed to change characteristics like the swimming speed, and the entire genome has been sequenced to facilitate experimental reproducibility[64]. Three main strains are used for research now: the Cambridge line, the Sager line, and the Ebersold/Levine line[61].

A typical wild-type cell is spheroid-shaped, $\sim 12\mu$m long and $\sim 9\mu$m wide[61]. Inside are all the standard eukaryotic organelles, including a cell nucleus, mitochondria, a Golgi apparatus, etc. A single eyespot is located near the equator that is used to perform phototactic motion towards light[65,66]. There is a single but large chloroplast, shaped like a horse shoe, where photosynthesis takes place. The chloroplast also contains a pyrenoid at the bottom of the cell, which is responsible for carbon fixation. Because of the sugar accumulation here the cell is slightly bottom-heavy, so gravity generates a gyrotactic torque that can turn the cell in the upward-swimming direction[67].

The most prominent organelles are the two slender flagella extruding from the front of the cell, each $\sim 12\mu$m in length and $\sim 0.25\mu$m thick, mounted on the cell wall via a basal body (**Fig. 1.2**b). The eukaryotic flagellum is more complex than the single-molecule bacterial helix, as it consists of over 500 different proteins[68]. The structure inside is called the 'axoneme', which is made of two central microtubules (basically long rigid protein rods) surrounded by nine microtubule pairs – this is often referred to as the standard 9+2 structure, which is universal in almost all lower- and higher-order organisms, including eukaryotic flagella, mammalian cilia and spermatozoa tails[68,69]. In fact, the flagellum is one of the oldest and most conserved structures in eurakyotic cells, including those of humans[70,71]. The central microtubule pair is attached to the tip of the flagellum, and they can slide with respect to the other nine pairs that are fixed at the basal body. The exact mechanism that generates the flagellar stroke is complex and not fully understood, but for this introduction it suffices to note that dynein molecular motor proteins[72] exert forces on the sliding microtubules to make them bend and initiate motion[73]. Consequently, Chlamy's two flagella beat in an equal and opposite fashion to one another, almost exactly in a single plane, like an Olympic

swimmer performing a breast stroke[74]. The typical beat frequency is ~ 50Hz, which leads to a net swimming speed of $\sim 100\mu$m/s. However, the velocity is time-varying as the body moves forwards approximately 3μm during the power stroke, but 1μm backwards during the recovery stroke, which leads to highly oscillatory flow fields[75].

A particularly interesting feature of Chlamy is that the two flagella can synchronise with one another[76]. This is important because the coordinated motion, sometimes called collective motion, of flagella plays a major role in more complex systems such as cell-cell signalling[77] and metachronal waves of cilia in the human respiratory tracts are able to transport viscous liquids very effectively[78,79]. Some researchers even suggest a connection to the initial stages of multicellularity[80,81]. Recent developments have shown that flagellar synchronisation can be explained with hydrodynamic interactions[82,83]. This has implications for the motion of Chlamy itself. When the flagella beat in phase the cell travels forward, but asynchronous beating allows the organism to make sharp turns, like the bacterial run-and-tumble mechanism[74,84]. Experiments have shown that the periodic breaststroke beating is recovered after 'phase-slips' due to transient hydrodynamic forcing[85], in good agreement with theoretical predictions[86,87].

1.1.1.3 Ciliated organisms

Rather than being propelled by a few large flagella mounted at the back (cf. bacteria) or front (cf. Chlamy) of the body, there are many species of unicellular organisms that are completely covered by a carpet of small flagella, called cilia. These ciliated organisms can swim by generating metachronal waves that travel along their surface, pushing liquid backward and hence driving the cell forward[88]. A very clear example of this 'squirming' motion is recorded for the *Opalina*[47] and the *Paramecium* protozoa[89,90], both approximately 200μm in size with typical swimming velocities of $10^3\mu$m/s (**Fig. 1.2**c). Another example is *Volvox carteri*, which is a spherical shell composed of up to 50.000 flagellate cells similar to *Chlamydomonas* that form a ciliary carpet[91], also $\sim 400\mu$m in diameter and swimming $\sim 10^2\mu$m/s. A very detailed list of many other ciliated species is given by Lighthill in his Von Neumann lecture[92].

This class of model organism, like Chlamy, has attracted considerable attention in the last few years because of the synchronisation between the cilia, particularly in connection with tissues of epithelial cells in humans[93–96]. Ciliary failure can lead to a number of diseases, called 'ciliopathies', including cystic fibrosis (CF), chronic obstructive pulmonary disease

(COPD) and primary ciliary dyskinesia (PCD)[97].

In the micro-swimmer literature, ciliated organisms are closely connected to a class of theoretical model swimmers called 'squirmers'[98,99]. In this model the swimmer-generated flows are determined by the slip velocity of the liquid at the cell surface, which couples well to the surface flows generated by the metachronal waves[24]. See §**1.2.6.2** for more details on this model.

1.1.1.4 Spermatozoa

The spermatozoon (motile sperm cell; cf. the non-motile 'spermatium') is key to the sexual reproduction of most animals and in particular mammals[100]. Because of the difficult path they have to follow to fertilise the egg, a selection procedure that is probably harsher than any job interview with only one in 10^7 candidates being successful[101], the cell must employ special strategies to find its way[102]. A number of guidance mechanisms has been suggested, including thermotaxis (motion with respect to temperature gradients)[103–105], chemotaxis (motion w.r.t chemical gradients)[106,107] and rheotaxis (motion w.r.t flow strength gradients)[108–111]. For mammalian sperm it is still very much a question of debate which of these is the dominant mechanism. However, for marine invertebrates like sea urchins there is a reasonable consensus that sperm cells are attracted by signalling peptides released by the egg[112,113].

The typical human spermatozoon has a head that carries the genetic material, 4.8μm long and 3.3μm wide[114], and a eukaryotic flagellum up to 20μm long (**Fig. 1.2**d), which is connected via a middle section that forms the basal body and is lined with mitochondria to generate energy (see §**1.1.1.2**). Most other mammalian cells also follow these dimensions closely, although an interesting exception is the giant sperm of the *Drosophila bifurca* fruit fly, measuring up to 58mm in length[115,116]. Propulsion is generated by a bending wave travelling down the flagellum[117]. The swimmer moves in a straight line when the beat is symmetrical about the axis that defines the swimming direction, but the introduction of an asymmetry leads to a steering mechanism[118,119] that is coupled with the cell's chemo-sensors[120] which can lead to complex sperm navigation along helical paths[121].

1.1.2 Synthetic micro-swimmers

Several classes of synthetic swimmers, often also called 'active particles', have emerged recently in order to understand the physics of biological micro-swimmers, but also to engineer new

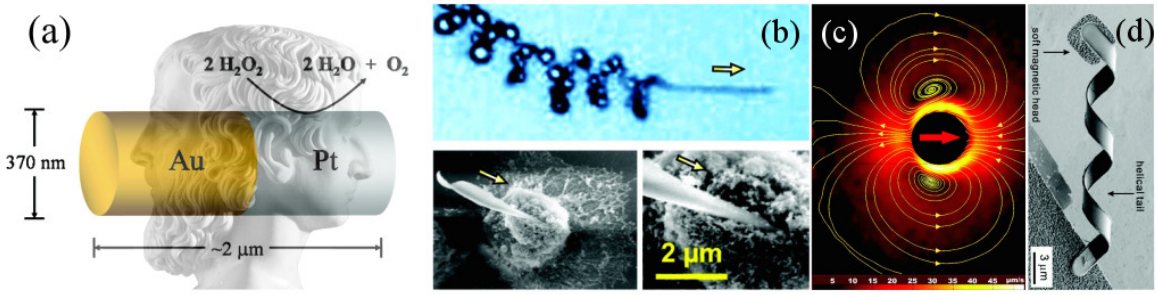

Figure 1.3: Synthetic model micro-swimmers: (a) Example of a Janus particle: A rod with gold and platinum at either end, with a chemical reaction is catalysed at the Pt side to drive the particle. Adapted from Paxton et al.[127]. (b) A tubular nano-jet catalyses a reaction inside a tube, which is conically and spirally shaped here so that it rotates and moves along a helical trajectory. Reproduced from Solovev et al.[128]. (c) The flow field produced by an active droplet in the laboratory frame, with streamlines (yellow) and magnitude (colour scale). Reproduced from Herminghaus et al.[129] (d) A magnetic helix particle, fabricated by the self-scrolling of helical nano-belts and driven by a magnetic head. Reproduced from Zhang et al.[130].

types of self-propelled vessels that can perform tasks in locations that cannot be reached by conventional probes[15,122–126] or allow minimally invasive medicine[27]. In the words of Geoffrey Ozin[25], "Such tiny machines, individually or assembled into designed architectures, might someday transport medicine in the human body, conduct operations in cells, move cargo around microfluidic chips, manage light beams, agitate liquids close to electrode surfaces, and search for and destroy toxic organic molecules in polluted water streams." This section aims to summarise how some of these 'nanomachine dreams' might be converted into 'dream nanomachines'.

1.1.2.1 Catalytic Janus particles

As mentioned in the Nobel lecture of Pierre-Gilles de Gennes[131], Janus particles are named[132] after the two-faced Roman god, because they have a surface with at least two different physical properties (**Fig. 1.3**a). The particles can become motile when energy is provided to them, either internally (e.g. by the use of a fuel) or externally (e.g. via the medium they sit in). Among the first experimental successes were the catalytic nano-rods[127,133], which are bimetallic Au-Pt rods where the chemical reaction $2H_2O_2 \rightarrow 2H_2O + O_2$ is catalysed only at the platinum end. Hence, an asymmetric and out-of-equilibrium distribution of reaction products is formed around the particle, such that it is driven forwards. The exact mechanism that provides the resultant forces is still under debate, but much theoretical work

has been done to understand this process called 'diffusio-phoresis'[134–140]. Other experimental realisations of this swimmer type are partially coated polystyrene or silica beads[141,142] or even light-activated colloidal surfers[143].

1.1.2.2 Thermo-phoretic particles

Another mechanism to generate self-propulsion is by creating thermal gradients around the particle, a process called 'thermo-phoresis'. This has been achieved by illuminating a half-coated bead with an intense light beam, such that a local temperature difference drives the particle forward[144–147]. Even though the energy is provided by an external source, all forces applied to the particle and the fluid are local, which strongly affects the local fluid mechanics (see §**1.2.4**)[145]. A very interesting extension of this mechanism is achieved by immersing the particles in a binary fluid mixture near the demixing critical point[148], which also allows to explore viscoelastic mixtures[149].

1.1.2.3 Tubular micro-jets

Whereas Janus particles employ an asymmetry in the surface lining, it is also possible to engineer symmetric particles that move. An example is the tubular micro-jet, a hollow cylinder with Pt inside and Au outside[150,151]. The catalysis happens inside the tube, so that oxygen bubbles emerge only from one end, driving the particle in the other direction by spontaneous symmetry breaking. Furthermore, if the tubes are rolled up asymmetrically they move in a corkscrew-like trajectory (**Fig. 1.3**b), allowing them to drill and embed themselves into biomaterials[128].

1.1.2.4 Active droplets

Active droplets are a special type of particle because they are not solid. One rendition is a water drop containing bromine fuel, immersed in oil with surfactant molecules at the interface[129,152,153]. The bromine reacts chemically at the interface, which by spontaneous symmetry breaking leads to propulsion due to Marangoni flows[154]. Another type is a droplet made of a liquid metal like EGaIn or Galistan in contact with Aluminium flakes in an electrolyte solution[155]. Particularly noteworthy of these active droplets is that they mimic the locomotion of 'squirming' organisms (see §**1.1.1.3**), since their propulsion is induced by interfacial slip flows (**Fig. 1.3**c).

1.1.2.5 Magnetic particles

The magnetic helix, turned by a rotating external magnetic field such that it drills its way through the liquid[130,156] (**Fig. 1.3**d), is perhaps the least complicated synthetic micro-swimmer but intricate follow-ups have appeared[157,158]. Note that these magnetic helices are not autonomous swimmers, because they are free of external forces but not of external torques. Other sophisticated magnetically actuated particles exist, including magnetic disks[159] and rotating dumb-bells[160]. Moreover, by linking a chain of magnetic beads attached to a red blood cell, an extraordinary swimmer was made that mimics the beating flagellum of a spermatozoon[161]. Finally, using a ferrofluid as 'digital material' it is possible to make logic gates for droplet computing[162].

1.2 Hydrodynamics of Micro-swimmers

In order to understand the behaviour of micro-swimmers, their dynamics or statistics, it is important to realise in what conditions they operate and to what forces they are subjected. By moving its body, a swimmer exerts forces on the surrounding liquid that generate flow fields. Subsequently, these flows can be reflected by other immersed or solid objects nearby. Reflected flows, in turn, affect the motion of the swimmer. This feedback loop of 'hydrodynamic interactions' can be described with a mathematical framework, which is outlined below.

1.2.1 The Stokes equations

The flow of liquids on macroscopic scales is governed by the Navier-Stokes equations[163],

$$\rho\left(\frac{\partial \boldsymbol{u}}{\partial t} + (\boldsymbol{u}\cdot\nabla)\boldsymbol{u}\right) = \boldsymbol{\nabla}\cdot\boldsymbol{S} + \boldsymbol{f}, \tag{1.1}$$

$$\frac{\partial \rho}{\partial t} + \nabla\cdot(\rho\boldsymbol{u}) = 0, \tag{1.2}$$

where $\boldsymbol{u}(\boldsymbol{x},t)$ is the velocity field of the fluid at position $\boldsymbol{x}$ and time t, $\rho(\boldsymbol{x},t)$ is the fluid density, $\boldsymbol{S}(\boldsymbol{u},\boldsymbol{x},t)$ is the stress tensor and $\boldsymbol{f}$ are other external force densities, e.g. gravity $\boldsymbol{f}_g = -\rho\boldsymbol{g}$. Here the first equation is derived from the momentum balance of a fluid parcel, or momentum conservation in the absence of external forces, and the second from conservation of mass. Further equations for energy and entropy balances do exist, but since we consider

isothermal systems, **Eqs. 1.1–1.2** fully describe the physics of interest. The stress tensor is given by a constitutive equation for a particular fluid [164]. Particularly, for a simple Newtonian fluid like water at room temperature and pressure the stress is

$$S_{ij} = -p\delta_{ij} + \mu\left(\frac{\partial u_i}{\partial x_j} + \frac{\partial u_j}{\partial x_i}\right) + \xi\delta_{ij}\frac{\partial u_k}{\partial x_k}, \tag{1.3}$$

using tensor notation in Cartesian coordinates where $i, j \in \{1, 2, 3\}$, δ_{ij} is the Kronecker delta, $p(\boldsymbol{x}, t)$ is the pressure, μ is the fluid's dynamic viscosity, and ξ is the bulk or volume viscosity. Inserting this tensor in **Eq. 1.1** yields

$$\rho\left(\frac{\partial \boldsymbol{u}}{\partial t} + (\boldsymbol{u}\cdot\nabla)\boldsymbol{u}\right) = -\boldsymbol{\nabla}p + \mu\nabla^2\boldsymbol{u} + (\xi + \mu/3)\boldsymbol{\nabla}(\boldsymbol{\nabla}\cdot\boldsymbol{u}) + \boldsymbol{f}. \tag{1.4}$$

In most systems of interest to micro-swimmer dynamics it is common to assume that the medium is incompressible, $\boldsymbol{\nabla}\cdot\boldsymbol{u} = 0$, so that the bulk viscosity terms do not contribute. Hence, **Eq. 1.4** reduces to the result first derived by Navier [165]

$$\rho\left(\frac{\partial \boldsymbol{u}}{\partial t} + (\boldsymbol{u}\cdot\nabla)\boldsymbol{u}\right) = -\boldsymbol{\nabla}p + \mu\nabla^2\boldsymbol{u} + \boldsymbol{f}. \tag{1.5}$$

Not all animals in this equation are equal [166], and to determine which of the terms are relevant in the world of micro-swimmers it is helpful to scale the time by a characteristic value T_0, the velocity field by U_0 and length by L_0. Hence, one can introduce the dimensionless variables $\tilde{\boldsymbol{x}} = \boldsymbol{x}/L_0$, $\tilde{t} = t/T_0$, $\tilde{\boldsymbol{u}} = \boldsymbol{u}/U_0$, $\tilde{p} = (p - p_{\text{atm}})/(\mu U_0/L_0)$, $\tilde{\boldsymbol{f}} = \boldsymbol{f}/(\mu U_0/L_0^2)$, and $\tilde{\nabla} = L_0\nabla$. Rewriting **Eq. 1.5** in terms of these variables yields

$$\mathrm{Re}_\circ\frac{\partial \tilde{\boldsymbol{u}}}{\partial \tilde{t}} + \mathrm{Re}(\tilde{\boldsymbol{u}}\cdot\tilde{\boldsymbol{\nabla}})\tilde{\boldsymbol{u}} = -\tilde{\boldsymbol{\nabla}}\tilde{p} + \tilde{\nabla}^2\tilde{\boldsymbol{u}} + \tilde{\boldsymbol{f}}, \tag{1.6}$$

where the Reynolds number and the oscillatory Reynolds number are

$$\mathrm{Re} = \frac{\rho U_0 L_0}{\mu} = \frac{U_0 L_0}{\nu}, \tag{1.7}$$

$$\mathrm{Re}_\circ = \frac{\rho L_0^2}{\mu T_0} = \frac{L_0^2}{\nu T_0}, \tag{1.8}$$

and $\nu = \mu/\rho$ is called the kinematic viscosity [8,10].

These numbers can be interpreted as the ratio between the inertial and viscous forces. By inserting the characteristic size and swimming speed of a bacterium (§**1.1.1.1**), $L_0 \sim 1\mu$m and $U_0 \sim 10\mu$m, together with $\rho = 10^3\text{kg/m}^3$ and $\mu = 10^{-3}\text{kg/ms}$, one finds $\mathrm{Re} \sim 10^{-5}$

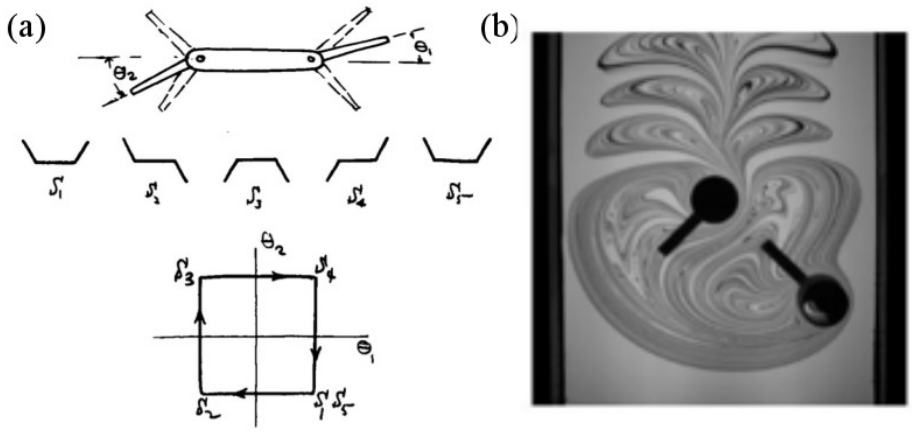

Figure 1.4: (a) Purcell's three-link swimmer has two degrees of freedom: the angles θ_1 and θ_2 of the two wings with respect to the body. It can only swim if it changes its conformation (middle) such that the angles move through a non-reciprocal loop in $\theta_1 - \theta_2$ space (bottom). Reproduced from Purcell[11]. (b) A droplet of ink is mixed into a viscous liquid with two paddles oriented at angles θ_1 and θ_2. If the mixing path in $\theta_1 - \theta_2$ space is retraced, the ink droplet reemerges unmixed, as shown in the film of G. I. Taylor[168]. Image reproduced from Olivier Dauchot[169].

so the viscosity is overwhelmingly dominant. Therefore, the Reynolds number of a typical micro-swimmer is often assumed to be zero, so the non-linear term in **Eq. 1.6** can be dropped. The importance of the oscillatory Reynolds number depends on the characteristic timescale T_0 compared to L_0/U_0. For slow processes compared to swimming it is common to define $T_0 = L_0/U_0$ so that $\mathrm{Re}_\circ = \mathrm{Re} \sim 0$. To study fast processes however, like flows near the rapidly rotating bacterial helix, the first term on the LHS of **Eq. 1.6** can be kept, leaving the linearised Landau-Lifshitz Navier-Stokes equation

$$\rho \frac{\partial \boldsymbol{u}}{\partial t} = -\boldsymbol{\nabla} p + \mu \nabla^2 \boldsymbol{u} + \boldsymbol{f}. \tag{1.9}$$

This equation allows to study time correlations in the fluid or propagation of pressure waves at large scales[167]. However, in the micro-swimmer systems studied in this thesis we assume $T_0 \sim L_0/U_0$, so **Eqs. 1.2,1.9** reduce to the Stokes equations

$$0 = -\boldsymbol{\nabla} p + \mu \nabla^2 \boldsymbol{u} + \boldsymbol{f}, \tag{1.10}$$

$$0 = \boldsymbol{\nabla} \cdot \boldsymbol{u}. \tag{1.11}$$

These equations are linear and time-independent, which has important implications for the strategies that swimmers must employ to achieve propulsion. The scallop theorem states

that, in the words of Edward Purcell[11], "I change my body into a certain shape and then I go back to the original shape by going through the sequence in reverse... So, if the animal tries to swim by a reciprocal motion, it can't go anywhere." Another way of phrasing this is that any effective swimming stroke cannot be reciprocal, so a swimmer must have more than one degree of freedom and break time-reversal invariance (**Fig. 1.4**a). Bacteria overcome this challenge with their complicated rotary motor[50], whereas sperm cells make the reciprocal beating of the flagellum non-reciprocal by allowing for extra degrees of freedom via elasticity[120]. *Chlamydomonas* is motile despite its stroke being almost reciprocal, although for every 3μm forwards it goes 1μm backwards during the recovery stroke (§**1.1.1.2**). The design of new micro-machines must take this difficulty into account[170].

A second consequence is that Stokesian liquids are hard to stir, firstly because large forces are required to drive viscous liquids and diffusion is slow, secondly because reciprocality leads to zero mixing, and thirdly because there are no intrinsic non-linearities that can lead to chaotic flows[171]. For example, **Fig. 1.4**b shows two paddles that have rotated to mix a droplet of ink into a viscous liquid. When the paddles are rotated in reverse the droplet reappears, whole[168,169,172–175]. Despite the difficulty, however, it is possible to engineer devices that mix efficiently[176,177], or break droplets into many smaller ones[178]. Another interesting way to approach chaotic fluid advection is by studying the topology of the liquid as it is stirred[179].

1.2.2 The Stokeslet

To solve the Stokes equations (**Eq. 1.10** and **Eq. 1.11**), the linear properties are key. The fundamental solution is the flow and pressure due to a point force, called a 'Stokeslet'. We write the external force $f_j^{\mathrm{S}}(\boldsymbol{x},t) = f_j(t)\delta^d(\boldsymbol{x}-\boldsymbol{y})$ in **Eq. 1.10**, where $\delta^d(\boldsymbol{x})$ is the Dirac delta function in d dimensions, and we aim to find a solution of the form

$$p^{\mathrm{S}}(\boldsymbol{x},\boldsymbol{y},t) \;=\; f_j\cdot\mathcal{P}_j, \qquad \text{and} \qquad u_i^{\mathrm{S}}(\boldsymbol{x},\boldsymbol{y},t) = f_j\cdot\mathcal{G}_{ij}, \tag{1.12}$$

where $\mathcal{P}_j$ and $\mathcal{G}_{ij}$ are called the Green's functions or Oseen tensors. Fourier transforming the Stokes equations **1.10**–**1.11**, we obtain

$$-ik_\alpha\hat{p} \;=\; -\mu k^2\hat{u}_\alpha + f_\alpha \qquad \text{and} \qquad -ik_\alpha\hat{u}_\alpha = 0, \tag{1.13}$$

where $\hat{p}$ and $\hat{u_\alpha}$ are the transformed pressure and velocity fields. Inserting **Eq. 1.12**, rewriting $f_\alpha = \delta_{\alpha\beta} f_\beta$ and dividing through f_β yields

$$-ik_\alpha \hat{\mathcal{P}}_\beta = -\mu k^2 \hat{\mathcal{G}}_{\alpha\beta} + \delta_{\alpha\beta}, \tag{1.14}$$

$$-ik_\alpha \hat{\mathcal{G}}_{\alpha\beta} = 0. \tag{1.15}$$

Multiplying **Eq. 1.14** through by k_α and using **Eq. 1.15** gives

$$-ik_\alpha k_\alpha \hat{\mathcal{P}}_\beta = k_\alpha \delta_{\alpha\beta} \tag{1.16}$$

$$\therefore \quad \hat{\mathcal{P}}_\beta = \frac{ik_\beta}{k^2}, \tag{1.17}$$

which is the solution of the pressure Green's function in Fourier space. For the velocity Green's function, we insert **Eq. 1.17** into **Eq. 1.14** to find the transformed solution

$$\mu \hat{\mathcal{G}}_{\alpha\beta} = \frac{\delta_{\alpha\beta}}{k^2} - \frac{k_\alpha k_\beta}{k^4}. \tag{1.18}$$

Inverse Fourier transforming **Eqs. 1.17–1.18** in three dimensions yields the Green's functions

$$\mathcal{P}_\beta(\boldsymbol{x}, \boldsymbol{y}) = -\partial_\beta \left(\frac{1}{4\pi r} \right), \tag{1.19}$$

$$\mathcal{G}_{\alpha\beta}(\boldsymbol{x}, \boldsymbol{y}) = \frac{1}{8\pi\mu} \left(\frac{\delta_{\alpha\beta}}{r} + \frac{r_\alpha r_\beta}{r^3} \right), \tag{1.20}$$

where $\boldsymbol{r} = \boldsymbol{x} - \boldsymbol{y}$ and $r = |\boldsymbol{r}|$. Therefore, the pressure and velocity fields of a three-dimensional Stokeslet are

$$p^{\mathrm{S}}(\boldsymbol{x}, \boldsymbol{y}, \boldsymbol{f}) = f_j(t) \cdot \frac{r_j}{4\pi r^3}, \tag{1.21}$$

$$u_i^{\mathrm{S}}(\boldsymbol{x}, \boldsymbol{y}, \boldsymbol{f}) = f_j(t) \cdot \frac{1}{8\pi\mu} \left(\frac{\delta_{ij}}{r} + \frac{r_i r_j}{r^3} \right). \tag{1.22}$$

Notice that this solution has a long-ranged character, as the flow decays with distance as $1/r$, which is a major property of Stokesian hydrodynamics [163].

1.2.3 The Faxén relations

Using the famous Stokes relation $\boldsymbol{f} = 6\pi\mu a_{\mathrm{c}} \boldsymbol{v}_{\mathrm{c}}$, the flow at position $\boldsymbol{x}$ generated by a sphere (or 'colloid') of radius a_{c} at position $\boldsymbol{y}$ that is pulled through a viscous liquid with velocity

$\boldsymbol{v}_c(t)$ can be written[180] in terms of **Eq. 1.22** as

$$\boldsymbol{u}^{\mathrm{c}}(\boldsymbol{r},\boldsymbol{v}_{\mathrm{c}}) = \left(1+\frac{a_{\mathrm{c}}^2}{6}\nabla^2\right)\boldsymbol{u}^{\mathrm{S}}(\boldsymbol{r},\boldsymbol{f}=6\pi\mu a_{\mathrm{c}}\boldsymbol{v}_{\mathrm{c}}) \tag{1.23}$$

$$= \boldsymbol{v}_{\mathrm{c}}\left(\frac{3a_{\mathrm{c}}}{4r}+\frac{a_{\mathrm{c}}^3}{4r^3}\right)+\boldsymbol{r}\frac{\boldsymbol{v}_{\mathrm{c}}\cdot\boldsymbol{r}}{r^2}\left(\frac{3a_{\mathrm{c}}}{4r}-\frac{3a_{\mathrm{c}}^3}{4r^3}\right), \tag{1.24}$$

where $\boldsymbol{r}=\boldsymbol{x}-\boldsymbol{y}$. Indeed, the flow at the surface satisfies the no-slip condition in the rest frame $\boldsymbol{u}^{\mathrm{c}}(r=a_{\mathrm{c}})=\boldsymbol{v}_{\mathrm{c}}$.

Conversely, using the Lorentz reciprocal theorem, it can be shown that the force and torque acting on a sphere translating with velocity $\boldsymbol{v}_c$ and rotating with angular velocity $\boldsymbol{\omega}_c$ in an external flow $\boldsymbol{u}^{\mathrm{E}}(\boldsymbol{x})$ with vorticity $\boldsymbol{\omega}^{\mathrm{E}}(\boldsymbol{x})$ are given by

$$\boldsymbol{F} = 6\pi\mu a_{\mathrm{c}}\left(1+\frac{a_{\mathrm{c}}^2}{6}\nabla^2\right)\boldsymbol{u}^{\mathrm{E}}(\boldsymbol{x})-6\pi\mu a_{\mathrm{c}}\boldsymbol{v}_{\mathrm{c}}, \tag{1.25}$$

$$\boldsymbol{T} = 8\pi\mu a_{\mathrm{c}}^3\left(\boldsymbol{\omega}^{\mathrm{E}}(\boldsymbol{x})-\boldsymbol{\omega}_{\mathrm{c}}\right), \tag{1.26}$$

which are referred to as the Faxén relations[163]. From these, for example, it is possible to estimate the advection velocity $\boldsymbol{v}_c$ of a spherical particle in an arbitrary ambient flow.

1.2.4 Multipole expansion of the swimmer-generated flow field

The flow fields generated by the propulsion of micro-swimmers have gathered a large interest from the fluid mechanics community[181–186] because they play an indispensable role in their ecological traits such as mechanosensing[187,188], energy expenditure[75], rheology[189–191], fluid mixing[192–198] and nutrient uptake[199–201]. Despite the widespread implications of swimmer-generated flows, the underlying hydrodynamics and its impact on the ecology of swimming cells have remained largely unexplored.

From the result of **Eq. 1.22**, an approximation of flow field at position $\boldsymbol{x}$ generated by a micro-swimmer can be found. Consider a swimmer located at position $\boldsymbol{y}_{\mathrm{s}}$ with a surface S located at position $\boldsymbol{y}=\boldsymbol{y}_{\mathrm{s}}+\boldsymbol{\xi}$. By changing its shape, the swimmer exerts forces and torques on the fluid. We model these forces as a distribution of Stokeslets, $\boldsymbol{f}(\boldsymbol{\xi})$, summed over the swimmer's surface $S(\boldsymbol{\xi})$, and define the relative position variable $\boldsymbol{r}=\boldsymbol{x}-\boldsymbol{y}_{\mathrm{s}}$, as shown in **Fig. 1.5**. Using **Eq. 1.22**, the swimmer-generated flow field is then given by

$$u_i^{\mathrm{sw}}(\boldsymbol{x},\boldsymbol{y}_{\mathrm{s}},\boldsymbol{p}_{\mathrm{s}}) = \int_{S(\boldsymbol{\xi})}\mathcal{G}_{ij}(\boldsymbol{x},\boldsymbol{y}_{\mathrm{s}}+\boldsymbol{\xi})f_j(\boldsymbol{\xi})dS = \int_{S(\boldsymbol{\xi})}\mathcal{G}_{ij}(\boldsymbol{r}-\boldsymbol{\xi},\boldsymbol{0})f_j(\boldsymbol{\xi})dS. \tag{1.27}$$

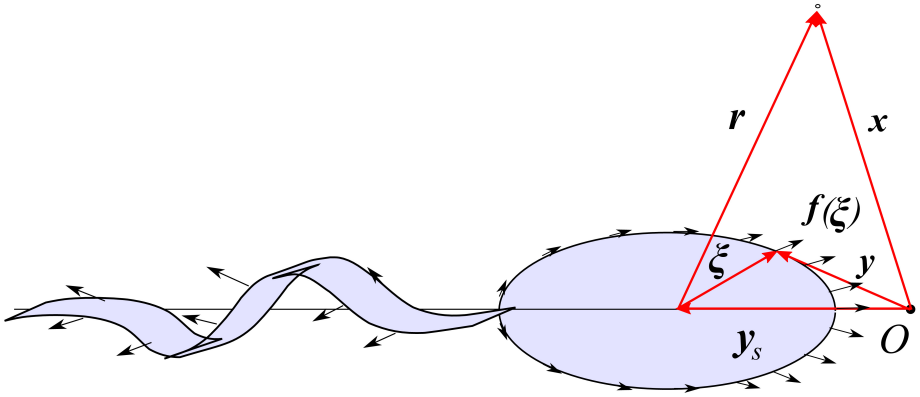

Figure 1.5: Geometry diagram for a swimmer in an infinite fluid. The swimmer generates a distribution of forces $\boldsymbol{f}(\boldsymbol{\xi})$ over its surface $S(\boldsymbol{\xi})$ acting on the fluid, and hence induces a fluid velocity field $\boldsymbol{u}^{\mathrm{sw}}(\boldsymbol{x}, \boldsymbol{y}_{\mathrm{s}}, \boldsymbol{p}_{\mathrm{s}})$.

Like in electrostatics[202], it is possible to perform a multipole expansion of the swimmer's velocity field. The field is a vector now, unlike the scalar-type electrostatic potential, but the same concepts apply. Expanding for small $\boldsymbol{\xi}$ values around the relative position $\boldsymbol{r}$ gives

$$u_i^{\mathrm{sw}}(\boldsymbol{r}) = \int_S \left(\mathcal{G}_{ij} - \frac{\partial \mathcal{G}_{ij}}{\partial r_k}\xi_k + \frac{1}{2}\frac{\partial^2 \mathcal{G}_{ij}}{\partial r_k \partial r_l}\xi_k\xi_l + \dots \right) f_j(\boldsymbol{\xi}) dS. \tag{1.28}$$

The Oseen tensor and its derivatives are independent of $\boldsymbol{\xi}$, thus

$$u_i^{\mathrm{sw}}(\boldsymbol{r}) = \mathcal{G}_{ij}\left(\int_S f_j dS\right) - \frac{\partial \mathcal{G}_{ij}}{\partial r_k}\left(\int_S f_j \xi_k dS\right) + \frac{1}{2}\frac{\partial^2 \mathcal{G}_{ij}}{\partial r_k \partial r_l}\left(\int_S f_j \xi_k \xi_l dS\right) + \dots \tag{1.29}$$

where the arguments have been omitted for transparency. We identify the successive integral expressions as the force strength tensor F_j, dipole moment tensor D_{jk}, and the quadrupole moment tensor Q_{jkl} etc. Hence we obtain the expansion

$$u_i^{\mathrm{sw}}(\boldsymbol{r}) = \mathcal{G}_{ij}\mathrm{F}_j - \mathcal{G}_{ijk}\mathrm{D}_{jk} + \frac{1}{2}\mathcal{G}_{ijkl}\mathrm{Q}_{jkl} - \frac{1}{3!}\mathcal{G}_{ijklm}\mathrm{O}_{jklm} + \dots, \tag{1.30}$$

where the multipole moment tensors are

$$\mathrm{F}_j = \int_S f_j dS, \qquad \mathrm{D}_{jk} = \int_S f_j \xi_k dS, \qquad \mathrm{Q}_{jkl} = \int_S f_j \xi_k \xi_l dS, \quad \dots, \tag{1.31}$$

and where the dipole singularity tensor $\mathcal{G}_{ijk}$, the quadrupole singularity tensor $\mathcal{G}_{ijkl}$, etc. are successive derivatives of the Oseen tensor $\mathcal{G}_{ij}$ with respect to $\boldsymbol{r}$. Therefore, the successive terms in **Eq. 1.30** scale as r^{-1}, r^{-2}, r^{-3}, etc. A more detailed explanation of the multipole expansion can be found in the work by Yeomans et al.[180] or Jeffrey and Onishi[203].

1.2.5 Physical significance of the multipole contributions

An autonomous swimmer cannot rely on external forces to move forwards. Hence, we assume that the total force $\mathrm{F}_j = 0\ \forall j$, if the effects of gravity are negligible. This assumption is true for swimmers that are neutrally buoyant, or if their sedimentation velocity is negligible compared to their swimming speed[204]. Therefore, the swimmer-generated flow field (**Eq. 1.30**) reduces to

$$\boldsymbol{u}^{\mathrm{sw}}(\boldsymbol{x}, \boldsymbol{y}_{\mathrm{s}}, \boldsymbol{p}_{\mathrm{s}}) \quad = \quad \boldsymbol{u}^{\mathrm{D}} + \boldsymbol{u}^{\mathrm{QU}} + \boldsymbol{u}^{\mathrm{O}} + \boldsymbol{u}^{\mathrm{H}} + \dots \tag{1.32}$$

which contains Stokes dipole $\boldsymbol{u}^{\mathrm{D}}(\boldsymbol{x}, \boldsymbol{y}_{\mathrm{s}}, \boldsymbol{p}_{\mathrm{s}})$, quadrupole $\boldsymbol{u}^{\mathrm{Q}}(\boldsymbol{x}, \boldsymbol{y}_{\mathrm{s}}, \boldsymbol{p}_{\mathrm{s}})$, octupole $\boldsymbol{u}^{\mathrm{O}}(\boldsymbol{x}, \boldsymbol{y}_{\mathrm{s}}, \boldsymbol{p}_{\mathrm{s}})$ and higher order terms. Moreover, many micro-swimmers have, to a good approximation, a shape that is cylindrically symmetric about the swimming direction. This helpfully restricts the number of non-zero components of the swimmer multipole moments. If the force distribution is symmetric about the swimming direction, $\boldsymbol{p}_{\mathrm{s}}$, many of the components in the multipole moment tensors $\mathrm{D}_{jk}, \mathrm{Q}_{jkl}$ vanish by symmetry. In the following subsections we provide explicit expressions of the residual multipole flow fields and describe their physical significance.

1.2.5.1 Dipolar contribution

Next to being force-free, an autonomous swimmer is also not subjected to any net external torques. Hence, together with the cylindrical symmetry, only one out of nine dipolar moments D_{jk} is non-zero and linearly independent[180]. Therefore the leading order term in **Eq. 1.32**, given in terms of the Stokeslet flow (**Eq. 1.22**), is the dipolar flow field

$$\boldsymbol{u}^{\mathrm{D}}(\boldsymbol{x}, \boldsymbol{y}_{\mathrm{s}}, \boldsymbol{p}_{\mathrm{s}}) = \kappa\ (\boldsymbol{p}_{\mathrm{s}} \cdot \tilde{\boldsymbol{\nabla}}) \boldsymbol{u}^{\mathrm{S}}(\boldsymbol{x}, \boldsymbol{y}_{\mathrm{s}}, 8\pi\mu\ \boldsymbol{p}_{\mathrm{s}}) \tag{1.33}$$

$$= \frac{\kappa}{r^3}(3\cos^2\theta - 1)\boldsymbol{r}, \tag{1.34}$$

where the derivative $\tilde{\boldsymbol{\nabla}}$ acts on the swimmer position $\boldsymbol{y}_{\mathrm{s}}$, θ is the angle between $\boldsymbol{p}_{\mathrm{s}}$ and $\boldsymbol{r}$, and κ is the dipole moment with units $[\mu\mathrm{m}^3/\mathrm{s}]$.

Physically this flow can be seen as generated by two forces, equal and opposite to one another, representing the balanced propulsion and drag. If the forces are pointing away from each other, the swimmer is called a 'pusher' with a positive dipole moment κ, whereas it is

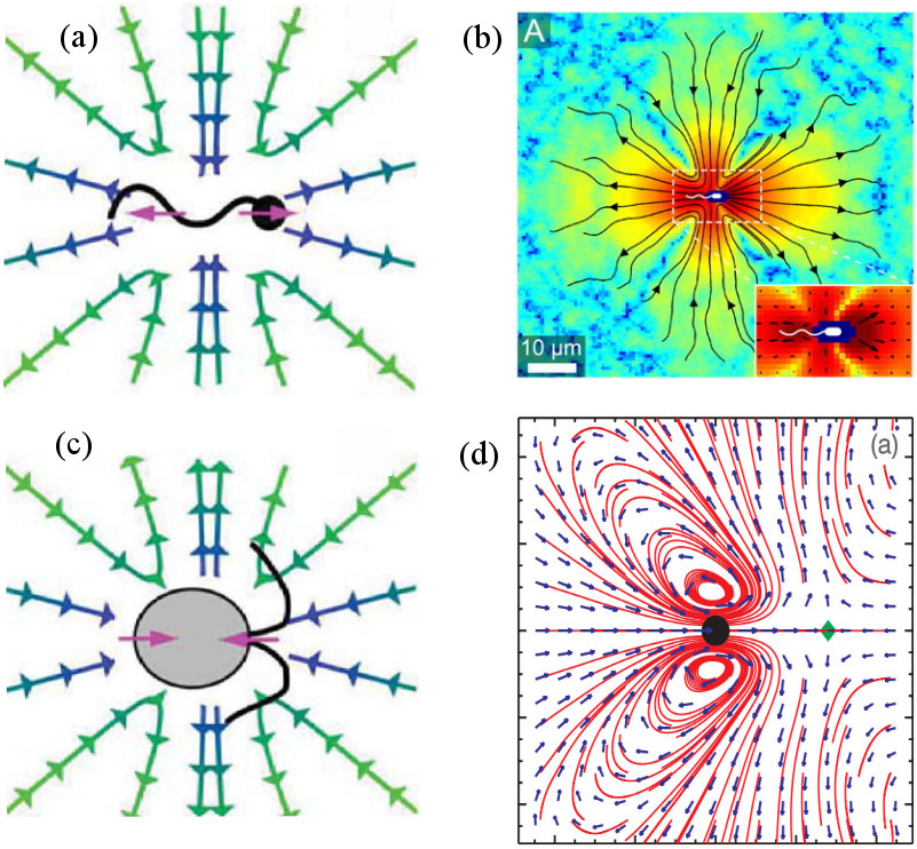

Figure 1.6: Schematic and experimentally measured flow fields generated by a pusher-type *E. coli* bacterium (a-b; $\kappa > 0$) and a puller-type *Chlamydomonas* alga (c-d; $\kappa < 0$). Adapted from Refs.[8,75,205].

negative for a 'puller' with the forces pointing towards each other (**Fig. 1.6**). The dipolar streamlines are oriented in the radial direction, with a cross-over from outward to inward flows at an angle $\theta = \arccos(1/\sqrt{3}) \sim 54.7°$. Pushers effectively push liquid forward with their head and backward with their tail, and suck liquid in along their waist to conserve liquid mass. This flow is called 'extensile'. Pullers effectively pull liquid in towards their body with their flagella, and out along the waist. This flow is called 'contractile'. The advantage of this nomenclature is that swimmers can be classified in a physically meaningful way according to their dipole moment κ, since the experimental technique of particle image velocimetry (PIV) can now be used to measure flow fields at microscopic levels directly[206]. For example, the flow field generated by *E. coli* bacteria has been measured in experiments[205] and determined to be extensile. *Chlamydomonas* algae flows were measured in a thin liquid film as a function of time throughout the beat cycle[75], and determined to be contractile. Other examples of pushers are sperm cells and dinoflagellates, and other pullers are *Tetraselmis suecica* or

Pyramimomas parkeae[207].

1.2.5.2 Quadrupolar contribution

Some swimmers, however, have the propulsion and drag forces spread out over their surface very equally, so that $\kappa \sim 0$. These are called 'neutral' swimmer with a predominantly quadrupolar flow field. Ciliated organisms (§**1.1.1.3**) and active droplets[152] are good examples. Some of these higher-order moments have been measured for the microphyte *Volvox carteri*[208]. The quadrupolar flow field of a cylindrically symmetric swimmer can be written as

$$\boldsymbol{u}^{\mathrm{QU}}(\boldsymbol{x}, \boldsymbol{y}_{\mathrm{s}}, \boldsymbol{p}_{\mathrm{s}}) = -\frac{1}{2}\left(Q_{\parallel}\tilde{\nabla}_{\parallel}^2 + Q_{\perp}\tilde{\nabla}_{\perp}^2 - 2Q_r(\boldsymbol{p}_{\mathrm{s}}\cdot\tilde{\boldsymbol{\nabla}})\tilde{\boldsymbol{\nabla}}\times\right)\boldsymbol{u}^{\mathrm{S}}(\boldsymbol{x}, \boldsymbol{y}_{\mathrm{s}}, 8\pi\mu\ \boldsymbol{p}_{\mathrm{s}}), \quad (1.35)$$

where $\tilde{\nabla}_{\parallel}^2 = (\boldsymbol{p}_{\mathrm{s}}\cdot\tilde{\boldsymbol{\nabla}})^2$ and $\tilde{\nabla}_{\perp}^2 = \tilde{\nabla}^2 - \tilde{\nabla}_{\parallel}^2$ are the Laplace operators parallel to, and in the plane perpendicular to, the swimming direction $\boldsymbol{p}_{\mathrm{s}}$ acting on the swimmer position $\boldsymbol{y}_{\mathrm{s}}$. $Q_{\parallel}$, $Q_{\perp}$ and Q_r are the quadrupole moments with units $[\mu\mathrm{m}^4/\mathrm{s}]$. **Eq. 1.35** can be rewritten in terms of the parallel quadrupole, source doublet and rotlet doublet flows as $\boldsymbol{u}^{\mathrm{QU}} = \boldsymbol{u}^{\mathrm{Q}} + \boldsymbol{u}^{\mathrm{SD}} + \boldsymbol{u}^{\mathrm{RD}}$, where

$$\boldsymbol{u}^{\mathrm{Q}}(\boldsymbol{x}, \boldsymbol{y}_{\mathrm{s}}, \boldsymbol{p}_{\mathrm{s}}) = -\frac{1}{2}\nu\ (\boldsymbol{p}_{\mathrm{s}}\cdot\tilde{\boldsymbol{\nabla}})^2\boldsymbol{u}^{\mathrm{S}}(\boldsymbol{x}, \boldsymbol{y}_{\mathrm{s}}, 8\pi\mu\ \boldsymbol{p}_{\mathrm{s}}), \quad (1.36)$$

$$\boldsymbol{u}^{\mathrm{SD}}(\boldsymbol{x}, \boldsymbol{y}_{\mathrm{s}}, \boldsymbol{p}_{\mathrm{s}}) = -\frac{1}{2}\sigma\ \tilde{\nabla}^2\boldsymbol{u}^{\mathrm{S}}(\boldsymbol{x}, \boldsymbol{y}_{\mathrm{s}}, 8\pi\mu\ \boldsymbol{p}_{\mathrm{s}}), \quad (1.37)$$

$$\boldsymbol{u}^{\mathrm{RD}}(\boldsymbol{x}, \boldsymbol{y}_{\mathrm{s}}, \boldsymbol{p}_{\mathrm{s}}) = -\frac{1}{2}\tau\ (\boldsymbol{p}_{\mathrm{s}}\cdot\tilde{\boldsymbol{\nabla}})\tilde{\boldsymbol{\nabla}}\times\boldsymbol{u}^{\mathrm{S}}(\boldsymbol{x}, \boldsymbol{y}_{\mathrm{s}}, 8\pi\mu\ \boldsymbol{p}_{\mathrm{s}}), \quad (1.38)$$

where $\nu = Q_{\parallel} - Q_{\perp}$, $\sigma = Q_{\perp}$ and $\tau = -2Q_r$ are referred to as the quadrupole, source doublet and rotlet doublet moments, respectively. The quadrupole flow corresponds at first order to the fore-aft asymmetries of the Stokeslet density along the swimmer's surface (**Fig. 1.5**). For example, this could describe the size difference of the bacterial flagella compared to the smaller head, shifting the propulsion force backwards with respect to the swimmer's body centre. Hence, we expect $\nu > 0$ for flagellated bacteria, such as *E. coli*. The source doublet flow field allows one to describe the flow around the swimmer body. This can help tracer particles to avoid encountering the singularity at the swimmer's body centre and hence account for the finite size of the cell. Ciliated organisms with a slip velocity at their surface, like *Volvox*, possess positive σ values, whereas for non-ciliated swimmers one would expect $\sigma < 0$ because this corresponds to the Faxén correction to the Stokeslet flow for a finite-sized solid sphere (**Eq. 1.23**). Finally, the term with coefficient τ is a rotlet doublet that represents

the rotation of the flagella and counter-rotation of the head. If $\tau > 0$, looking from tail to head, the flagella (resp. head) rotate in the (resp. counter) clock-wise direction.

1.2.5.3 Octupolar contribution

The octupolar velocity field for a cylindrically symmetric swimmer is

$$\boldsymbol{u}^{\mathrm{O}}(\boldsymbol{x}, \boldsymbol{y}_{\mathrm{s}}, \boldsymbol{p}_{\mathrm{s}}) \;=\; (\boldsymbol{p}_{\mathrm{s}} \cdot \tilde{\boldsymbol{\nabla}}) \left[\frac{O_{\parallel}}{6} \tilde{\nabla}_{\parallel}^2 + \frac{O_{\perp}}{2} \tilde{\nabla}_{\perp}^2 + \frac{O_r}{2} (\boldsymbol{p}_{\mathrm{s}} \cdot \tilde{\boldsymbol{\nabla}}) \tilde{\boldsymbol{\nabla}} \times \right] \boldsymbol{u}^{\mathrm{S}}(\boldsymbol{x}, \boldsymbol{y}_{\mathrm{s}}, 8\pi\mu\, \boldsymbol{p}_{\mathrm{s}}), \qquad (1.39)$$

where $O_{\parallel}$, $O_{\perp}$ and O_r are the parallel, perpendicular and rotlet octupolar coefficents respectively. These terms are fore-aft symmetric, and hence describe more detailed near-field features of the swimmer in the radial and azimuthal directions. The hexadecapolar flow field also has three coefficients, $H_{\parallel}$, $H_{\perp}$ and H_r, and may be obtained by acting on **Eq. 1.39** with $(\boldsymbol{p}_{\mathrm{s}} \cdot \tilde{\boldsymbol{\nabla}})$. These terms are fore-aft anti-symmetric and hence describe more detailed near-field features of the swimmer in the longitudinal direction. Higher order flow fields may be derived in the same fashion.

1.2.5.4 Time dependence

In general, the multipole moments are time-dependent quantities that relate to details of the swimming stroke. If the stroke period τ_s is small compared to a typical swimming timescale, say the time taken to swim one body-length, τ_a, then the swimming parameters may be approximated by constants obtained through time-averaging over the swimming stroke. A non-zero stroke period, however, may give rise to additional average drift of tracer particles, analogous to Stokes drift. To first order, the magnitude of this effect is proportional to τ_s/τ_a. E.g., for *E. coli* we have $V \sim 20\mu\mathrm{m}/s$ and body length $l_{\mathrm{sw}} \sim 5\mu$m, so $\tau_a^{-1} \sim 4$ Hz compared to the stroke frequency $\tau_s^{-1} \sim 100$ Hz[209], which gives a good separation of time scales. For *C. reinhardtii* $\tau_a^{-1} \sim 100/8 = 13$ Hz and $\tau_s^{-1} \sim 50$ Hz[210].

1.2.6 Theoretical micro-swimmers

Using this mathematical framework, it is possible to think of theoretical model micro-swimmers that reproduce certain physical features in a simplified but analytically tractable way. By using these models it is possible to understand the behaviour of biological swimmers, and to overcome physical barriers and improve the design of synthetic swimmers.

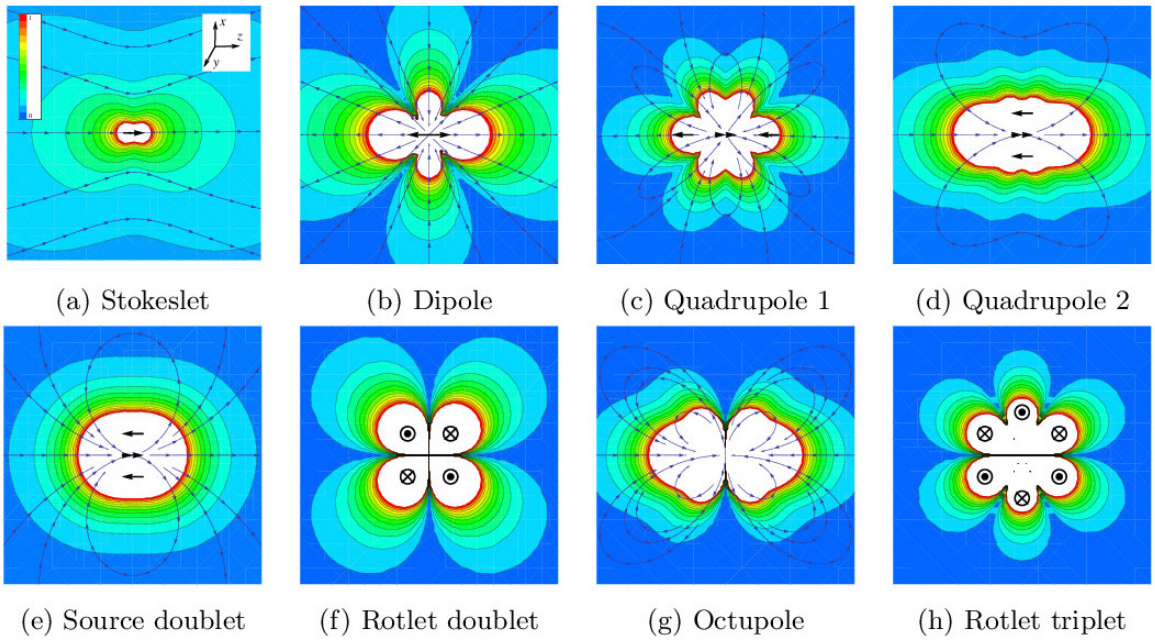

(a) Stokeslet (b) Dipole (c) Quadrupole 1 (d) Quadrupole 2

(e) Source doublet (f) Rotlet doublet (g) Octupole (h) Rotlet triplet

Figure 1.7: Flow fields produced by a micro-swimmer corresponding to different multipole expansion singularities, as seen in the (z, ρ) plane in the laboratory frame, where the swimmer is located at the origin and the swimming direction is from left to right. Colours portray the relative velocity magnitude ranging from zero (blue) to unity (red) and white denotes the singularity centre. Arrows indicate the velocity direction in the (z, ρ) plane, except in figures (*f, h*) where the direction is directly into and out of the plane indicated by the $\otimes$ and $\odot$ symbols respectively.

1.2.6.1 Multipole swimmers

Perhaps the simplest theoretical model is the dipolar swimmer (**Fig. 1.6**). This model can be extended with higher-order terms so that the 'multipole swimmer', as the name implies, generates a flow field that is given by a multipole expansion, **Eq. 1.32**. **Fig. 1.7** gives a pictorial summary of the multipole contributions up to octupolar order. These flow fields are all singular at the swimmer position, so the swimmer is effectively point-like unless steric or other non-hydrodynamic interactions are included in the equations of motion to avoid close-range contact. The disadvantage of this model, therefore, is that near-field effects cannot be taken into account without very many terms, so other models could be preferable to study this regime. On the other hand, the advantage is that each term in the multipole expansion can be linked with a physical property of the swimmer. Furthermore, far-field hydrodynamics are generally well approximated with the inclusion of a limited number of terms. Therefore, the multipole swimmer features often in this thesis (see §**1.3.1**).

1.2.6.2 Squirmers

The squirmer model was introduced by Lighthill[98] to examine squirming motion of nearly spherical deformable bodies. Later an extension of this model was used by Blake[99] to study ciliary propulsion using a spherical envelope approach (**Fig. 1.8**a). A squirmer is modelled as a sphere, with a finite radius a_{sw}, with a prescribed tangential slip velocity at its surface given by

$$u_\theta^{\mathrm{sw}}(\boldsymbol{y}_{\mathrm{s}}, \boldsymbol{p}_{\mathrm{s}}, t) = \sum_{n=1}^{\infty} -\frac{2}{n(n+1)} B_n \mathrm{P}_n^1(\cos\theta), \tag{1.40}$$

where θ is the angle between the position on the surface and the swimming direction $\boldsymbol{p}_{\mathrm{s}}$, the coefficients $B_n(t)$ determine the 'squirming modes' and $\mathrm{P}_n^1(x)$ are the associated Legendre polynomials of the first kind. The first mode determines the swimming velocity, $v_{\mathrm{s}} = 2B_1/3$, and the resulting flow field tends to a source doublet in the far field (**Fig. 1.7**e). The second mode is associated with the dipole moment, with $B_2 \propto -\kappa$ (**Fig. 1.7**b). Indeed, all modes can be mapped to the multipole expansion in the far field[204], but the near field is not singular but always has a finite slip velocity at the squirmer surface. Note that a radial flow velocity component can also be included, as in Lighthill's original paper[98].

Squirmers are a good model for ciliated organisms (§**1.1.1.3**) or active droplets (§**1.1.2.4**), since they do not have a no-slip surface but generate slip flows that are approximately tangential to the body. This model has been used to study swimmer-swimmer interactions in dilute[211,212] and concentrated suspensions of squirmers[213], as well as interactions between swimmers and external flows[214,215]. Squirmers have been studied using Lattice-Boltzmann[215–217], multi-particle-collision-dynamics[218–220], and other hydrodynamic solvers[187,213,221–224]. The model has many appealing features, for instance, the ability to specify the exact hydrodynamic character of the swimmers and the possibility to add lubrication corrections[204]. Recently, the squirmer model has also been extended to ellipsoidal swimmers[224].

1.2.6.3 Linked-sphere swimmers

Since the flow field generated by a sphere is known exactly (**Eq. 1.24**), it is possible to estimate the flows generated by swimmers constructed from two or more linked spheres. The links can be seen as rods that are assumed to be thin enough not to influence any flows, and contractile or extensile forces between the spheres are carried by these. Vic's swimmer[226],

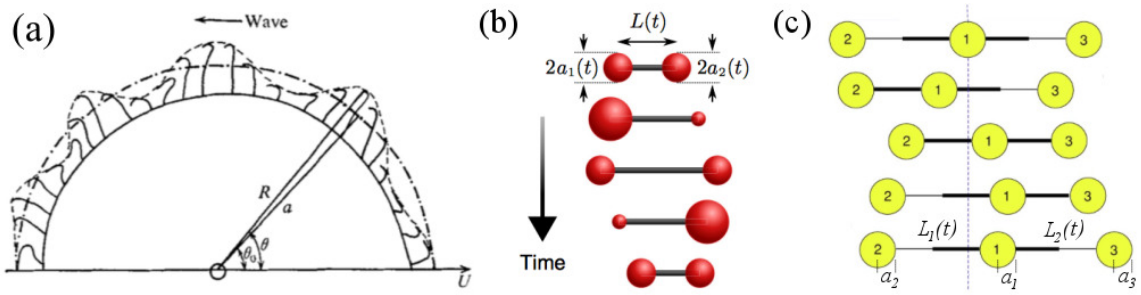

Figure 1.8: Theoretical model micro-swimmers: (a) The squirmer model, where metachronal waves generated by an array of cilia induce an effective slip flow tangential to the swimmer surface. Reproduced from Blake[99]. (b) The non-reciprocal swimming stoke of Vic's two-sphere swimmer in 4 stages. Reproduced from Yeomans et al.[180]. (c) The non-reciprocal swimming stoke of the three-sphere swimmer in 4 stages. Adapted from Najafi and Golestanian[225].

which is based on an earlier linked-sphere model[227], is made of two spheres of oscillatory radii $a_1(t)$ and $a_2(t)$ separated a distance $L(t)$ apart, where

$$a_1(t) = a_0 + \lambda \sin(\omega t + \phi_1), \quad a_2(t) = a_0 + \lambda \sin(\omega t + \phi_2), \quad L(t) = L_0 + \xi \sin(\omega t). \tag{1.41}$$

The particle can swim by breaking non-reciprocality as follows (**Fig. 1.8**b): First it enlarges the back bead and diminishes the front bead in size. Secondly, it pushes the two beads apart with equal and opposite forces, but the smaller bead experiences less drag and moves forward more. Thirdly, the front bead is made bigger and the back bead smaller. Finally, the swimmer contracts the two beads, but now the back bead is pulled forward. Assuming that $a_0, \lambda, \xi \ll L_0$, the time-averaged swimming speed is found[226] to be

$$\langle v_{\mathrm{sw}} \rangle = \frac{\lambda \omega \xi}{4a_0} \left(1 - \frac{3a_0}{2L_0}\right)^{-1} \sin\left(\frac{\phi_1 - \phi_2}{2}\right) \cos\left(\frac{\phi_1 + \phi_2}{2}\right). \tag{1.42}$$

Note that if the bead sizes oscillate in phase, $\phi_1 = \phi_2$, there is no net motion due to the scallop theorem (**Fig. 1.4**). The time-averaged flow field generated by Vic's swimmer at distances $r > L_0$ is dipolar (**Eq. 1.33**) with a known dipole moment $\langle \kappa \rangle \propto \langle v_{\mathrm{sw}} \rangle a_0 L_0$.

An interesting extension of the two-sphere swimmer is that of apolar 'dumb-bell' swimmers with spheres that do not oscillate in size, $\lambda = 0$. An individual dumb-bell swimmer cannot move, but a collection of dumb-bells *can* move if they oscillate out of phase[228,229]. This way, tethered swimmers could be used as a micro-pump.

The three-sphere swimmer by Najafi and Golestanian[225] has beads with constant radii

a_1, a_2, a_3 and performs a swimming stoke by contracting two rods (**Fig. 1.8**c) according to

$$L_1(t) = l_1 + \lambda_1 \sin(\omega t + \phi_1), \qquad L_2(t) = l_2 + \lambda_2 \sin(\omega t + \phi_2). \tag{1.43}$$

The time-averaged swimming speed[230] is then given by

$$\langle v_{\text{sw}} \rangle = \frac{1}{2} \frac{3a_1a_2a_3}{(a_1 + a_2 + a_3)^2} \left(\frac{1}{l_1^2} + \frac{1}{l_2^2} - \frac{1}{(l_1 + l_2)^2} \right) \lambda_1 \lambda_2 \omega \sin(\phi_1 - \phi_2). \tag{1.44}$$

This model has been used to examine the effect of an external load or a cargo container[231,232].

Further extensions of this class of theoretical models are the generalised three-sphere swimmer that features a two-dimensional stroke and the linear four-sphere and multi-sphere filament swimmers[233]. Linked spheres provide excellent models to examine swimmer-tracer interactions[180,226] and swimmer-swimmer interactions[234–237].

1.3 Complex Fluids and Environments

So far we have considered swimmers in an open fluid without any interactions with objects or each other. In reality, however, both biological and synthetic micro-swimmers must operate in a complex environment. This complexity could arise from confinement (e.g. between channel walls), externally imposed flows, viscoelasticity, or thermal and biological fluctuations. In this section we introduce how these effects can be modelled and how they affect the swimmer's motion.

1.3.1 Swimmer equations of motion

In order to model the dynamics of micro-swimmers, we use a model based on the multipole swimmer (§**1.2.6.1**). To account for the swimmer's finite size, we model it as a prolate ellipsoid of semi-major and minor axes a and b, respectively. It should be noted that we do not account separately for the swimmer's body and flagella, but we model the swimmer's shape as an ellipsoid with an aspect ratio that includes the flagellar length. For convenience of computation we express the swimmer orientation in spherical polar co-ordinates, $\boldsymbol{p}_{\text{s}} = -(\cos\theta\cos\phi, \sin\theta, \cos\theta\sin\phi)$. When the system of interest is symmetric about the z axis, θ may be set to zero at the initial time without loss of generality.

Following examples from the literature[214,238,239], we write the equations of motion for a

micro-swimmer as

$$\dot{\boldsymbol{y}}_{\mathrm{s}} = \boldsymbol{v}^{\mathrm{A}} + \boldsymbol{v}^{\mathrm{ST}} + \boldsymbol{v}^{\mathrm{HI}} + \boldsymbol{v}^{\mathrm{F}} + \boldsymbol{v}^{\mathrm{VE}} + \boldsymbol{v}^{k_{\mathrm{B}}T}, \tag{1.45}$$

$$\dot{\boldsymbol{p}}_{\mathrm{s}} = \left(\boldsymbol{\Omega}^{\mathrm{A}} + \boldsymbol{\Omega}^{\mathrm{ST}} + \boldsymbol{\Omega}^{\mathrm{HI}} + \boldsymbol{\Omega}^{\mathrm{F}} + \boldsymbol{\Omega}^{\mathrm{VE}} + \boldsymbol{\Omega}^{k_{\mathrm{B}}T} + \boldsymbol{\Omega}^{\mathrm{RT}}\right) \times \boldsymbol{p}_{\mathrm{s}}. \tag{1.46}$$

The contributions to the motion come from active self-propulsion (characterised by velocity $\boldsymbol{v}^{\mathrm{A}}$ and angular velocity $\boldsymbol{\Omega}^{\mathrm{A}}$), steric interactions with surfaces ($\boldsymbol{v}^{\mathrm{ST}}$ and $\boldsymbol{\Omega}^{\mathrm{ST}}$), hydrodynamic interactions with surfaces ($\boldsymbol{v}^{\mathrm{HI}}$ and $\boldsymbol{\Omega}^{\mathrm{HI}}$), advection and rotation by a background flow ($\boldsymbol{v}^{\mathrm{F}}$ and $\boldsymbol{\Omega}^{\mathrm{F}}$), cross-streamline migration and rotation due to viscoelasticity ($\boldsymbol{v}^{\mathrm{VE}}$ and $\boldsymbol{\Omega}^{\mathrm{VE}}$), and stochastic dynamics due to thermal noise ($\boldsymbol{v}^{k_{\mathrm{B}}T}$ and $\boldsymbol{\Omega}^{k_{\mathrm{B}}T}$) or run-and-tumble dynamics (controlled by $\boldsymbol{\Omega}^{\mathrm{RT}}$). In the following sections we discuss each of these terms in turn.

The active terms are simplified for an axisymmetric swimmer so that it moves with a swimming velocity $\boldsymbol{v}^{\mathrm{A}} = v_{\mathrm{s}}\boldsymbol{p}_{\mathrm{s}}$ and $\boldsymbol{\Omega}^{\mathrm{A}} = 0$. However, asymmetries in the swimming stroke can result in both translational and rotational modes of motion, since they induce torques that significantly perturb the swimming path leading to circular motion. Circular swimming in a bulk fluid has been observed in experiments of biological[240] and synthetic[241,242] micro-swimmers. However, the time-scale of rotational motion can be much larger than those of other characteristics, such as the time taken to navigate in narrow channels or run-and-tumble motion. In this thesis we will only consider translational activity and set $\boldsymbol{\Omega}^{\mathrm{A}} = 0$, but adding this term back in would be an interesting extension.

1.3.2 Surfaces

Surfaces, interfaces and confinements are ubiquitous in microbial environments[8,243], and most micro-swimmer experiments are performed near surfaces such as microscope slides. Beyond simply containing microbes and their surrounding fluids, surfaces and interfaces alter the behaviours, dynamics and even biological traits exhibited by swimming cells[8,188]. Specifically, both in biological and synthetic systems swimmers often tend to accumulate near surfaces, as observed experimentally[59,205,244–251] and explained theoretically in terms of long-range hydrodynamic interactions and collisions of cells with the surface[91,238,246,247,252–263].

Living near surfaces can provide a variety of benefits to microbes over life in bulk fluids. Whereas interfaces may be the source of oxygen and sunlight, solid surfaces accumulate sediments including nutrients and offer anchoring points for the formation of extracellular

matrices and biofilms[264,265]. On the other hand, for a synthetic swimmer the effect of surfaces can be detrimental, as they might get damage from it before reaching the final target. Even when it is not damaged and remains moving, a swimmer can be trapped in bound orbits[253,266–270]. Still, the interactions of biological or artificial swimmers with surfaces can be used to drive a micro-rotor, using only the energy provided by an active suspension[271–273]. Hence, it is an ongoing quest to determine what mechanisms govern these interactions.

1.3.2.1 Swimmer-generated flow field near a surface

In order to begin understanding how surfaces and interfaces impact the flow field generated by microbes, we return to the multipole model (§**1.2.4**). We define the flow in the absence of any boundaries as $\boldsymbol{u}^{\mathrm{sw}\infty}$, the flow with boundaries present as $\boldsymbol{u}^{\mathrm{sw}}$ and the difference, $\boldsymbol{u}^{\mathrm{sw}*} = \boldsymbol{u}^{\mathrm{sw}} - \boldsymbol{u}^{\mathrm{sw}\infty}$ is called the 'auxiliary' or 'reflected' flow.

Close to a boundary the confinement affects the flow field as it introduces extra boundary conditions to the solutions of the Stokes equations (**1.10-1.11**). For a free-slip surface such as a liquid-air interface there is a no-penetration and a no-shear condition. For liquid-solid boundaries there is a no-slip boundary condition. These boundary conditions can be satisfied by the method of images[202], as outline below.

The image system of a Stokeslet (**Eq. 1.22**) for an infinite, flat, free-slip boundary is a direct reflection. If the boundary is located in plane $z = 0$, then the image Stokeslet is located at $\boldsymbol{y}^* = \mathrm{M} \cdot \boldsymbol{y}$, where the mirror matrix is $\mathrm{M} = \mathrm{diag}(1, 1, -1)$. The resulting image flow is $\boldsymbol{u}^{\mathrm{S}*}(\boldsymbol{x}, \boldsymbol{y}^*, \boldsymbol{f}) = \mathcal{T} \cdot \boldsymbol{f}$, where the free-slip boundary tensor is

$$\mathcal{T}_{ij}(\boldsymbol{x}, \boldsymbol{y}^*) \quad = \quad \mathrm{M}_{jk}\mathcal{G}_{ik}(\boldsymbol{x}, \boldsymbol{y}^*) = \frac{\mathrm{M}_{jk}}{8\pi\mu}\left(\frac{\delta_{ik}}{r^*} + \frac{r_i^* r_k^*}{(r^*)^3}\right), \tag{1.47}$$

where $\boldsymbol{r}^* = \boldsymbol{x} - \boldsymbol{y}^*$ and $r^* = |\boldsymbol{r}^*|$.

For a no-slip boundary the image system is more complicated because all three components of the velocity field must vanish at the boundary. The solution was derived first by Lorentz using the reciprocal theorem. Later it was rederived by Blake[183] using a Fourier transform approach that yields a more intuitive solution in the form of a Green's function, so that the velocity field can be written in the form of **Eq. 1.47**. This Green's function, often called the Blake tensor, is

$$\mathcal{B}_{ij}(\boldsymbol{x}, \boldsymbol{y}^*) = \frac{1}{8\pi\mu}\left[-\left(\frac{\delta_{ij}}{r^*} + \frac{r_i^* r_j^*}{r^{*3}}\right) + 2h\mathrm{M}_{jl}\frac{\partial}{\partial r_l^*}\left(\frac{h r_i^*}{r^{*3}} - \left(\frac{\delta_{i3}}{r^*} + \frac{r_i^* r_3^*}{r^{*3}}\right)\right)\right], \tag{1.48}$$

where the height $h = \boldsymbol{y}_\mathrm{s} \cdot \hat{\boldsymbol{e}}_z > 0$. For a Stokeslet oriented parallel (or perpendicular) to the boundary this image system can be decomposed into three parts. The first part is a Stokeslet of equal magnitude f but pointing in the opposite direction. The second is an asymmetric dipole, sometimes called the Stokes doublet (symmetric dipole $\boldsymbol{u}^\mathrm{D}$), with dipole coefficient D_{13} (D_{11}) equal to $2hf$. The third part is source doublet $\boldsymbol{u}^\mathrm{SD}$ oriented in the opposite (same) direction with magnitude $\sigma = 2h^2 f$. Hence, the Blake tensor can be rewritten as

$$\mathcal{B}_{ij}(\boldsymbol{x}, \boldsymbol{y}^*) = (-\delta_{jk} + 2h\delta_{k3}\tilde{\partial}_j + h^2 \mathrm{M}_{jk}\tilde{\nabla}^2)\mathcal{G}_{ik}(\boldsymbol{x}, \boldsymbol{y}^*), \tag{1.49}$$

which is an implicit function of $\boldsymbol{x}$ and $\boldsymbol{y}$, where the derivatives $\tilde{\partial}_j = \frac{\partial}{\partial y_j} = \mathrm{M}_{jl}\frac{\partial}{\partial y_l^*}$ and $\tilde{\nabla}^2 = \tilde{\partial}_l\tilde{\partial}_l$ are with respect to the force position $\boldsymbol{y}$.

The swimmer-generated flow field near a surface can now be written in terms of these tensors, by replacing the Stokeslets $\boldsymbol{u}^{\mathrm{S}\infty}(\boldsymbol{x}, \boldsymbol{y}_\mathrm{s}, \boldsymbol{p}_\mathrm{s})$ in **Eqs. 1.33-1.39** with the effective Stokeslets $\boldsymbol{u}^\mathrm{S}(\boldsymbol{x}, \boldsymbol{y}_\mathrm{s}, \boldsymbol{p}_\mathrm{s}) = (\mathcal{G} + \mathcal{B}) \cdot \boldsymbol{p}_\mathrm{s}$ or $(\mathcal{G} + \mathcal{T}) \cdot \boldsymbol{p}_\mathrm{s}$ for a no-slip or free-slip boundary respectively. The advantage of this formalism is that the flow can still be written in terms of the Oseen tensor and derivatives thereof.

1.3.2.2 Steric Interactions with a surface

Consider a surface in the plane $z = 0$ with a normal vector $\boldsymbol{n} = \hat{\boldsymbol{e}}_z$ so that the swimmer is oriented with respect to the wall with an angle $\varphi = \arccos(\hat{\boldsymbol{e}}_z \cdot \boldsymbol{p}_\mathrm{s})$ and located at height $h = \hat{\boldsymbol{e}}_z \cdot \boldsymbol{y}_\mathrm{s}$. Steric interactions with the surfaces are modelled by a repulsive force and torque, which at zero Reynolds number result in the linear and angular velocities

$$\boldsymbol{v}^\mathrm{ST}(\boldsymbol{y}_\mathrm{s}, \boldsymbol{p}_\mathrm{s}, \boldsymbol{n}) = -\frac{\partial}{\partial h}U(h, \varphi), \tag{1.50}$$

$$\boldsymbol{\Omega}^\mathrm{ST}(\boldsymbol{y}_\mathrm{s}, \boldsymbol{p}_\mathrm{s}, \boldsymbol{n}) = -\frac{\partial}{\partial \varphi}U_r(h, \varphi). \tag{1.51}$$

Different prescriptions of steric interaction potentials U, U_r have been used in the literature[266,274,275], but at least qualitatively these lead to the same physical behaviour. An example of a hard-core repulsion prescription is

$$\boldsymbol{v}^\mathrm{ST} = \frac{v_\mathrm{s} A(\varphi)^{12}}{z^{12}}\hat{\boldsymbol{e}}_z, \tag{1.52}$$

$$\boldsymbol{\Omega}^\mathrm{ST} = a^2|\boldsymbol{v}^\mathrm{ST}|\xi^{-1}G\sin(2\varphi)\,\hat{\boldsymbol{e}}_y, \tag{1.53}$$

so that a microbe facing the surface would be at equilibrium at the distance of closest approach between the swimmer's body and the boundary[275,276]. For an ellipsoidal swimmer, that distance is $A(\varphi) = \sqrt{a^2 + (b^2 - a^2)\cos^2\varphi}$ and ξ is the rotational drag coefficient with units of volume. The angular dependence $\sin(2\varphi)$ on $\mathbf{\Omega}^{\mathrm{ST}}$ seems a crude approximation, but recent experiments have shown this to be a reasonable assumption[247].

1.3.2.3 Hydrodynamic Interactions with a surface

Knowing the flow fields that a motile microbe produces within a film allows us to model the hydrodynamic interactions with the bounding surfaces. The swimmer's motion is modified by the flow field it generates (**Eq. 1.32**) because it is advected and rotated by the reflection of this flow in the boundaries. The surface-induced translational and rotational velocities are then found by solving the Faxén relations (**Eq. 1.25**) for the force-free and torque-free swimmer. Writing terms up to second order in particle length gives

$$\boldsymbol{v}^{\mathrm{HI}}(\boldsymbol{y}_{\mathrm{s}}, \boldsymbol{p}_{\mathrm{s}}) = \left(1 + \frac{1}{6}a^2\gamma^{-2}\nabla^2\right)\boldsymbol{u}^*(\boldsymbol{x})|_{\boldsymbol{x}=\boldsymbol{y}_{\mathrm{s}}}, \tag{1.54}$$

$$\mathbf{\Omega}^{\mathrm{HI}}(\boldsymbol{y}_{\mathrm{s}}, \boldsymbol{p}_{\mathrm{s}}) = \left[\frac{1}{2}\boldsymbol{\nabla}\times\boldsymbol{u}^* + G\boldsymbol{p}_{\mathrm{s}}\times(\mathbf{\Gamma}^*\cdot\boldsymbol{p}_{\mathrm{s}})\right]_{\boldsymbol{x}=\boldsymbol{y}_{\mathrm{s}}}, \tag{1.55}$$

where the derivatives are with respect to the position $\boldsymbol{x}$, the geometry factor $G = \frac{\gamma^2-1}{\gamma^2+1} \in [0, 1)$ is a function of the aspect ratio $\gamma = a/b$ of the elongated swimmer, and $\mathbf{\Gamma}^* = (\nabla\mathbf{u}^* + (\nabla\mathbf{u}^*)^T)/2$ is the strain rate tensor. The image flow $\boldsymbol{u}^*$ for a single surface is obtained from **Eq. 1.47** or **Eq. 1.49**. In chapter §4 we show how it can be derived for a liquid film geometry with parallel slip and no-slip surfaces.

1.3.3 Interactions with an external flow

Background flows are omnipresent in microbial habitats, both in the ocean and micro-channels[277]. Flow gradients lead to shearing than can strongly affect microbial swimming and spatial distributions[239,278]. Moreover, externally imposed flows can guide bacteria to migrate upstream near surfaces[279]. Motion with respect to flow strength gradients (rheotaxis) has been observed in various experimental setups, both in the presence of boundaries[280] and in open fluids[281].

As a result, there has been a substantial increase of interest in modelling the interplay between micro-swimmers and externally imposed flows[111,214,275,282–285]. Here, we model the

advection and rotation of a swimmer by solving the Faxén relations, as for reflected swimmer-generated flows discussed in §**1.3.2.3**, which yields the same expressions (**1.54-1.55**) with the image flow $\boldsymbol{u}^*$ replaced by the background flow $\boldsymbol{u}^{\mathrm{F}}$.

1.3.4 Viscoelasticicity

The liquids in which micro-organisms or robots must propel are often not simple Newtonian liquids. This can be because of polymers or other elastic molecules dissolved in the fluid, so that the simple constitutive equation for the stress tensor (**Eq. 1.3**) in the Navier-Stokes equations no longer holds. Consequently, viscoelastic effects can change the flows generated by swimmers $\boldsymbol{u}^{\mathrm{SW}}$ and the background flow $\boldsymbol{u}^{\mathrm{F}}$. An every-day example is the square-shaped 'plug' flow that emerges when squeezing a tube of tooth paste[286], which would have been shaped like a parabola for a Newtonian Poiseuille flow[287]. Another counterintuitive example is the possibility to walk on a swimming pool filled with water and cornstarch flour, as numerous YouTube clips attest.

Similar unexpected effects have been reported for micro-swimmers in non-Newtonian fluid flows[190,191,288,289]. Important correlations have been found between non-Newtonian behaviour of the fluid and pathological phenomena. Gastric mucus viscoelasticity affects swimming of *H. pylori*, an abundant pathogen in the stomach and leading cause of ulcers[290–292]. It has been shown that viscoelasticity is a more crucial factor in controlling the maximum velocity of lyme disease pathogen *B. burgdorferi* through skin than even chemical composition[293]. Viscoelastic properties of mucus have a remarkable impact on the swimming of spermatozoa and sperm-egg encounter rates[109]. Indeed, in Chapter §**3** we discuss viscoelastic effects on the upstream motion of swimmers in channels, such as sperm cells in the Fallopian tube. However, many questions related to viscoelasticity are still unresolved. The swimming speed of microbes has been said to increase or decrease depending on the swimmer and liquid model used[294–303]. It should also be noted that ordinary Newtonian liquids surrounded by elastic boundaries show interesting features that deserve further exploration[304].

1.3.5 Thermal and biological fluctuations

Finally, the last terms in the equations of motion (**1.45–1.46**) represent thermal noise, but also biological fluctuations as often featured in many biological systems[85,94,263,305–309]. We

model the thermal part as white noise that obeys the relations

$$\langle \boldsymbol{v}^{k_{\mathrm{B}}T}(t)\rangle = 0, \qquad \langle \boldsymbol{v}^{k_{\mathrm{B}}T}(t)\cdot\boldsymbol{v}^{k_{\mathrm{B}}T}(t')\rangle = 6D\delta(t-t'), \tag{1.56}$$

$$\langle \boldsymbol{\Omega}^{k_{\mathrm{B}}T}(t)\rangle = 0, \qquad \langle \boldsymbol{\Omega}^{k_{\mathrm{B}}T}(t)\cdot\boldsymbol{\Omega}^{k_{\mathrm{B}}T}(t')\rangle = 4D_r\delta(t-t'), \tag{1.57}$$

where the brackets represent an ensemble average and the translational and rotational diffusion constants are D and D_r. For a non-motile particle in the absence of flows and boundaries, the diffusional mean-squared displacement and loss of orientational memory after a time t is

$$\langle(\boldsymbol{y}_{\mathrm{s}}(t)-\boldsymbol{y}_{\mathrm{s}}(0))^2\rangle = 6Dt, \tag{1.58}$$

$$\langle(\boldsymbol{p}_{\mathrm{s}}(t)-\boldsymbol{p}_{\mathrm{s}}(0))^2\rangle = 2(1-\exp(-2D_rt)). \tag{1.59}$$

However, for motile swimmers this result changes significantly because the coupling between the deterministic activity $\boldsymbol{v}^{\mathrm{A}}$ and the rotational thermal noise $\boldsymbol{\Omega}^{k_{\mathrm{B}}T}$ leads to

$$\langle(\boldsymbol{y}_{\mathrm{s}}(t)-\boldsymbol{y}_{\mathrm{s}}(0))^2\rangle = 6Dt + \frac{2v_{\mathrm{s}}^2}{D_r}\left(t+\frac{1}{D_r}(\exp(-2D_rt)-1)\right) \tag{1.60}$$

$$= 6\left(D+\frac{v_{\mathrm{s}}^2}{3D_r}\right)t = 6D_{\mathrm{eff}}t \qquad \text{for } t \gg D_R^{-1}. \tag{1.61}$$

This effective diffusion coefficient D_{eff} can be ~ 100 times (!!) larger than D for typical bacteria (§1.1.1.1) with $D \sim 1\mu\mathrm{m}^2/\mathrm{s}$, $D_r \sim 1\mu\mathrm{m}^2/\mathrm{s}$ and $v_{\mathrm{s}} \sim 25\mu\mathrm{m/s}$.

Finally, the run-and tumble motion is modelled as a sudden change of direction with a probability $P_T = \delta t/\tau_r$ during a small time-step interval δt, where τ_r is the average time between tumble events. This is a Poisson process with $D_r = \pi^2/\tau_r$ as effective rotational diffusion constant.

1.4 Overview of the Thesis

This thesis is composed of six related studies concerning the 'Hydrodynamics of micro-swimmers in complex fluids and environments'. Here we outline the content of each chapter, and touch on the potential wider implications. As such, this section §1.4 is aimed at a slightly wider audience than the specialist readership, and I hope a curiosity can be triggered from these initial remarks. In addition to the six main chapters (§2–7), the final chapter reviews our findings more formally and provides an outlook for future research (§8).

1.4.1 Chapter 2

In chapter §2 we investigate the effect of a micro-swimmer on its liquid environment. The main question is how microbe-generated flows could affect the motion of tracer particles, which could represent nutrients, toxins or other extracellular molecules. We find that the tracer entrainment is enhanced in the vicinity of a boundary, as if a little bulldozer pushes the particles forwards, despite the no-slip boundary condition that inhibits advection at the surface. This is explained with hydrodynamics: Swimmer flows are 'reflected' by the boundary and add to the tracer displacement. Moreover, for a fluidised interface with a free-slip condition, the tracer trajectories are doubled in size and the final tracer displacement increases by a factor four. This effect could greatly enhance tracer diffusion, as is observed in recent experiments, and the mathematical model laid out here could input into a more quantitative calculation of increased diffusion constants. Organisms could benefit from stirring their environments to increase nutrient uptake by sweeping sedimented molecules up from boundaries.

1.4.2 Chapter 3

In chapter §3 we investigate the effect of the environment on a micro-swimmer. Sperm and microbial cells must often move through complex, springy and sticky bodily fluids, such as mucus, blood and gastric flows in the stomach. To make matters worse, they must often swim upstream. Our work predicts that swimming cells in biological flows naturally exploit fluid properties to reorient towards the centre of channels where they migrate upstream. The swimming cells reorient because of their motion through mucus-like fluids that flow, which differs from sperm in non-flowing fluids where they accumulate at walls. We explain that cells move upstream more quickly in fluids that thicken (like cornstarch when stirred) because they can spend more time in slower flows near walls, where they have the chance to move further upstream. These insights suggest a new sorting mechanism to differentiate microbes by adjusting the flow speed relative to swimming speeds of cells. Since swimming speed is used to assess the fertility of human semen, we suggest that fertility estimates might be improved by performing measurements in mucus-like fluids. Then all the sperm would swim upstream along the centreline of applied flows where they can have a fair race, without some cheating sperm sneaking up along the walls.

1.4.3 Chapter 4

In chapter §4 the attention is shifted to swimmers in a liquid film. Almost no life is found on completely dry surfaces, but countless microbial habitats are associated with liquid films, including e.g. moist skin or plant leaves. Water is the key ingredient to life itself, it dissolves all necessary nutrients, and it allows for micro-organisms to swim and spread their population further. To understand the hydrodynamics of swimming in a film, we developed a mathematical framework to compute swimmer-generated flows bounded by a solid wall and a liquid-air interface. Organisms can use these flow fields to feel each other's presence, to stir nutrients around, or even to reduce the power required to swim. We find that hydrodynamic interactions attract swimmers more strongly to the wall than to the air interface. Once the microbes are at the bottom wall, we see they are likely to stay there. This could lead to the formation of large encapsulated colonies that stick to a surface, called biofilms. These biofilms are can severely damage tissues and are hard treat with antibiotics. Hence, it is important to apprehend the initial stages of swimming to attachment and vice versa.

1.4.4 Chapter 5

In chapter §5 we develop our swimmer model further and introduce background flows. Microbial colonies that stick to surfaces or tissues are difficult to remove. The simplest way to try to detach them is to scrub them off, for example when brushing one's teeth, but the exertion of mechanical forces can damage fragile tissues and most microbes are concealed in cavities or crevices that are hard to reach. Hence, a less invasive yet thorough treatment can be to rinse microbes off the surfaces. However, our research shows that washing swimming bacteria from clean surfaces works well only up to a point. At large flow strengths detachment becomes less effective, but instead an optimal flow strength exists, so there is a sweet spot for rinsing bacteria away. In liquid films, a critical flow strength is first needed to peel microbial swimmers off surfaces. If much stronger flows are applied then the interplay between the flowing film and the swimming causes the microbes to move back towards the surface, where they are more likely to form biofilms. Preventing the formation of biofilms reduces the need to apply biocides to hauls and maritime structures, lowers the chances of infection of medical implants, and generally keeps submerged equipment working optimally.

1.4.5 Chapter 6

In chapter §6 we develop a new method to perform detailed simulations with 'Raspberry swimmers'. Raspberry swimmers are the *in silico* representatives of biological micro-organisms or synthetic micro-robots. Their name derives from their structure as they are composed of closely packed and coupled drupelets. Raspberry swimmers can be constructed with any shape desired, just like edible Raspberries are cultivated in various colours and shapes. By applying a force to the Raspberry and an equal and opposite counterforce to the surrounding liquid, representing propulsion and drag respectively, we create a model swimmer that is free of external forces and moves autonomously. The Lattice-Boltzmann computer algorithm then allows to solve the flow fields around a Raspberry swimmer for a given force and body conformation. We find the flows are very different for point-, sphere-, rod-, and cylinder-shaped swimmers, and we illuminate the flow characteristics. Finally, the model is tested for consistency by cross-checking against results obtained earlier for different swimmer models.

1.4.6 Chapter 7

In chapter §7 we use our model Raspberry swimmers to study their dynamics in a confined geometry. Except in the ocean, almost all micro-organisms must move with little space in enclosed environments such as a liquid film on skin, a little pore in soil, a cavity, crevice or channel. Micro-robots designed to deliver drugs inside the body must also move through narrow capillaries. In order to study their interactions with walls we employ our Raspberry swimmers to perform detailed computer simulations of a micro-channel fabricate. As recently observed for synthetic self-propelled droplets, we find that in channels wider than a few body sizes the swimmers begin to oscillate between one wall and the other. This is explained because the flows they generate are reflected by the channel walls to reorient them. Oscillations can grow in size for certain swimmer shapes, but the Raspberry swimmers can also be designed such that they repel the walls and move smoothly along the channel centreline. These insights could perhaps be used to avoid micro-robots from colliding with objects or sticking to surfaces. They could then navigate safely to fulfil their tasks.

CHAPTER 2

Tracer Trajectories and Displacement due to a Micro-swimmer near a Surface

> "My health may be better preserved if I exert myself less, but in the end doesn't each person give his life for his calling?"
>
> Clara Schumann (1819–1896)

2.1 Introduction

As micro-organisms move they set up velocity fields which stir the surrounding fluid (§**1.2.4**). The displacement of tracer particles in the flow leads to enhanced diffusion, or stirring. This is thought to confer a biological advantage by increasing nutrient supply[200,201,310] and may have application to enhance mixing in microfluidic channels[192]. Stirring was first measured experimentally in concentrated suspensions[311] and later in dilute suspensions in various geometries[193,195,196]. Simulations of microswimmer suspensions also shows enhanced diffusivities[194,312–315].

To understand enhanced diffusion in a dilute swimmer suspension it is helpful to first consider the motion of a single tracer particle in the flow field of a passing swimmer. Conversely, understanding the features of tracer trajectories obtained in experiments may help analyze propulsion and flows created by micro-swimmers. Analyzing typical tracer trajectories is the main purpose of this chapter. It has recently been shown that, for a swimmer that moves along an infinite straight trajectory, tracer particles far from the swimmer move in

closed loops, whereas those close to the swimmer are entrained by its motion[316,317]. However, in reality bacterial paths are not infinite but often can be approximated by straight lines interspersed with random reorientation phases, called runs and tumbles respectively[55]. The effect of random reorientations on tracer diffusion has been considered in[226,318–320]. Here we will discuss the effect of finite swimmer paths on individual tracer trajectories. Most experiments on micro-swimmers are performed in finite geometries (see §**1.3.2**). Therefore, here we extend the research on tracer trajectories near an individual swimmer to the cases where the swimmer is close to a no-slip or free-slip boundary.

In §**2.2** we use the multipole expansion for the most usual physical case of an axisymmetric swimmer (§**1.2.5**). This allows us to set up a perturbation theory in r^{-1} for the tracer displacement, where r is the distance from the swimmer. Using this framework, we obtain the trajectories of tracer particles as a swimmer moves along a straight path of finite length, considering the cases of a boundary absent or present.

We show in particular how a suitable choice of dipolar and quadrupolar coefficients in the multipole expansion can be used to account for flows created by swimmers having finite effective size. Therefore, the multipole expansion can be employed to study features of tracer trajectories both in the far-field and the near-field of micro-swimmers. An example is the entrainment of tracer particles as the swimmer passes close by.

In §**2.3** we present results for a swimmer in an unbounded fluid. These are based both on numerical solutions of the tracer equation of motion and the perturbation expansion. We compute terms up to sixth order in r^{-1} to collect enough information to study the transition from an infinite to a finite swimming path. The tracer paths have a loop-like structure with a size that scales as r^{-1}. The loops are almost closed with a final displacement of order r^{-3} for an infinite swimming path. For a finite swimming path the loops open up further, giving rise to substantial tracer displacements. We also show that another significant contribution to tracer displacements stems from spiralling of particles about the swimmer axis when micro-swimmers propel by rotating their flagella.

In §**2.4** we present results for a swimmer moving along a path parallel to a no-slip boundary. We show that even though fluid motion is inhibited near the boundary, tracer particles are pulled along the swimming direction, for pushers and pullers alike, and even more so for swimmers that produce quadrupolar flow fields. Moreover for swimmers close to the boundary the tracer particles are displaced in the plane perpendicular to the swimming

direction even for non-rotating micro-swimmers. We repeat our calculations for a swimmer near a free-slip boundary, and describe the main similarities and differences.

Our results are summarised and discussed in §**2.5**. Please note that this chapter is accompanied by a Supplementary Information (SI) file at URL[321].

2.2 Mathematical model

Consider a micro-swimmer moving in the direction $\boldsymbol{p}_{\mathrm{s}} = \hat{\boldsymbol{e}}_z$ along a line a distance H above and parallel to a plane boundary located at $x = 0$. We assume the swimmer moves with constant speed v_{s} so that it is located at position $\boldsymbol{y}_{\mathrm{s}} = \boldsymbol{R}(t) = (R_z^{\mathrm{int}} + v_{\mathrm{s}}t)\,\hat{\boldsymbol{e}}_z + H\hat{\boldsymbol{e}}_x$ at time t. By its motion the swimmer generates a flow field given by **Eq. 1.32**. Hence, we aim to study a tracer particle initially located at position $\boldsymbol{r}_{\mathrm{T}}^{\mathrm{int}} = x_{\mathrm{T}}^{\mathrm{int}}\hat{\boldsymbol{e}}_x + y_{\mathrm{T}}^{\mathrm{int}}\hat{\boldsymbol{e}}_y + z_{\mathrm{T}}^{\mathrm{int}}\hat{\boldsymbol{e}}_z$ at $t = 0$, and after time t at position $\boldsymbol{r}_{\mathrm{T}}(t)$. In the case of a swimmer in an unbounded fluid, in the limit $H \to \infty$, it is convenient to switch to a cylindrical coordinate system so that $\boldsymbol{R}(t) = (R_z^{\mathrm{int}} + v_{\mathrm{s}}t)\,\hat{\boldsymbol{e}}_z$ and $\boldsymbol{r}_{\mathrm{T}}^{\mathrm{int}} = \rho_{\mathrm{T}}^{\mathrm{int}}\hat{\boldsymbol{e}}_\rho + z_{\mathrm{T}}^{\mathrm{int}}\hat{\boldsymbol{e}}_z$. For brevity, we will write $\rho = \rho_{\mathrm{T}}^{\mathrm{int}}$ from now onwards.

The tracer displacement is defined as $\boldsymbol{\Delta r}_{\mathrm{T}}(t) = \boldsymbol{r}_{\mathrm{T}}(t) - \boldsymbol{r}_{\mathrm{T}}^{\mathrm{int}}$, and the final tracer displacement after the swimmer has passed is $\boldsymbol{\Delta r}_{\mathrm{T}}^{\infty} = \lim_{t\to\infty} \boldsymbol{\Delta r}_{\mathrm{T}}(t)$. The relative position vectors of the tracer particle with respect to the swimmer and its image system are written as $\boldsymbol{r} = \boldsymbol{r}_{\mathrm{T}}^{\mathrm{int}} - \boldsymbol{R}(t)$ and $\boldsymbol{r}^* = \boldsymbol{r}_{\mathrm{T}}^{\mathrm{int}} - \boldsymbol{R}^*(t)$ respectively, where $\boldsymbol{R}^* = \mathrm{M}\boldsymbol{R}$ with $\mathrm{M} = \mathrm{diag}(-1, 1, 1)$. This geometry is depicted in **Fig. 2.1**.

2.2.1 Modelling the swimmer's near-field

We show that including quadrupole terms in the expansion of the swimmer velocity field allows us to model the swimmer body and hence avoid the singularities of the multipole expansion at the origin. Consider the flow field in the rest frame of the swimmer, $\boldsymbol{u}^{\mathrm{rest}} = \boldsymbol{u}^{\mathrm{lab}} - v_{\mathrm{s}}\hat{\boldsymbol{e}}_z$, where the laboratory frame flow fields are listed in §**1.2.5**. The flow field of a purely dipolar pusher, given by **Eq. 1.33** with $\kappa > 0$, is shown in the swimmer rest frame in **Fig. 2.2a**. Notice a stagnation point a distance z^* directly in front of the swimmer. This point corresponds to $\hat{\boldsymbol{e}}_z \cdot \boldsymbol{u}^{\mathrm{D,rest}}(z^*) = 0$, which can be inverted to give $z^* = \sqrt{2\kappa/v_{\mathrm{s}}}$. The incoming fluid moves around the stagnation point and the streamlines join again at the singularity. However, the near-field behaviour is unphysical because of the singularity – as expected for a far-field expansion.

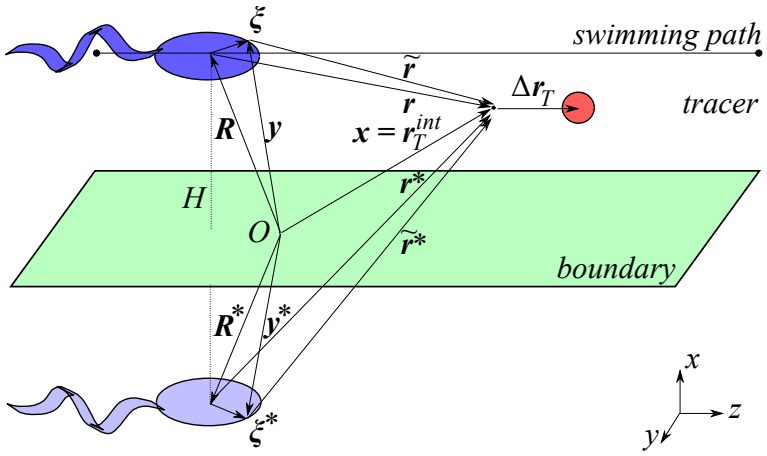

Figure 2.1: Geometry diagram for a micro-swimmer moving along a path parallel to a boundary. The unit vector normal to the boundary is $\hat{\boldsymbol{n}} = \hat{\boldsymbol{e}}_x$ and the swimmer moves at a distance H from the boundary with velocity v_s in the z-direction. Note that the axes are displayed in the bottom-right corner, not at the origin O, for clarity.

Next we consider the source doublet flow given by **Eq. 1.37** with $\sigma \equiv Q_{\parallel} = Q_{\perp}$ and $Q_r = 0$, and shown in the swimmer rest frame in **Fig. 2.2b**. For this multipole there is a surface of streamlines connecting two stagnation points in front and behind the swimmer. There is no flow crossing this surface, the separatrix, and hence the singularity region is separated from the rest of the flow. Therefore we can argue that, even though the swimmer is described by point singularities, it has an effective finite size. For a pure source doublet the position of the separatrix can be calculated exactly. Details of this calculations are given in **SI-§3**. The result is a spherical shell with radius

$$a_{\mathrm{sw}} = \left(\frac{2\sigma}{v_s}\right)^{1/3}. \tag{2.1}$$

Figure **2.2c** shows the case when a dipole term is added to the flow field, in addition to the source doublet. If $|\kappa| \ll |\sigma|/a_{\mathrm{sw}}$ the separatrix remains approximately spherical with radius a_{sw} given by **Eq. 2.1**. If $|\kappa|$ takes larger values, the separatrix changes shape. Indeed, the shape can be adjusted by tuning the dipole and quadrupole parameters. For instance, **Fig. 2.2d** shows a separatrix with an elongated shape, approximately 4μm long and 2μm wide, characteristic of rod-shaped bacteria or the head of a mammalian spermatozoon[114]. In **SI-§3** we show that the separatrix exists for all finite values of κ provided $Q_{\perp} > 0$ and

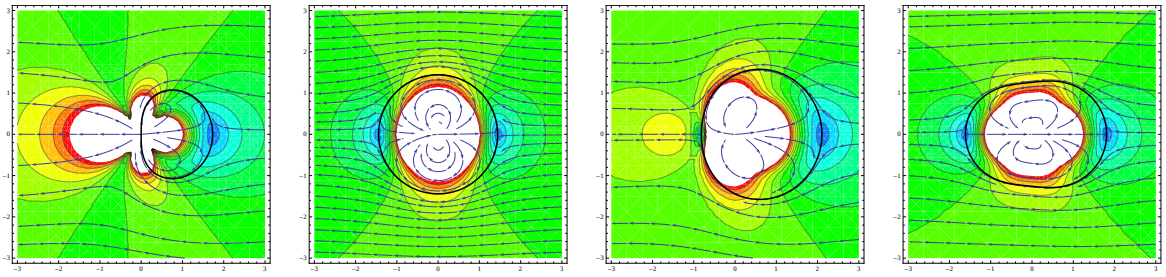

(a) Pure dipole $\kappa = 30\mu\text{m}^3/s$, $Q_\parallel = 0\mu\text{m}^4/s$, $Q_\perp = 0\mu\text{m}^4/s$.

(b) Source doublet $\kappa = 0$, $Q_\parallel = 30\mu\text{m}^4/s$, $Q_\perp = 30\mu\text{m}^4/s$.

(c) Combined $\kappa = 30\mu\text{m}^3/s$, $Q_\parallel = 30\mu\text{m}^4/s$, $Q_\perp = 30\mu\text{m}^4/s$.

(d) Combined $\kappa = 5\mu\text{m}^3/s$, $Q_\parallel = 10\mu\text{m}^4/s$, $Q_\perp = 30\mu\text{m}^4/s$.

Figure 2.2: Flow fields corresponding to the given multipoles in the rest frame of a micro-swimmer moving with velocity $v_\text{s} = 20\mu\text{m/s}$. Inclusion of quadrupole terms results in formation of a closed surface of streamlines separating the flow into the internal and external regions, see (b), (c) and (d). The external region is singularity-free and can model the flow field of a finite size swimmer. The separatrix shape can be adjusted by tuning the quadrupole parameters. It can, for example, produce elongated shapes characteristic of the head of a mammalian spermatozoon, see (d). Here colours portray the velocity magnitude, ranging from zero (blue) through v_s (green) to $2v_\text{s}$ (red) and white denotes the singularity center. Arrows indicate the velocity direction in the (z, ρ) plane. The thick black line is the separatrix.

$-1 < Q_\parallel/Q_\perp < 2$, and we derive an explicit expression for its position.

This result will turn out to be convenient throughout this chapter when numerically integrating tracer displacements, as it provides a useful and physically reasonable way of accounting for the near-field structure of flows created by micro-organisms.

2.2.2 Expansion of the tracer equation of motion

We aim to generate an expression for the tracer displacement as a power series in $1/r$. The tracer particle is advected directly by the fluid, and its equation of motion is

$$\frac{d\boldsymbol{r}_\text{T}}{dt} = \boldsymbol{u}^\text{sw}\left(\boldsymbol{r}_\text{T} - \boldsymbol{R}; \hat{\boldsymbol{e}}_z\right) + \boldsymbol{u}^\text{sw*}\left(\boldsymbol{r}_\text{T} - \boldsymbol{R}^*; \hat{\boldsymbol{e}}_z\right), \tag{2.2}$$

which is an implicit equation subject to the initial condition $\boldsymbol{r}_\text{T}^\text{int}$, and where we explicitly write $\boldsymbol{u}^\text{sw*}$, the velocity field of the image system, needed when a boundary is present. **Eq. 2.2** can either be solved numerically or one can proceed analytically if the tracer displacement is small compared to the distance to the swimmer, $|\boldsymbol{\Delta r}_\text{T}| \ll |\boldsymbol{r}| \ \forall t$. If the swimming motion is with a constant speed v_s, then taking the time-derivative of this condition yields the equivalent condition $|\partial_t \boldsymbol{r}_\text{T}(t)| = |\boldsymbol{u}^\text{sw}| \ll v_\text{s} \ \forall t$.

We change variables in **Eq. 2.2** to write $\frac{d\boldsymbol{r}_\text{T}}{dt} = \frac{d\boldsymbol{\Delta r}_\text{T}}{dt} = \boldsymbol{u}^\text{sw}\left(\boldsymbol{r} + \boldsymbol{\Delta r}_\text{T}\right) + \boldsymbol{u}^\text{sw*}\left(\boldsymbol{r}^* + \boldsymbol{\Delta r}_\text{T}\right)$

and expand for small values of $\boldsymbol{\Delta r}_{\mathrm{T}}$ to give

$$\begin{aligned}\frac{d\boldsymbol{\Delta r}_{\mathrm{T}}}{dt} &= \{\boldsymbol{u}^{\mathrm{sw}}[\boldsymbol{r}] + \boldsymbol{u}^{\mathrm{sw}*}[\boldsymbol{r}^*]\} + (\boldsymbol{\Delta r}_{\mathrm{T}} \cdot \boldsymbol{\nabla})\{\boldsymbol{u}^{\mathrm{sw}}[\boldsymbol{r}] + \boldsymbol{u}^{\mathrm{sw}*}[\boldsymbol{r}^*]\} \\ &+ \frac{1}{2}(\boldsymbol{\Delta r}_{\mathrm{T}} \cdot \boldsymbol{\nabla})^2\{\boldsymbol{u}^{\mathrm{sw}}[\boldsymbol{r}] + \boldsymbol{u}^{\mathrm{sw}*}[\boldsymbol{r}^*]\} + O\left(\frac{|\boldsymbol{\Delta r}_{\mathrm{T}}|}{r}\right)^3. \end{aligned} \tag{2.3}$$

To solve for $\boldsymbol{\Delta r}_{\mathrm{T}}$ as a power series in $1/r$ we write

$$\boldsymbol{\Delta r}_{\mathrm{T}}(t) = \Delta\boldsymbol{r}_{\mathrm{T}}^{(1)} + \Delta\boldsymbol{r}_{\mathrm{T}}^{(2)} + \Delta\boldsymbol{r}_{\mathrm{T}}^{(3)} + \ldots, \tag{2.4}$$

where the terms $\Delta\boldsymbol{r}_{\mathrm{T}}^{(n)}$ scale as r^{-n}. Since the swimmer moves with a constant speed v_{s} along z we may write $\frac{d}{dt} = v_{\mathrm{s}}\frac{d}{dR_z} = -v_{\mathrm{s}}\frac{d}{dr_z} = -v_{\mathrm{s}}\frac{\partial r}{\partial z}\frac{d}{dr}$. Therefore, the time derivatives $\partial_t\Delta\boldsymbol{r}_{\mathrm{T}}^{(n)}$ scale as r^{-n-1}. Hence, substituting **Eq. 2.4** into **Eq. 2.3**, using **Eq. 1.32** and equating successive powers of $1/r$ yields

$$\partial_t\boldsymbol{\Delta r}_{\mathrm{T}}^{(1)} = \boldsymbol{u}^{\mathrm{D}}, \tag{2.5}$$

$$\partial_t\boldsymbol{\Delta r}_{\mathrm{T}}^{(2)} = \boldsymbol{u}^{\mathrm{QU}}, \tag{2.6}$$

$$\partial_t\boldsymbol{\Delta r}_{\mathrm{T}}^{(3)} = \boldsymbol{u}^{\mathrm{O}} + \left(\boldsymbol{\Delta r}_{\mathrm{T}}^{(1)} \cdot \boldsymbol{\nabla}\right)\boldsymbol{u}^{\mathrm{D}}, \tag{2.7}$$

$$\partial_t\boldsymbol{\Delta r}_{\mathrm{T}}^{(4)} = \boldsymbol{u}^{\mathrm{H}} + \left(\boldsymbol{\Delta r}_{\mathrm{T}}^{(2)} \cdot \boldsymbol{\nabla}\right)\boldsymbol{u}^{\mathrm{D}} + \left(\boldsymbol{\Delta r}_{\mathrm{T}}^{(1)} \cdot \boldsymbol{\nabla}\right)\boldsymbol{u}^{\mathrm{QU}}, \quad \ldots \tag{2.8}$$

where we have used the short-hand notation $\boldsymbol{u}^{\mathrm{D}} = \boldsymbol{u}^{\mathrm{D}}(\boldsymbol{r}(t),\ \hat{\boldsymbol{e}}_z)$ and similarly for $\boldsymbol{u}^{\mathrm{QU}}$, $\boldsymbol{u}^{\mathrm{O}}$ etc., and where the image system flow fields are incorporated in the $\boldsymbol{u}$'s.

The tracer trajectory can be found by integrating **Eqs. 2.5-2.8** successively, and substituting the resulting expressions into the higher order equations of motion. In **SI-**§4.1 we describe this procedure for a swimmer in an unbounded fluid and in **SI-**§4.2 and 4.3 we repeat the calculations for a swimmer near a no-slip and free-slip boundary respectively.

2.3 Results: swimmer in an unbounded fluid

We now present results for the trajectory of a tracer particle when a micro-swimmer moves along a straight path of finite length. In §**2.3.1** we discuss tracer displacements in the radial and swimming direction in the (ρ, z) plane and in §**2.3.2** we examine spiralling of tracers in the (x, y) plane. In §**2.3.3** we address the limit of infinite swimming path lengths.

2.3.1 Tracer loops in the (ρ, z) plane

Figure **2.3** shows the tracer displacements. The values of the swimming speed and the dipole strength were chosen to correspond to a *E. coli* bacterium[205]. As the run length $2L$ between two tumbling events of *E. coli* varies from 5 to 30 μm[55], we have chosen $2L = 10\mu$m to emphasize the effects of a finite length swimming path. Different initial tracer positions are depicted by planes of small black dots at $z_{\mathrm{T}}^{\mathrm{int}} = -8, -6, \ldots, 6, 8\mu$m. Coloured dots show the final tracer positions after the swimmer has completed its run. In several cases trajectories are also shown, running from the open circles to the black dots. These results were obtained from a numerical solution of **Eq. 2.2**.

Results for a purely dipolar pusher ($\kappa > 0$) are shown in **Fig. 2.3a**. The tracer trajectories form loops in the region adjacent to the swimming path, where $|z_{\mathrm{T}}^{\mathrm{int}}| \ll L$, as previously shown by Dunkel et al.[226]. The shape of the trajectory is triangular for a dipolar swimmer and is a smaller three-loop structure for a purely quadrupolar swimmer. Notice that the tracer trajectories almost close on themselves, but there is a finite opening of the loop that defines the final tracer displacement $\boldsymbol{\Delta r}_{\mathrm{T}}$.

Far away from the swimming path, where $|\boldsymbol{r}_{\mathrm{T}}^{\mathrm{int}}| \gg L$, the final displacement scales as $1/r$ and reflects the dipolar flow field because the swimming path approximates a point source, $\lim_{r\gg L} \boldsymbol{\Delta r}_{\mathrm{T}} = \boldsymbol{u}^{\mathrm{sw}}\Delta t$, where $\Delta t = 2L/v_{\mathrm{s}}$. Additional quadrupole moments do not affect the far-field displacement, as shown in **Fig. 2.3b**, since these terms decay as $1/r^2$. Tracers in front of a pusher are moved forwards, while those behind the swimmer are moved backwards. Displacement along the radial direction is towards the swimming path for $|z_{\mathrm{T}}^{\mathrm{int}}| < L$ and away from the swimming path for $|z_{\mathrm{T}}^{\mathrm{int}}| > L$. For the equivalent puller ($\kappa \to -\kappa$) the tracers move over the loops in the opposite direction and the displacement in the far-field reverses sign, as shown in **Fig. 2.3c**.

Closer to the swimming path the tracer displacement does not simply reflect the flow field as the higher order advective terms in **Eq. 2.3** become significant. In other words, there is interference between the tracer displacements caused by different multipole components of the swimmer velocity field, as seen in the second term of **Eq. 2.7**. We observe that, predominantly, tracer trajectories are larger as the initial distance to the swimming path $\rho_{\mathrm{T}}^{\mathrm{int}}$ decreases. For tracers that start adjacent to the swimming path, where $|\boldsymbol{r}_{\mathrm{T}}^{\mathrm{int}}| \ll L$, the final tracer displacement vanishes along the ρ direction. Along the z direction it becomes

increasingly negative as ρ decreases, for purely dipolar pushers and pullers alike[317]. However, as shown in **Fig. 2.3a**, it becomes unphysical to use the pure dipolar swimmer model for tracers close to the swimmer where we expect entrainment in the forwards direction. Furthermore, the pure dipole model neglects the effects of finite body size important for tracers close to the swimmer, as discussed in §**2.2.1**.

Therefore, we present results in **Fig. 2.3b** and **2.3c** for tracer trajectories near a finite size swimmer obtained by taking $Q_{\parallel} = Q_{\perp} = 5\mu\text{m}^4/\text{s}$, corresponding to a swimmer with a characteristic size $a_{\text{sw}} \approx 1\mu\text{m}$. The effect of the finite swimmer body size is clearly seen in the transition from backward-displacement to forward-entrainment for tracers with an initial position in the middle of the swimming path, at $z_{\text{T}}^{\text{int}} = 0$, around $\rho_{\text{T}}^{\text{int}} \approx 0.4\mu\text{m}$. This transition can be calculated analytically for particles initially located close to the swimming path, *i.e.* in the limit $|\boldsymbol{r}_{\text{T}}^{\text{int}}| \ll L$. In §**2.3.3** we present a detailed calculation and discussion of entrainment effects due to quadrupolar and higher order terms.

The finite swimmer body size is also responsible for the shape of the tracer trajectories around $z_{\text{T}}^{\text{int}} = 5$. This becomes apparent in **Fig. 2.3d**, where the trajectories are plotted in the rest-frame of the swimmer. Here the tracer trajectories are explicitly shown for $z_{\text{T}}^{\text{int, rest}} = 10\mu\text{m}$ and final displacements are shown for $z_{\text{T}}^{\text{int, rest}} = 2, 4, \ldots, 18\mu\text{m} = z_{\text{T}}^{\text{int, lab}} + 10\mu\text{m}$ compared to the laboratory frame. The tracers are advected by the flow, following a trajectory around the swimmer located at $z = 5\mu\text{m}$, and ending up in the same positions as the tracers in **Fig. 2.3b**. The trajectories do not cross the separatrix around the swimmer, as discussed in §**2.2.1**.

2.3.2 Azimuthal tracer displacements

Swimmers that rotate as they swim, such as numerous biological cells that propel by rotating their flagella, will also displace tracers in the azimuthal direction. Hence, a tracer trajectory will spiral about the direction of the swimmer. Since swimmers are torque-free as well as force-free, their heads and tails rotate in the opposite directions and may cause the tracer spiral trajectories to change chirality as the swimmer passes by. The resulting net azimuthal tracer displacement is far from obvious and will depend on the distance between the tracer and the swimmer path. We describe it using analytical results for tracers far from the swimmer path and numerical results for tracers closer to the swimmer path.

Far from the swimming path an analytic expression showing the contributions of the

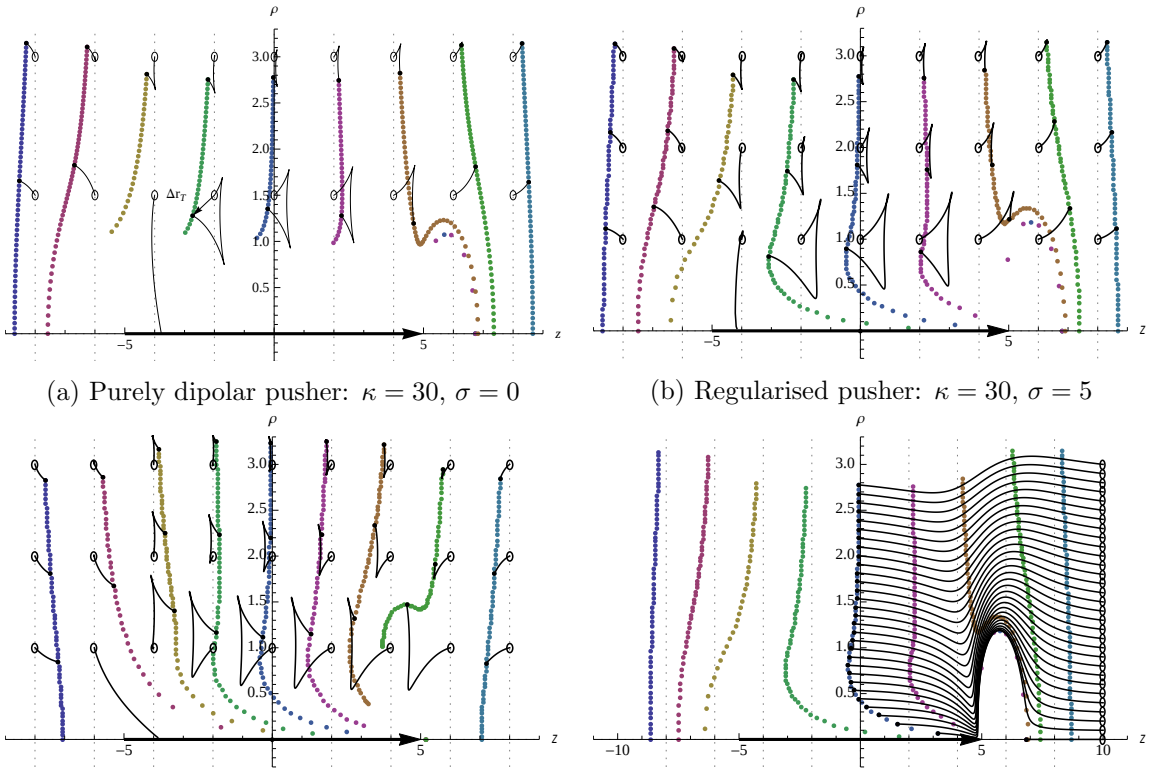

(a) Purely dipolar pusher: $\kappa = 30$, $\sigma = 0$

(b) Regularised pusher: $\kappa = 30$, $\sigma = 5$

(c) Regularised puller: $\kappa = -30$, $\sigma = 5$

(d) Same as (b) in swimmer's rest frame

Figure 2.3: Tracer trajectories and final displacements due to a micro-swimmer in an unbounded fluid. The swimming speed and the dipole strength characteristic for the *E. coli* bacterium have been used: $\kappa = 30\mu\text{m}^3/\text{s}$ and $v_\text{s} = 20\mu\text{m/s}$. Quadrupole strengths $Q_\parallel = Q_\perp = 5\mu\text{m}^4/\text{s}$ were chosen in (b-d) to represent a swimmer with a characteristic size $a_\text{sw} \approx 1\mu\text{m}$. All higher order multipole coefficients set to zero. The trajectories are computed using numerical integration of **Eq. 2.2**. Figures (a-c) are in the laboratory frame, where the swimmer moves along a finite line from $-5\mu\text{m}$ to $L = 5\mu\text{m}$. Initially, tracers are located in planar sheets perpendicular to the z-axis at $z_\text{T}^\text{int} = -8, -6, \ldots, 6, 8\mu\text{m}$, uniformly distributed between $\rho = 0$ and $\rho = 3\mu\text{m}$, and shown by small back circles. The final positions of the tracer sheets are depicted by larger, coloured dots. Several trajectories of individual tracers are also shown as light, black lines, running from starting points denoted by open circles to ending points denoted by closed dots. (a) Purely dipolar pusher. (b) Regularised pusher with finite size. (c) The equivalent puller with finite size. Figure (d) is equivalent to (b) in the rest-frame of the micro-swimmer, which itself is located at $z = 5\mu\text{m}$, tracers were initially located $z_\text{T}^\text{int} = 2, 4, \ldots, 16, 18\mu\text{m}$, and final tracer positions are shown after a time $\Delta t = 2L/v_\text{s}$ has passed. Full tracer trajectories are shown for the planar sheet $z_\text{T}^\text{int} = 10\mu\text{m}$.

different multipoles to the tracer displacements follows from **Eqs. 4.3-4.8** of the SI. Let us consider swimmers with a finite path from $-L$ to L and tracers located initially in the midplane $z_{\mathrm{T}}^{\mathrm{int}} = 0$. To the lowest orders in ρ^{-1}, where $\rho \gg L$ and noting that we use the short-hand notation $\rho \equiv \rho_{\mathrm{T}}^{\mathrm{int}}$, the tracer displacement is

$$\boldsymbol{\Delta r}_{\mathrm{T}}^{L} = -\frac{\kappa}{v_{\mathrm{s}}}\frac{2\rho L}{r_L^3}\hat{\boldsymbol{e}}_\rho + \frac{2L^3(Q_\parallel - 2Q_\perp) - (Q_\parallel + Q_\perp)L\rho^2}{v_{\mathrm{s}} r_L^5}\hat{\boldsymbol{e}}_z + \frac{O_r}{v_{\mathrm{s}}}\frac{6\rho L}{r_L^5}\hat{\boldsymbol{e}}_\phi + O\left(\frac{1}{\rho^3}\right) \quad (2.9)$$

where $r_L^2 = L^2 + \rho^2$. The first, dipolar, term confirms our conclusion that for a pusher (puller) the tracer is attracted to (repelled from) the swimming path. The second, quadrupolar, term corresponds to displacement along the swimming direction. The third term in **Eq. 2.9**, leading to azimuthal tracer displacement, is the octupolar rotlet. It is notable that the lower order quadrupolar rotlet term does not appear here because, due to the forward-backward symmetry of the quadrupole rotlet velocity field component, the tracer is rotated in one direction by the head but then in the opposite direction by the tail through an equal angle. This angle, which may be relevant to fluid stirring, is

$$\Delta\phi_{\mathrm{T}} = \frac{\Delta r_{\mathrm{T}}^{\phi}}{\rho} = -\frac{2Q_r}{v_{\mathrm{s}}}\left(\frac{1}{\rho^3} - \frac{1}{r_L^3}\right) + O\left(\frac{1}{\rho^4}\right), \quad (2.10)$$

using **SI-Eq. 4.8**. For long swimming path lengths $\Delta\phi_{\mathrm{T}}$ tends to a finite value for a given value of ρ.

Close to the swimmer path **Eq. 2.9** is invalid as the higher order terms become important. These terms correspond to interference between the tracer displacements. In particular, the tracer displacement due to the dipole and the quadrupole rotlet components interfere in **Eq. 2.8**. Hence, the cancellation of the net azimuthal tracer displacement due to the forward-backward symmetry of the quadrupole rotlet velocity field does not occur even for tracers initially placed in the mid-plane. Therefore we should expect enhanced fluid stirring in the azimuthal direction near the swimmer. In the limit $|\boldsymbol{r}_{\mathrm{T}}^{\mathrm{int}}| \ll L$ this effect can be quantified analytically and we will present these results in §**2.3.3**. Here we analyse the enhancement of azimuthal stirring close to the swimmer for a finite swimming path using numerical calculations.

Fig. 2.4 shows the net tracer displacement in the azimuthal direction for a finite size swimmer having the quadrupole rotlet strength $Q_r = 10\mu\mathrm{m}^4/s$. The enhancement of azimuthal stirring due to interference of the dipole and quadrupole rotlet terms is highlighted

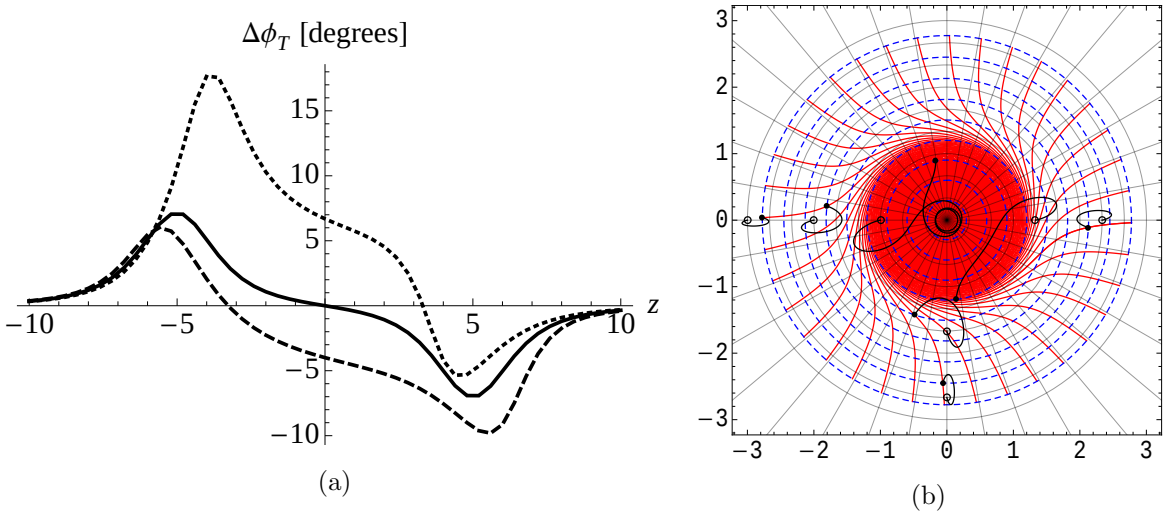

(a) (b)

Figure 2.4: Azimuthal tracer displacement due to a rotating micro-swimmer moving along a finite path, from -5 to 5μm. Parameters used are κ variable, $Q_r = 10\mu\text{m}^4/s$, $Q_\parallel = Q_\perp = 1\mu\text{m}^4/s$, $v_\text{s} = 20\mu$m/s, and all other multipole coefficients are set to zero. (a) Dependence of the azimuthal displacement on κ. Initially, tracers are located along a line with $\rho = 2\mu$m and $z_\text{T}^\text{int} \in [-10, 10]\mu$m. Final tracer positions are found numerically for $\kappa = 0$ (solid), $\kappa = +30$ (dotted), and $\kappa = -30\mu\text{m}^3/s$ (dashed). (b) Displacements projected on the (x, y) plane, with $\hat{\boldsymbol{e}}_z$ pointing into the paper. $\kappa = 30\mu\text{m}^3/s$. Tracers are initially located in the plane $z_\text{T}^\text{int} = 0$, distributed on a grid, shown in light grey, with $\rho_\text{T}^\text{int} \in [0, 3]\mu$m with spacing $h_\rho = 1/3\mu$m and $\phi_\text{T}^\text{int} \in [-\pi, \pi]$ with spacing $h_\phi = 2\pi/36 = 10°$. The final tracer displacement is shown by means of the transformed grid. Examples of tracer trajectories, initially located at $\rho_\text{T}^\text{int} = 1, 4/3, \ldots, 3\mu$m, run from open circles to black dots.

in **Fig. 2.4a**. When $\kappa = 0$ tracers starting at $z_\text{T}^\text{int} = 0$ have the net azimuthal displacement $\Delta\phi_\text{T} = 0$. However, addition of a positive (pusher) dipole term leads to a significant increase of the displacement. A negative (puller) dipole term would also result in a significant displacement, though of a lesser magnitude than for a pusher of the same absolute dipole strength. At the two extrema $z_\text{T}^\text{int} = \pm L$ tracers are only rotated in one direction by the head (or tail). Inserting the parameters of **Fig. 2.4a** and $L \to 2L$ into **Eq. 2.10** gives $\Delta\phi_\text{T} = \mp 7.1°$ at $z_\text{T} = \pm 5\mu$m, in good agreement with the numerical results. At larger z the interference effect becomes negligible and the $\Delta\phi_\text{T}$ corresponding to different κ values converge on the same curve.

Fig. 2.4a shows that overall pushers are more efficient at stirring fluid in the azimuthal direction than pullers of the same absolute dipole strength. This observation has a simple explanation: in **Eq. 2.9** we have shown for a finite straight swimming path that tracers are attracted to the path if the swimmer is a pusher and repelled from it if the swimmer is a puller. Consequently, tracers spend more time closer to the path of a pusher and the interference effect is stronger. As the attraction/repulsion effect decays with the swimming

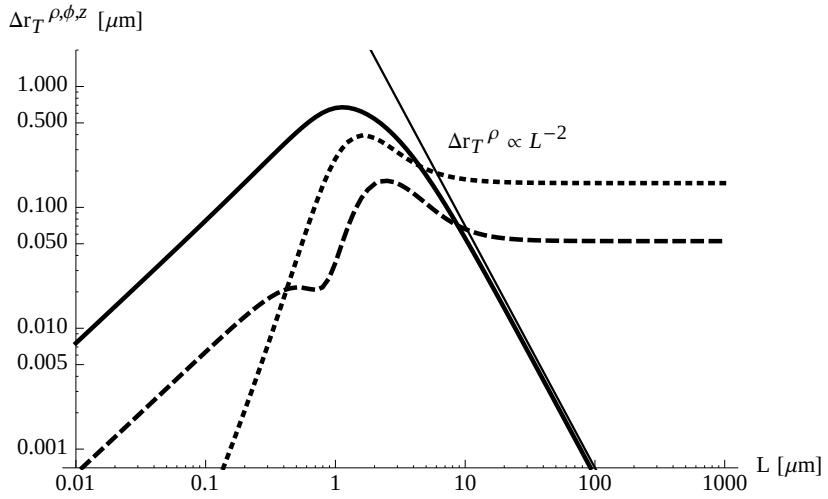

Figure 2.5: Dependence of the tracer displacement $\boldsymbol{\Delta r}_{\mathrm{T}}$ on the swimming path length $2L$. Initially, the tracer is located at $z_{\mathrm{T}}^{\mathrm{int}} = \phi_{\mathrm{T}}^{\mathrm{int}} = 0$ and $\rho_{\mathrm{T}}^{\mathrm{int}} = 2\mu$m. Final displacements, obtained numerically, in the ρ, ϕ, z-directions are denoted by the solid, dotted and dashed line respectively. Parameters used are: $v_{\mathrm{s}} = 20\mu$m/s, $\kappa = 30\mu\mathrm{m}^3/\mathrm{s}$, $Q_{\parallel} = Q_{\perp} = 5\mu\mathrm{m}^4/\mathrm{s}$ and $Q_r = 1\mu\mathrm{m}^4/\mathrm{s}$. All other multipole coefficients are set to zero.

path length L, this difference between pushers and pullers wanes accordingly. Indeed, we will show in §**2.3.3** that for an infinite swimmer path the azimuthal tracer displacement is dominated by a term proportional to $\kappa Q_r/v_{\mathrm{s}}^2$ that has the same magnitude for pushers and pullers of equal absolute dipole strength.

In **Fig. 2.4b** the tracer displacement is shown in the (x, y) plane for tracers initially located at $z_{\mathrm{T}}^{\mathrm{int}} = 0$ for $\kappa > 0$. Far away from the swimming path, whilst being attracted to the swimming path, the tracers are first rotated in the negative (anti-clockwise) ϕ direction as the swimmer moves from $-L$ to 0 then back in the positive ϕ direction as the swimmer moves from 0 to L. For example, the tracer trajectories starting between $\rho_{\mathrm{T}}^{\mathrm{int}} = 2\mu$m and 3μm show this well. The magnitude of the rotation is again predicted by **Eq. 2.10**. Close to the swimming path there is a strong rotation of tracer particles in the positive (clockwise) ϕ direction. This positive angular displacement corresponds to the dotted line in **Fig. 2.4a**. In particular, the tracer trajectory starting at $\rho_{\mathrm{T}}^{\mathrm{int}} = 1\mu$m illustrates that a pusher first attracts the tracer particle towards the swimming path, rotates it several times about the z-axis, and then repels it back to a ρ value close to the initial value $\rho_{\mathrm{T}}^{\mathrm{int}}$.

2.3.3 Tracer motion in the limit $|\boldsymbol{r}_{\mathrm{T}}^{\mathrm{int}}| \ll L$

We now consider tracer particles which are located near a long swimming path, so that $|\boldsymbol{r}_{\mathrm{T}}^{\mathrm{int}}| \ll L$. For $L \to \infty$ the lowest order expression for the net tracer displacement (**Eq. 2.9**)

vanishes. Physically this means that tracer trajectories become, generally, almost closed loops. Indeed, numerical results for the tracer displacement as a function of the swimming path length L, presented in **Fig. 2.5**, show that the ρ-component of the displacement decays as $\boldsymbol{\Delta r}_{\mathrm{T}}^{\rho} \sim L^{-2}$. This dependence follows directly from the first term in **Eq. 2.9**. The z and ϕ-components, however, remain finite for large swimming path lengths. In order to describe this behaviour analytically we need to take into account higher order terms in the expansion for the tracer displacement (**Eq. 2.4**).

In **SI-**§4.1 we compute contributions up to the sixth order inclusive, which gives us enough information to study a both short swimming path (**Eq. 2.9**) and also the two leading order contributions in powers of $1/\rho$ along each of the directions z, ρ and ϕ in the limit $L \to \infty$. Hence, writing terms up to $O\left(1/\rho^6\right)$ we obtain the final tracer displacement

$$\begin{aligned}\boldsymbol{\Delta r}_{\mathrm{T}}^{\infty} &= \left(-\frac{\pi\kappa^2}{16v_{\mathrm{s}}^2}\frac{1}{\rho^3} + \frac{9\pi(9Q_{\parallel}^2 + 14Q_{\parallel}Q_{\perp} + 41Q_{\perp}^2)}{1024v_{\mathrm{s}}^2}\frac{1}{\rho^5} - \frac{9\pi\kappa(3O_{\parallel} + 7O_{\perp})}{256v_{\mathrm{s}}^2}\frac{1}{\rho^5}\right)\hat{\boldsymbol{e}}_z \\ &+ \left(\frac{9\pi\kappa Q_r}{8v_{\mathrm{s}}^2}\frac{1}{\rho^4} - \frac{225\pi(2Q_r(O_{\perp} + O_{\parallel}) + O_r(Q_{\perp} + 3Q_{\parallel}) + 2\kappa H_r)}{512v_{\mathrm{s}}^2}\frac{1}{\rho^6}\right)\hat{\boldsymbol{e}}_{\phi}. \qquad (2.11)\end{aligned}$$

First, consider the final tracer displacement in the swimming direction, $\hat{\boldsymbol{e}}_z$. Far from the swimmer, for large ρ values, the κ^2 dipole term dictates a tracer displacement along the negative z direction that scales as $\Delta r_z \propto \rho^{-3}$. This far-field result is the same for both pushers and pullers, since it is proportional to κ^2. Closer to the swimming path, the negative displacement is countered by a forward-entrainment due to the quadrupole term, which is positive for all values of $Q_{\parallel}$ and $Q_{\perp}$. We have already seen this behaviour for tracers that start close to the middle of a finite swimming path in **Fig. 2.3b**. In principle the octupole and higher order terms, which will depend on individual swimmer details, could contribute to a backwards displacement, although eventually a forward entrainment is expected very close to the swimmer due to the no-slip boundary condition at its surface. So, in general, although **Eq. 2.11** is only guaranteed to be exact in the limit of large ρ, it gives a qualitatively correct picture of tracer displacements even for tracers initially located close to the swimmer. In particular, there is a characteristic critical radius $\rho = \rho_c$ where the displacement in the swimmer direction changes sign:

$$\rho_c = \frac{3\sqrt{9Q_{\parallel}^2 + 14Q_{\parallel}Q_{\perp} + 41Q_{\perp}^2 - 4\kappa(3O_{\parallel} + 7O_{\perp})}}{8\kappa}. \qquad (2.12)$$

For $\rho \gg \rho_c$ the far-field dipole approximation holds whereas for $\rho \ll \rho_c$ the near-field dominates the tracer displacement. Notice that substituting the parameters of **Fig. 2.3b** into **Eq. 2.12** gives $\rho_c = 0.5\mu$m, in reasonable agreement with the numerical results, given the small value $L = 5$ chosen to emphasize the effects of a finite swimming path.

In the angular direction, $\hat{\boldsymbol{e}}_\phi$, **Eq. 2.11** shows that the displacement of tracer particles about the z-axis scales as $\Delta r^\phi \propto \kappa Q_r \rho^{-4}$ far from the swimming path. Therefore a micro-swimmer with a head (tail) rotating in the (counter) clock-wise direction will stir particles in the counter clock-wise direction in the far-field. Dividing by the trajectory circumference $2\pi\rho$, the number of revolutions made by a tracer scales as ρ^{-5}. Inserting the parameters of **Fig. 2.4b** into **Eq. 2.11** gives ~ 2.7 revolutions for a tracer particle with $\rho_{\mathrm{T}}^{\mathrm{int}} = 1\mu$m, which is in reasonable quantitative agreement with the figure where the particle is rotated ~ 3.2 times around the swimming path.

Along the radial direction, $\hat{\boldsymbol{e}}_\rho$, our calculations show that all contributions to the final tracer displacement vanish up to order $O(\rho^{-7})$ and numerical integration of the implicit differential **Eq. 2.2** also shows no resultant displacement to within machine precision. Although for $L = \infty$ the tracer does move along $\hat{\boldsymbol{e}}_\rho$, it returns to its original distance from the swimming path ρ_{int} once the swimmer has moved past. Physically, this is reasonable as we are assuming the fluid to be incompressible. That is, if $\Delta r_{\mathrm{T}}^\rho$ had a finite negative (positive) value, constant for all initial tracer positions $z_{\mathrm{T}}^{\mathrm{int}}$ along the infinite swimming path, then this would lead to a singular accumulation (depletion) of particles at the z-axis, which would violate incompressibility. The final tracer displacement must be divergence free and hence the radial displacement vanishes for a long swimming path.

2.4 Results: swimmer moving parallel to a boundary

In experiments, micro-swimmers are often observed in the presence of boundaries and in biological systems micro-organisms often tend to accumulate near surfaces, as described by Spagnolie and Lauga[238], Berke et al.[246], Li et al.[248]. Therefore, we next present results for tracer trajectories and final displacements due to a micro-swimmer moving parallel to a planar surface. Compared to a swimmer moving in an unbounded fluid with swimming path length L, the swimmer body size a_{sw} (**SI-Eq. 3.9**) and the entrainment radius ρ_c (**2.12**), there is an additional length-scale in this system, the distance H between the swimmer and

the boundary.

As in §**2.3**, we start by describing numerical results for the tracer trajectories where parameters were chosen to represent a typical *E. coli* bacterium near a no-slip boundary in **Fig. 2.6**. We also show analogous results for a free-slip boundary in **Fig. 2.7** and summarise similarities and differences between the two boundary types. In analogy to §**2.3**, in the SI we aim to develop a more quantitative understanding of tracer motion, particularly in terms of the distance H. In **SI-**§4.2 and 4.3 we compute tracer displacements up to fourth order, for the no-slip and free-slip boundaries respectively, and in **SI-**§6 and 7 we discuss these in the limit of an infinite swimming path.

In **Fig. 2.6** and **2.7** we show tracer displacements and several trajectories for a swimmer moving from $-L$ to $+L$ parallel to the boundary. These results were obtained by numerically integrating **Eq. 2.2** including the appropriate image term. The image system of a swimmer near a free-slip boundary is simply a mirror swimmer. Near a no-slip boundary, however, the image of a dipolar pusher (puller) is the equivalent puller (pusher) plus more complex terms of quadrupolar and octupolar structure (see **SI-**§2.6). To see the effect of the boundary it is useful to compare with **Fig. 2.3** and **2.4** for swimming in an infinite fluid, $H = \infty$. Close to the swimming path the tracer displacements are almost independent of H and the results of §**2.3.3** hold. However far from the swimmer, and also between the swimmer and the surface, there are boundary effects because here the distances to the swimmer and to the image are comparable.

Fig. 2.6a and **2.7a** show the tracer displacement in the (x, z) plane. Far away from the swimmer and the free-slip boundary the trajectories are doubled in size, since the swimmer and its mirror image cooperate. For the no-slip boundary, however, the dipolar terms of the swimmer and image cancel (in **SI-Eq. 4.21**), so that the tracer trajectories are no longer triangular loops as for a dipolar swimmer but instead the dominant quadrupolar terms give a smaller 3-loop trajectory.

Consider now what happens close to the boundary. Our first observation is that despite a no-slip boundary condition, there is a significant forward-displacement of tracer particles between the swimming path and the boundary. Also for a finite swimming path, tracers that start at $z > 0$ tend to be displaced forwards. For the free-slip boundary this effect is about 3 times larger with the absence of the no-slip constraint.

This is emphasised in **Fig. 2.6b** and **2.7b** which show the longitudinal displacement in

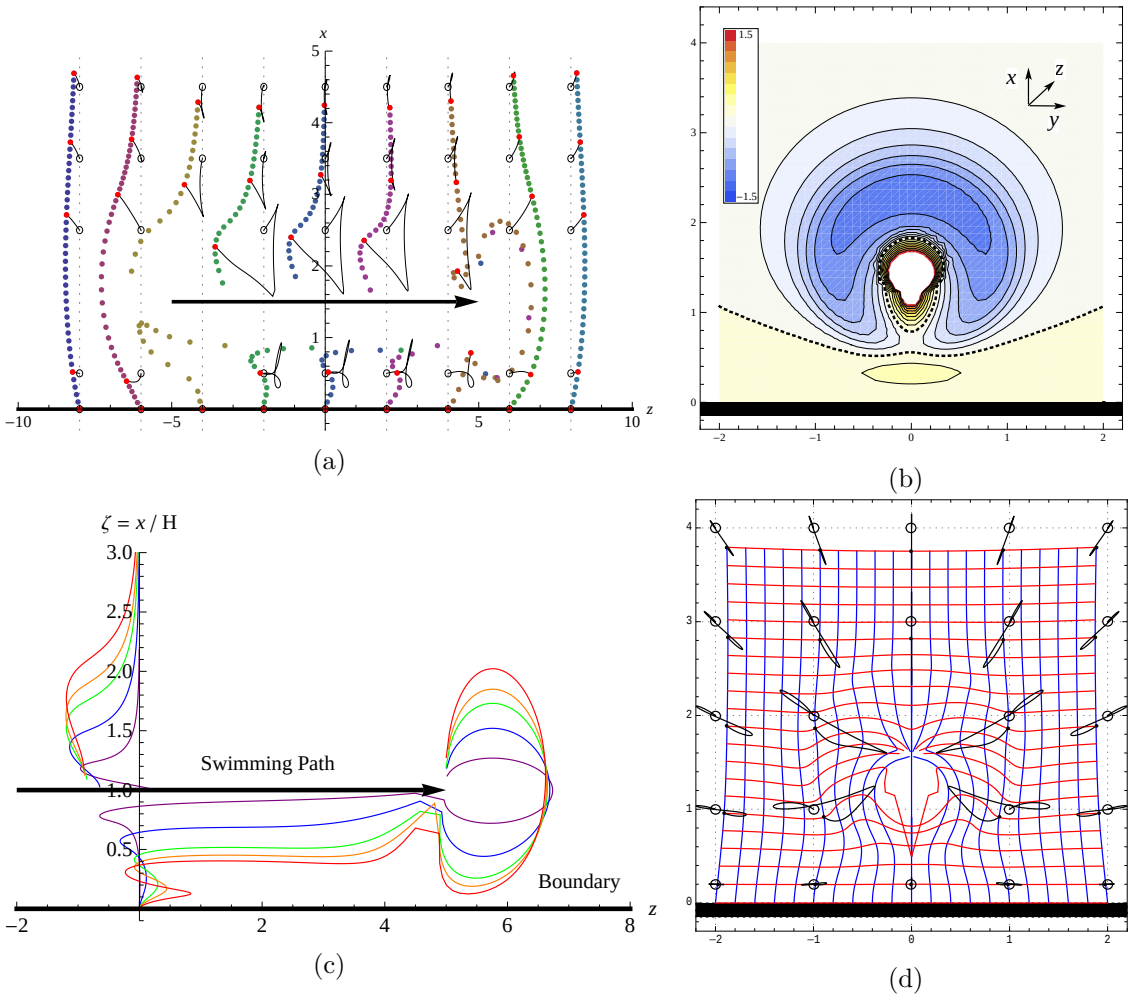

Figure 2.6: Numerical results for tracer displacements and trajectories due to a micro-swimmer moving along a finite path parallel to a no-slip boundary. The units of length and time are μm and s. The swimming path is from -5 to 5. The boundary is denoted by a thick black line. Several tracer trajectories are shown as light, black curves, running from starting points denoted by open circles to ending points denoted by closed red dots. The trajectories were computed using numerical integration of **Eq. 2.2**. Parameters used are $\kappa = 30$, $Q_{\parallel} = Q_{\perp} = 1$, $v_s = 20$. All other multipoles are set to zero. (a) Tracer displacements in the $x - z$ plane for $H = 1.5$. Initially, tracers are located in sheets perpendicular to the boundary at $y_T^{int} = 0$ and $z_T^{int} = -8, -6, \ldots, 6, 8$, uniformly distributed between $x_T^{int} = 0$ and 4.5, as shown by small black dots. The final positions are shown by larger dots in various colours. (b) $x - y$ cross section showing the displacement along the z axis of tracers which start in the plane $z_T^{int} = 0$ for $H = 1.5$. Colours indicate the magnitude of the displacement. White indicates strong forward entrainment (displacements > 1.5). (c) Dependence of tracer trajectories in the $x - z$ plane on distance from the boundary H. The x axis is scaled w.r.t. H but the z axis is not scaled. Initially, tracers are located along the line $y_T^{int} = z_T^{int} = 0$. The final positions are shown by continuous lines in red, orange, green, blue and purple for $H = 1, 1.2, 1.4, 2, 4$ respectively. (d) $x - y$ cross section showing the in-plane displacement of tracers which start in the plane $z_T^{int} = 0$. The swimmer rotation strength $Q_r = 0$. Tracers are initially uniformly distributed on a grid with $0 \le x_T^{int} \le 4$ and $-2 \le y_T^{int} \le 2$ with spacing $h = 1/5$. The final displacement is depicted by means of the transformed grid.

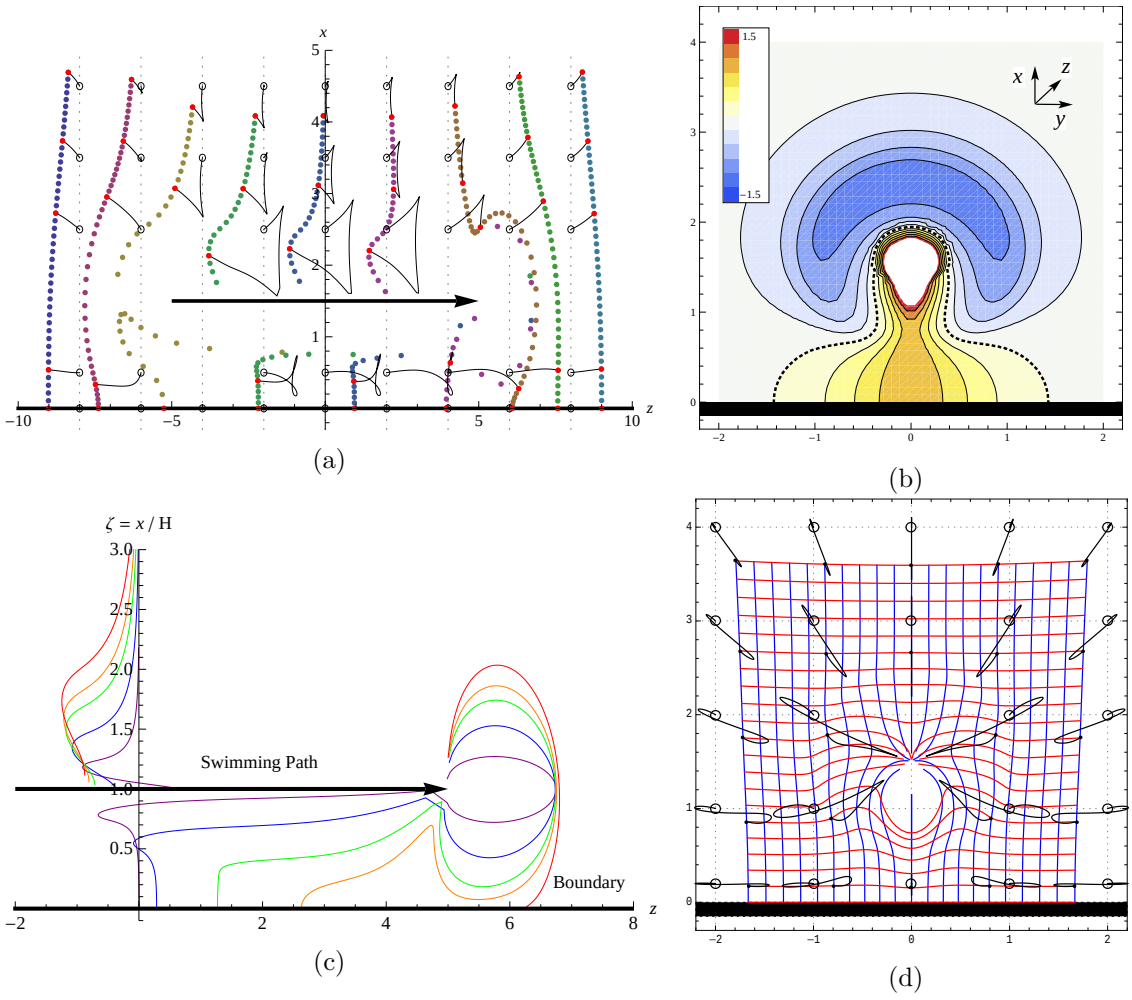

Figure 2.7: Numerical results for tracer displacements and trajectories due to a micro-swimmer moving along a finite path parallel to a free-slip boundary. Apart from the boundary type, this figure is identical to **Fig. 2.6**.

the $x-y$ plane for tracers initially at $z=0$. The maximum forwards displacement between swimmer and boundary is about 0.3μm in the no-slip case compared to 1μm for the free-slip boundary. Comparing **Fig. 2.6b** and **2.7b** shows that the longitudinal displacement is positive in the far-field for the no-slip boundary but negative for the free-slip boundary.

Fig. 2.6c and **2.7c** show the dependence of the tracer displacements on H. Note that in this figure the x axis is scaled w.r.t. H but the z axis is not scaled. The purple curve for $H=4\mu$m approaches the unbounded swimmer case. As H decreases the forwards displacement between the swimmer and the boundary increases as $\kappa^2/v_s^2H^3$, and is maximum at $\zeta=0$ and $\zeta_m=0.3$ for the free-slip and no-slip boundary respectively. For small H values, compared to the other system length-scales, the near-field entrainment interferes with the forwards displacement at the boundary. For the no-slip boundary this shifts the maximum to lower ζ values and for the free-slip boundary this merges the entrainment of the boundary and near-field, so that at $H=a_{sw}$ the swimmer acts like a little bulldozer.

In **Fig. 2.6d** and **2.7d** the tracer displacements in the transverse directions, along x and y, are shown in the (x,y) plane for $z=0$. Despite the fact that $Q_r=0$, representing a non-rotating swimmer, we find significant mixing of tracer particles in the transverse directions, up to 0.8μm close to the swimming path for a no-slip boundary. With decreasing H, the strength of this effect increases as $\kappa Q_\perp/v_s^2H^4$, independently of $Q_\parallel$. Furthermore, tracers near a free-slip boundary are not attracted towards the swimming path, *cf.* the limit $H\to\infty$ given by **Eq. 2.9**, but towards the boundary instead.

In **SI-**§6 and 7 we describe the tracer motion near a free-slip and no-slip surface respectively in terms of a pertubative expansion analogous to that in §**2.3.3**. Hence, we find analytic expressions in terms of the experimental parameters H, v_s, L, κ etc. for the additional boundary-induced entrainment and transverse stirring of tracer particles.

2.5 Discussion

In this chapter we have studied the way in which an axisymmetric swimmer moves tracer particles as it swims through a fluid, concentrating on straight swimming trajectories of finite and infinite length, in an unbounded fluid and parallel to a surface, considering both slip and no-slip boundary conditions. Numerical results were obtained by integrating the equations of tracer motion. Analytical results followed from expanding the tracer displacement in powers

of r^{-1}, the inverse distance between swimmer and tracer.

We started by considering a finite swimming path from $z = -L$ to L. Far from the swimmer the tracer particles move in loop-like trajectories with a size that scales as κ/ρ, where κ is the strength of the swimmer dipole moment and $\rho = \min r(t)$, the distance between tracer and swimming path. As the swimmer trajectory becomes infinitely long the tracer trajectories tend to almost closed loops, but a finite final net displacement remains that is backwards relative to the swimming direction and scales as $-\kappa^2/\rho^3$. The introduction of a slip surface doubles the loops in size, and for an infinite swimming path enhances the final tracer displacement by a factor four. For a no-slip boundary, however, the far-field tracer loops are much smaller, with a final radial displacement that scales as κ/ρ^3 for a finite swimmer trajectory crossing over to a scaling $+\kappa^2/\rho^5$ in the swimming direction for an infinite swimming path.

Closer to the swimmer the tracer particles still move in loop-like trajectories. However they are now entrained by the swimmer, showing a significant net forwards displacement. We show that this can usefully be modelled by including quadrupolar terms in the flow field. These lead to a surface around the singularity across which there is no flow, mimicking a finite swimmer size and removing the problem of the singularities in the multipole expansion of the flow field. A proper combination of the quadrupole coefficients can model the near-field of swimmers of the elongated shapes typical of many micro-organisms.

Along the surface itself tracer particles are displaced forwards along the swimming direction, both for slip and for no-slip boundaries, for pushers and for pullers. As the distance H between the boundary and the swimming path increases, the forward displacement wanes as κ^2/H^3.

To quantify these effects consider a typical swimmer with parameters chosen to represent an *E. coli* bacterium, $\kappa = 30\mu\mathrm{m}^3/\mathrm{s}, v_\mathrm{s} = 20\mu\mathrm{m/s}$ and $L = 5\mu\mathrm{m}$. A tracer particle initially located at $z_\mathrm{T}^\mathrm{int} = 0$ and $\rho_\mathrm{T}^\mathrm{int} = 1.5\mu\mathrm{m}$ follows a triangular loop-like trajectory of size $\sim 1\mu\mathrm{m}$. Its final displacement is $\sim 0.25\mu\mathrm{m}$ against the swimming direction. The crossover from final backward displacement to forward entrainment, if we take the quadrupole strengths $Q_{\parallel,\perp} = 5\mu\mathrm{m}^4/s$, occurs at a distance $\rho_c \sim 3Q_{\parallel,\perp}/\kappa \sim 0.5\mu\mathrm{m}$ from the swimming path. Close to a slip boundary, if the swimmer moves at a distance $H = 1.5\mu\mathrm{m}$, the tracer particle is displaced $\sim 0.9\mu\mathrm{m}$ along the swimming direction, compared to $\sim 0.3\mu\mathrm{m}$ for a no-slip boundary.

Non-rotating swimmers do not displace tracers in the azimuthal direction when they swim far from the boundaries. A rotating swimmer with the head rotating in the clock-wise direction (and the tail rotating in the counter clock-wise direction) rotates tracer particles in the counter clock-wise direction. For example, for a swimmer with rotation strength $Q_r = 10\mu\text{m}^4/s$, a tracer particle initially located a distance $\rho = 1\mu\text{m}$ from the swimming path can be rotated up to ~ 3 times around it. For a pusher this stirring effect is larger than for a puller, as it first attracts a tracer towards the swimming path, where the azimuthal flow is stronger, before repelling it back to its initial radius $\rho_{\text{T}}^{\text{int}}$.

Close to a boundary even non-rotating swimmers create fluid flows in the plane perpendicular to the swimming direction. This may be ecologically significant as a mechanism for resuspension of small sedimented particles. The strength of this effect scales as the product $\kappa Q_{\perp}$.

Loop-like tracer trajectories have been observed in several experiments with biological[195] and non-biological swimmers[126], but quantitative matching of our results to experiment at this point is difficult due to the unpredictability of swimmer trajectories and insufficient quality of experimental data. Currently, however, new experimental techniques are being developed that could allow simultaneous observation of multiple trajectories of tracer particles[59]. Also, development of artificial microswimmers that are more easily controllable could provide the data for a quantitative match between theory and experiment.

Throughout this chapter we neglect the smearing effect of Brownian fluctuations on the tracer trajectories. Its relative importance depends on the physical size of advected particles and is typically weak for particles larger than one micron[193]. Moreover, the effect of Brownian fluctuations on mixing can be accounted for by adding the Brownian and the biogenic contributions to the effective tracer diffusion coefficient[198].

Our results connect well to recent works[315,319,320] that address recent observations of non-Gaussian tracer displacement[193,195,201,318]. Our expressions could input into a more accurate calculation of the displacements distribution and of the diffusion coefficient by accounting for a finite swimmer size. This latter provides a cut-off for large particle displacements. Hence, in the long run the distribution will converge to a Gaussian. Furthermore, we expect enhanced biomixing in fluid layers near boundaries since tracers are entrained further. This prediction is in agreement with the experiments by Mino et al.[196], but it provides an alternative explanation for this effect. Our expressions could allow for a first approximation of the

anisotropic tracer diffusion coefficients near an interface as a function of H.

This chapter has only considered swimming paths oriented parallel to the boundary, motivated by experiments by Molaei et al.[59] that show that the tumbling of wild-type *E. coli* is suppressed up to distances 20μm from a no-slip surface, and when they tumble the reorientations are largely skewed towards the surface-parallel directions. Nevertheless, the analysis may easily be extended for swimmers approaching or leaving the boundary at a given angle or along a defined trajectory[214,238] or moving in, say, a circular trajectory[253,322]. Moreover, it would be of interest to understand the effect of other types of confinement, such as between two parallel flat plates or inside a thin liquid film on tracer trajectories. The single swimmer problem provides a step towards estimating the tracer motion and diffusion due to a suspension or beam of swimmers, and how this is altered by the presence of a boundary.

CHAPTER 3

Sorting of micro-swimmers in viscoelastic fluids

"Be careful about reading health books. You may die of a misprint."

Mark Twain (1835–1910)

3.1 Introduction

Whereas the work in chapter §2 assumes that the swimmers move in straight lines parallel to a boundary, real motile micro-organisms can undergo more complicated dynamics as they inhabit confined and complex micro-environments. Geometrical constraints are a key regulator of rheotaxis, the reorientation of swimmers in response to externally imposed flows[110], and are essential in the design of microfluidic devices for drug delivery systems, hematology and cytometry[323,324]. Additionally, the complexity of embedding fluids is crucial. One important aspect of the complexity arises from the dual fluidic and elastic (viscoelastic) behaviour of many biological fluids such as mucus and extracellular matrix gels[325–327] or blood at macroscopic length-scales[328–330].

Despite the widespread implications of viscoelastic effects on biological processes, research on motile microorganism dynamics in confined environments is largely limited to Newtonian fluids[214,239,262,275,283,289,304,331–334]. Recently, a large number of studies have considered locomotion in quiescent non-Newtonian fluids at the scale of micro-swimmers, in experiment, simulations and theory[294–297,299–302], but little is known about the dynamical behaviour of swimmers subject to large-scale non-Newtonian flows.

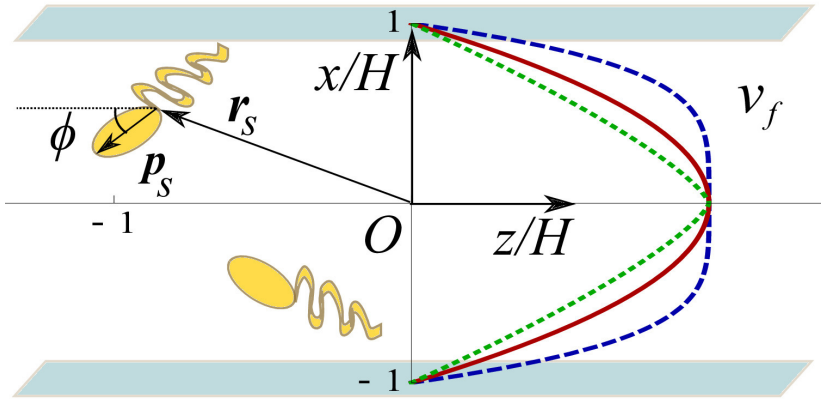

Figure 3.1: Schematic of a microswimmer at position $\boldsymbol{r}_{\mathrm{s}}$ and moving with speed v_{s} in the direction $\boldsymbol{p}_{\mathrm{s}}$ subject to a viscoelastic flow within a microchannel of height $2H$. The Poiseuille flow $\boldsymbol{v}^{\mathrm{F}}$ is shown for shear-thinning (blue, dashed), Newtonian (red, solid) and shear-thickening (green, dotted) fluids.

In this chapter, we use our theoretical framework for individual micro-organisms swimming in confined, flowing micro-biological environments of non-Newtonian fluids (§1.3.1). We study the macroscopic effects of shear-dependent viscosity and viscoelasticity, both in separation and in conjunction, for a weakly viscoelastic fluid. Image systems are used, regularizing the hydrodynamic interaction of micro-swimmers with the walls, and swimmer trajectories are characterised. Shear-dependent viscosity is seen to greatly impact the upstream motion of motile cells and our analysis shows that the presence of normal stress differences in viscoelastic fluids results in a remarkable upstream migration along the centre line. We provide quantitative measures of the upstream motion and propose a novel sorting mechanism for motile organisms in confined viscoelastic flows.

3.2 Model

A single microorganism of radius a is modelled as swimming in flowing, incompressible, non-Newtonian fluid within a channel of height $2H$ (**Fig. 3.1**). We use the equations of motion (**1.45-1.46**) without thermal noise ($\boldsymbol{v}_{\mathrm{B}}^{k}T$ and $\boldsymbol{\Omega}_{\mathrm{B}}^{k}T$) or run-and-tumble fluctuations $\boldsymbol{\Omega}^{\mathrm{RT}}$, initially with a Newtonian Poiseuille background flow $\boldsymbol{v}^{\mathrm{F}} = v_{\max}(1-(x/H)^2)\hat{\boldsymbol{e}}_z$ and $\boldsymbol{\Omega}^{\mathrm{F}} = \frac{1}{2}\boldsymbol{\nabla}\times\boldsymbol{v}^{\mathrm{F}}$. The translational invariance of these along the y and z directions allows us to consider motion of swimmers in the $y=0$ plane and orientation can be represented as $\boldsymbol{p}_{\mathrm{s}} = -\sin(\phi)\hat{\boldsymbol{e}}_x - \cos(\phi)\hat{\boldsymbol{e}}_z$, where $\phi\in[-\pi,\pi]$ is the angle in the $x-z$ plane. Upstream swimming corresponds to $\phi=0$ and downstream to $\pm\pi$ (**Fig. 3.1**). Consequently, the

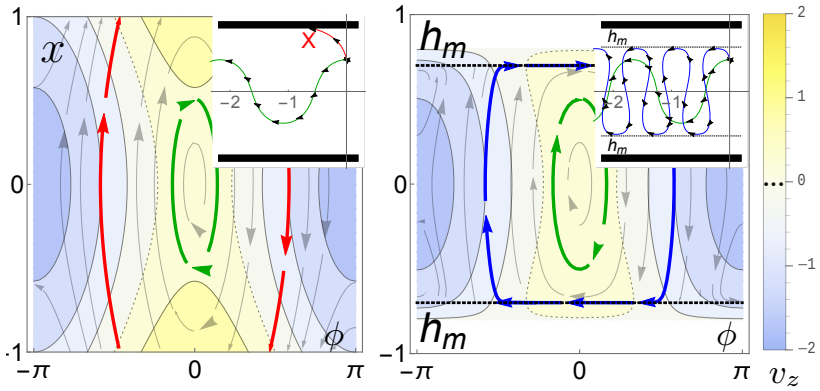

(a) Non-regularised HI (b) Regularised HI

Figure 3.2: Typical trajectories for swimmer dynamics in a Newtonian Poiseuille flow shown in $x-\phi$ phase space, and in the $x-z$ plane (insets). The swimmer and maximum flow velocities are $v_s = 1$ and $v_{max} = 0.75$, and the dipole moment is $\kappa = 0$. a) Non-regularised HI, $\sigma = 0$. b) Regularised HI with $\sigma = (3/10)^3$ so that $h_m = 3/10$. The background colours indicate the velocity in the z direction.

dynamics of the system can be represented by two coupled equations, $\dot{x} = \dot{x}(x, \phi)$ and $\dot{\phi} = \dot{\phi}(x, \phi)$, and a third uncoupled equation $\dot{z} = \dot{z}(x, \phi)$. We nondimensionalise lengths by half the channel height, H, and velocities by the swimming speed, v_s. Therefore, changes in the swimming speed due to viscoelasticity, as studied in Refs.[294–297,299–302], are readily incorporated in this model.

3.3 Results

3.3.1 Newtonian liquid

In a Newtonian fluid, this system shows the emergence of swinging and tumbling microswimmer trajectories in Poiseuille flow[214,283]. Upstream-oriented swimmers are rotated by background vorticity so that they oscillate about the centre line (**Fig. 3.2**(a-b); green trajectory). For large oscillation amplitudes, however, the swimmer runs into the walls (**Fig. 3.2**(a); red trajectory). Because of the proximity, HI with the boundaries must be included[214]. Simply including the far-field force dipole of strength κ and an image system consisting of a superposition of point-force singularities[238] in the HI produces non-physical singular flow fields near the walls, unless a physical cut-off length is provided.

We construct a more physical representation by including a source doublet of strength σ in the swimmer's flow and image fields, producing a more accurate near-field flow and

regularising the HI with the boundaries. This ensures that the swimmer is turned away from the boundaries by the closest distance of approach $h_m = (\sigma/v_s)^{1/3}$, which sets a natural cut-off and gives an effective size. This may be understood to be its hydrodynamic radius, $a_h = (2\sigma/v_s)^{1/3}$, as discussed in §**2.2.1**, which we expect to be directly proportional to the swimmer size; $a_h \sim a$, and thus $h_m \sim a$. E.g. *Volvox* has $\sigma \sim 10^9 \mu_{\mathrm{m}}{}^4/_{\mathrm{s}}$ and $v_s \sim 10^2 \mu_{\mathrm{m/s}}$,[208] so that $a_h \sim 270\mu_{\mathrm{m}}$ compared to $a \sim 200\mu$m. By including the near-field correction, unphysical swimmer-wall contact is ruled out and the swimmer trajectory runs parallel to the wall with the offset h_m (**Fig. 3.2**(b); blue trajectory). To consistently account for finite swimmer size effects, we also include the Faxén corrections to the flow induced translational, $\boldsymbol{v}^{\mathrm{F}}$, and angular velocity, $\boldsymbol{\Omega}^{\mathrm{F}}$, of the swimmer (**Eq. 1.54**).

3.3.2 Effect of shear-dependent viscosity

Non-Newtonian effects modify the background flow and trajectories of micro-swimmers. Non-Newtonian fluids generally feature two properties different from a Newtonian counterpart — namely, shear dependent viscosity and normal stress differences. Here shear-thinning and -thickening effects are accounted for via a power-law fluid model $\eta = \eta_0(\dot{\gamma}/\dot{\gamma}_0)^{n-1}$, where $\dot{\gamma}$ is the shear rate, η_0 is the viscosity at the shear-rate $\dot{\gamma}_0$, and n is the shear-thinning parameter. The background Poiseuille flow of a power-law fluid is

$$\boldsymbol{v}^{\mathrm{F}}(\boldsymbol{r}) \quad = \quad v_{\max}\left(1 - \left(\frac{|x|}{H}\right)^{\frac{1+n}{n}}\right)\hat{\boldsymbol{e}}_z, \tag{3.1}$$

where $v_{\max}$ is the maximum flow speed. This results in a stronger (weaker) flow near the walls, in shear-thinning (-thickening) fluids compared to a Newtonian fluid with the same $v_{\max}$ (**Fig. 3.1**). HI with the walls remain approximately Newtonian for weakly non-Newtonian fluids since the asymmetric correction for a dipolar swimmer[335,336] decays rapidly as $\sim r^{-3}$,[337,338] which is small compared to the Newtonian contribution and amounts to a minor correction on the quadrupolar term.

The upstream motion of a swimmer is enhanced in a shear-thickening fluid compared to a shear-thinning counterpart without normal stresses (**Fig. 3.3** and Supplemental Material movie 1 at URL[339]). This is associated with changes in vorticity in the vicinity of the walls. The stronger vorticity of the shear-thinning fluid near the wall results in a more rapid reorientation towards the centre line. Consequently, the swimmer has less time to move upstream.

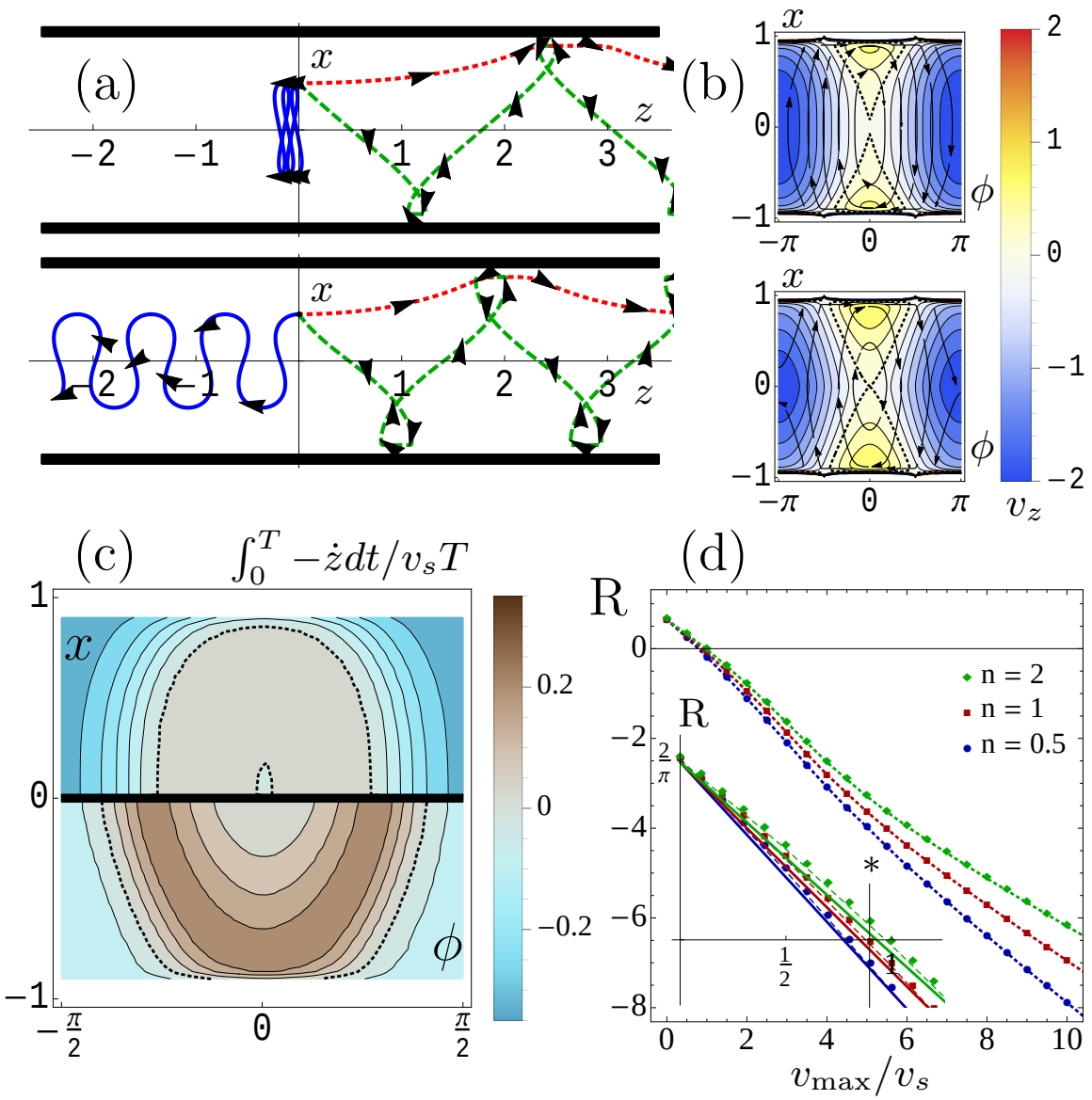

Figure 3.3: Swimmer dynamics in Poiseuille flow of a shear-thinning ($n = \frac{1}{2}$) and -thickening fluid ($n = 2$) without normal stresses, shown in the upper and lower halves of subfigures (a-c). $v_s = v_{max} = 1$, $\kappa = 0$ and $\sigma = (1/10)^3$. a) Trajectories in the $x - z$ plane, with initial position $\boldsymbol{r}_s = (0, 1/2)$ and orientations $\phi = 0$ (blue), $\pi/2$ (green), and π (red). b) Trajectories in $x - \phi$ phase space. The background colours indicate the velocity in the z direction. c) Upstream swimming velocity, $-\dot{z}$, averaged over a large time, for all upstream-oriented initialisations in $x - \phi$ space. d) Upstream retention ratio, defined by (c) averaged over these initial conditions, as a function of the flow speed. Points show full numerical solutions, dashed lines show theoretical predictions, and solid lines show the limit $v_{max} \ll v_s$, Eq.(3.2). The inset focusses on this limit.

An initially upstream oriented swimmer (**Fig. 3.3**(a); blue trajectory) in a shear-thinning fluid moves a short distance upstream after the first oscillation about the centre line, whereas the swimmer in the shear-thickening fluid progresses an order of magnitude further. Swimmers initially orientated towards the walls (dashed green trajectories) are carried by the flow, but in a shear-thickening fluid they move further upstream near the walls. Similarly, swimmers

initially orientated downstream (dotted red trajectories) experience an enhanced downstream motion in a shear-thinning fluid. This demonstrates that the dynamics in flowing non-Newtonian environments can have a more significant effect on motion than relatively small modifications to the swimming speed in quiescent non-Newtonian fluids[294–297,299–302].

If $v_{\max} = v_s$, swimmers oriented directly upstream at the centre line do not progress, while those that oscillate about the centre line experience less counterflow on average and therefore are able to migrate upstream (**Fig. 3.3**(b-c)). However, if the oscillations about the centre line are too large, the swimmer cannot move upstream. Therefore, the effective upstream motility is not well described by any given trajectory but rather by a retention ratio[340], the ratio of the time-averaged z-component of swimmer velocity to the swimming speed, $R = \left\langle T^{-1} \int_0^T -\dot{z}(t; x_0, \phi_0) dt \right\rangle / v_s$, where we average over all upstream-oriented trajectories $x_0 \in [-H + h_m, H - h_m]$ and $\phi_0 \in [-\pi/2, \pi/2]$. The upstream retention ratio can be determined numerically (**Fig. 3.3**(d); points) and be approximated analytically. A conserved quantity of motion can be found by integrating $\dot{x}/\dot{\phi}$, giving $\mathcal{C} = 1 + \frac{1}{2} v_{\max} |x|^{(1+n)/n} - v_s \cos\phi$. Hence, the distance travelled along z per oscillation can be computed, $D = \int_{traj} \dot{z} dt$, as well as the period, $T = \int_{traj} dt$. Dividing these and averaging over the initial conditions gives $R = -\langle \frac{D}{v_s T} \rangle$ (**Fig. 3.3**(d); dashed lines). In the limit of $v_{\max} \ll v_s$ we find the linear relation (**Fig. 3.3**(d); solid lines)

$$R = \frac{2}{\pi} - \frac{2 + 9n + 7n^2}{2 + 10n + 12n^2} \frac{v_{\max}}{v_s}. \tag{3.2}$$

Hence, the difference in upstream retention ratio for shear-thinning and -thickening fluids grows with increasing flow speed. This determines the crossover between upstream or downstream motion of the majority of swimmers where $R = 0$ (see inset of **Fig. 3.3**(d)). The slopes change at larger flow speeds, $v_{\max} > 4v_s$, when the tumbling trajectories start to outnumber the oscillating trajectories[214] and the full solution for R must be applied (dashed lines). In this $v_{\max} \gg v_s$ regime, the difference in upstream retention ratio for shear-thinning and -thickening fluids can be large (**Fig. 3.3**(d)). For $v_{\max} = 10v_s$, the shear thickening ($n = 2$) R-value differs by 33% from the shear-thinning ($n = 1/2$) value, which is substantial compared to the $5 - 10\%$ change in swimming speed observed in quiescent non-Newtonian fluids[294–297,299–302].

The significant modification of upstream retention ratios in non-Newtonian fluids can

have important consequences in micro-biological flows. For instance, our results suggest that a motile *H. pylori*, swimming with an average velocity of $27\mu m/s$[291] and subjected to gastric mucosal flow with a similar velocity and $n = 0.5$, would have a 50% reduction in upstream retention ratio than if it were swimming in a Newtonian fluid flow ($n = 1$). Since the velocity of the mucosal flow can vary broadly[341] and n can be as small as ~ 0.15,[291,341,342] this serves as a conservative example.

3.3.3 Effect of normal stress differences

In addition to shear-dependent viscosities, many micro-biological fluids are characterised by viscoelastic normal stress differences. To describe these, with a power-law viscosity, we employ the second-order fluid model[343]. Instead of **Eq. 1.3**, we use the stress tensor $S_{ij} = -p\delta_{ij} + \eta(\dot{\gamma})D^{(1)}_{ij} - \frac{1}{2}\psi_1 D^{(2)}_{ij} + (\psi_1 + \psi_2)D^{(1)}_{ik}D^{(1)}_{kj}$, where ψ_1 and ψ_2 are the first and second normal stress coefficients and $D^{(1)}_{ij}$ and $D^{(2)}_{ij}$ are the Rivlin-Eriksen tensors. The Deborah number is $\mathrm{De} = \frac{\psi_1 - 2\psi_2}{\eta}\frac{v_{\max}}{H} \ll 1$. The normal stress coefficients characterize the fluid elasticity. These terms do not alter the undisturbed flow profile of Eq. (3) in the absence of swimmers. However, the disturbance flow around a finite-sized swimmer in combination with non-uniform shear across the channel results in a normal stress imbalance that causes a lateral migration across streamlines. Normal stress-induced migration of passive, inertialess particles in pressure-driven flow is well documented[288,344–351]. To determine the migration velocity we use Chan and Leal's solution for general quadratic flow[345] by expanding the background flow profile (**Eq. 3.1**) about the swimmer position, as reported previously[288]. In our system, the migration velocity is then

$$\boldsymbol{v}^{\mathrm{VE}} = -\psi_n \left(\frac{|x|}{H}\right)^{\frac{3-2n}{n}} \hat{\boldsymbol{e}}_x, \tag{3.3}$$

where $\psi_n = \psi_s a^2 v_{\max}^{3-n}\gamma_0^{n-1} f(n)/\eta_0 H^{4-n}$, $f(n) = 5(1+n)^{3-n}/36n^{4-n}$ and $\psi_s = \psi_1 - 2\psi_2$. The function ψ_n encapsulates both the non-Newtonian effects of normal stress differences and shear-dependent viscosity. A viscoelastic torque $\boldsymbol{\Omega}^{\mathrm{VE}}$ is not included in the equation of motion **Eq. 1.46**, because this term is not significant compared to the vorticity when $\mathrm{De} \ll 1$ and, by symmetry of the swimmer, does not lead to preferred orientations.[288]

In both the shear-thinning and -thickening cases with normal stresses, the swimmer is driven to the centre line, and the coupling between motility and streamline migration rotates the swimmer to move upstream along the centre line (**Fig. 3.4**(a)). Unlike in a Newtonian

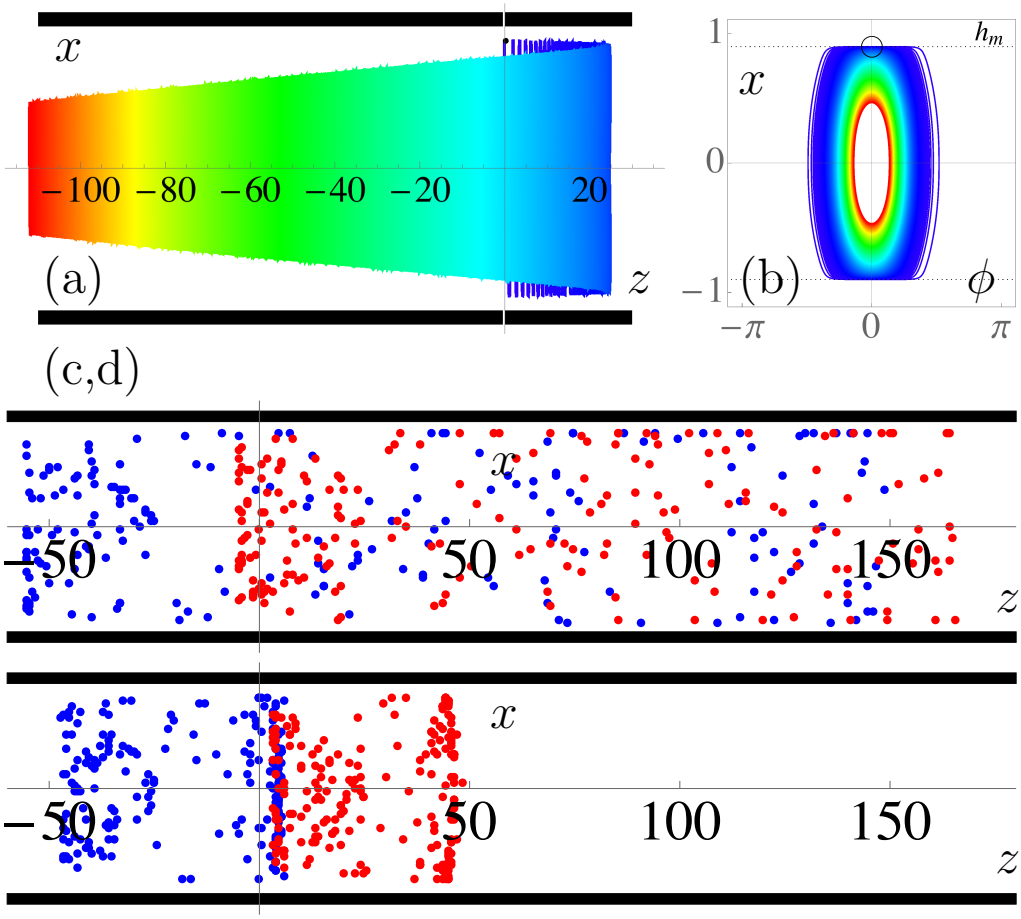

Figure 3.4: Swimmer dynamics in Poiseuille flow of a shear-thinning viscoelastic fluid with $De = 0.1$, $n = 0.8$, and $v_{\max} = 1v_s$. The swimmer parameters are $a = 0.1$, $v_s = 1$, $\kappa = 0$ and $\sigma = 10^{-3}$. a) Oscillating trajectory in the $x - z$ plane with initial position $\boldsymbol{r}_s = (0, 0.9)$ and orientations $\phi = 0$. b) Corresponding trajectory in $x - \phi$ phase space. Colours indicate time progressing, from $t = 0$ (blue) to $t = 1000$ (red). The swimmer is focussed towards the centre line and are reoriented to move upstream. c-d) Two ensembles of swimmers, with $v_s = 1.1$ (blue) and $v_s = 0.9$ (red), are released from a random x-position and orientation in the channel at $z = 0$. In a Newtonian fluid (c), the swimmers are dispersed but in a viscoelastic fluid (d) they remain clustered and are sorted according to swimming speed over time.

fluid, the oscillations about the centre line are now damped in amplitude as the phase space origin ($x = \phi = 0$) is a stable, attractive spiral (**Fig. 3.4**(b)). The attraction is stronger for shear-thinning than shear-thickening fluids.

We analyse this effect by linearising the equations of motion **(1.45-1.46)** about the origin so that $(\dot{\phi}, \dot{x})^T = \boldsymbol{M}(\phi, x)^T$ where

$$\boldsymbol{M} = \begin{pmatrix} -\frac{3\kappa}{4} & v^{\mathrm{F}} + \frac{3\sigma}{2} \\ -v_s + \frac{\sigma}{4} + \frac{3\nu}{2} & \frac{3\kappa}{2} - \psi_n \end{pmatrix}. \tag{3.4}$$

In $\boldsymbol{M}$, ψ_n and dipolar HI terms are responsible for the spiral. Away from the walls,

viscoelasticity dominates over HI effects and the eigenvalues of $\boldsymbol{M}$ without HI are found to be $\lambda_{\pm} = \frac{1}{2}(-\psi_n \pm \sqrt{\psi_n^2 - 4v_{\max}v_s})$. Hence, the origin is a stable fixed point if $\psi_n^2 > 4v_{\max}v_s$ with two real negative (attractive) eigenvalues. Otherwise, the origin is a stable spiral with complex eigenvalues and negative real parts, meaning that swimmers perform damped oscillations about the centre line as verified in **Fig. 3.4**(a,b). Because the function $f(n)$ decreases monotonically with n, ψ_n is larger for shear-thinning fluids and therefore the attraction towards the centre line is greater.

3.4 Discussion

Swimmers in flowing viscoelastic fluids tend to move upstream along the centre line after some time, regardless of initial position or upstream orientation. This effect is more pronounced in shear-thinning than shear-thickening flows. It allows for a sorting mechanism to select swimmers with a given swimming speed larger than the tunable Poiseuille flow, as demonstrated in **Fig. 3.4**(c,d), where distributions of swimmers with different self-propulsion velocities are initially introduced at random positions and orientations in the channel in Newtonian and shear-thinning viscoelastic fluids. Unlike for the Newtonian fluid, swimmers with larger motility are separated by moving upstream in the viscoelastic fluid (see Supplemental Material movies 2,3 at URL[339]). It is worth noting that we expect this sorting mechanism to be robust against translational and orientational noise since small amounts of noise will keep the oscillation size nonzero, enhancing the upstream retention ratio and hence the sorting.

To summarize, unlike the prevalent boundary accumulation in quiescent Newtonian fluids, swimmers' trajectories show oscillatory motion about the centre line. Average migration against Poiseuille flows is enhanced (reduced) in shear-thickening (-thinning) fluids compared to simple Newtonian fluids. It is not necessary that the non-Newtonian nature of these fluids be appreciable on the microscale since altered trajectories arise from differences in vorticity at macroscopic scales. This constitutes a substantial change to the effective upstream motility, that is comparable to or greater than observed changes in motility due to microscopic effects on swimming in quiescent non-Newtonian fluids[294–297,299–302]. The oscillations are damped towards the centre line in the presence of viscoelastic normal stress differences resulting in direct upstream migration. This offers a sorting mechanism to differentiate motile micro-organisms according to speed.

CHAPTER 4

Hydrodynamics of Micro-swimmers in Films

Responding to the remark: 'In science, you're never sure of anything':

> "The idea that one might be wrong, that is not a weakness, it is one of the Grandeurs of science. Albert Einstein said: 'No experiment will ever prove that I'm correct, but only one experiment at any time can prove that I am wrong'. If everybody had this feeling of the possibility that they might be wrong, it would be the end of bigotry; the end of fanaticism."
>
> Prof. Edmond H. Fischer (1920–)

4.1 Introduction

In chapter §3 we considered a micro-channel with two parallel no-slip surfaces. However, innumerable habitats of small organisms are characterised as films. Confinement between a rigid substrate and an interface is particularly fascinating with respect to microbial life, since it offers the immediate presence of two surfaces with differing properties. Intense biological activities and accumulations of swimming cells are often associated with films[187,352,353]. Indeed, countless species of bacteria secrete their own extracellular polymeric substances in order to form biofilms[354–356], within which they then move. Films on passive or living substrates allow pathogens to swim or even swarm in order to colonise a wide variety of surfaces including soil, plant leaves, animal tracts or skin[243,357,358]. Hence, many experimental setups used for studies of various aspects of swimming cell dynamics essentially confine a culture of micro-organisms between a substrate and liquid-liquid or liquid-air interface. Liquid-air

interfaces have recently attracted interest because of bioremediation of oil consuming bacteria at oil spill sites[359–361].

The majority of research has focused on the effect of solid boundaries on swimming dynamics. In particular, the accumulation of bacteria at solid walls has been well demonstrated, both theoretically and in the experiments, as discussed in §**1.3.2**. However, less intensely studied is the motion of micro-swimmers near fluid-fluid interfaces[75,284,361–364] and, to the best of our knowledge, theoretical studies of motility in liquid films in contact with solid substrates (**Fig. 4.1**) are rarely reported in the literature, despite their natural prevalence[365].

In this chapter, a detailed hydrodynamic description of swimmer dynamics within viscous films is developed by deriving the three-dimensional flows of a Stokeslet in a liquid film using a recursive series of image systems (§**4.2.1**). Moreover, in the Appendix that accompanies this chapter we also derive the exact solution using the method developed by Liron and Mochon [184] (§**4.A**). Hence, we examine the effect of film height on the multipole flows generated by a swimming micro-organism. (§**4.2.2** and §**4.B**). Comparing the recursive series and the exact solution demonstrates their respective advantages and disadvantages in various regimes of film thickness (§**4.2.3** and §**4.C**). We conclude that the series solution is more amenable to a hydrodynamic multipole expansion and for numerically computing hydrodynamic interactions with the surfaces when the micro-swimmer is small compared to the film thickness. In §**4.3** these results are used to predict the trajectories of ideal micro-swimmers. We explicitly map the dynamics and boundary accumulation of ideal cells defined by each successive hydrodynamic multipole moment (§**4.3.1**–§**4.3.3**). Employing our findings (§**4.3.4**), we propose an experimental method to determine a swimmer's rotary multipole coefficient, and its three-dimensional position under a microscope by measuring the radius of curvature of its projected trajectory.

4.2 Flow fields in a film

To derive the flow fields generated by a microbe swimming within a film constrained between a rigid wall and a free surface, we use a multipole expansion of the Stokes flow solution in a film. Performing such a multipole expansion requires a tractable analytic form of the hydrodynamic fields due to a force singularity (Stokeslet) within a viscous incompressible film of height H and dynamic viscosity μ. While the fundamental flow fields between two

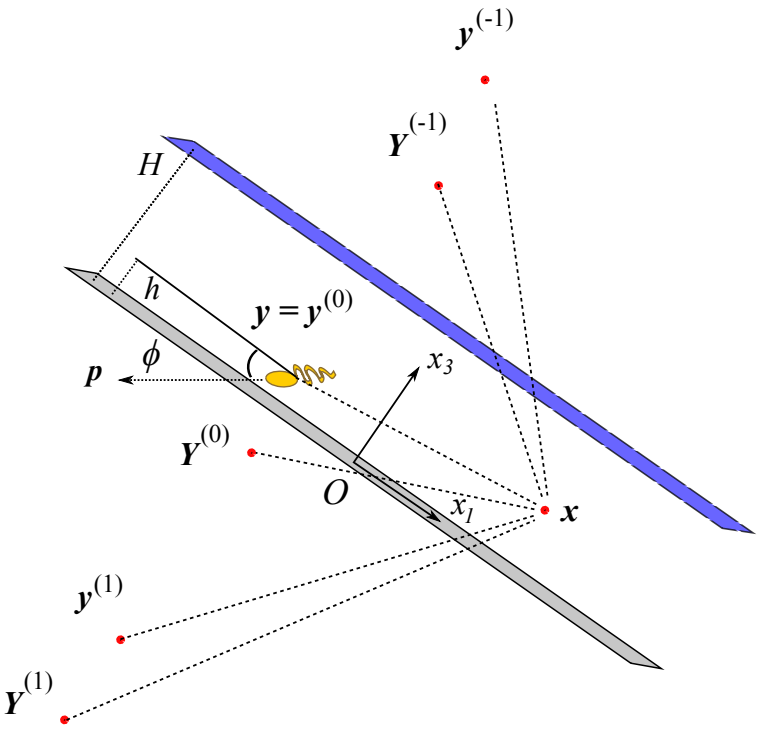

Figure 4.1: Schematic showing the geometry of a micro-swimmer in a film at $\boldsymbol{y}_{\text{s}} = \boldsymbol{y}^{(0)}$ with orientation $\boldsymbol{p}_{\text{s}}$. Within the film micro-swimmers generate Stokesian flow fields that are found using a method of successive images at positions $\boldsymbol{y}^{(m)}, \boldsymbol{Y}^{(m)}$, shown by the red points. The swimmer and each of its infinite series of images contribute to the flow at any point $\boldsymbol{x}$.

parallel boundaries have been found using a Fourier transform method[184], we will present an analytical form that is particularly amenable to including the higher multipole moments required to accurately model micro-swimmers. This method is based on successive image reflections for finding the Stokeslet flow in a film. Previous studies have used a similar framework for studying the flow produced by mobile colloids[367]. To test our recursive series solution and establish the regimes where it is applicable, we derive the exact solution of the Stokeslet flow in a liquid film in §**4.A** by extending the method by Liron and Mochon[184].

4.2.1 Liquid film Stokeslet flow

We aim to solve the Stokes equations (**1.10**–**1.11**) for the flow in a liquid film $\boldsymbol{u}^{\text{F}}$ at position $\boldsymbol{x} = (x_1, x_2, x_3)$ due to a point force $\boldsymbol{f}^{\text{S}} = \boldsymbol{f}\ \delta^3(\boldsymbol{x} - \boldsymbol{y})$ (Stokeslet) that acts at position $\boldsymbol{y} = (y_1, y_2, y_3 = h)$. The boundary conditions are the no-slip condition $\boldsymbol{u}(\boldsymbol{x}, t) = 0$ at the solid wall $x_3 = 0$ and both impermeability $u_3(\boldsymbol{x}, t) = 0$ and no-shear $\partial_3 \boldsymbol{u}(\boldsymbol{x}, t) = 0$ at the interface $x_3 = H$. In an unbounded fluid, the Green's function is the Oseen tensor $\mathcal{J}_{ij}(\boldsymbol{x}, \boldsymbol{y})$, which is derived in §**1.2.2**. If the film height is taken to infinity ($H \to \infty$), then only the

single no-slip boundary remains at $x_3 = 0$ and the Stokeslet flow field $\boldsymbol{u}^S$ is altered by the addition of an auxiliary flow field, that can be written in terms of a system of images. This image flow field is given by the Blake tensor (**Eq. 1.49** with $h = y_3$), which is centred at the position $\boldsymbol{Y}^{(0)} = (y_1, y_2, -y_3) = \mathrm{M} \cdot \boldsymbol{y}$. The tensor $\mathcal{B}_{ij}(\boldsymbol{x}, \boldsymbol{Y}^{(0)})$ is recorded in the first row of **Table 4.1**. Similarly, if only a shear-free interface is present at $x_3 = H$, the auxiliary flow field of the Stokeslet flow is a direct reflection centred at the position $\boldsymbol{Y}^{(-1)} = (y_1, y_2, 2H - y_3)$, with the corresponding free-slip boundary tensor given by **Eq. 1.47**. This result $\mathcal{T}_{ij}(\boldsymbol{x}, \boldsymbol{Y}^{(-1)})$ is recorded in row two of **Table 4.1**.

When both boundaries are present, the image system at $\boldsymbol{Y}^{(0)}$ corrects the boundary conditions at the solid no-slip wall ($x_3 = 0$) but disturbs the boundary conditions at the film interface ($x_3 = H$), and vice versa for the image at $\boldsymbol{Y}^{(-1)}$. This difficulty can be overcome by using an infinite series of images to find the flow that satisfies the film Stokes equations. That is, the image system at $\boldsymbol{Y}^{(0)}$ (or $\boldsymbol{Y}^{(-1)}$) can be reflected in the interface (or wall) to form a secondary image system at position $\boldsymbol{y}^{(-1)}$ (or $\boldsymbol{y}^{(1)}$), and so on. Hence, the positions of the image systems are

$$\boldsymbol{y}^{(m)} = (y_1, y_2, y_3 - 2mH), \tag{4.1}$$

$$\boldsymbol{Y}^{(m)} = (y_1, y_2, -y_3 - 2mH), \tag{4.2}$$

where $m = 0, \pm 1, \pm 2, \ldots$.

Fig. 4.1 schematically shows the series of images. As the number of images goes to infinity, the boundary conditions at both boundaries are satisfied. **Table 4.1** lists the procedure to find the image system tensors $\mathcal{G}_{ij}$, and hence the velocity fields, of the first few image systems of a Stokeslet in a film. **Table 4.2** gives the resulting expressions of these tensors explicitly. The tensor of a given image system can be obtained by replacing all the Oseen tensors $\mathcal{J}_{ij}$ in the tensor of the previous image system by the appropriate Blake tensor $\mathcal{B}_{ij}$ or free-slip boundary tensor $\mathcal{T}_{ij}$ given by **Eqs. 1.48-1.47**, respectively. It is key that all resulting expressions are still in terms of Oseen tensors and their derivatives, which can again be replaced at the next reflection operation. Hence, by successively repeating the reflection operations (denoted by B or T for a 'bottom' or 'top' surface, operating from right to left), the image system tensor and thus the velocity field of the image systems is found via the

recursion relations

$$\mathcal{G}_{ij}(\boldsymbol{x}, \boldsymbol{Y}^{(m)}) = \mathrm{B}\, \mathcal{G}_{ij}(\boldsymbol{x}, \boldsymbol{y}^{(-m)}), \tag{4.3}$$

$$\mathcal{G}_{ij}(\boldsymbol{x}, \boldsymbol{Y}^{(-m)}) = \mathrm{T}\, \mathcal{G}_{ij}(\boldsymbol{x}, \boldsymbol{y}^{(m-1)}), \tag{4.4}$$

$$\mathcal{G}_{ij}(\boldsymbol{x}, \boldsymbol{y}^{(m)}) = \mathrm{B}\, \mathcal{G}_{ij}(\boldsymbol{x}, \boldsymbol{Y}^{(-m)}), \tag{4.5}$$

$$\mathcal{G}_{ij}(\boldsymbol{x}, \boldsymbol{y}^{(-m)}) = \mathrm{T}\, \mathcal{G}_{ij}(\boldsymbol{x}, \boldsymbol{Y}^{(m-1)}), \tag{4.6}$$

where $m \geq 1$, and the reflection operators B and T act linearly on all the Oseen tensors $\mathcal{J}_{ij}$ present in the image system tensor $\mathcal{G}_{ij}$, as defined in **Table 4.1**. The foundations of the recursion relations are

$$\mathcal{G}_{ij}(\boldsymbol{x}, \boldsymbol{Y}^{(0)}) = \mathrm{B}\, \mathcal{J}_{ij}(\boldsymbol{x}, \boldsymbol{y}^{(0)}) = \mathcal{B}_{ij}(\boldsymbol{x}, \boldsymbol{Y}^{(0)}), \tag{4.7}$$

$$\mathcal{G}_{ij}(\boldsymbol{x}, \boldsymbol{Y}^{(-1)}) = \mathrm{T}\, \mathcal{J}_{ij}(\boldsymbol{x}, \boldsymbol{y}^{(0)}) = \mathcal{T}_{ij}(\boldsymbol{x}, \boldsymbol{Y}^{(-1)}). \tag{4.8}$$

From these rules we obtain the Green's function in a film from the infinite series

$$\mathcal{F}_{ij}(\boldsymbol{x}, \boldsymbol{y}) = \sum_{m=-\infty}^{\infty} \left[\mathcal{G}_{ij}(\boldsymbol{x}, \boldsymbol{y}^{(m)}) + \mathcal{G}_{ij}(\boldsymbol{x}, \boldsymbol{Y}^{(m)}) \right], \tag{4.9}$$

giving the film Stokeslet flow $u_i^{\mathrm{F}}(\boldsymbol{x}, \boldsymbol{y}, \boldsymbol{f}) = \mathcal{F}_{ij} f_j$.

This successive reflection method can also be used to construct the flow fields in more general confinement geometries, such as the flow bounded by two no-slip plates or the flow between a no-slip and a fluid-fluid (partial-slip) interface, by using the appropriate reflection operations, instead of those in **Eqs. 1.48-1.47**. Furthermore, Staben et al.[185] showed that the flow field generated by a Stokeslet between two no-slip plates can be written as two Blake images and a rapidly decaying integral term. We anticipate that the same could achieved for the Stokeslet flow in a liquid film.

4.2.2 Effect of film height on swimmer-generated flow fields

A micro-organism is modelled as a multipole swimmer, as is introduced in §**1.3.1**. Unless otherwise stated we use a as the characteristic swimmer size throughout the text. The organism is located at position $\boldsymbol{y}_{\mathrm{s}}$ with orientation $\boldsymbol{p}_{\mathrm{s}}$, swimming in a film of height H (**Fig. 4.1**). Without loss of generality we set $\theta = 0$ at the initial time, so that the swimmer orientation is $\boldsymbol{p}_{\mathrm{s}} = -(\cos\phi, 0, \sin\phi)$. The swimmer-generated flow field is written in terms

(n)	Position	Replace	with
(0)	$\boldsymbol{y}^{(0)}$	—	$\mathcal{J}_{ij}(\boldsymbol{x},\boldsymbol{y}^{(0)})$
(1)	$\boldsymbol{Y}^{(0)}$	$\mathrm{B}\mathcal{J}_{ij}(\boldsymbol{x},\boldsymbol{y}^{(0)})$	$\mathcal{B}_{ij}(\boldsymbol{x},\boldsymbol{Y}^{(0)}) = (-\delta_{jk} + 2y_3\delta_{k3}\tilde{\partial}_j + y_3^2\mathrm{M}_{jk}\tilde{\nabla}^2)\mathcal{J}_{ik}(\boldsymbol{x},\boldsymbol{Y}^{(0)})$
(2)	$\boldsymbol{Y}^{(-1)}$	$\mathrm{T}\mathcal{J}_{ij}(\boldsymbol{x},\boldsymbol{y}^{(0)})$	$\mathcal{T}_{ij}(\boldsymbol{x},\boldsymbol{Y}^{(-1)}) = \mathrm{M}_{jk}\mathcal{J}_{ik}(\boldsymbol{x},\boldsymbol{Y}^{(-1)})$
(3)	$\boldsymbol{y}^{(-1)}$	$\mathrm{T}\mathcal{J}_{ij}(\boldsymbol{x},\boldsymbol{Y}^{(0)})$	$\mathrm{M}_{jk}\mathcal{J}_{ik}(\boldsymbol{x},\boldsymbol{y}^{(-1)})$
(4)	$\boldsymbol{y}^{(1)}$	$\mathrm{B}\mathcal{J}_{ij}(\boldsymbol{x},\boldsymbol{Y}^{(-1)})$	$(-\delta_{jk} + 2(2H - y_3)\delta_{k3}\mathrm{M}_{jl}\tilde{\partial}_l + (2H - y_3)^2\mathrm{M}_{jk}\tilde{\nabla}^2)\mathcal{J}_{ik}(\boldsymbol{x},\boldsymbol{y}^{(1)})$
(5)	$\boldsymbol{Y}^{(1)}$	$\mathrm{B}\mathcal{J}_{ij}(\boldsymbol{x},\boldsymbol{y}^{(-1)})$	$(-\delta_{jk} + 2(2H + y_3)\delta_{k3}\tilde{\partial}_j + (2H + y_3)^2\mathrm{M}_{jk}\tilde{\nabla}^2)\mathcal{J}_{ik}(\boldsymbol{x},\boldsymbol{Y}^{(1)})$
(6)	$\boldsymbol{Y}^{(-2)}$	$\mathrm{T}\mathcal{J}_{ij}(\boldsymbol{x},\boldsymbol{y}^{(1)})$	$\mathrm{M}_{jk}\mathcal{J}_{ik}(\boldsymbol{x},\boldsymbol{Y}^{(-2)})$
(7)	$\boldsymbol{y}^{(-2)}$	$\mathrm{T}\mathcal{J}_{ij}(\boldsymbol{x},\boldsymbol{Y}^{(1)})$	$\mathrm{M}_{jk}\mathcal{J}_{ik}(\boldsymbol{x},\boldsymbol{y}^{(-2)})$
(8)	$\boldsymbol{y}^{(2)}$	$\mathrm{B}\mathcal{J}_{ij}(\boldsymbol{x},\boldsymbol{Y}^{(-2)})$	$(-\delta_{jk} + 2(4H - y_3)\delta_{k3}\mathrm{M}_{jl}\tilde{\partial}_l + (4H - y_3)^2\mathrm{M}_{jk}\tilde{\nabla}^2)\mathcal{J}_{ik}(\boldsymbol{x},\boldsymbol{y}^{(2)})$
(9)	$\boldsymbol{Y}^{(2)}$	$\mathrm{B}\mathcal{J}_{ij}(\boldsymbol{x},\boldsymbol{y}^{(-2)})$	$(-\delta_{jk} + 2(4H + y_3)\delta_{k3}\tilde{\partial}_j + (4H + y_3)^2\mathrm{M}_{jk}\tilde{\nabla}^2)\mathcal{J}_{ik}(\boldsymbol{x},\boldsymbol{Y}^{(2)})$
(10)	$\boldsymbol{Y}^{(-3)}$	$\mathrm{T}\mathcal{J}_{ij}(\boldsymbol{x},\boldsymbol{y}^{(2)})$	$\mathrm{M}_{jk}\mathcal{J}_{ik}(\boldsymbol{x},\boldsymbol{Y}^{(-3)})$
(11)	$\boldsymbol{y}^{(-3)}$	$\mathrm{T}\mathcal{J}_{ij}(\boldsymbol{x},\boldsymbol{Y}^{(2)})$	$\mathrm{M}_{jk}\mathcal{J}_{ik}(\boldsymbol{x},\boldsymbol{y}^{(-3)})$
(12)	$\boldsymbol{y}^{(3)}$	$\mathrm{B}\mathcal{J}_{ij}(\boldsymbol{x},\boldsymbol{Y}^{(-3)})$	$(-\delta_{jk} + 2(6H - y_3)\delta_{k3}\mathrm{M}_{jl}\tilde{\partial}_l + (6H - y_3)^2\mathrm{M}_{jk}\tilde{\nabla}^2)\mathcal{J}_{ik}(\boldsymbol{x},\boldsymbol{y}^{(3)})$
(13)	$\boldsymbol{Y}^{(3)}$	$\mathrm{B}\mathcal{J}_{ij}(\boldsymbol{x},\boldsymbol{y}^{(-3)})$	$(-\delta_{jk} + 2(6H + y_3)\delta_{k3}\tilde{\partial}_j + (6H + y_3)^2\mathrm{M}_{jk}\tilde{\nabla}^2)\mathcal{J}_{ik}(\boldsymbol{x},\boldsymbol{Y}^{(3)})$
⋮	⋮	⋮	⋮

Table 4.1: Recursion relations for the successive image systems of a Stokeslet in a liquid film. The first image system of the Oseen tensor (**Eq. 1.22**) from reflection in the bottom wall is the Blake tensor (**Eq. 1.48**), and the second image from reflection in the top interface is the mirrored Oseen tensor (**Eq. 1.47**). Subsequent image systems are obtained from further reflection operations with B denoting the "bottom" (no-slip wall) and T the "top" (no-shear interface), that operate linearly on all the Oseen tensor terms $\mathcal{J}_{ij}$ of the image system tensor $\mathcal{G}_{ij}$.

(n)	Image system tensor $\mathcal{G}_{ij}(\boldsymbol{x},\boldsymbol{y}^{(m)}$ or $\boldsymbol{Y}^{(m)}) =$
(0)	$\mathcal{J}_{ij}(\boldsymbol{x},\boldsymbol{y}^{(0)})$
(1)	$(-\delta_{jk} + 2y_3\delta_{k3}\tilde{\partial}_j + y_3^2\mathrm{M}_{jk}\tilde{\nabla}^2)\mathcal{J}_{ik}(\boldsymbol{x},\boldsymbol{Y}^{(0)})$
(2)	$\mathrm{M}_{jk}\mathcal{J}_{ik}(\boldsymbol{x},\boldsymbol{Y}^{(-1)})$
(3)	$(-\delta_{jk} + 2y_3\delta_{k3}\tilde{\partial}_j + y_3^2\mathrm{M}_{jk}\tilde{\nabla}^2)\mathrm{M}_{kl}\mathcal{J}_{il}(\boldsymbol{x},\boldsymbol{y}^{(-1)})$
(4)	$\mathrm{M}_{jk}(-\delta_{kl} + 2(2H - y_3)\delta_{l3}\mathrm{M}_{ko}\tilde{\partial}_o + (2H - y_3)^2\mathrm{M}_{kl}\tilde{\nabla}^2)\mathcal{J}_{il}(\boldsymbol{x},\boldsymbol{y}^{(1)})$
(5)	$(-\delta_{jk} + 2y_3\delta_{k3}\tilde{\partial}_j + y_3^2\mathrm{M}_{jk}\tilde{\nabla}^2)\mathrm{M}_{kl}(-\delta_{lo} + 2(2H + y_3)\delta_{o3}\tilde{\partial}_l + (2H + y_3)^2\mathrm{M}_{lo}\tilde{\nabla}^2)\mathcal{J}_{io}(\boldsymbol{x},\boldsymbol{Y}^{(1)})$
(6)	$\mathrm{M}_{jk}(-\delta_{kl} + 2(2H - y_3)\delta_{l3}\mathrm{M}_{kp}\tilde{\partial}_p + (2H - y_3)^2\mathrm{M}_{kl}\tilde{\nabla}^2)\mathrm{M}_{lo}\mathcal{J}_{io}(\boldsymbol{x},\boldsymbol{Y}^{(-2)})$
(7)	$(-\delta_{jk} + 2y_3\delta_{k3}\tilde{\partial}_j + y_3^2\mathrm{M}_{jk}\tilde{\nabla}^2)\mathrm{M}_{kl}(-\delta_{lo} + 2(2H + y_3)\delta_{o3}\tilde{\partial}_l + (2H + y_3)^2\mathrm{M}_{lo}\tilde{\nabla}^2)\mathrm{M}_{op}\mathcal{J}_{ip}(\boldsymbol{x},\boldsymbol{y}^{(-2)})$
⋮	⋮

Table 4.2: Explicit expressions of the image system tensors $\mathcal{G}_{ij}$ of the first few image systems of a Stokeslet in a liquid film. The indices $i,j,k,l,o,p \in \{1,2,3\}$ and repeated indices are summed over. Added together, these tensors yield the Green's function in a film (**Eq. 4.9**).

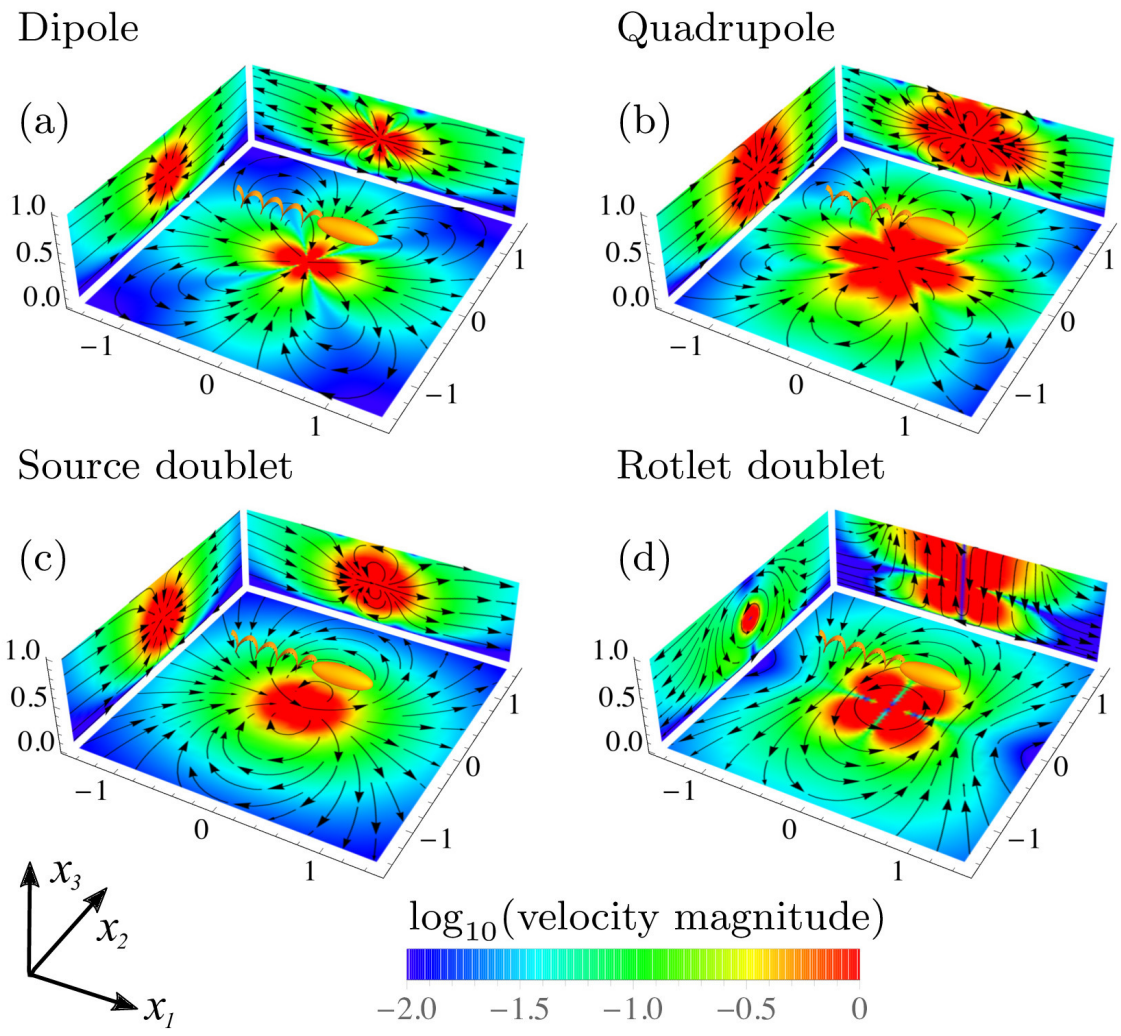

Figure 4.2: Flow fields produced by a micro-swimmer at the centre of a film of height H, obtained using the recursive series method with $n = 9$ images. Shown are (a) Dipolar $\boldsymbol{u}^{\mathrm{D}}$, **Eq. 1.33**, (b) Quadrupolar $\boldsymbol{u}^{\mathrm{Q}}$, **Eq. 1.36**, (c) Source doublet $\boldsymbol{u}^{\mathrm{SD}}$, **Eq. 1.37**, and (d) Rotlet doublet $\boldsymbol{u}^{\mathrm{RD}}$, **Eq. 1.38**. The flow fields shown correspond to planar cuts close to the swimmer, $x_1 = -a$, $x_2 = a$ and $x_3 = h - a$, where $h = H/2$, $a = H/100$ and all lengths in the figure are scaled with respect to H. The schematic swimmer points in the swimming direction $\boldsymbol{p}_{\mathrm{s}} = \hat{\boldsymbol{e}}_1$. Colormaps show the velocity magnitude normalised by its maximum on a logarithmic scale, ranging from 10^{-2} (blue) to 1 (red), and are superimposed by streamlines (black lines).

of a multipole expansion (**Eq. 1.32**) of the Stokes flow solution in the film (**Eq. 4.9**). For example, the dipolar flow is given by replacing $\boldsymbol{u}^{\mathrm{S}}$ with $\boldsymbol{u}^{\mathrm{F}}(\boldsymbol{x}, \boldsymbol{y}, 8\pi\mu\, \boldsymbol{p}_{\mathrm{s}})$ in **Eq. 1.33**. These multipole flow fields are shown in **Fig. 4.2** for a swimmer oriented parallel to the film surfaces.

In a film of sufficiently large thickness the flow field is relatively unaffected by the boundaries (**Fig. 4.3**a). Upon decreasing the height of the film, the flow profiles in the $x_1 - x_3$ and $x_2 - x_3$ planes remain unaffected, except near the surfaces where the boundary conditions must be satisfied. However, as the thickness of the film is reduced the flow field in

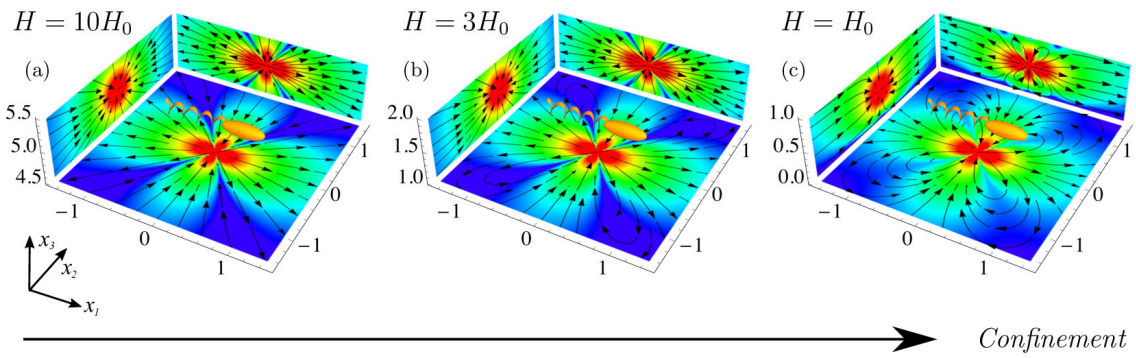

Figure 4.3: The flow field generated by a micro-swimmer is modified in thin films. Panels (a,b,c) show flow fields for decreasing values of the film height, $H = 10H_0$, $H = 3H_0$, and $H = H_0$, respectively. The micro-swimmer is located at the middle of the film, at $h = H/2$, and oriented in the direction $\boldsymbol{p}_s = \hat{\boldsymbol{e}}_1$. Although the flow is purely dipolar far away from the boundaries (a), this lower-order multipole is screened with increasing confinement and a recirculating flow pattern appears (b,c). The number of images, planar cuts and colour legends are defined as in **Fig. 4.2**.

the $x_1 - x_2$ plane is modified and recirculating flow patterns appear close to the swimming cell (**Fig. 4.3**b). Such patterns are reminiscent of those seen for a Stokeslet between two parallel plates[184]. The recirculating regions are enhanced in size as the film thickness is further reduced (**Fig. 4.3**c) compared to the size of the swimmer.

The effect of reducing the film thickness on altering the flow structure is understood by considering the minimisation of the energy dissipation by a self-propelled organism in Stokes flow. As the thickness of the film is reduced, the propulsion energy is more effectively dissipated by the boundaries. This introduces a length scale of order $\sim H$ beyond which the primary contributions to the flow field are screened. As a result of the emergence of this screening length, the flow field is suppressed in the plane normal to the film height and recirculating flow patterns are formed.

To understand the case of strong confinement, we derive the Stokeslet and swimmer-generated flow fields in the thin-film limit (§**4.B**). In this limit, the flows in the i direction due to a swimmer pointing in the j direction decay exponentially with the lateral distance if either i or j or both are equal to three (*i.e.* directed perpendicular to the film). Only the parallel components of the flow do not decay exponentially, and those have a half-parabolic profile along x_3. The Stokeslet has a recirculating pattern of two loops in the $x_1 - x_2$ plane, the dipole has four loops, the quadrupole has six loops, and the source doublet maintains its bulk-flow structure with two loops (**Fig. 4.10**). The solution for higher order multipoles

between two no-slip surfaces, which we have not found elsewhere in the literature, are the same, but with a parabolic profile along x_3. These thin-film limit expressions could be used, for example, to model swimmer-swimmer interactions in films of thickness comparable to the swimmer size.

4.2.3 Comparison to the exact solution

To establish the length scales for which the recursive series solution (§4.2.1) is applicable, we compare it to the exact solution (§4.A). There are four important length scales in the system of a micro-swimmer in a liquid film: the organism size a, the film height H, the distance to the nearest surface $\hat{h} = \min(h, H - h)$, and the size of the flow region of interest, measured by the distance from the swimmer to where the flow is evaluated $r = |\boldsymbol{x} - \boldsymbol{y}_s|$.

Fig. 4.4 shows the flow fields generated by a Stokeslet in a liquid film, using the recursive image series (left panels) and the exact solution (right panels). The Stokeslet is located at a distance $h = 0.45H$ from the bottom wall and is oriented in the direction parallel (top panels) and perpendicular (bottom panels) to the film surfaces. Close to the point force, where $a \sim r \ll \hat{h} < H$, the flow in a bulk fluid given by the Oseen result (**Eq. 1.22**) is recovered. If the film height is increased, with h kept constant so that $a \sim r \sim h \ll H$, then the Blake result (**Eq. 1.48**) is recovered (see details in §4.C, **Fig. 4.11**). Similarly, if the Stokeslet is located close to the top interface, the local flows can also be described with a single image system (**Eq. 1.47**). However, for a Stokeslet in the middle of the film ($\hat{h} \sim H$), the image systems above and below the film contribute with equal significance.

If one is interested in distant flows, ($a < \hat{h} \sim H \ll r$; **Fig. 4.4**, outside the white dashed lines), the regime equivalent to the thin-film limit (§4.B), then all images are approximately equidistant from the point $\boldsymbol{x}$ so that many terms are required in the series to eliminate differences between the two methods. If one is interested in local flows ($a < r < \hat{h} \sim H$; **Fig. 4.4**, inside the white dashed lines), then there is good agreement between the recursive image series (left panels) and the exact solution (right panels), even with a limited number of images ($n = 9$). This can be understood because in this domain the series converges and can be truncated, as discussed quantitatively in §4.C and below. Since this work is concerned with the effect of hydrodynamic interactions with film surfaces on the dynamics of micro-swimmers, the recursive image series method is seen to be accurate.

Convergence of the swimmer-generated flow fields at the surfaces is shown in **Fig. 4.5**

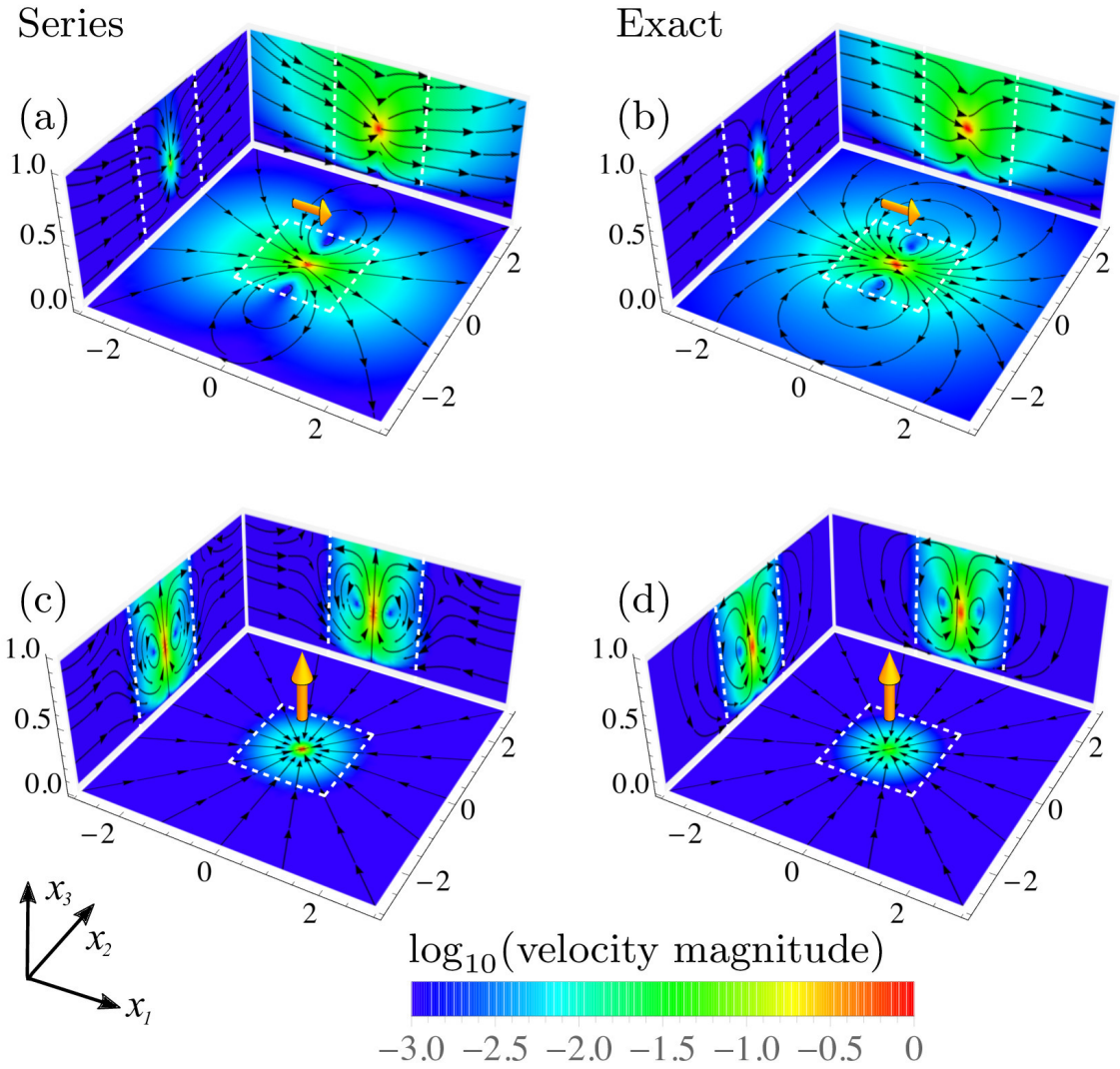

Figure 4.4: Comparison of flow fields produced by a Stokeslet in a liquid film using the solution obtained with the recursive series method (left panels; §**4.2.1**), where $n = 9$ images have been used; and the exact solution (right panels; §**4.A**). The film has height H, the Stokeslet is located at $h = 0.45H$ just beneath the centre, an arbitrary non-trivial point, and it is oriented in the x_1 direction (a,b) or in the x_3 direction (c,d). The planar cuts and colour legends are defined as in **Fig. 4.2**. The white dashed lines mark the region $\frac{r_1}{H}, \frac{r_2}{H} < 1$, inside which the series solution is accurate.

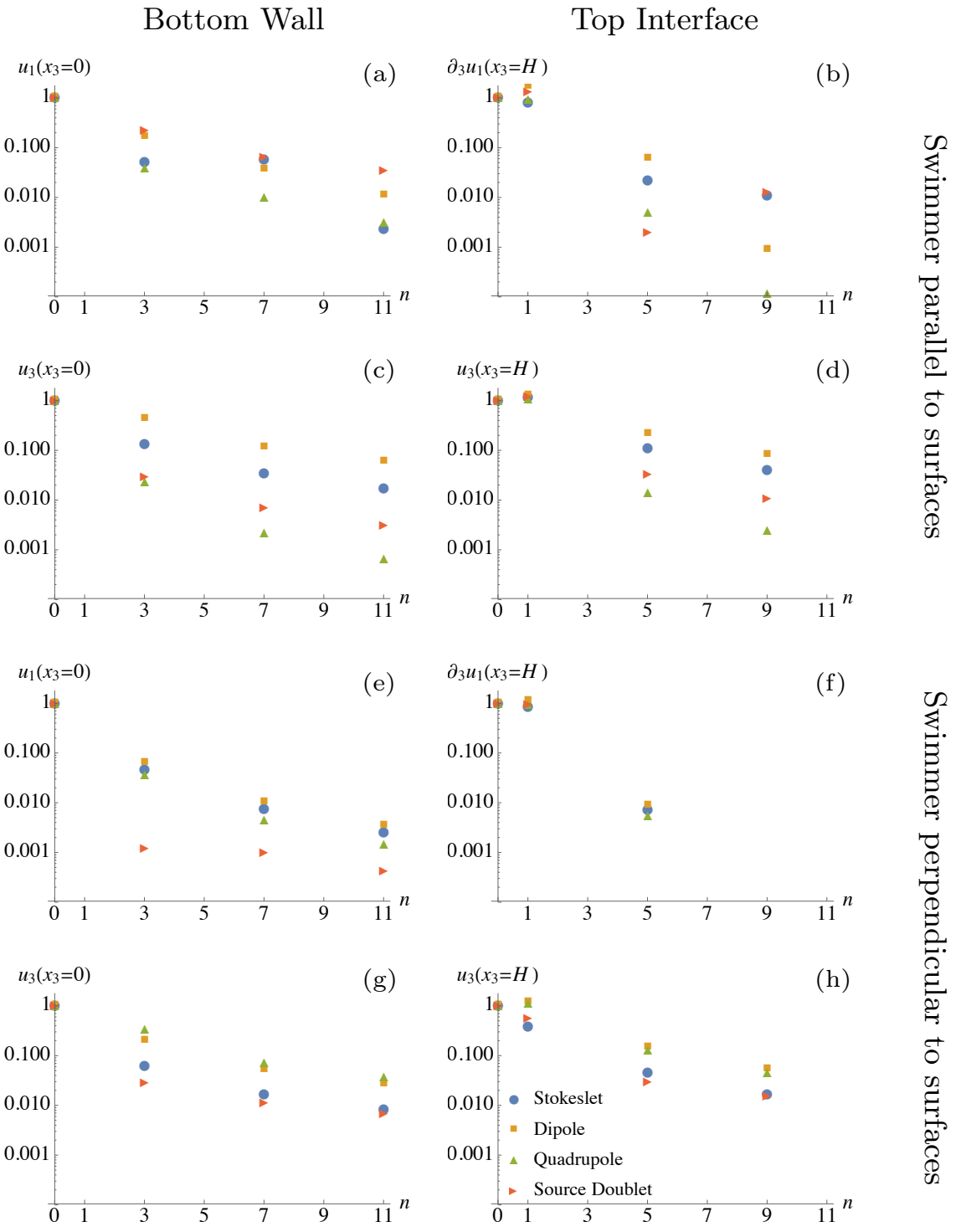

Figure 4.5: Convergence of the flow fields generated by a micro-swimmer in a film as a function of the number of images n, normalised with respect to the value if only the swimmer itself is present ($n = 0$), on a logarithmic scale. Only odd values of n are shown, which corresponds to pairs of image systems being added on both sides of the film. The swimmer is located just underneath the middle of the film $\boldsymbol{y} = (0, 0, 0.45H)$, and the flow is sampled at arbitrary points on the two surfaces $\boldsymbol{x} = (0, H/4, 0)$ and $\boldsymbol{x} = (0, H/4, H)$. In panels (a-d) the swimmer is oriented in the $\hat{\boldsymbol{e}}_1$ direction, and in panels (e-h) the swimmer is oriented in the $\hat{\boldsymbol{e}}_3$ direction. The convergence of the boundary conditions is shown at the bottom wall (a,c,e,g), and top interface (b,d,f,h) for the normal and parallel flow components. Note that if no marker is shown, the value is exactly zero.

as a function of the number of images used in the recursive series. The values of the flow (or shear rate) at the boundaries are shown, and these must approach zero to accurately calculate the flows. Here $n = 0$ means no images are present, and only the flow generated by the Stokeslet in bulk is considered. As n increases more image reflections are included, where the image numberings are defined in **Table 4.1**. The swimmer location is chosen near the centre of the film, as a worst-case scenario, and we show the flows at the surfaces where the boundary effects are strongest and the convergence is the slowest, with $\hat{h} \sim H \sim r$. Both at the bottom wall (**Fig. 4.5**; left panels) and the top interface (**Fig. 4.5**; right panels), however, the correction to the flow field is small after only a few images. Furthermore, with $n = 1, 5, 9, \ldots$ image systems included the boundary conditions at the bottom wall are satisfied exactly, and similarly with $n = 3, 7, 11, \ldots$ the top interface boundary conditions are fully satisfied. This feature of the recursive series method can be leveraged if an exact boundary condition is required at one of the two surfaces. For thin films compared to the swimmer size, or distances much greater than the film height, more images will be required for a given accuracy. The convergence can be justified by noting that each term of each image decays as $\sim (-1)^m |2mH|^{-1}$. Since at every image reflection point $(\boldsymbol{y}(m), \boldsymbol{Y}^{(m)})$ the leading term is a Stokeslet pointing in the direction opposite to the one at the previous reflection point, this infinite series of alternatingly opposing Stokeslets converges and can be expressed as converging integral expressions (§**4.A.2**). For a dipole swimmer the leading terms decay as $\sim (-1)^m |2mH|^{-2}$, so the infinite series of alternatingly opposing dipoles converges more rapidly.

In short, the recursive series can compute flows accurately in the region $r < H$ for any h, x_3 (**Fig. 4.4**, inside the white dashed lines). This is a region of particular interest since it is, by construction, where the swimmer resides and where perturbations to the flow fields are most significant. Secondly, one requires $a \ll \hat{h}$ to evaluate hydrodynamic interactions with surfaces using the multipole expansion, but it is noteworthy that Spagnolie and Lauga [238] argue that far-field hydrodynamic interactions give surprisingly accurate results even for small swimmer-wall separations $a \sim \hat{h}$. When these two conditions are satisfied, we find that $n = 9$ images are sufficient to describe micro-swimmer flows with an error less than $\sim 1\%$. Therefore in this work, we utilise $n = 9$ images in all presented figures.

The advantage of the traditional Fourier transform solution is that it is exact and provides access to all regions of the film. In particular, it converges rapidly in regions far from the

swimmer, $r \gg H$, and therefore a tractable expression for the flows in the far-field limit can be extracted (§4.B). On the other hand, this exact solution can be more tedious to handle, especially when taking derivatives, as is necessary for a multipole expansion of a swimming microbe. In comparison, the image series in **Eq. 4.9** is constructed purely from the Oseen tensor and its derivatives, and can be manipulated with ease, both analytically and computationally. The best choice of method therefore depends on the purpose in mind. In the far field the Fourier transform method excels, and in the near field the recursive series method is more convenient. Since we are interested in local hydrodynamics, we work with the latter in the remainder of this chapter.

4.3 Swimmer dynamics in a liquid film

Knowing the flow fields that a motile microbe produces within a film allows us to model the hydrodynamic interactions with the bounding surfaces. In this section we will describe the effects of these hydrodynamic interactions on the swimmer dynamics. Because we focus on the effect of surface accumulation at the bottom wall and the liquid air interface, we consider swimmers much smaller than the film height, $a \ll H$. Furthermore, for simplicity we do not include swimmer-swimmer interactions. In this regime, all flows of interest are in the region $r < H$ where the use of the recursive series solution is appropriate (see §4.2.3).

We consider the equations of motion **(1.45–1.46)**, where in addition to the swimmer's activity ($\boldsymbol{v}^{\mathrm{A}}$) the motion of a swimming cell is affected by steric and hydrodynamic interactions with the bounding planes ($\boldsymbol{v}^{\mathrm{ST}}$ and $\boldsymbol{v}^{\mathrm{HI}}$). For simplicity, steric interactions are assumed to be adequately represented by hard-sphere interactions[214]. The hydrodynamic interactions with the surfaces are given by the equations discussed in §1.3.2.3. Hence, in the following sections we describe the effects of individual multipole contributions of the swimmer-generated flow field (**Eq. 1.32**) on the swimmer dynamics within a film.

4.3.1 Dipolar term hydrodynamic interactions

To determine the dipolar hydrodynamic interactions with the film surfaces, we insert the auxiliary dipolar flow field (**Eq. 1.33**; $\boldsymbol{u}^{\mathrm{D}^*} = \boldsymbol{u}^{\mathrm{D}} - \boldsymbol{u}^{\mathrm{D}\infty}$) into **Eqs. (1.54-1.55)**. The first

(n)	Pos.	v_1^{D}, v_2^{D}	v_3^{D}	Ω_1^{D}, Ω_2^{D}	Ω_3^{D}
(1)	$\boldsymbol{Y}^{(0)}$	$\frac{1}{\zeta^2}$	$-\frac{1}{\zeta^2}$	$\frac{1}{\zeta^3}$	0
(2)	$\boldsymbol{Y}^{(-1)}$	0	$\frac{2}{3(\zeta-1)^2}$	$-\frac{1}{(\zeta-1)^3}$	0
(3)	$\boldsymbol{y}^{(-1)}$	$-(\zeta-2)\,\zeta$	$\frac{1}{3}\left(-3\zeta^2+8\zeta-2\right)$	$1-2\zeta$	0
(4)	$\boldsymbol{y}^{(1)}$	$(\zeta-2)\,\zeta$	$\zeta^2-\frac{4\zeta}{3}-\frac{2}{3}$	$2\zeta-3$	0
(5)	$\boldsymbol{Y}^{(1)}$	$\frac{4(\zeta-1)\zeta}{(\zeta+1)^5}$	$-\frac{2\left(\zeta^3+13\zeta^2-\zeta-1\right)}{3(\zeta+1)^5}$	$\frac{\zeta(\zeta+14)-3}{(\zeta+1)^5}$	0
(6)	$\boldsymbol{Y}^{(-2)}$	$-\frac{1}{(\zeta-2)^2}$	$\frac{1}{(\zeta-2)^2}$	$-\frac{1}{(\zeta-2)^3}$	0
(7)	$\boldsymbol{y}^{(-2)}$	$-\frac{1}{4}\,(\zeta-1)^{\,2}$	$\frac{1}{4}\left(-\zeta^2+3\zeta-1\right)$	$\frac{1}{8}\,(1-4\zeta)$	0
(8)	$\boldsymbol{y}^{(2)}$	$\frac{1}{4}\,(\zeta-1)^{\,2}$	$\frac{1}{4}\left(\zeta^2-\zeta-1\right)$	$\frac{1}{8}\,(4\zeta-7)$	0
(9)	$\boldsymbol{Y}^{(2)}$	$\frac{\zeta^4+8\zeta^3+72\zeta^2-32\zeta+16}{(\zeta+2)^6}$	$-\frac{\zeta^4+8\zeta^3+96\zeta^2-16}{(\zeta+2)^6}$	$\frac{\zeta(\zeta(\zeta+6)+140)-56}{(\zeta+2)^6}$	0
(10)	$\boldsymbol{Y}^{(-3)}$	$\frac{4(\zeta-2)(\zeta-1)}{(\zeta-3)^5}$	$\frac{2\left(\zeta^3-19\zeta^2+63\zeta-57\right)}{3(\zeta-3)^5}$	$-\frac{(\zeta-18)\zeta+29}{(\zeta-3)^5}$	0
⋮	⋮	⋮	⋮	⋮	⋮
prefactor		$\frac{3\kappa}{4H^2}p_1p_3$, $\frac{3\kappa}{4H^2}p_2p_3$	$\frac{3\kappa}{8H^2}(p_1^2+p_2^2-2p_3^2)$	$\frac{3\kappa}{8H^3}p_2p_3$, $-\frac{3\kappa}{8H^3}p_1p_3$	

Table 4.3: Dipolar hydrodynamic interactions of a micro-swimmer with the surfaces of a film. Given are the boundary-induced translational and rotational velocities due to the first image systems (**Table 4.1** and **Table 4.2**) as a function of non-dimensionalised swimmer position $\zeta = y_3/H$ and orientation $\boldsymbol{p} = (p_1, p_2, p_3)$ with respect to the no-slip wall at $\zeta = 0$ and free-slip interface at $\zeta = 1$. In each case, the functional term listed is to be multiplied by the stated prefactor. For simplicitly, we consider small swimmers with respect to the film height, so the higher-order Faxén term proportional to a^2 in **Eq. 1.54** is omitted here.

(n)	Pos.	v_1^{SD}, v_2^{SD}	v_3^{SD}	Ω_1^{SD},Ω_2^{SD}	Ω_3^{SD}
(1)	$\boldsymbol{Y}^{(0)}$	$\frac{1}{\zeta^3}$	$\frac{1}{\zeta^3}$	$\frac{1}{\zeta^4}$	0
(2)	$\boldsymbol{Y}^{(-1)}$	$-\frac{1}{2(\zeta-1)^3}$	$-\frac{1}{4(\zeta-1)^3}$	0	0
(3)	$\boldsymbol{y}^{(-1)}$	$\frac{1}{2}\,(5-3\zeta)$	$\frac{1}{4}\,(3\zeta-7)$	-1	0
(4)	$\boldsymbol{y}^{(1)}$	$\frac{1}{2}\,(3\zeta-1)$	$\frac{1}{4}\,(-3\zeta-1)$	1	0
(5)	$\boldsymbol{Y}^{(1)}$	$\frac{\zeta(\zeta+20)-5}{2(\zeta+1)^5}$	$\frac{\zeta(\zeta+32)+7}{4(\zeta+1)^5}$	$\frac{8}{(\zeta+1)^5}$	0
(6)	$\boldsymbol{Y}^{(-2)}$	$-\frac{1}{(\zeta-2)^3}$	$-\frac{1}{(\zeta-2)^3}$	$-\frac{1}{(\zeta-2)^4}$	0
(7)	$\boldsymbol{y}^{(-2)}$	$\frac{1}{8}\,(5-3\zeta)$	$\frac{1}{16}\,(3\zeta-8)$	$-\frac{1}{4}$	0
(8)	$\boldsymbol{y}^{(2)}$	$\frac{1}{8}\,(3\zeta-1)$	$\frac{1}{16}\,(-3\zeta-2)$	$\frac{1}{4}$	0
(9)	$\boldsymbol{Y}^{(2)}$	$\frac{\zeta(\zeta(\zeta+6)+108)-40}{(\zeta+2)^6}$	$\frac{\zeta(\zeta(\zeta+6)+84)+32}{(\zeta+2)^6}$	$\frac{(\zeta+2)^2+80}{(\zeta+2)^6}$	0
(10)	$\boldsymbol{Y}^{(-3)}$	$-\frac{(\zeta-24)\zeta+39}{2(\zeta-3)^5}$	$-\frac{(\zeta-36)\zeta+75}{4(\zeta-3)^5}$	$\frac{8}{(\zeta-3)^5}$	0
⋮	⋮	⋮	⋮	⋮	⋮
prefactor		$-\frac{\sigma}{4H^3}p_1$, $-\frac{\sigma}{4H^3}p_2$	$-\frac{\sigma}{H^3}p_3$	$\frac{3\sigma}{8H^4}p_2$, $-\frac{3\sigma}{8H^4}p_1$	

Table 4.4: Same as **Table 4.3**, but for source doublet hydrodynamic interactions.

(n)	Pos.	v_1^{RD}, v_2^{RD}	v_3^{RD}	Ω_1^{RD}, Ω_2^{RD}	Ω_3^{RD}
(1)	$\boldsymbol{Y}^{(0)}$	0	0	$-\frac{3}{\zeta^4}$	$\frac{1}{\zeta^4}$
(2)	$\boldsymbol{Y}^{(-1)}$	$-\frac{1}{(\zeta-1)^3}$	0	$-\frac{1}{(\zeta-1)^4}$	$\frac{1}{(\zeta-1)^4}$
(3)	$\boldsymbol{y}^{(-1)}$	$1-\zeta$	0	3	1
(4)	$\boldsymbol{y}^{(1)}$	$\zeta-1$	0	-3	-1
(5)	$\boldsymbol{Y}^{(1)}$	$\frac{\zeta(\zeta+8)-1}{(\zeta+1)^5}$	0	$\frac{\zeta-15}{(\zeta+1)^5}$	$-\frac{1}{(\zeta+1)^4}$
(6)	$\boldsymbol{Y}^{(-2)}$	0	0	$\frac{3}{(\zeta-2)^4}$	$-\frac{1}{(\zeta-2)^4}$
(7)	$\boldsymbol{y}^{(-2)}$	$\frac{1}{4}(2-\zeta)$	0	$\frac{7}{16}$	$-\frac{1}{16}$
(8)	$\boldsymbol{y}^{(2)}$	$\frac{\zeta}{4}$	0	$-\frac{7}{16}$	$\frac{1}{16}$
(9)	$\boldsymbol{Y}^{(2)}$	$\frac{32(2\zeta-1)}{(\zeta+2)^6}$	0	$\frac{-3\zeta(\zeta+4)-172}{(\zeta+2)^6}$	$\frac{1}{(\zeta+2)^4}$
(10)	$\boldsymbol{Y}^{(-3)}$	$-\frac{(\zeta-12)\zeta+19}{(\zeta-3)^5}$	0	$-\frac{\zeta+13}{(\zeta-3)^5}$	$\frac{1}{(\zeta-3)^4}$
$\vdots$	$\vdots$	$\vdots$	$\vdots$	$\vdots$	$\vdots$
prefactor		$-\frac{3\tau}{4H^3}p_2p_3$, $\frac{3\tau}{4H^3}p_1p_3$		$\frac{3\tau}{8H^4}p_1p_3$, $\frac{3\tau}{8H^4}p_2p_3$	$\frac{3\tau}{16H^4}(p_1^2+p_2^2-2p_3^2)$

Table 4.5: Same as **Table 4.3**, but for rotlet doublet hydrodynamic interactions.

two image systems give

$$v_1^{\mathrm{D}} = \kappa\frac{\sin(2\phi)}{16}\left(\frac{a^2\gamma^{-2}}{(H-h)^4}-\frac{3a^2\gamma^{-2}}{h^4}+\frac{6}{h^2}\right), \tag{4.10}$$

$$v_3^{\mathrm{D}} = \kappa\frac{3\cos(2\phi)-1}{32}\left(\frac{-a^2\gamma^{-2}}{(H-h)^4}+\frac{3a^2\gamma^{-2}}{h^4}+\frac{4}{(H-h)^2}-\frac{6}{h^2}\right), \tag{4.11}$$

$$\Omega_2^{\mathrm{D}} = \kappa\frac{3\sin(2\phi)}{64}\left(\frac{4+2G-2G\cos(2\phi)}{(H-h)^3}+\frac{4+3G-G\cos(2\phi)}{h^3}\right). \tag{4.12}$$

The complete list of dipolar hydrodynamic interactions due to the first 10 image systems is given in **Table 4.3** for a small swimmer, with $a \ll H$ in **Eq. 1.54**, in terms of the dimensionless position $\zeta = h/H$.

A pusher-type swimmer is attracted towards both surfaces and tends to align parallel to them (**Fig. 4.6**a)[238,246]. The $h-\phi$ phase space in **Fig. 4.6**a shows stable fixed points at $h = b, H-b; \phi = 0, \pi, 2\pi$ demonstrating that the specific trajectories shown (red, blue and green trajectories) are representative of the general behaviour of pusher swimmers in films.

A puller, on the other hand, tends to orient perpendicular to the planar boundaries (**Fig. 4.6**b). A puller's stable fixed points are found at $h = a, H-a; \phi = \pm\pi/2$. For both pusher and puller types, the hydrodynamic interactions are a factor of $3/2$ stronger at the solid, no-slip bottom wall than the no-shear free interface. All dipolar swimmers initially oriented parallel to the surfaces and located below a critical height h^* will accumulate at the bottom wall. E.g. the blue trajectories in **Fig. 4.6**a and **Fig. 4.6**b correspond to $h = H/2 < h^*$

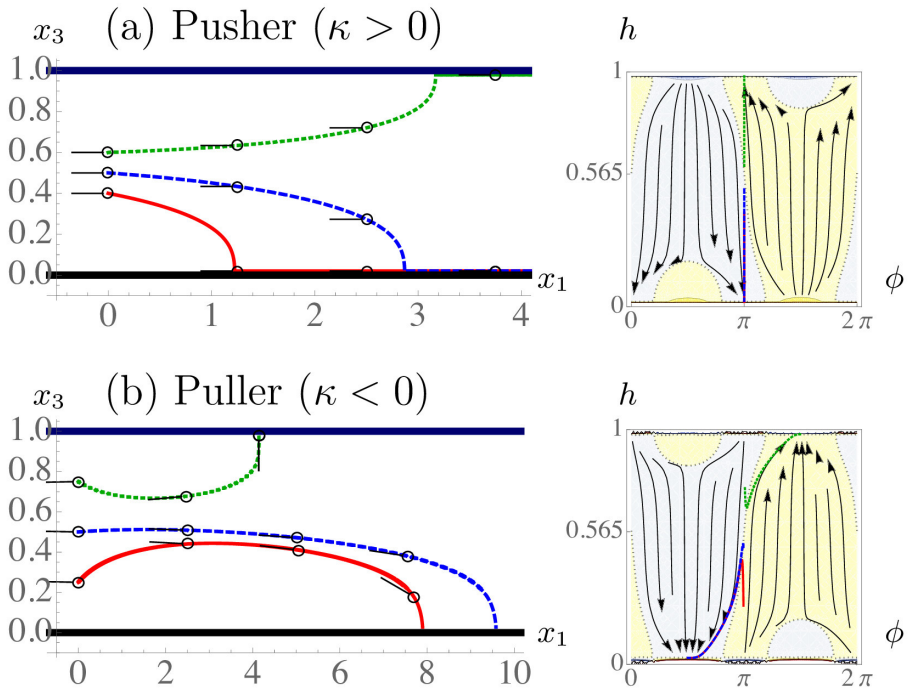

Figure 4.6: The effect of dipolar hydrodynamic interactions on the dynamics of a micro-swimmer in a film. Swimmer trajectories in real $x_1 - x_3$ space are shown in the left hand panels, and the right hand panels show the same dynamics in $h - \phi$ phase space. For simplicity we consider spherical swimmer bodies. The swimmer size is small compared to the film height, $a = b = H/100$. The background colours in the phase space plots indicate the sign of the velocity in the x_3 direction, where yellow is upward swimming and light blue is downward swimming. a) A pusher swimmer with $\kappa = 1/20\,[H^2 v_s]$. b) The equivalent puller with $\kappa = -1/20\,[H^2 v_s]$. All other multipole moments are set to zero. The schematic black micro-organisms indicate the swimming direction.

and demonstrate that cells which began swimming parallel to the surfaces along the centre line accumulate at the bottom wall. An analytic estimate for this critical height can be obtained using the first two image systems (**Eq. 4.10-4.12**). This gives $h^* \approx \left(3 - \sqrt{6}\right) H$ compared to the numerically determined value $h^* = 0.565H$, which is different by 2.6%. In brief, hydrodynamic interactions attract both pushers and pullers more toward the no-slip wall than toward the film interface, when averaged over all initial swimmer positions and orientations.

4.3.2 Source doublet term hydrodynamic interactions

For ciliated micro-organisms, such as *Paramecium* and *Volvox*, the source doublet coefficient $\sigma > 0$. For non-ciliated but flagellated organisms, one expects the coefficient $\sigma < 0$. **Table 4.4** lists the hydrodynamic interactions of a small swimmer with the surfaces due to its source

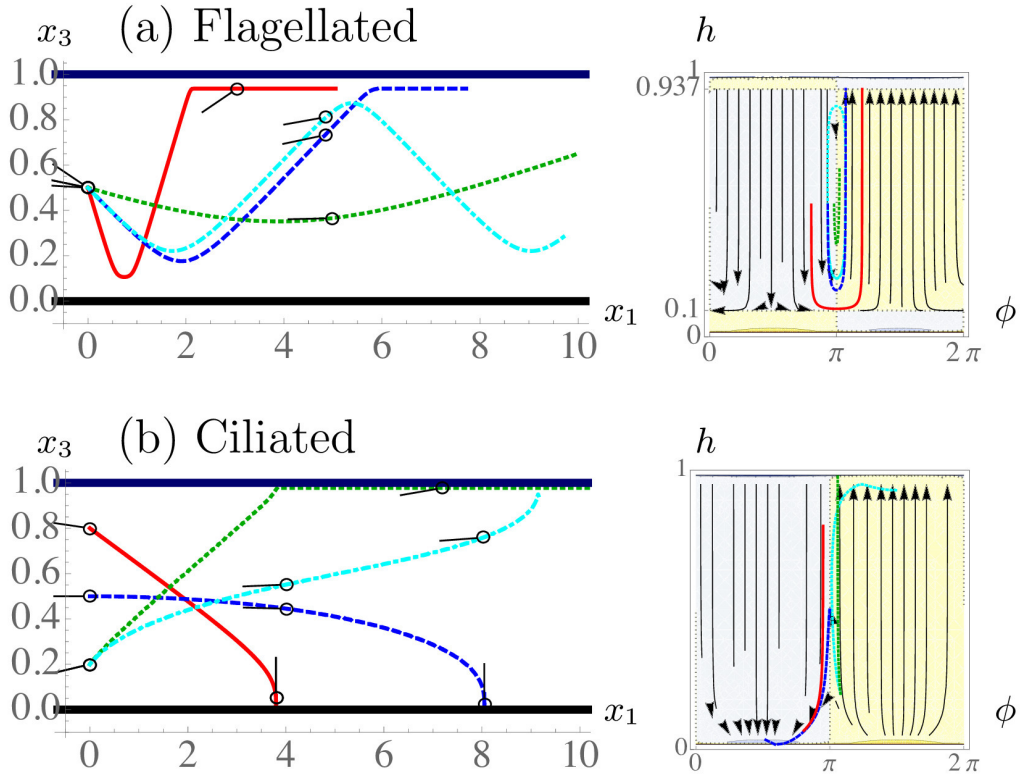

Figure 4.7: The effect of source doublet hydrodynamic interactions on the dynamics of a micro-swimmer in a film, as defined in **Fig. 4.6**. a) A ciliated swimmer with $\sigma = (1/10)^3 \left[H^3 v_s\right]$ so that the distances of closest approach are $h^B = H/10$ and $H - h^T = 0.937H$. b) A flagellated sphere with $\sigma = -(1/10)^3 \left[H^3 v_s\right]$. The cyan trajectories are for non-spherical swimmers with an aspect ratio of $\gamma = 3$ with $a/3 = b = H/100$.

doublet flow field. The first two image systems give

$$v_1^{SD} = \sigma \frac{\cos(\phi)}{8}\left(-\frac{2a^2\gamma^{-2}}{h^5} + \frac{1}{(H-h)^3} + \frac{2}{h^3}\right), \tag{4.13}$$

$$v_3^{SD} = \sigma \frac{\sin(\phi)}{4}\left(-\frac{2a^2\gamma^{-2}}{h^5} + \frac{1}{(H-h)^3} + \frac{4}{h^3}\right), \tag{4.14}$$

$$\Omega_2^{SD} = \sigma \frac{3\cos(\phi)}{32}\left(\frac{G(\cos(2\phi)-3)}{(H-h)^4} + \frac{-3G\cos(2\phi)+9G+4}{h^4}\right). \tag{4.15}$$

While the force dipole is the most significant contribution to the hydrodynamic interactions attracting swimmers to the film surfaces, we find that the higher-order terms can account for a boundary repulsion if $\sigma > 0$ (**Fig. 4.7**a). This can be understood since the source doublet component of the flow field regularises the singular description of the swimmer's flow field and hence gives the swimmer an effective characteristic hydrodynamic size, $a^H = \sqrt[3]{2\sigma/v_s}$, as discussed in §**2.2.1**. When the source doublet contribution is significant, the hydrodynamic size can be substantially larger than the characteristic geometric size of the swimmer a, which can aid escape from boundaries or keep the swimmers from coming in direct contact with

surfaces. The corresponding hydrodynamic interactions turn a swimmer away from a no-slip wall, so that the distance of closest approach is $h^{\mathrm{B}} = a^{\mathrm{H}}/2^{1/3}$. Likewise, close to a free-slip interface, the closest distance of approach is $h^{\mathrm{T}} = a^{\mathrm{H}}/2$.

For spherical ($\gamma = 1$) ciliated swimmers the angular velocity vanishes near the top no-shear interface. Such swimmers are only turned away from the bottom boundary and therefore the source doublet leads to accumulation at the top surface. The red and dark blue trajectories in **Fig. 4.7**b show this explicitly and the $h - \phi$ phase space shows that all swimmers that initially approach the bottom wall are turned away and accumulate at the film interface where they have the same orientation as that with which they initially approached the bottom wall. Ciliated swimmers that initially approach the interface immediately accumulate there, maintaining their initial angle (**Fig. 4.7**a).

Elongated ($\gamma > 1$) ciliated swimmers, however, are subject to an additional angular velocity at the top surface, which also turns the swimmer away. Hence, accumulation at both boundaries can be prevented by the action of the source doublet and the elongated swimmer ($\gamma = 3$) oscillates between the two surfaces (cyan trajectory in **Fig. 4.7**a.)

Non-ciliated organisms with $\sigma < 0$, conversely, are bound more strongly to the surfaces than ciliated swimmers. The source doublet hydrodynamics for any swimmer initially oriented towards the wall act to further orient the swimmer towards a head-on collision with the wall (**Fig. 4.7**b; red and blue trajectories). This is because a spherical body that translates past a solid wall also rotates in a rolling fashion due to hydrodynamic interactions[163]. In the case of a swimmer this effect points the propulsion direction towards the boundary, thus trapping the swimmer. The $h - \phi$ phase space shows that all swimmers initially oriented towards the wall approach the stable fixed point at $h = h^{\mathrm{B}}; \phi = \pm\pi/2$. Spherical swimmers initially oriented towards the top interface move with a roughly constant ϕ and keep that orientation, which is similar to ciliated swimmers (**Fig. 4.7**a). Elongated swimmers, instead, rotate towards the interface (cyan trajectory).

In summary, higher-order hydrodynamic moments are required to fully characterize swimmer dynamics in confined geometries as large hydrodynamic radii, $a^{\mathrm{H}} \gg a$, can lead to non-trivial trajectories and hence particle distributions.

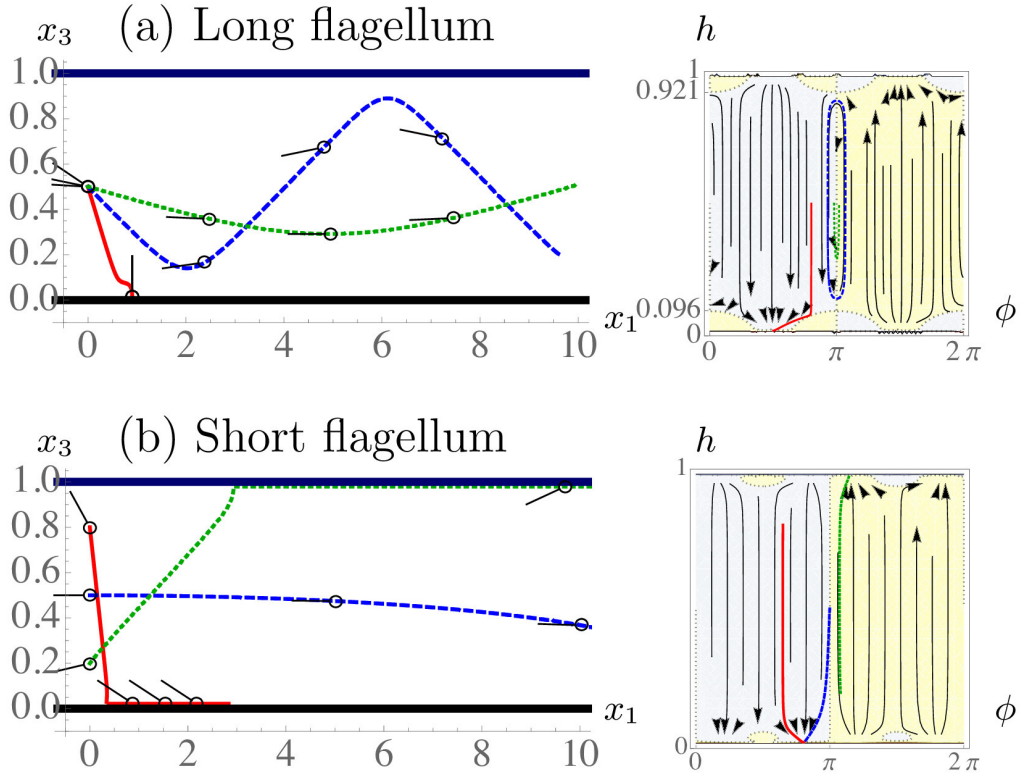

Figure 4.8: The effect of quadrupolar hydrodynamic interactions on the dynamics of a micro-swimmer in a film, as defined in **Fig. 4.6**. a) A swimmer with a long flagellum and small body , $\nu = (1/10)^3 \left[H^3 v_s\right]$ and $h^B = 0.096H$ and $H - h^T = 0.921H$. b) A swimmer with a short flagellum and big body, $\nu = -(1/10)^3 \left[H^3 v_s\right]$.

4.3.3 Quadrupolar term hydrodynamic interactions

Next, we characterise the impact of the quadrupolar term (**Eq. 1.36**). This describes the weighting of propulsion forces towards the posterior end of flagellated organisms and therefore accounts for the fore-aft asymmetry. Accounting for the first two images gives

$$\begin{aligned} v_1^Q &= \nu \frac{\cos(\phi)}{128}\left(\frac{3a^2\gamma^{-2}(5\cos(2\phi)-3)}{(h-H)^5} + \frac{4a^2\gamma^{-2}(5-11\cos(2\phi))}{h^5}\right. \\ &+ \left.\frac{4(3\cos(2\phi)-1)}{(H-h)^3} + \frac{54\cos(2\phi)-26}{h^3}\right), \end{aligned} \tag{4.16}$$

$$\begin{aligned} v_3^Q &= \nu \frac{\sin(\phi)}{32}\left(\frac{a^2\gamma^{-2}(5\cos(2\phi)+1)}{(h-H)^5} - \frac{2a^2\gamma^{-2}(7\cos(2\phi)+3)}{h^5}\right. \\ &+ \left.\frac{4(3\cos(2\phi)+1)}{(H-h)^3} + \frac{2(9\cos(2\phi)+5)}{h^3}\right), \end{aligned} \tag{4.17}$$

$$\begin{aligned} \Omega_2^Q &= \nu \frac{3\cos(\phi)}{512}\left(\frac{2(3G\cos(4\phi)-4(2G+5)\cos(2\phi)-11G+12)}{(H-h)^4}\right. \\ &+ \left.\frac{-3G\cos(4\phi)+12(G+4)\cos(2\phi)+79G-16}{h^4}\right). \end{aligned} \tag{4.18}$$

For swimmers with long flagella and small bodies, the quadrupolar coefficient is positive, $\nu > 0$ (**Fig. 4.8**a). For small angles of approach measured from the surface tangent (blue and green trajectories), the swimmer is turned away from the top and bottom surfaces. Such swimmers with $\phi \approx \pi$ perpetually oscillate between the two bounding surfaces. However, for larger angles of approach the swimmer can get stuck at the fixed point $\phi = \pi/2$ pitched downwards (**Fig. 4.8**b, red trajectory), or pitched upwards at $\phi = -\pi/2$. This mechanism could help prevent the flagella from touching the surface, facilitating an easier escape. For a spherical swimmer (as in **Fig. 4.8**) both fixed points are stable. However, the stability decreases at the bottom wall with increasing elongation γ, which favours top-surface accumulation.

Conversely, swimmers with a large body and small flagella, i.e. $\nu < 0$, are only weakly rotated towards the boundaries (**Fig. 4.8**b, blue trajectory). Interestingly, such swimmers have different fixed points than the others: The majority of the fixed points in **Figs. 4.6, 4.7, 4.8** are at $\phi = 0, \pm\pi/2, \pm\pi$ with the exception of **Fig. 4.8**b where swimmers have fixed points at an exceptional angle to the surfaces ($\phi = \pm\pi/4$).

Like the source doublet hydrodynamics, the quadrupolar term turns the swimmer away from both the no-slip and no-shear surfaces for small angles of approach measured from the surface tangent. The distance of nearest approach allowed by the quadrupolar term is $h^{\mathrm{B}} = \sqrt[3]{7\nu/8v_{\mathrm{s}}}$ for the no-slip wall and $h^{\mathrm{T}} = \sqrt[3]{\nu/2v_{\mathrm{s}}}$ for the no-shear interface. While it is well known that it is energetically favourable for small colloids to reside at interfaces, this is not commonly observed for microbes in the presence of air-water interfaces. The source doublet and quadrupolar distance of nearest approach provides a possible explanation for cases when $a < h^{\mathrm{T}}$.

4.3.4 Rotlet doublet term hydrodynamic interactions

Lastly, we describe the hydrodynamic interactions due to the rotlet doublet flow field of strength τ, representing the counter-rotating swimmer head and tail. **Table 4.5** lists the hydrodynamic interactions due to this term in the flow field. A swimmer immediately above a single no-slip boundary moves in circles in the plane parallel to the boundary. *E. coli* bacteria are observed to move in the clockwise direction, as seen from the liquid side, but in the counter-clockwise direction near a free-slip surface[238,245,362,368,369]. In a film these effects are additive. **Fig. 4.9**(a) shows the radius of curvature of the circular trajectory $R(h, \gamma)$ as a function of the swimmer's position in the film h and its aspect ratio γ. Using the first two

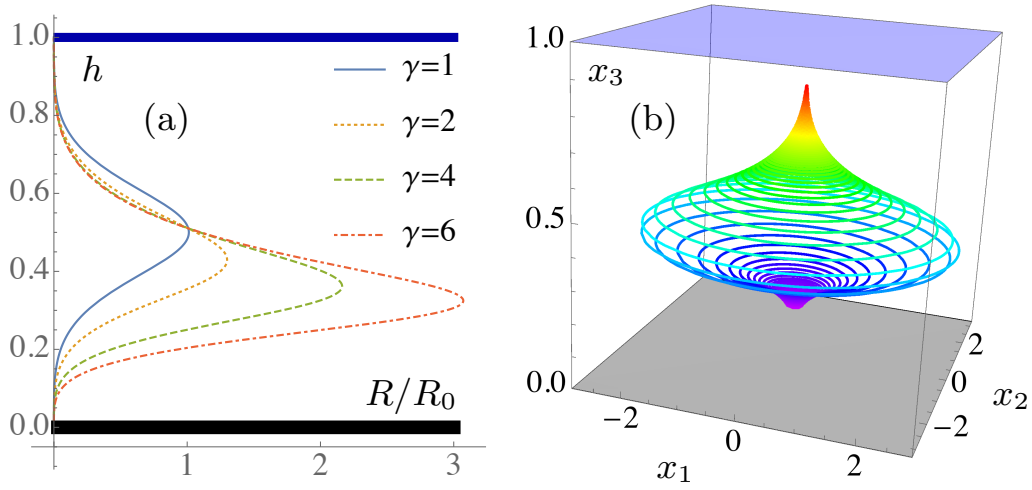

Figure 4.9: Spiralling trajectories in a film due to the counter-rotation of a swimmer's head and tail. (a) Radius of curvature $R(h,\gamma)$ of the swimmer moving in circles in the plane parallel to the surfaces for various aspect ratios γ, normalised with respect to $R_0 = R(\frac{H}{2}, 1)$. (b) An example trajectory of an elongated swimmer ($\gamma = 4$) that has just escaped from the bottom wall, with a small out-of-plane angle $\phi = 0.1°$. Colours indicate time passing, ranging from violet to red. The rotlet doublet coefficient is $\tau = 1/10\,[H^3 v_s]$, all other multipole coefficients are set to zero, and $n = 9$ images have been used.

image systems ($n = 2$) gives an analytic estimate of the radius of curvature

$$R(h,\gamma) \approx \frac{16 v_s}{3\tau}\left(\frac{1-G}{h^4} + \frac{1+G}{(H-h)^4}\right)^{-1}, \tag{4.19}$$

where $G = \frac{\gamma^2-1}{\gamma^2+1}$. This function is maximised in the middle of the film, at $h = H/2$, if the swimmer has a spherically symmetric body. The maximum radius of curvature is then $R_0 = R(\frac{H}{2}, \gamma = 1) \approx v_s H^4/6\tau$. For an elongated swimmer the function $R(h, \gamma > 1)$ is no longer symmetric about the film centre line: the radius of curvature is larger near the bottom wall but smaller near the top surface. Consequently, elongated swimmers' trajectories bend more near the water-air interface (**Fig. 4.9**b).

In microfluidic experiments the radius of curvature of swimming trajectories can be used to determine whether micro-organisms are located near the top or bottom microscope slide, as was shown qualitatively in experiments by Guidobaldi et al.[370]. More quantitatively, the knowledge of the function $R(h,\gamma)$ now allows one to compute the exact vertical position h by inverting **Eq. 4.19**. The rotlet doublet coefficient τ can also be determined with this equation using the maximum in radius of curvature in the middle of the film. This may be more reliable and effective than earlier calibration techniques used near a single surface, where an accurate measurement of the swimmer-wall separation is critical and higher-order

multipole terms and lubrication effects are hard to separate out.

Between two no-slip walls such as two glass slides, the rotary coefficient τ is challenging to determine because the maximum radius of curvature R_0 is infinite. However, once the parameters γ, τ, H are deduced in the film, the vertical position h between two microscope slides can be computed from experimentally measured radii of curvature, using the equivalent of **Eq. 4.19** for two paralel no-slip plates: $R(h,\gamma) \approx \frac{16v_s}{3\tau}\left(\frac{1-G}{h^4} - \frac{1-G}{(H-h)^4}\right)^{-1}$. Moreover, the parameters can be used in different experimental geometries, such as a lubrication layer (solid-liquid-liquid) or a floating oil film (liquid-liquid-air) for which similar expressions for $R(h,\gamma)$ can be computed.

4.4 Conclusions

Surfaces and interfaces are ubiquitous in the microscopic world of microbial swimmers and one of the most important mechanisms by which they impact the behaviour and dynamics of microscopic life is through hydrodynamic flows. To analyse these, we have derived the Stokes flow Green's function in a viscous film via a recursion relation for a series of images. The multipole expansion of this fundamental solution provides the detailed flow fields of a force- and torque-free micro-swimmer. By comparing this recursive series to the exact solution, we find that $n = 9$ images are sufficient to describe local hydrodynamic interactions with the bounding surfaces.

Using these results, we studied surface accumulation of swimmers in a thick film, distinguishing between the wall and the liquid-air interface. Here the hydrodynamic flows determine the trajectory and dynamics of a single organism. Pusher- and puller-type dipolar swimmers are attracted to both boundaries, though there is a long-ranged bias to accumulate at the no-slip wall. We give an analytic approximation distinguishing which initial conditions lead to accumulation at the solid wall. However, we also find that quadrupolar and source doublet hydrodynamic interactions are important in modulating the interface versus wall accumulation, regardless of initial conditions. Ciliated swimmers (with a positive source doublet moment) are turned away from the bottom wall and accumulate at the top interface. On the other hand, non-ciliated swimmers (with a negative source doublet moment) are more strongly bound to the no-slip wall because the swimming direction is rotated down towards the rigid boundary. Additional quadrupolar terms due to the swimmer's fore-aft

asymmetry further contribute to this, but also result in more complicated dynamics such as trajectories oscillating between the surfaces. When the rotlet doublet contribution is included the swimmer possesses rotary dynamics within the plane and we have analytically predicted the radius of curvature of these trajectories at all points within viscous films for both spherical and elongated swimmers. The formula derived allows to first calibrate the rotlet doublet coefficient in a film, and then determine the out-of-plane position of swimmers in a film or other geometries, such as between microscope slides, from experimentally available radii of curvature.

In addition, we note that decreasing the film height leads to the appearance of recirculating flow patterns, for which we provide expressions in the thin-film limit. These flows could potentially affect motility-related traits such as nutrient uptake and the energy expenditure of cells within films. Likewise, the screening of hydrodynamic flows within films seen here is expected to have important consequences for mechanosensing and predator-prey interactions between microbes within films. These flow fields are a necessary prerequisite for future simulations of the dynamics of micro-swimmers and of motility-based phenomena within films. Particularly, our thin-film limit expressions could be used to model swimmer-swimmer interactions in films of thickness comparable to the organism size, where swarming and collective motion have been observed.

4.A Exact solution of Stokeslet flow in a liquid film

In this section, we derive the flow fields generated by a Stokeslet in a liquid film of uniform thickness using a Fourier transform method. We follow the method of Liron and Mochon [184] for a Stokeslet between parallel flat plates using the appropriate boundary conditions for a film (no-slip at the bottom wall and no-shear at the top interface).

4.A.1 Formulation of the problem

In order to find the flows due to a Stokeslet in the liquid film, we split the solution in two parts. For the velocity and pressure Green's functions, respectively, we write

$$\mathcal{F}_{ij} = \mathcal{V}_{ij} + \mathcal{W}_{ij}, \qquad i,j \in \{1,2,3\}, \tag{4.20}$$

$$\mathcal{P}_{j} = \mathcal{Q}_{j} + \mathcal{S}_{j}, \tag{4.21}$$

where the first part ($\mathcal{V}_{ij}$, $\mathcal{Q}_j$), which we call the series part, accounts for the singularity in the film and satisfies some of the boundary conditions at the film surfaces. As detailed in the next section, the series part is composed of an infinite series of image reflections of the Oseen tensor (**Eq. 1.22**), and contains the Stokeslet singularity in the region $0 \leq x_3 \leq H$.

The second part ($\mathcal{W}_{ij}$, $\mathcal{S}_j$), called the auxiliary solution, is then added to the first to satisfy the other boundary conditions. Because this part does not contain any singularities in the region $0 \leq x_3 \leq H$ the Stokes equations reduce to the homogeneous equations

$$\partial_i \mathcal{S}_j = \mu \nabla^2 \mathcal{W}_{ij}, \tag{4.22}$$

$$\partial_i \mathcal{W}_{ij} = 0, \tag{4.23}$$

with boundary conditions

$$\mathcal{W}_{ij} = -\mathcal{V}_{ij} \quad \text{on } x_3 = 0, \tag{4.24}$$

$$\mathcal{W}_{3j} = -\mathcal{V}_{3j} \quad \text{on } x_3 = H, \tag{4.25}$$

$$\partial_3 \mathcal{W}_{\alpha j} = -\partial_3 \mathcal{V}_{\alpha j} \quad \text{on } x_3 = H, \tag{4.26}$$

where here and throughout this Appendix, the Greek-letter indices $\alpha, \beta \in \{1, 2\}$ only run over the directions parallel to the film surfaces.

4.A.2 Infinite series of image reflections

The first part of the solution consists of the infinite series of image reflections of the Stokeslet flow in bulk, as in the work of Liron and Mochon [184]. The images reflected in the top and bottom surface are located at

$$\boldsymbol{y}^{(m)} = (y_1, y_2, y_3 - 2mH), \tag{4.27}$$

$$\boldsymbol{Y}^{(m)} = (y_1, y_2, -y_3 - 2mH), \quad m = 0, \pm 1, \pm 2, \ldots \tag{4.28}$$

Here the original Stokeslet is located at $\boldsymbol{y}^{(0)}$, and the relative distances with respect to any point in the film are defined as $\boldsymbol{r}^{(m)} = \boldsymbol{x} - \boldsymbol{y}^{(m)}$ and $\boldsymbol{R}^{(m)} = \boldsymbol{x} - \boldsymbol{Y}^{(m)}$. Hence, the series part of the total flow field is

$$\mathcal{V}_{ij} = \frac{1}{8\pi\mu} \sum_{m=-\infty}^{\infty} \left[\left(\frac{\delta_{ij}}{r^{(m)}} + \frac{r_i^{(m)} r_j^{(m)}}{(r^{(m)})^3} \right) - \left(\frac{\delta_{ij}}{R^{(m)}} + \frac{R_i^{(m)} R_j^{(m)}}{(R^{(m)})^3} \right) \right], \tag{4.29}$$

where $r^{(m)} = |\boldsymbol{r}^{(m)}|$ and $R^{(m)} = |\boldsymbol{R}^{(m)}|$, and the corresponding pressure is

$$\mathcal{Q}_j = \frac{1}{4\pi} \sum_{m=-\infty}^{\infty} \left[\frac{r_j^{(m)}}{(r^{(m)})^3} - \frac{R_j^{(m)}}{(R^{(m)})^3} \right]. \tag{4.30}$$

This flow and pressure combination satisfies the Stokes equations, as the point force at $\boldsymbol{y}^{(0)}$ is included, and all other images lie outside the fluid region $0 \le x_3 \le H$.

Note that this image series is *not* the same as the series discussed in §**4.2.1**. Here we only consider Stokeslet reflections, and not successive Blake [183] reflections that contain derivatives of the Stokeslet as well. Therefore, this series can be written as an integral expression without any truncation. This is achieved with the Lipshitz integral

$$\frac{1}{\sqrt{\rho^2 + a^2}} = \int_0^\infty J_0(\rho\lambda) e^{-|a|\lambda} d\lambda \tag{4.31}$$

where we identify $\rho^2 = (x_1 - y_1)^2 + (x_2 - y_2)^2 = r_1^2 + r_2^2 = r_\alpha r_\alpha$, with the standard summation convention, but with the indices α, β taking the values 1 and 2 only. Hence, by summing the geometric series of the exponential factors, the velocity field can be written as

$$\begin{aligned}
4\pi\mu\mathcal{V}_{ij} &= \delta_{ij} \int_0^\infty J_0(\rho\lambda) \frac{\sinh \lambda h}{\sinh \lambda H} \sinh \lambda(H - x_3) d\lambda \\
&+ \delta_{i\alpha}\delta_{j\beta} \frac{r_\alpha r_\beta}{\rho} \int_0^\infty \lambda J_1(\rho\lambda) \frac{\sinh \lambda h}{\sinh \lambda H} \sinh \lambda(H - x_3) d\lambda \\
&- \delta_{i3}\delta_{j3} \int_0^\infty \lambda J_0(\rho\lambda) \frac{d}{d\lambda} \left[\frac{\sinh \lambda h}{\sinh \lambda H} \sinh \lambda(H - x_3) \right] d\lambda \\
&+ \mathrm{sgn}(x_3 - h)(\delta_{i3}\delta_{j\alpha} + \delta_{i\alpha}\delta_{j3}) r_\alpha \int_0^\infty \lambda J_0(\rho\lambda) \frac{\sinh \lambda h}{\sinh \lambda H} \cosh \lambda(H - x_3) d\lambda \\
&\quad \text{for } x_3 \ge h.
\end{aligned} \tag{4.32}$$

For $x_3 < h$, **Eq. 4.32** is used but with x_3 replaced by $H - x_3$ and h by $H - h$ under the integral signs. Similarly, the pressure is

$$\begin{aligned}
2\pi\mathcal{Q}_j &= \delta_{j\alpha} \frac{r_\alpha}{\rho} \int_0^\infty \lambda J_1(\rho\lambda) \frac{\sinh \lambda h}{\sinh \lambda H} \sinh \lambda(H - x_3) d\lambda \\
&+ \mathrm{sgn}(x_3 - h)\delta_{j3} \int_0^\infty \lambda J_0(\rho\lambda) \frac{\sinh \lambda h}{\sinh \lambda H} \cosh \lambda(H - x_3) d\lambda, \quad x_3 \ge h.
\end{aligned} \tag{4.33}$$

Again, for $x_3 < h$, one replaces x_3 by $H - x_3$ and h by $H - h$ under the integral signs only, using the minus sign for the second term.

From the infinite series expressions (4.32–4.33), we derive the boundary conditions (4.24–

4.26) on the auxiliary solution $\mathcal{W}_{ij}$. On the bottom wall (using 4.32 for $x_3 < h$), we have

$$4\pi\mu\mathcal{W}_{ij}(x_3 = 0) = (\delta_{i3}\delta_{j\alpha} + \delta_{i\alpha}\delta_{j3})r_\alpha \int_0^\infty \lambda J_0(\rho\lambda)\frac{\sinh\lambda(H-h)}{\sinh\lambda H}d\lambda. \tag{4.34}$$

Similarly, on the liquid-air interface

$$4\pi\mu\mathcal{W}_{3j}(x_3 = H) = -\delta_{j\alpha}r_\alpha \int_0^\infty \lambda J_0(\rho\lambda)\frac{\sinh\lambda h}{\sinh\lambda H}d\lambda \qquad \text{for } i = 3, \tag{4.35}$$

$$\begin{aligned}\partial_3 4\pi\mu\mathcal{W}_{ij}(x_3 = H) &= \delta_{ij}\int_0^\infty \lambda J_0(\rho\lambda)\frac{\sinh\lambda h}{\sinh\lambda H}d\lambda \\ &+ \delta_{i\alpha}\delta_{j\beta}\frac{r_\alpha r_\beta}{\rho}\int_0^\infty \lambda^2 J_1(\rho\lambda)\frac{\sinh\lambda h}{\sinh\lambda H}d\lambda \quad \text{for } i = 1, 2.\end{aligned} \tag{4.36}$$

In the next two sections, we transform the equations (4.22–4.23) together with these boundary conditions into Fourier space and hence find a solution.

4.A.3 Auxiliary solution in Fourier Space

To proceed, we define the two-dimensional Fourier transform and its inverse transform for an arbitrary function $\psi(r_1, r_2, x_3)$ as

$$\hat{\psi}(\lambda_1, \lambda_2, x_3) = \frac{1}{2\pi}\int_{-\infty}^\infty\int_{-\infty}^\infty \psi(r_1, r_2, x_3)e^{+\mathrm{i}(\lambda_1 r_1 + \lambda_2 r_2)}dr_1 dr_2, \tag{4.37}$$

$$\psi(r_1, r_2, x_3) = \frac{1}{2\pi}\int_{-\infty}^\infty\int_{-\infty}^\infty \hat{\psi}(\lambda_1, \lambda_2, x_3)e^{-\mathrm{i}(\lambda_1 r_1 + \lambda_2 r_2)}d\lambda_1 d\lambda_2. \tag{4.38}$$

The Stokes equations (4.22–4.23) are then transformed into

$$-\mathrm{i}\lambda_\alpha\delta_{\alpha i}\hat{\mathcal{S}}_j + \delta_{i3}\frac{\partial}{\partial x_3}\hat{\mathcal{S}}_j = \mu\left(\frac{\partial^2}{\partial x_3^2} - \xi^2\right)\hat{\mathcal{W}}_{ij}, \tag{4.39}$$

$$-\mathrm{i}\lambda_\alpha\hat{\mathcal{W}}_{\alpha j} + \frac{\partial}{\partial x_3}\hat{\mathcal{W}}_{3j} = 0, \tag{4.40}$$

where the conjugate of ρ^2 is $\xi^2 = \lambda_1^2 + \lambda_2^2$. The pressure must obey the Laplace equation $\nabla^2\mathcal{S}_j = 0$ and so we have $(\partial_3^2 - \xi^2)\hat{\mathcal{S}}_j = 0$.

The general solution to this equation, following Liron & Mochon, can be written as

$$\hat{\mathcal{S}}_j = B_j \sinh\xi(H - x_3) + C_j\cosh\xi(H - x_3), \tag{4.41}$$

and the solution to equation (4.39) is then

$$\begin{aligned}\hat{\mathcal{W}}_{ij} &= B_{ij}\sinh\xi(H-x_3)+C_{ij}\cosh\xi(H-x_3)\\ &+ (B_j\delta_{i3}+C_j\delta_{\alpha i}\mathrm{i}\lambda_\alpha/\xi)x_3\sinh\xi(H-x_3)\\ &+ (C_j\delta_{i3}+B_j\delta_{\alpha i}\mathrm{i}\lambda_\alpha/\xi)(x_3-H)\cosh\xi(H-x_3).\end{aligned} \tag{4.42}$$

The coefficients, $\{B_j, C_j, B_{ij}, C_{ij}\}$, are coupled through the transformed incompressibility condition. Inserting the transformed pressure and velocity fields (4.41–4.42) into (4.40) yields the relations

$$C_j = \xi H B_j + \xi B_{3j} + \mathrm{i}\lambda_\beta C_{\beta j}, \tag{4.43}$$

$$B_j = -\xi H C_j + \xi C_{3j} + \mathrm{i}\lambda_\beta B_{\beta j}. \tag{4.44}$$

These coefficients will now be found by applying the boundary conditions on $\hat{\mathcal{W}}_{ij}$.

4.A.4 Transforming the boundary conditions

The boundary conditions (4.34–4.36) for the liquid film can be transformed by recognising that the integral form in which they appear is the (inverse) zeroth order Hankel transform. Therefore, these transform to

$$4\pi\mu\hat{\mathcal{W}}_{ij}(x_3=0) = -\mathrm{i}(\delta_{i3}\delta_{j\alpha}+\delta_{i\alpha}\delta_{j3})\frac{\partial}{\partial\lambda_\alpha}\left[\frac{\sinh\xi(H-h)}{\sinh\xi H}\right] \qquad \forall i, \tag{4.45}$$

$$4\pi\mu\hat{\mathcal{W}}_{ij}(x_3=H) = +\mathrm{i}\delta_{i3}\delta_{j\alpha}\frac{\partial}{\partial\lambda_\alpha}\left[\frac{\sinh\xi h}{\sinh\xi H}\right] \qquad \text{for } i=3, \tag{4.46}$$

$$\partial_3 4\pi\mu\hat{\mathcal{W}}_{ij}(x_3=H) = \delta_{i\alpha}\delta_{j\beta}\left(2\delta_{\alpha\beta}+\frac{\lambda_\alpha\lambda_\beta}{\xi}\frac{\partial}{\partial\xi}\right)\frac{\sinh\xi h}{\sinh\xi H} \quad \text{for } i=1,2. \tag{4.47}$$

Here, it should be noted that the indices $\alpha, \beta \in \{1, 2\}$, so for $j = 3$ the right-hand sides of equations (4.46) and (4.47) are equal to zero.

4.A.5 Solving the transformed auxiliary solution

By equating these transformed boundary conditions to the ansatz (4.42), the coefficients $\{B_{ij}, C_{ij}\}$ are determined to be

$$\begin{aligned}
B_{\alpha\beta} &= \frac{1}{2\pi\xi^2}\left(-2\delta_{\alpha\beta}\frac{\sinh\xi h}{\sinh\xi H}\xi + 2\pi\mathrm{i}(B_\beta - H\xi C_\beta)\lambda_\alpha - \frac{\partial}{\partial\xi}\left[\frac{\sinh\xi h}{\sinh\xi H}\right]\lambda_\alpha\lambda_\beta\right), \\
B_{\alpha 3} &= \frac{\mathrm{i}(B_3 - H\xi C_3)\lambda_\alpha}{\xi^2}, \\
B_{3j} &= HC_j\coth\xi H + \mathrm{i}\delta_{j\alpha}\frac{H-h}{2\pi\xi}\frac{\sinh\xi h}{\sinh\xi H}\lambda_\alpha, \\
C_{\alpha\beta} &= \frac{\tanh\xi H}{2\pi\xi^2}\left(2\delta_{\alpha\beta}\frac{\sinh\xi h}{\sinh\xi H}\xi + 2\pi\mathrm{i}(B_\beta(\xi H\coth\xi H - 1) + C_\beta\xi H)\lambda_\alpha + \frac{\partial}{\partial\xi}\left[\frac{\sinh\xi h}{\sinh\xi H}\right]\lambda_\alpha\lambda_\beta\right), \\
C_{\alpha 3} &= \frac{\mathrm{i}\lambda_\alpha\tanh\xi H}{4\pi\xi^2}\left(-\frac{2\xi}{\sinh\xi H}\frac{\partial}{\partial\xi}\left[\frac{\sinh\xi(H-h)}{\sinh\xi H}\right] + 4\pi(B_3(\xi H\coth\xi H - 1) + C_3\xi H)\right), \\
C_{3j} &= \frac{\delta_{j\alpha}}{2\pi\xi}\frac{\partial}{\partial\xi}\left[\frac{\sinh\xi h}{\sinh\xi H}\right]\mathrm{i}\lambda_\alpha,
\end{aligned} \tag{4.48}$$

where the pressure coefficients are

$$B_j = -\mathrm{i}\delta_{j\alpha}\lambda_\alpha\frac{1}{2\pi\xi}\frac{\sinh\xi h}{\sinh\xi H}, \tag{4.49}$$

$$C_\alpha = -\frac{\mathrm{i}\lambda_\alpha}{2\xi H - \sinh 2\xi H}\frac{1}{\pi\xi}\left(\xi h\sinh\xi(H-h) + \sinh\xi h\sinh\xi H\right), \tag{4.50}$$

$$C_3 = -\frac{\sinh\xi H}{2\xi H - \sinh 2\xi H}\frac{\xi}{\pi}\frac{\partial}{\partial\xi}\left[\frac{\sinh\xi(H-h)}{\sinh\xi H}\right]. \tag{4.51}$$

Inserting the coefficients (4.48–4.51) into equations (4.41–4.42), we obtain complete expressions for the transformed velocity and pressure. These must be inverse transformed to obtain $\mathcal{W}_{ij}$ and $\mathcal{S}_j$, as described next.

4.A.6 Inverse transforming the auxiliary solution

The transformed auxiliary solution (4.41–4.42) must now be inverse transformed. We first consider $\mathcal{W}_{11}$, which has a term proportional to unity and another to λ_1^2.

$$4\pi\mu\mathcal{W}_{11} = \int_0^\infty \frac{4\sinh\xi h\sinh\xi x_3}{\xi\sinh 2\xi H}J_0(\rho\xi)\xi d\xi + \frac{\partial}{\partial r_1}\frac{r_1}{\rho}\int_0^\infty \hat{A}_{11}(\xi, x_3)J_1(\rho\xi)\xi^2 d\xi \tag{4.52}$$

where

$$\begin{aligned}\hat{A}_{11} &= -\frac{1}{\xi^3(\sinh(2H\xi)-2H\xi)}\Big(2\sinh(\xi(H-x_3))\\ &(\sinh(h\xi)\sinh(H\xi)(\coth(H\xi)(H^2\xi^2\mathrm{csch}^2(H\xi)-1)\\ &+\xi(x_3-2H))+h\xi^2(H-x_3)\sinh(\xi(h-H)))\\ &+\cosh(\xi(H-x_3))(2\sinh(h\xi)(\sinh(H\xi)\\ &+\xi(2H-x_3)\cosh(H\xi)+H\xi(\xi(x_3-H)\mathrm{csch}(H\xi)-2\mathrm{sech}(H\xi)))\\ &-2hH\xi^2\tanh(H\xi)\sinh(\xi(h-H)))+2h\xi\cosh(h\xi)\\ &(2H\xi\mathrm{csch}(2H\xi)-1)\sinh(\xi x_3)\Big). \end{aligned} \tag{4.53}$$

Similarly, with $\hat{A}_{11}=\hat{A}_{22}$, we have

$$4\pi\mu\mathcal{W}_{22} = \int_0^\infty \frac{4\sinh\xi h\sinh\xi x_3}{\xi\sinh 2\xi H}J_0(\rho\xi)\xi d\xi+\frac{\partial}{\partial r_2}\frac{r_2}{\rho}\int_0^\infty \hat{A}_{22}(\xi,x_3)J_1(\rho\xi)\xi^2 d\xi \tag{4.54}$$

For $i=\alpha\neq j=\beta$, there is only one term proportional to $\lambda_\alpha\lambda_\beta$, so

$$4\pi\mu\mathcal{W}_{\alpha\beta} = \frac{\partial}{\partial r_\beta}\frac{r_\alpha}{\rho}\int_0^\infty \hat{A}_{\alpha\beta}(\xi,x_3)J_1(\rho\xi)\xi^2 d\xi, \tag{4.55}$$

where

$$\begin{aligned}\hat{A}_{12}=\hat{A}_{21} &= -\frac{1}{\xi^3(\sinh 2H\xi-2H\xi)}\Big(2\sinh(\xi(H-x_3))(\sinh(h\xi)\sinh(H\xi)\\ &(\coth(H\xi)(H^2\xi^2\mathrm{csch}^2(H\xi)-1)+\xi(x_3-2H))+h\xi^2(H-x_3)\sinh(\xi(h-H)))\\ &+\cosh(\xi(H-x_3))(2\sinh(h\xi)(\sinh(H\xi)+\xi(2H-x_3)\cosh(H\xi)\\ &+H\xi(\xi(x_3-H)\mathrm{csch}(H\xi)-2\mathrm{sech}(H\xi)))-2hH\xi^2\tanh(H\xi)\sinh(\xi(h-H)))\\ &+2h\xi\cosh(h\xi)(2H\xi\mathrm{csch}(2H\xi)-1)\sinh(\xi x_3)\Big). \end{aligned} \tag{4.56}$$

For $i=3, j=\alpha$ there is only one term proportional to λ_α, so

$$4\pi\mu\mathcal{W}_{3\alpha} = \frac{r_\alpha}{\rho}\int_0^\infty \hat{A}_{3\alpha}(\xi,x_3)J_1(\rho\xi)\xi^2 d\xi, \tag{4.57}$$

where

$$\begin{aligned}\hat{A}_{31}=\hat{A}_{32} &= \frac{1}{\xi}h\frac{\cosh(h\xi)}{\sinh(\xi H)}\cosh(\xi(H-x_3))\\ &+ \frac{1}{\xi}\frac{1}{2H\xi-\sinh(2H\xi)}\frac{1}{\sinh(\xi H)}\Big(\cosh(\xi(H-x_3))(\sinh(h\xi)(-2H^2\xi\coth(H\xi)\\ &\quad +(2H-x_3)\cosh(2H\xi)+x_3)+2h\xi(x_3-H)\sinh(H\xi)\sinh(\xi(h-H)))\\ &\quad +\sinh(\xi(H-x_3))(2hH\xi\cosh(H\xi)\sinh(\xi(h-H))\\ &\quad +\sinh(h\xi)((h-2H+x_3)\sinh(2H\xi)-2H\xi(h-H+x_3)))\Big). \qquad (4.58)\end{aligned}$$

For $i=\alpha, j=3$, there is also only one term proportional to λ_α, so

$$4\pi\mu\mathcal{W}_{\alpha 3} = \frac{r_\alpha}{\rho}\int_0^\infty \hat{A}_{\alpha 3}(\xi,x_3)J_1(\rho\xi)\xi^2 d\xi, \qquad (4.59)$$

where

$$\begin{aligned}\hat{A}_{13}=\hat{A}_{23} &= \frac{1}{\xi}\frac{1}{2H\xi-\sinh(2H\xi)}\frac{1}{\sinh(\xi H)}\Big(((h-2H)\sinh(h\xi)-h\sinh(\xi(h-2H)))\\ &\quad (\xi(x_3-H)\sinh(\xi(H-x_3))+(H\xi\coth(H\xi)-1)\cosh(\xi(H-x_3)))\Big) \qquad (4.60)\end{aligned}$$

For $i=j=3$,

$$4\pi\mu\mathcal{W}_{33} = \int_0^\infty \hat{A}_{33}(\xi,x_3)J_0(\rho\xi)\xi d\xi, \qquad (4.61)$$

where

$$\begin{aligned}\hat{A}_{33} &= \frac{\xi}{2H\xi-\sinh(2H\xi)}\frac{1}{\sinh(\xi H)}\Big(((h-2H)\sinh(h\xi)-h\sinh(\xi(h-2H)))\\ &\quad ((x_3-H)\cosh(\xi(H-x_3))+H\coth(H\xi)\sinh(\xi(H-x_3)))\Big). \qquad (4.62)\end{aligned}$$

Finally, the auxiliary pressure field is given by

$$\mathcal{S}_j = \int_0^\infty \left[\delta_{\alpha j}\frac{r_\alpha}{\rho}\hat{A}_\alpha(\xi,x_3)J_1(\rho\xi)\xi^2+\delta_{3j}\hat{A}_3(\xi,x_3)J_0(\rho\xi)\xi\right]d\xi, \qquad (4.63)$$

where

$$\begin{aligned}\hat{A}_1 = \hat{A}_2 &= \frac{1}{\pi\xi}\frac{\cosh\xi(H-x_3)}{2H\xi-\sinh(2H\xi)}\Big(h\xi\sinh(\xi(h-H))-\sinh(h\xi)\sinh(H\xi)\Big)\\ &- \frac{1}{2\pi\xi}\frac{\sinh\xi h}{\sinh\xi H}\sinh\xi(H-x_3), \qquad (4.64)\\ \hat{A}_3 &= \frac{\xi}{2\pi}\frac{1}{2H\xi-\sinh(2H\xi)}\frac{\cosh\xi(H-x_3)}{\sinh\xi H}\\ &\cdot\Big(-2H\sinh(h\xi)-h\sinh(\xi(h-2H))+h\sinh(h\xi)\Big). \qquad (4.65)\end{aligned}$$

The final solution for the flow $\boldsymbol{u}^{\mathrm{F}}$ and pressure P^{F} generated by a Stokeslet of force strength $\boldsymbol{f}$ in a liquid film is then obtained by adding the expressions for the image series (4.32–4.33) and the auxiliary solution (4.52–4.63), so that

$$u_i^{\mathrm{F}} = \mathcal{F}_{ij}f_j \quad \text{where} \quad \mathcal{F}_{ij} = \mathcal{V}_{ij} + \mathcal{W}_{ij}, \qquad (4.66)$$

and

$$P^{\mathrm{F}} = \mathcal{P}_j f_j \quad \text{where} \quad \mathcal{P}_j = \mathcal{Q}_j + \mathcal{S}_j. \qquad (4.67)$$

4.B Velocity and pressure in the thin-film limit

In this section, we consider the solution outlined in Appendix §**4.A** in the thin-film limit where the film height is much smaller than the lateral distances between the flow source and the point where the flow is evaluated ($H \ll \rho$). This limit can also be seen as the far-field limit when all distances are large compared to the film height. To achieve this result, we follow Liron and Mochon[184] further, and transform the integral expressions into an alternative form. Once we have obtained the thin-film expression for the Stokeslet, we continue to derive the thin-film flows and pressures generated by a force-free and torque-free micro-swimmer through the use of a multipole expansion (§**4.2.2**). This could be particularly relevant in the study of hydrodynamically interacting microbes with a size comparable to the film height, when neighbouring organisms are a distance of more than one film height apart in the ρ direction.

4.B.1 Stokeslet in a thin liquid film

To transform the integral expressions in equations (4.32–4.33) and (4.52–4.63), we use the Hankel transformation[184] p 296, given by

$$\int_0^\infty J_\nu(b\xi)\xi^{\nu+1}F(\xi)d\xi = \mathrm{i}\pi(\text{sum of residues in the upper half plane of } F(z)z^{\nu+1}H_\nu^{(1)}(bz) \text{ including one half of the residue at } z=0), \tag{4.68}$$

where b is real, $F(z)$ is an even function of z that decays exponentially to zero on the real axis as Re $z \to \pm\infty$, and the integral is taken over the Hankel contour C in the complex plane[184] Figure 3. Using this Hankel transformation, the integrals can be written as infinite series

$$\int_0^\infty J_0(\rho\xi)\frac{\sinh\xi h}{\sinh\xi H}\sinh\xi(H-x_3)d\xi = \frac{2}{H}\sum_{n=1}^{\infty}\sin\frac{n\pi h}{H}\sin\frac{n\pi x_3}{H}K_0\left(\frac{n\pi\rho}{H}\right), \tag{4.69}$$

$$\int_0^\infty \xi J_1(\rho\xi)\frac{\sinh\xi h}{\sinh\xi H}\sinh\xi(H-x_3)d\xi = \frac{2}{H}\sum_{n=1}^{\infty}\frac{n\pi}{H}\sin\frac{n\pi h}{H}\sin\frac{n\pi x_3}{H}K_1\left(\frac{n\pi\rho}{H}\right). \tag{4.70}$$

By identifying the singularities in the functions $\hat{A}_{ij}$, the residues can be found and hence the integrals in equations (4.52–4.61) can be transformed.

For a Stokeslet bounded between a no-slip wall and a parallel no-shear interface, this leads to a far-field velocity field $\mathcal{F}_{ij}$ that decays exponentially with ρ if either i or j or both are equal to three. Therefore, the only components of the flow that do not decay exponentially are those oriented parallel to the surfaces, if the Stokeslet is also oriented parallel to the surfaces. These are flows with a half-parabolic profile with a maximum at the top interface

$$\mathcal{F}_{ij} \sim -\frac{3H}{\pi\mu}\frac{x_3}{H}\left(1-c\frac{x_3}{H}\right)\frac{h}{H}\left(1-c\frac{h}{H}\right)\frac{1}{\rho^2}\left[\frac{\delta_{\alpha\beta}}{2}-\frac{r_\alpha r_\beta}{\rho^2}\right]\delta_{i\alpha}\delta_{j\beta}+\mathcal{O}\left(e^{-\rho/H}\right), \tag{4.71}$$

where $c = 1/2$. The structure of this flow in the $x_1 - x_2$ plane is shown in **Fig. 4.10**a. The corresponding pressure due to a Stokeslet in a thin film is given by

$$\mathcal{P}_j \sim \frac{3}{2\pi H}\frac{h}{H}\left(1-c\frac{h}{H}\right)\frac{r_\alpha}{\rho^2}\delta_{j\alpha}+\mathcal{O}\left(e^{-\rho/H}\right). \tag{4.72}$$

The same far-field analysis can be performed for a Stokeslet bounded between two parallel plates[184]. The r_1 and r_2 dependence of these solutions are identical, and the solution is

obtained by simply setting $c = 1$. Both thin-film/far-field solutions can be classified as having the structure of a two-dimensional source doublet. That is, if a 2D source generates a flow $s_i = r_i/\rho^2$, then a 2D source doublet oriented in the j direction generates a flow $d_{ij} = -\partial_j s_i = -\delta_{ij}/\rho^2 + 2r_i r_j/\rho^4$.

4.B.2 Micro-swimmer in a thin liquid film

We now extend this result to deduce the flows generated by a force-free and torque-free micro-swimmer in a thin liquid film. We do this by expressing the swimmer-generated flows by a multipole expansion, as introduced in §**4.2.2**, written as

$$\boldsymbol{u}\left(\boldsymbol{x},\boldsymbol{y},\boldsymbol{p}\right) \;= \boldsymbol{u}^{\mathrm{D}} + \boldsymbol{u}^{\mathrm{Q}} + \boldsymbol{u}^{\mathrm{SD}} + \boldsymbol{u}^{\mathrm{RD}} + \ldots, \tag{4.73}$$

where the swimmer is located at the position $\boldsymbol{y}$ and oriented in the direction $\boldsymbol{p}$, and the multipole contributions are the Stokes dipole $\boldsymbol{u}^{\mathrm{D}}$, the quadrupole $\boldsymbol{u}^{\mathrm{Q}}$, the 3D source doublet $\boldsymbol{u}^{\mathrm{SD}}$, and the rotlet doublet $\boldsymbol{u}^{\mathrm{RD}}$. Each contribution to the multipole expansion can be written in terms of derivatives of the Green's function in the thin film (**Eq. 4.71**), as given by **Eqs. 1.33–1.38**.

If we look at flows parallel to the film surfaces ($i = 1, 2$) and the swimmer is also oriented parallel to the surfaces ($\boldsymbol{p} = \hat{\boldsymbol{e}}_j$ with $j = 1, 2$), then the leading dipolar contribution to the flow field far from the swimmer is given by

$$u_i^{\mathrm{D}}(\boldsymbol{x},\boldsymbol{y},\hat{\boldsymbol{e}}_j) \;=\; -24\kappa H \frac{x_3}{H}\left(1 - c\frac{x_3}{H}\right)\frac{h}{H}\left(1 - c\frac{h}{H}\right)\left[\frac{2\delta_{ij}r_j}{\rho^4} + \frac{r_i}{\rho^4} - \frac{4r_i r_j^2}{\rho^6}\right], \tag{4.74}$$

with $c = 1/2$ for the film. The quadrupole term is

$$u_i^{\mathrm{Q}}(\boldsymbol{x},\boldsymbol{y},\hat{\boldsymbol{e}}_j) \;=\; -36\nu H \frac{x_3}{H}\left(1 - c\frac{x_3}{H}\right)\frac{h}{H}\left(1 - c\frac{h}{H}\right)\left[\frac{\delta_{ij}}{\rho^4} - \frac{4\delta_{ij}r_j^2}{\rho^6} - \frac{4r_i r_j}{\rho^6} + \frac{8r_i r_j^3}{\rho^8}\right], \tag{4.75}$$

and the 3D source doublet is

$$u_i^{\mathrm{SD}}(\boldsymbol{x},\boldsymbol{y},\hat{\boldsymbol{e}}_j) \;=\; -24c\sigma \frac{x_3}{H^2}\left(1 - c\frac{x_3}{H}\right)\left[\frac{\delta_{ij}}{2\rho^2} - \frac{r_i r_j}{\rho^4}\right]. \tag{4.76}$$

For flows ($i = 3$) or swimmers ($j = 3$) oriented perpendicular to the film surfaces, the dipolar, quadrupolar and source dipole flow fields decay exponentially in the far field.

Fig. 4.10 shows the flow fields generated by a Stokeslet (a) or by the dipole and higher-order multipoles of a force- and torque-free microswimmer (b–d). The Stokeslet flow consists

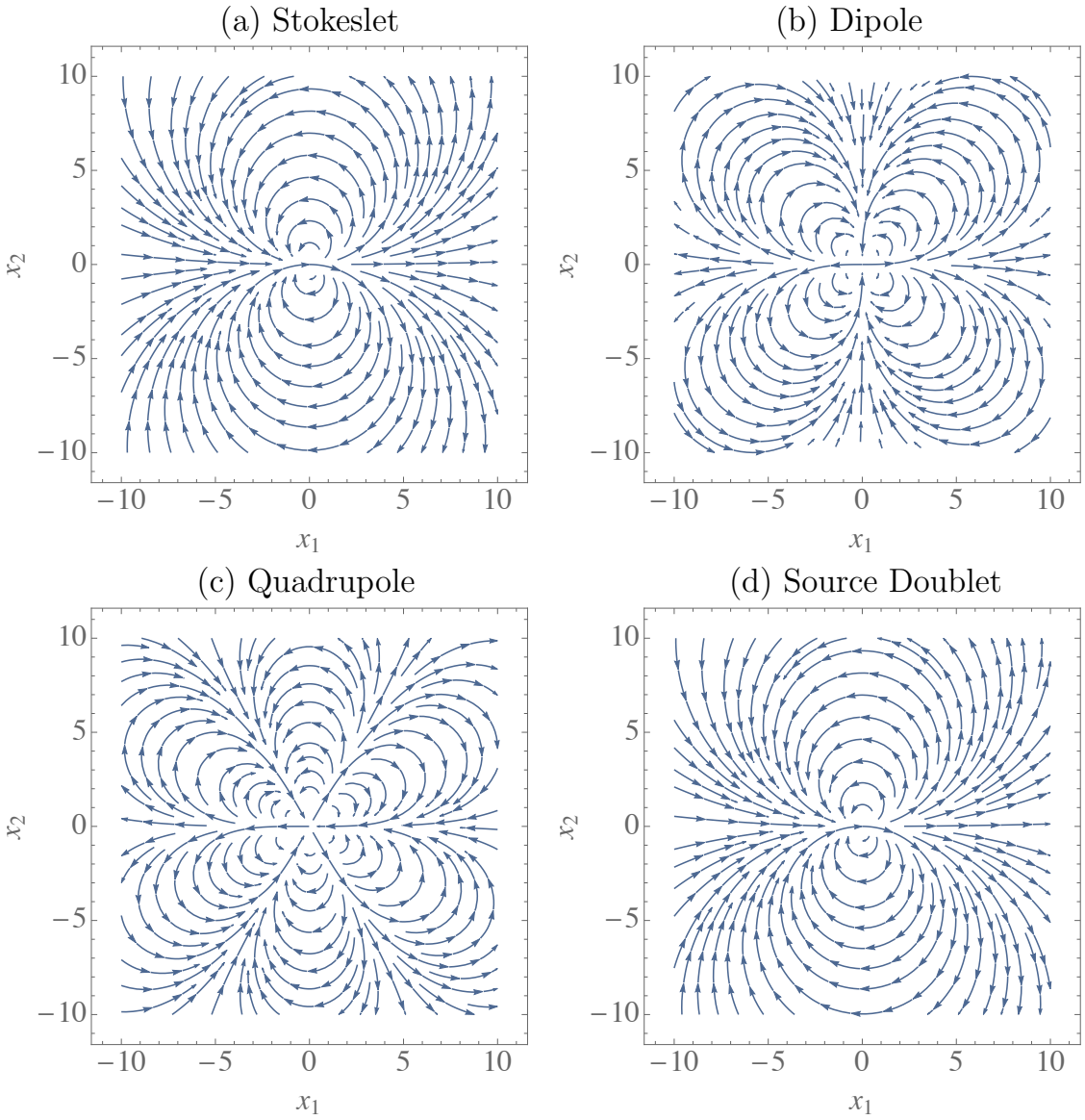

Figure 4.10: Flow fields generated by a micro-swimmer in the thin-film limit, equivalent to the limit far from the swimmer in the lateral direction, so that $H \ll \rho$. The swimmer is oriented parallel to the film surfaces, in the positive x_1 direction. Shown are streamlines in the $x_3 = H$ plane for the (a) Stokeslet, (b) Stokes dipole, (c) quadrupole and (d) source doublet.

of a recirculating flow pattern of two loops, whereas the dipole has four loops, the quadrupole has six loops, and the source doublet maintains its bulk-flow structure with two loops. These recirculating flow patterns are an effect of the minimisation of energy dissipation of Stokesian flow, because the energy loss by vortices (shear gradients) becomes less and less significant compared to viscous dissipation by the boundaries with increasing confinement.

4.B.3 Micro-swimmer between parallel plates

For completeness, we also give the flow fields generated by a micro-swimmer in a channel composed of two closely spaced parallel flat plates. The structure of these flows is identical to those in a thin liquid film (4.74–4.76), but using the prefactor $c = 1$.

4.C Comparison between the recursive series and the exact solution

In **Fig. 4.11** we show the velocity profiles generated by a Stokeslet for various film heights H. We compare the solutions obtained with the recursive series method (§**4.2.1**) and with the exact solution (Appendix §**4.A**). The left panels show the absolute flow values for both solutions (points and solid lines, respectively), and the right panels show their relative difference. Note that the same parameters have been chosen as in Liron and Mochon [184] so that a direct comparison can also be made with **Figs. 4–6** therein.

The flow structure is displayed in the left panels of **Fig. 4.11**. Flows parallel to the film surfaces due to a Stokeslet also oriented parallel, (**Fig. 4.11**a), are half-parabolic in the thin-film limit, as discussed in Appendix §**4.B**. For film heights comparable to the swimmer height (blue dotted line; $H = 2h$) the no-shear condition is still satisfied at the top interface, and the flow is still half-parabolic near the bottom wall. The overall profile however is non-trivial. In the thick-film limit (black line; $H \to \infty$) the single-wall result is recovered. Flows oriented perpendicular to the surfaces (**Fig. 4.11**c,g) are not half-parabolic, but vanish at both $x_3 = 0, H$. If the Stokeslet is oriented parallel to the surfaces (**Fig. 4.11**a,c), the values do not cross zero, whereas for Stokeslets oriented perpendicular (**Fig. 4.11**e,g) they do to satisfy incompressibility. In agreement with the conclusion by Liron and Mochon [184], if $H < 8h$, we find that the effect of the second surface cannot be neglected.

Lastly, we discuss the relative difference between the two solutions, defined as $|(\mathcal{F}_{ij}^{\text{series}} -$

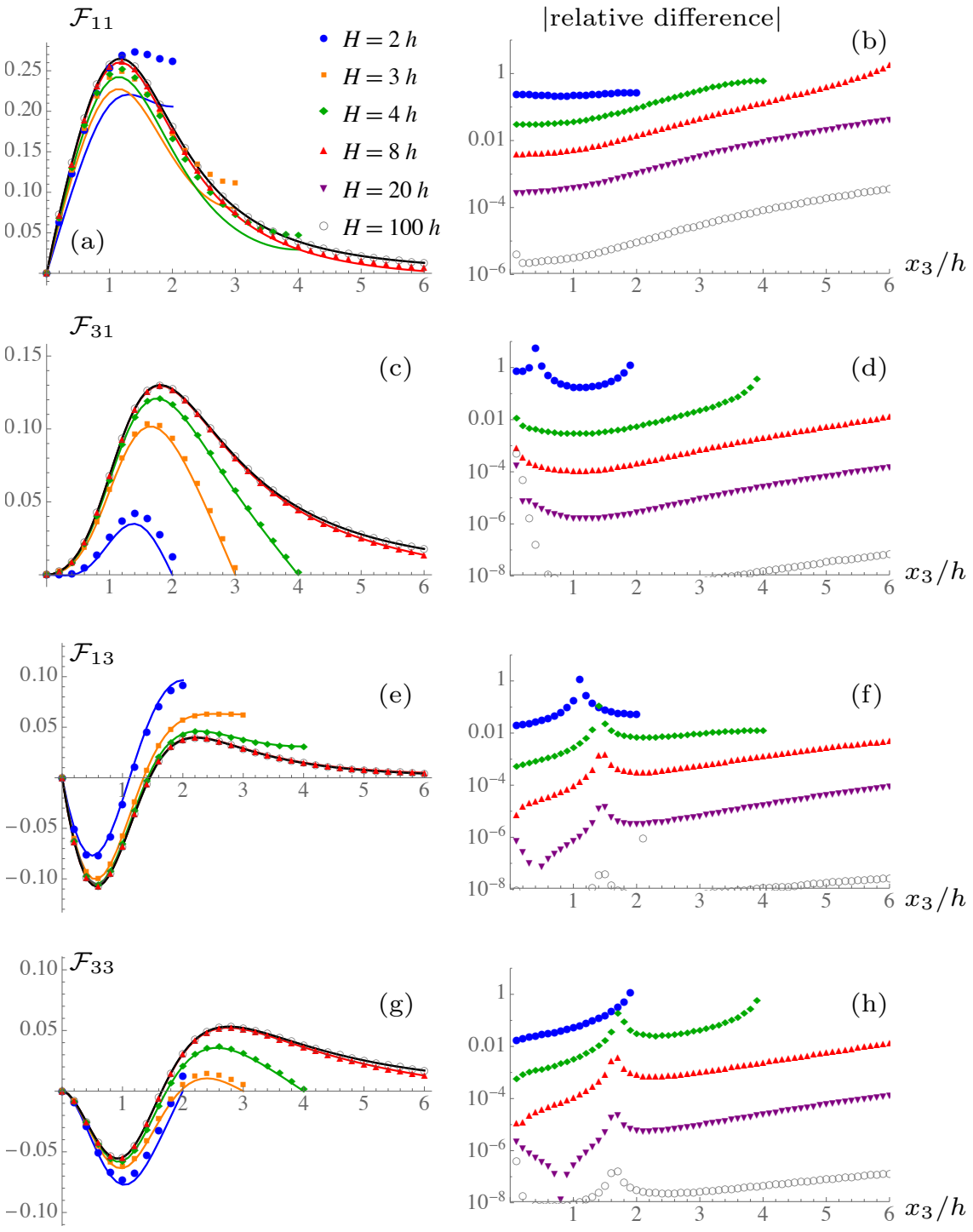

Figure 4.11: Comparison of the velocity profiles of the Stokeslet flow $u_i^{\mathrm{S}}(\boldsymbol{x}, \boldsymbol{y}, f\hat{\boldsymbol{e}}_j) = \mathcal{F}_{ij} f$ for various values of the film height H, as a function of the dimensionless coordinate x_3/h, with a constant Stokeslet position $y_3 = h$ and constant $r_1 = r_2 = h$. The Stokeslet is oriented parallel (a–d; $\boldsymbol{f} = f\hat{\boldsymbol{e}}_1$) or perpendicular (e–h; $\boldsymbol{f} = f\hat{\boldsymbol{e}}_3$) to the film surfaces, and has force strength $f = 4\pi\mu$. The left panels show flows obtained with the exact solution (solid lines), and with the recursive series method (points), where $n = 9$ images have been used. The right panels show the relative difference between the values obtained from the two methods. The solid black line represents the case of $H \to \infty$, where only one no-slip wall is present, plotted using the Blake solution (**Eq. 1.48**).

$\mathcal{F}_{ij}^{\text{exact}})/\mathcal{F}_{ij}^{\text{exact}}|$, and thus the accuracy of the recursive series solution (**Fig. 4.11**, right panels). The agreement is not acceptable in the thin-film limit, $h \sim r_1 < H$, as more images are required because they become approximately equidistant to the point of interest. However, the agreement is good for large films heights, $h \sim r_1 \ll H$, where the series can be safely truncated. For example, if $H = 100h$ the error is $< 10^{-4}$ for all x_3 values, with the largest error at the top interface and the smallest error at the bottom surface as the series solution satisfies the no-slip boundary conditions exactly with $n = 9$ images.

CHAPTER 5

Dynamics and statistics of micro-swimmers in flowing films

"Wisdom begins in wonder."

Socrates (469–399 BC)

5.1 Introduction

In chapter §4 we have shown how hydrodynamics affect micro-swimmer dynamics near boundaries in a liquid film as surfaces, interfaces and confinements are ubiquitous in microbial environments[8,243]. Here we extend these results by including background flows and run-tumble dynamics, focussing on biological traits. No-slip surfaces locally slow flows and may provide peaceful respite from violent mixing. However, an unavoidable consequence of no-slip surfaces embedded in flows is shearing and, though microbes at surfaces may not be subject to large velocities, they are commonly subjected to non-negligible shears[110]. The interplay of a flowing fluid and swimming cells has been studied recently for Newtonian[111,214,239,275,280,282–285] and non-Newtonian fluids[190,191,288,289]. Additionally, biological systems often feature large fluctuations that affect the dynamics of living cells[85,94,263,305–309]. Together, these works emphasise the pivotal roles of confinement, the background flow and noise as determinants of swimmer trajectories in micro-environments. However, despite the widespread implications the combined effects of motility, external flows, hydrodynamics and biological non-determinism remain obscure due to the complexity of the dynamics.

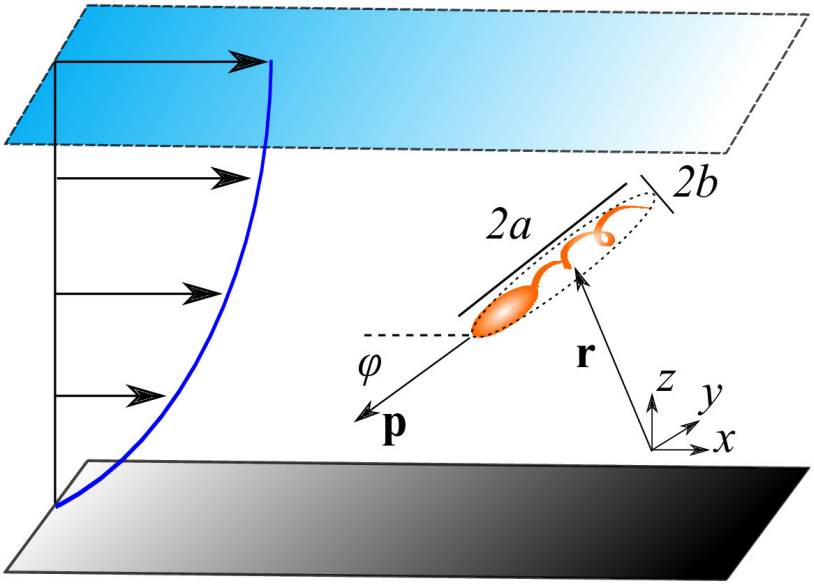

Figure 5.1: A micro-swimmer immersed in a liquid film. The film flows in the x direction, indicated by the arrows and the parabolic velocity profile. The micro-swimmer is advected and rotated by this flow, and interacts with the film surfaces, sterically, and hydrodynamically through its self-generated flow field. Angles $-\pi/2 < \phi < \pi/2$ indicate upstream orientation.

In this chapter, we present a comprehensive description of the dynamics and statistics of swimming microbes in flowing films. We focus on two classes of model micro-organisms: flagellated swimmers, like *E. coli* bacteria, and ciliated swimmers, such as *Volvox carteri* microphytes. To model swimming trajectories and the distribution of micro-swimmers within films, we consider the various contributions to a swimmer's equations of motion, first separately then concurrently. We begin by considering only the effects of external flow and steric interactions with the film boundaries (§**5.2**) before including detailed hydrodynamic interactions with the two surfaces (§**5.3**). Additionally, stochastic effects must also be accounted for. We scrutinise the swimmer distributions that will arise in flowing films because swimmers are subjected to thermal noise (§**5.4.1**). It is well known that the primary source of biological stochasticity in many flagellated microbes is run-tumble dynamics, whereas ciliated organisms are subject to enhanced Brownian fluctuations, e.g. due to cilia beating out of synchrony. Run-tumble dynamics are seen to prevent boundary accumulation more successfully than equivalent levels of enhanced Brownian noise (§**5.4.2**). Our results have implications for the control of cell distributions within flowing films, and highlight the cellular swimming strategies against which defouling schemes must contend.

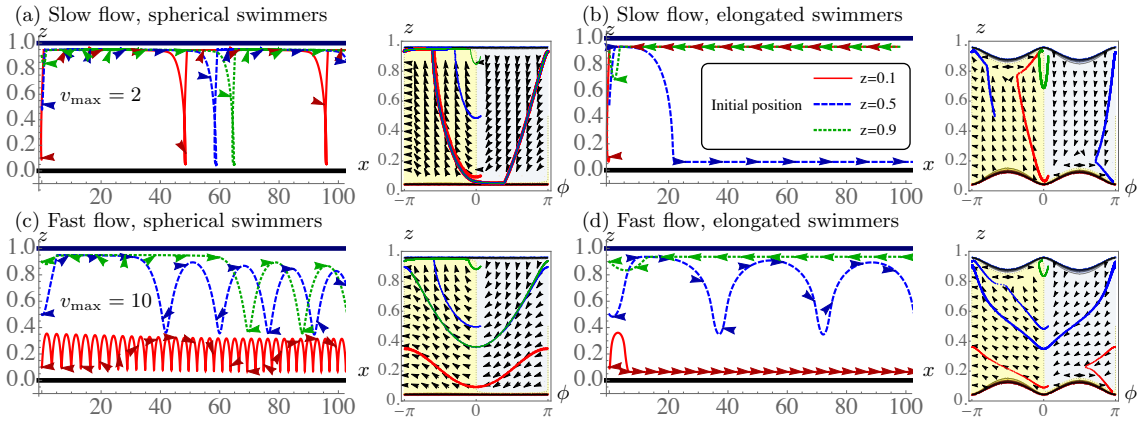

Figure 5.2: Deterministic trajectories of a micro-swimmer in a liquid film flowing from left to right, with steric interactions but without hydrodynamic interactions. Three trajectories are shown with initial orientation $\phi = 0.1$, $x = 0$ and $z = 0.1, 0.5, 0.9$ in solid red, dashed blue and dotted green lines, respectively, where the x and z axes are normalised with respect to the channel height H. The background flow is (a,b) slow: $v_{max} = 2v_s$ and (c,d) fast: $v_{max} = 10v_s$. The swimmer body shape is (a,c) spherical (like *Volvox*) with $a = b = H/20$ and (b,d) elongated (like *E. coli*) with aspect ratio $\gamma = 3$, size $a = 3b = 3H/20$ and rotational drag coefficient $\xi = 10a^3$. (Main panels) Dynamics in real $x - z$ space. Motion is from left to right, along with the background flow, and arrows indicate the direction of swimmer orientation. (Side panels) Corresponding dynamics in $\phi - z$ phase space. Background colours indicate the sign of the z component of the swimmer velocity. The white regions are inaccessible for the swimmer due to the steric interactions.

5.2 Swimming cell trajectories with steric interactions

We consider a motile swimming microbe within a flowing film, with a bottom no-slip wall at $z = 0$ and a no-shear top interface at height $z = H$. As before, the micro-swimmer is modelled following §1.3.1 with position $\boldsymbol{r}_s = (x, y, z)$. The translational invariance of the equations of motion (1.45-1.46) along the directions parallel to the surfaces allows us to consider motion of swimmers in the $y = 0$ plane where we take the flow along the x direction. Hence, the swimmer orientation is represented in cylindrical coordinates as $\boldsymbol{p}_s = -(\cos\phi, 0, \sin\phi)$, where upstream orientation corresponds to $\phi = 0$ (**Fig. 5.1**).

We begin by examining the simplified picture that microbes swim in a flowing film where their interactions with the film boundaries are purely steric. Several recent studies have considered pure kinematic interaction of swimmers with solid boundaries in the search for non-hydrodynamic mechanisms of boundary accumulation[258,371]. Neglecting hydrodynamic interactions is expected to give qualitatively relevant conclusions but not quantitative results. In §5.3 and §5.4 we characterise the roles of hydrodynamic interactions and noise, respectively, but until then we only use equations (1.45-1.46) with $\{\boldsymbol{v}^{HI}, \boldsymbol{v}^{k_BT}, \boldsymbol{\Omega}^{HI}, \boldsymbol{\Omega}^{k_BT}, \boldsymbol{\Omega}^{RT}\} = \boldsymbol{0}$.

The background fluid flow in the x direction is prescribed with a half-parabolic profile[372],

$$\boldsymbol{u}^{\mathrm{F}}(\boldsymbol{r}) = v_{\max}\left[2\frac{z}{H} - \frac{z^2}{H^2}\right]\hat{\boldsymbol{e}}_x, \tag{5.1}$$

which has a maximum speed $v_{\max}$ at $z = H$. The flow $\boldsymbol{u}^{\mathrm{F}}$ enacts a drag on a swimmer at position $\boldsymbol{r}$, which induces the velocity $\boldsymbol{v}^{\mathrm{F}}$ and angular velocity $\boldsymbol{\Omega}^{\mathrm{F}}$. The flow-induced translational and rotational velocities of the force-free and torque-free swimmer are

$$\boldsymbol{v}^{\mathrm{F}} = v_{\max}\left[2\frac{z}{H} - \frac{z^2}{H^2}\right]\hat{\boldsymbol{e}}_x, \tag{5.2}$$

$$\boldsymbol{\Omega}^{\mathrm{F}} = v_{\max}\left[\frac{H-z}{H^2}\left(1 - G\cos 2\phi\right)\right]\hat{\boldsymbol{e}}_y. \tag{5.3}$$

Steric interactions with the surfaces are modelled by a repulsive force and torque, as in §**1.3.2.2** but for two surfaces, resulting in the linear and angular velocities

$$\boldsymbol{v}^{\mathrm{ST}} = v_{\mathrm{s}}A(\phi)^{12}\left(\frac{1}{z^{12}} - \frac{1}{(H-z)^{12}}\right)\hat{\boldsymbol{e}}_z, \tag{5.4}$$

$$\boldsymbol{\Omega}^{\mathrm{ST}} = a^2 v_{\mathrm{st}}\xi^{-1}G\sin(2\phi)\,\hat{\boldsymbol{e}}_y. \tag{5.5}$$

The trajectories of a microbial swimmer in a flowing film (without hydrodynamic interactions or noise) are shown in **Fig. 5.2**. The vorticity of the background flow is strongest at the bottom wall but vanishes at the top, turning an upstream-oriented swimmer up towards the film interface. In slowly flowing films, spherical swimmers, such as *Volvox*, remain there whilst being advected downstream and slowly rotated, until their orientation is sufficiently changed to swim down into the film, where the vorticity is larger. Hence, the swimmer 'dips' down but quickly finds itself returned towards the free interface once again, only for the process to repeat (**Fig. 5.2**a).

Elongated swimmers, such as *E. coli*, tend to reside at the top surface longer due to their Jeffery orbits[283] (**Fig. 5.2**b). Furthermore, the steric interactions reorient the long bodies parallel to the surface. When an elongated swimmer is oriented in the upstream direction at the top interface, the vorticity and steric torque due to motility counter each other, leading to a stable fixed point in phase space at $(\phi = 0, z = H - b)$ (red and green trajectories). The downstream-oriented fixed point is unstable at the top of the film, because the vorticity and steric torque cooperate, so that the swimmer can move away from the top interface (blue trajectory). Conversely, at the bottom wall the (upsteam-) downstream-orientation

fixed point is (unstable) stable, as shown by the red trajectory. Therefore, even without hydrodynamics, steric interactions can cause trapping of elongated swimmers at surfaces, oriented downstream at the bottom wall and upstream at the interface, in agreement with simulations[256] and experiments[247].

At sufficiently large flow speeds, an additional type of trajectory can be observed: A fast rotation ('spinning') of swimmers. Spinning trajectories are confined to the lower regions of the film where, due to the strong vorticity of the flow, the swimmer is rotated rapidly. Hence, its motility averages to zero, leaving the swimmer vorticity-trapped. For spherical *Volvox*, we see spinning in the lower region of the film without trapping at the bottom wall (**Fig. 5.2**c; red trajectory). In the top region, swimmers start 'dipping' but interact sterically with the top surface. Therefore, they are forced to follow the trajectory exactly between dipping and spinning in the middle region (blue and green trajectories). This special trajectory is called the separatrix, in which swimmers dip from the top, down to a critical height z^*. Elongated *E. coli* also feature dipping and spinning in the middle region (**Fig. 5.2**d; blue trajectory), but in the top and bottom regions they can get trapped close to the surfaces (red and green trajectories). The chance of encountering a surface is smaller when the motility is averaged to zero in rapid rotation, thus the probability of spinning increases with flow speed.

The transition between dipping and spinning is defined by the separatrix in phase space. Dipping trajectories are above this line and spinning trajectories below the separatrix. The lowest point in the film that this special trajectory can reach is the critical height,

$$z^* = \left(1 - \frac{2}{\sqrt{v_{\max}/v_s}}\right) H, \tag{5.6}$$

both for spherical *Volvox* and elongated *E. coli*. Therefore, the separatrix touches the bottom wall at a critical flow $v_{\max} = 4v_s$. Spinning trajectories do not exist below that flow. The larger the flow rate, the larger the fraction of phase space taken up by spinning trajectories, and therefore the probability of finding these trajectories in the lower regions of the film.

In summary, these results show that in the absence of hydrodynamic interactions and noise, the background flow and steric interactions of a micro-swimmer with the boundaries lead to distinct swimmer trajectories depending critically on background flow speed. Above the critical flow speed $v_{\max} > 4v_s$ a swimmer is likely to be observed spinning near the bottom boundary due to trapping in the high-vorticity region, whereas if $v_{\max} < 4v_s$ swimmers tend to reside near the top surface.

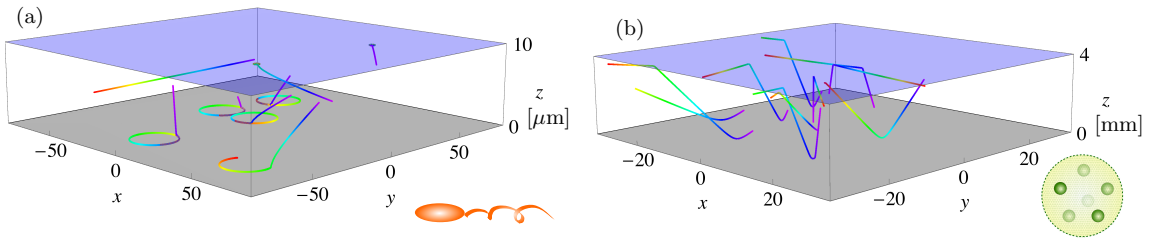

Figure 5.3: Typical deterministic swimming trajectories in a quiescent film for two different organism types: (a) *E. coli* bacteria as an example of flagellated swimmers. $H = 10\mu$m, $a = 1.5\mu$m, $b = 0.5\mu$m, $v_s = 50\mu$m/s, $\kappa = 30\mu$m^3/s, $\sigma = -25\mu$m^4/s, $\nu = 25\mu$m^4/s, $\tau = -8.3\mu$m^4/s and $\xi = 1\mu$m^3. Axes units are in μm. (b) *Volvox* microphytes as an example of ciliated swimmers. $H = 4$mm, $a = b = 200\mu$m, $v_s = 100\mu$m/s, $\kappa = 10^6\mu$m^3/s, $\sigma = 10^9\mu$m^4/s and $\nu = \tau = 0\mu$m^4/s. Axes units are in mm. (a,b) All other multipole moments are set to zero. Trajectories result from numerical integration of the equations of motion. Colour indicates time passing, ranging from violet ($t = 0$) to red ($t = 2$s for (a) and $t = 4$s for (b)). Inset images show typical examples of flagellated and ciliated organisms.

5.3 Trajectories of swimmers with hydrodynamic interactions

In addition to differing size and shape, *Volvox* and *E. coli* have pronouncedly different swimming strategies. *E. coli* propels itself forwards by rotating long exterior helical filaments, whereas *Volvox* beats many cilia that are small compared to the organism size. Consequently, they have very different hydrodynamic interactions with the bounding surfaces of the film through the swimmer-generated flow field[246]. We utilise the hydrodynamic interactions with the film boundaries ($\boldsymbol{v}^{\mathrm{HI}}$ and $\boldsymbol{\Omega}^{\mathrm{HI}}$), that are derived in Chapter §**4**. We then use our results to describe the specific hydrodynamic effects on trajectories of our example swimmers (§**5.3.1**) and study the opposing effects of hydrodynamic boundary accumulation versus peeling of swimmers from the bottom wall by flow (§**5.3.2**).

5.3.1 Two specific examples: *E. coli* and *Volvox*

Here we apply our model to two specific example organisms of different classes: the flagellated *E. coli* bacterium and the ciliated *Volvox carteri* microphyte. Many of the micro-swimmers occurring in nature can be classified in one of these two categories. For a detailed list of species, we refer to e.g. Lighthill[92]. Using experimental data we estimate the swimming parameters including the multipole coefficients and swimming speed, and use these to calculate the swimming trajectories.

For *E. coli*, we estimate the dimensions as $a = 1.5\mu$m and $b = 0.5\mu$m. The dipole strength has been measured as $\kappa \approx 30\mu$m^3/s[205]. The source doublet coefficient is expected to be

negative for a non-ciliated organism and can be estimated from an approximate hydrodynamic size $a_{\mathrm{H}} \sim 1\mu$m and swimming speed $v_{\mathrm{s}} \approx 50\mu\mathrm{m/s}$[52], leading to $\sigma \approx -\frac{1}{2}a_{\mathrm{H}}^3 v_{\mathrm{s}} \approx -25\mu\mathrm{m}^4/\mathrm{s}$. Similarly, we estimate the quadrupolar coefficient $\nu \approx 25\mu\mathrm{m}^4/\mathrm{s}$ for a flagellated bacterium. The rotlet dipole coefficient τ can be estimated from experimental measurements of the radius of curvature of swimming trajectories near surfaces[245,253,362,368,373]. Using a radius of curvature $R \approx 20\mu$m, aspect ratio $\gamma = 3$ and swimming height $z = b \approx 0.5\mu$m gives $\tau \approx \frac{32z^4 v_{\mathrm{s}}}{3R(1-G)} \approx -8.3\mu\mathrm{m}^4/\mathrm{s}$, where $G = \frac{\gamma^2-1}{\gamma^2+1}$ and the minus sign corresponds to swimming in the clock-wise direction above the no-slip wall. To emphasise the effects of a relatively thin film, we choose $H = 20b = 10\mu$m.

For *Volvox*, we estimate the dimensions as $a = b = 200\mu$m, and for the film height we choose $H = 20b = 4$mm. The primary multipole coefficients have been measured as $\kappa \approx 10^6\mu\mathrm{m}^3/\mathrm{s}$ and $\sigma \approx 10^9\mu\mathrm{m}^4/\mathrm{s}$ as has the swimming velocity $v_{\mathrm{s}} \approx 100\mu\mathrm{m/s}$[208]. This type of organism is fore-aft symmetric and so $\nu \approx 0$, and it does not have rotating flagella so we also expect $\tau \approx 0$. *Volvox* is not always neutrally buoyant and therefore a Stokeslet flow field should be present, but we neglect the effects of gravity here, assuming the sedimentation speed is smaller than the swimming speed. This model would, however, be even more appropriate for the many smaller ciliated micro-organisms in nature[92] of which the multipole coefficients have not yet been measured directly.

Fig. 5.3 shows typical trajectories for the two example organisms in the absence of flow. Random initial positions and orientations were chosen to show the diversity of the dynamics. *E. coli*-like organisms tend to accumulate at the surfaces (**Fig. 5.3**a), with a small bias towards the bottom wall because of the dipolar hydrodynamic interactions, and they remain tightly bound there because of quadrupolar hydrodynamics, in agreement with earlier calculations (see §**4.3**). At both surfaces the swimmers move in clockwise circles, but the radius of curvature of the trajectories at the bottom wall is larger than at the top interface by a factor of $\gamma^2 + \mathcal{O}(b^2/H^2) \approx 9$ due to the body elongation. *Volvox*-like organisms, in contrast, turn away from the bottom wall but assemble at the top interface (**Fig. 5.3**b). The hydrodynamic binding to the top interface is not so strong as that of the bacteria, because of the positive source doublet moment. With a small fluctuation this allows for motion away from the interface into the film, before returning back to the top again.

The resulting trajectories for these different swimmer types could offer important biological implications. Micro-organisms such as *E. coli* bacteria might have developed into slender

and fairly fore-aft symmetric bodies that tend to accumulate at boundaries, e.g. to facilitate biofilm formation. Likewise, sperm cells could benefit from the ability to swim upstream along the walls of the female reproductive tract. On the other hand, ciliated organisms like the *Paramecium* protozoa or *Volvox* tend to accrue at the top interface only, which could be beneficial to collect oxygen or to facilitate photosynthesis.

5.3.2 Flow-induced peeling

Next, we re-introduce the external flow to the dynamics of the swimming microbes, in addition to steric and hydrodynamic interactions with the surfaces. The trajectories for swimmers including hydrodynamic interactions (**Fig. 5.3**) are substantially modified because of the additional vorticity of the background flow. They more closely resemble the swimming paths of **Fig. 5.2** far from the surfaces. However, close to the surfaces, and particularly near the bottom wall where the vorticity is largest, there is a competition between the external flow field and the hydrodynamic interactions with the wall.

The external flow can prevent hydrodynamic interaction-induced boundary accumulation by peeling swimmers off the bottom wall. This detachment from surfaces by imposed flows has been demonstrated recently in experiments[280]. In **Fig. 5.4** the minimum flow strength required to detach a swimmer from the bottom wall is shown as a function of dipole moment κ and source doublet moment σ. Notice the asymmetry – a pusher can be washed off more easily than its equivalent puller. Recall that both *E. coli* and *Volvox* are pushers with $\kappa > 0$. Neutral swimmers ($\kappa = 0$; steric interactions only) can accumulate at the surfaces in strong confinement, but can also be detached with small background flows.

We theoretically estimate the critical flow speed required to detach swimmers from the bottom wall by equating the angular velocity of the dipolar interactions ($\mathbf{\Omega}^{\mathrm{D}}$ given in **Eq. 4.12**) and of the flow (**Eq. 5.3**). Considering only two images and spherical swimmers, we obtain

$$\left.\frac{v_{\max}}{v_{\mathrm{s}}}\right|_{\mathrm{crit}} = \frac{3}{16}\frac{H\,|\kappa|}{a^3 v_{\mathrm{s}}}\,|\sin 2\phi_c|\,, \tag{5.7}$$

where ϕ_c is the critical angle that the swimmer must rotate through to overcome the hydrodynamic barrier. Note that this expression scales linearly with the film height, because the local vorticity decreases with increasing H. This equation is straightforwardly generalised

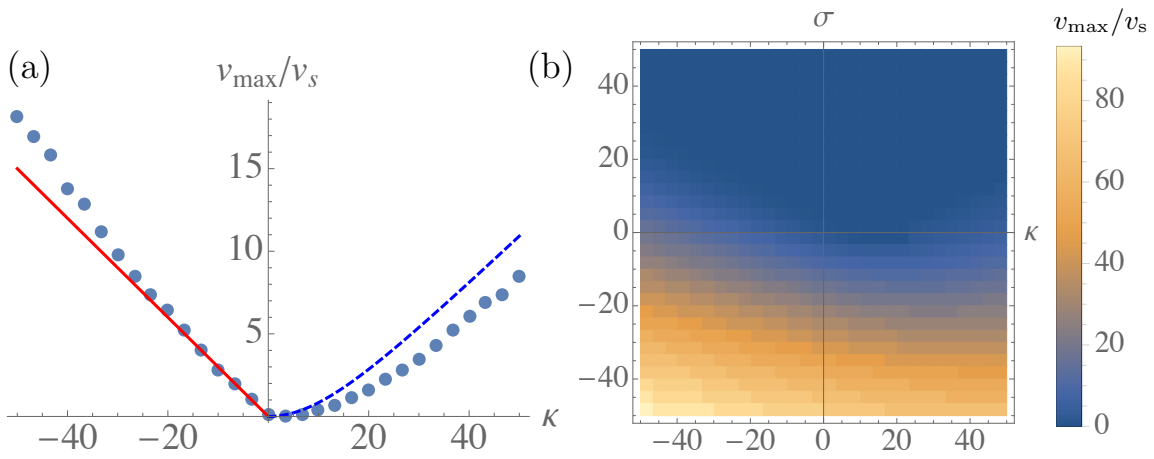

Figure 5.4: Minimum flow strength required to peel micro-swimmers off the bottom wall of a liquid film, for (a) A swimmer with only a variable dipole moment κ [μm$^3/s$]. (b) A swimmer with variable dipole and source doublet moment σ [μm$^4/s$]. Lines in (a) show theoretical predictions for a puller (red, solid) and pusher (blue, dashed) from **Eq. 5.7**. Blue dots in (a) and contours in (b) result from numerical integration of the equations of motion. Included are motility, external flow, steric and hydrodynamic interactions with the walls, but no noise. All other multipole coefficients are zero. Swimmers are released facing the bottom wall ($z = a$, $\phi = \pi/2$). Film height $H = 10\mu$m, swimmer dimensions $a = b = 0.5\mu$m and swimming speed $v_s = 50\mu$m/s.

to account for elongated swimmers, such as *E. coli*, by replacing the radius a with the distance of closest approach between the ellipsoid and the wall, $A(\phi) = \sqrt{a^2 + (b^2 - a^2)\cos^2\phi}$. Furthermore, by defining a dimensionless number $\lambda = a^3 v_{\max}/\kappa H$ that characterises the degree of detachment by external flows (**Table 5.1**), **Eq. 5.7** can be recast as $\lambda_{\text{crit}} = 3\,|\sin 2\phi_c|\,/16$, which is independent of the swimming speed. Here $\lambda < \lambda_{\text{crit}}$ corresponds to attachment and $\lambda > \lambda_{\text{crit}}$ to detachment.

For pullers, the equilibrium orientation without flow is pointing towards the wall, $\phi = \pi/2$. Hence, pullers must turn upwards over the hydrodynamic barrier from $\phi_c = \pi/2$ to the orientation parallel to the wall, $\phi = (0, \pi)$, in order to swim away. Inserting this angle ϕ_c and the figure parameters into **Eq. 5.7** gives a prediction for the minimum flow strength required for pullers (red line in **Fig. 5.4**a).

Pushers are oriented parallel to the wall at equilibrium, but they must also overcome the attraction towards the bottom wall. Therefore, the angle at which the pushers can swim away, using two image systems, is given by the requirement that

$$-\sin\phi_c > \frac{3}{16}\frac{\kappa}{v_s a^2}(3\cos 2\phi_c - 1). \tag{5.8}$$

Inserting the resulting angle ϕ_c into **Eq. 5.7** gives a prediction for the minimum flow strength

required for pushers (blue dashed line in **Fig. 5.4**a). Since the angle is smaller for pushers than for pullers, the former can escape from the surface more easily.

The inclusion of higher-order multipoles in the hydrodynamic interactions with the surfaces changes the critical flow speed (**Fig. 5.4**b). Flagellated swimmers with source doublet moment $\sigma < 0$ are more tightly bound to the wall, thus requiring a stronger flow to peel them off. Pushers such as *E. coli* in **Fig. 5.3**a with $\kappa = 30\mu\text{m}^3/s$ and $\sigma = -25\mu\text{m}^4/s$ require $v_{\max} \approx 25v_\text{s}$ compared to $\approx 2.5v_\text{s}$ when $\sigma = 0$. Non-ciliated pullers such as *Chlamydomonas reinhardtii* with both $\kappa, \sigma < 0$ are even more tightly bound. Ciliated swimmers with $\sigma > 0$, on the other hand, are much less strongly attracted to the wall (**Fig. 5.3**b) and hardly need any flow for detachment.

5.4 Swimmer distributions

Swimmer trajectories in real microbial environments are subject to stochastic fluctuations. Having established the deterministic features of the swimmer trajectories in the presence of flow, steric and hydrodynamic interactions, we now examine the distributions of micro-swimmers if noise, originating from both thermal fluctuations and run-tumble dynamics, is added. This is important because measuring distributions of swimming cells is easier in many experimental setups than following individual trajectories. For simplicity, in the following we examine archetypal spherical swimmers with a dominant contribution from dipolar hydrodynamic interactions.

We model the thermal/Brownian noise as drawn from a Gaussian distribution so that the mean squared displacement and angular displacement are $\langle|\boldsymbol{r}(t) - \boldsymbol{r}(0)|^2\rangle = 6Dt$ and $\langle|\phi(t) - \phi(0)|^2\rangle = 2D_r t$ in the large-time limit, where D and D_r are the translational and rotational Brownian diffusion coefficients, respectively. For typical micron-sized swimmers we approximate the thermal diffusion coefficients as $D \approx 0.25\mu\text{m}^2/s$ and $D_\text{r} = 0.2\text{rad}^2/\text{s}$. We assume that these diffusion coefficients are isotropic and remain constant as a function of film height. To be concrete, we consider a narrow film of height $H = 10\mu\text{m}$ and organisms of dimensions $a = b = 0.5\mu\text{m}$ and swimming velocity $v_\text{s} = 50\mu\text{m/s}$.

When only thermal noise is considered, the swimmers' trajectories are deterministic over a timescale of crossing the film. Once they reach a surface, there is a competition between the noise, flow and hydrodynamic interactions. Using only the dipolar contribution from the first

image system ($\boldsymbol{v}^{\mathrm{D}}, \boldsymbol{\Omega}^{\mathrm{D}}$ given in §4.3.1), we define translational and rotational Hydrodynamic Interaction Péclet numbers to be

$$\mathrm{Pé}^{\mathrm{HI}} \equiv \frac{v^{\mathrm{HI}} a}{D} = \frac{3\kappa}{8b^2}\frac{a}{D}, \tag{5.9}$$

$$\mathrm{Pé}_{\mathrm{r}}^{\mathrm{HI}} \equiv \frac{\Omega^{\mathrm{HI}}}{D_r} = \frac{3\kappa}{16b^3}\frac{1}{D_{\mathrm{r}}}. \tag{5.10}$$

With a dipole strength of $\kappa = 30\mu\mathrm{m}^3/\mathrm{s}$, we estimate $\mathrm{Pé}^{\mathrm{HI}} \sim 100$ and $\mathrm{Pé}_{\mathrm{r}}^{\mathrm{HI}} \sim 200$. Since both $\mathrm{Pé}^{\mathrm{HI}}$, $\mathrm{Pé}_{\mathrm{r}}^{\mathrm{HI}} \gg 1$, thermal noise is not sufficient to allow swimmers to overcome hydrodynamic attraction to the surfaces, in the absence of a background flow. Experiments have shown that flagellated bacteria have smaller passive rotational diffusion coefficients than unflagellated cells[205,308], so $\mathrm{Pé}_{\mathrm{r}}^{\mathrm{HI}} \sim 200$ represents a conservative estimate. Consequently, other mechanisms must be employed by swimming cells to prevent boundary accumulation within films.

In §5.4.1, we first study the combined effect of Brownian noise and external flow on distributions of archetypal micro-swimmers, i.e. *neutral* swimmers, *pushers* and *pullers*. In §5.4.2, we add non-thermal fluctuations and investigate the impact of the nature of this noise by comparing swimmers subject to run-and-tumble dynamics (*tumblers*) and enhanced Brownian noise (*drifters*).

5.4.1 Prevention of boundary accumulation by external flow

§5.2 described the effect of flow on steric swimmers without noise. In §5.3 we included hydrodynamic interactions with the surfaces, but still excluded noise. In this section, we investigate the combined effects of steric and hydrodynamic interaction, film flow, and thermal noise.

The accumulation of swimmers at the surfaces is evaluated using the swimmer density distribution $\rho(z,\phi)$, normalised such that $(2\pi H)^{-1}\int_0^H\int_{-\pi}^{\pi}\rho(z,\phi)d\phi dz = 1$. This distribution is established by solving the equations of motion **(1.45–1.46)** numerically for a population of 10^4 swimmers that are initially distributed at random positions $z \in [0, H]$ and orientations $\phi \in [-\pi, \pi]$. The simulation is continued until the distribution $\rho(z,\phi)$ reaches a steady state. Subsequently, the spatial distribution is found by integrating over the angular coordinates, $f(z) = (2\pi)^{-1}\int_{-\pi}^{\pi}\rho(z,\phi)d\phi$, and similarly for the orientational distribution, $g(\phi) = H^{-1}\int_0^H \rho(z,\phi)dz$. The fraction of swimmers at the bottom wall and top interface are evaluated as $f_{\mathrm{w}} = H^{-1}\int_0^{\epsilon} f(z)dz$ and $f_{\mathrm{i}} = H^{-1}\int_{H-\epsilon}^{H} f(z)dz$, where $\epsilon = 1.1a$ to allow for

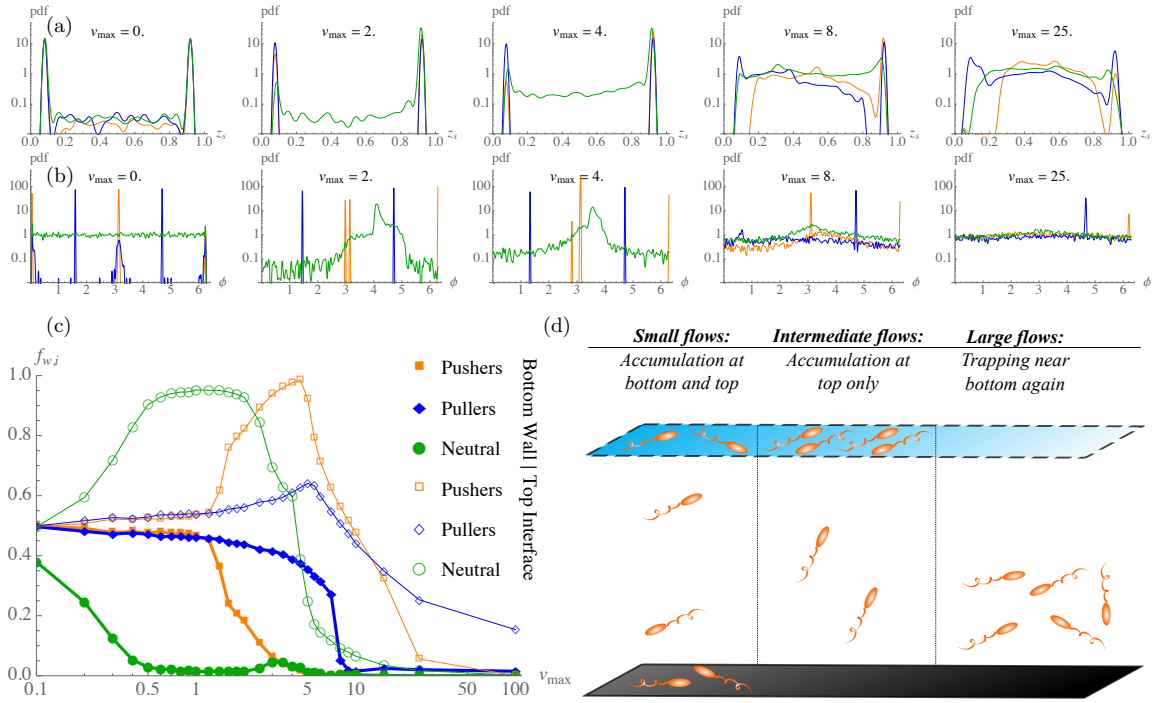

Figure 5.5: Prevention of boundary accumulation of micro-swimmers due to an external flow in a film. Statistics are shown for an ensemble of 10^4 swimmers, 30 seconds after release from a random position and orientation, when distributions have reached steady-state. (a) Distributions of swimmer position across the film for various background flow rates. (b) Distributions of swimmer orientation. (c) Fraction of swimmers at the bottom wall (f_w; filled symbols) and top interface (f_i; empty symbols). (d) Schematic of the observed dynamics. Colours indicate *neutral* swimmers (green circles), *pushers* (orange squares) and *pullers* (blue diamonds). Parameters used are film height $H = 10\mu$m, swimmer dimensions $a = b = 0.5\mu$m, swimming speed $v_s = 50\mu$m/s, thermal diffusion coefficients $D = 0.25\mu\text{m}^2/\text{s}$ and $D_r = 0.2\text{rad}^2/\text{s}$, dipole strength $\kappa = 30\mu\text{m}^3/\text{s}$ and all other multipole coefficients are set to zero. Flow rates are normalised with respect to the swimming speed, v_s, and the z axis is normalised with respect to the channel height H.

small fluctuations.

Fig. 5.5 shows distributions of swimmer positions and orientations as a function of the background flow for *neutral* swimmers ($\kappa = 0$), *pushers* ($\kappa > 0$) and *pullers* ($\kappa < 0$), while subject to thermal diffusion. In the absence of a background flow, the swimmers accumulate at the two surfaces due to steric and hydrodynamic interactions, with a small bias towards the bottom wall for the pushers and pullers due to the stronger hydrodynamic dipolar interactions near no-slip surfaces (**Fig. 5.5**a; first window). Once trapped, the equilibrium orientation for pushers is parallel to both surfaces (**Fig. 5.5**b, orange peaks at $\phi = 0, \pm\pi$). Pullers are bound more strongly since their equilibrium orientation is perpendicular to the surface (blue peaks at $\pm\pi/2$). Indeed, Schaar et al.[220] have shown that the detention times of pullers in the absence of external flow can be several orders of magnitudes larger than those of pusher

or source doublet swimmers.

Introduction of a small flow is enough to drive the majority of neutral swimmers towards the top surface (**Fig. 5.5**a; second window). The transition to free interface accumulation is a general trend for all swimmer types, but occurs at different flow speeds for each. The fraction of neutral swimmers at the bottom wall (f_w) drops rapidly to zero around $v_{max} \approx 0.5 v_s$ and at the top interface the fraction (f_i) rises to unity (**Fig. 5.5**c; green circles). Pushers start to get detached from the bottom wall around $v_{max} \approx 2v_s$ (orange squares), which is a bit smaller than the value predicted in §**5.3.2** for deterministic swimmers (**Fig. 5.4**a; $v_{max} \approx 2.5 v_s$ at $\kappa = 30\mu m^3/s$). This is because the noise occasionally kicks microbes away from the wall. By $v_{max} \approx 4v_s$ (**Fig. 5.5**a; third window), the majority of pushers have accumulated at the top interface. Pullers remain attached until a flow of strength $v_{max} \approx 8v_s$ is applied (blue diamonds), also a bit smaller than the deterministic equivalent $\approx 9v_s$. The distributions across the film show this in more detail (**Fig. 5.5**a,b; windows 2, 3 & 4 for the three swimmer types respectively).

Interestingly, by further increasing the flow speed, swimmers can again get trapped near the bottom wall. This is not due to hydrodynamic interactions but rather is directly related to the 'spinning' trajectories in high-vorticity flows that were described in §**5.2**. Consequently, at high flow rates swimmers do not accumulate in the regions of smaller vorticity near the top interface. This is consistent with earlier findings of shear-trapping by Rusconi et al.[239]. It occurs because, whereas the vorticity alone is too small at the top surface to reinject swimmers into the film at a significant rate, small thermal fluctuations can lead swimmers to the high-vorticity region where they get trapped. Therefore, the number density of swimmers in the film is again larger near the bottom wall for flow rates $v_{max} > 8v_s$, and the accumulation at the top surface is suppressed entirely at large flow rates (**Fig. 5.5**c and **Fig. 5.5**a,b; last two windows).

In summary, the results show that in the absence of the background flow the swimmers accumulate at the top and bottom surfaces. Introducing flow and thermal Brownian noise can substantially modify distributions of swimmers in the film (**Fig. 5.5**d). For moderate flow rates they are peeled off the bottom wall and accumulate at the top interface. However, for large flow rates the swimmers can get vorticity-trapped near the bottom wall again. This counter-intuitive result suggests that faster flow rates are not always the best strategy to discourage wall accumulation and the consequent initiation of biofilms. Instead, there is a

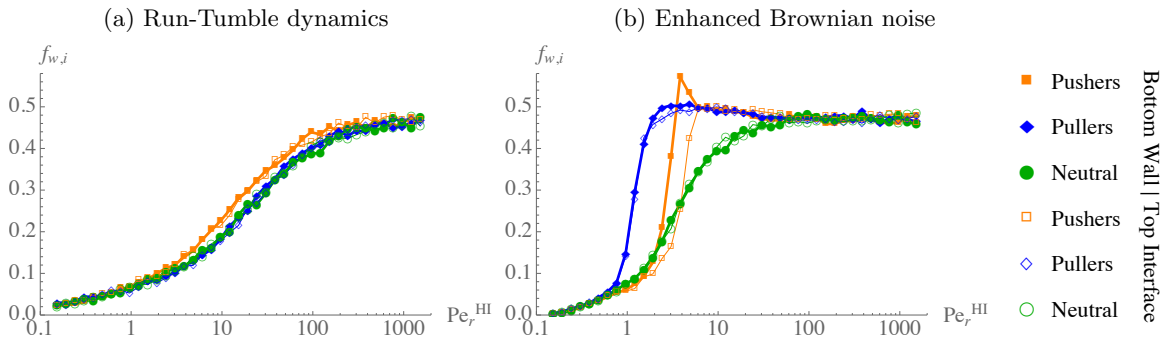

Figure 5.6: Prevention of boundary accumulation of micro-swimmers due to (a) run-and-tumble dynamics and (b) Gaussian-distributed enhanced Brownian noise, evaluated at the same rotational HI Péclet number. Statistics are shown for an ensemble of 10^4 swimmers, after 10 seconds of release from a random position and orientation, when the distributions have reached steady-state. Shown is the fraction of swimmers at the bottom wall (f_w; solid lines) and top interface (f_i; dotted lines). Colours indicate pushers (orange), pullers (blue) and neutral swimmers (green). Parameters used are film height $H = 100\mu$m, swimmer dimensions $a = b = 0.5\mu$m, swimming speed $v_\mathrm{s} = 50\mu$m/s, dipole strength $\kappa = 30\mu\mathrm{m}^3/\mathrm{s}$, all other multipole coefficients are set to zero and there is no background flow.

finite range of intermediate flows within which the top-accumulation is optimised.

5.4.2 Prevention of boundary accumulation by run-tumble dynamics

Typical microbial swimmers do not rely solely on thermal noise to prevent boundary accumulation — the HI Péclet numbers (**Eqs. 5.9-5.10**) are much too large. Many micro-organisms have developed different mechanisms to actively change their orientation at a given moment. This could be an effective enhanced rotational Brownian noise, e.g. due to cilia which temporarily beat out of synchrony[85,94,374–376] or to inhomogeneous external influences[309]. Moreover, many microbial species make use of a 'tumbling' mechanism that allows them to suddenly change their orientation, rather than slowly decorrelating over time[55]. Various tumbling mechanisms have been observed, including ones based on flagellar unbundling[51,209] and flagellar buckling instabilities[57] for bacteria. Such strategies are not limited to flagellated bacteria but are also employed by ciliated organisms such as *Paramecium* that suddenly eject trichocysts[377].

In this section, we measure the extent to which such mechanisms cause boundary detachment by comparing swimmers with run-tumble dynamics (*tumblers*) to swimmers subject to a Gaussian-distributed enhanced Brownian noise (*drifters*) of the same effective rotational diffusion coefficient.

Fig. 5.6 shows the fraction of tumblers and drifters at the film surfaces for a given run

time between tumble events, $\tau_r \in [0.01, 100]$s. This range corresponds to $\text{Pé}_r^{\text{HI}} \in [0.1, 1000]$, since the effective rotational diffusion coefficient is $D_r^{\text{eff}} = \pi^2/(2\tau_r)$. In agreement with the expectations, microbes of all swimmer types are seen to accumulate at the two surfaces at large HI Péclet numbers.

Tumblers can detach fairly easily from the surfaces when the HI Péclet number is reduced (**Fig. 5.6**a), because sudden decorrelating tumbling events are momentarily sufficient to overcome the hydrodynamic attraction. With increasing tumbling rate, there is a gradual crossover from surface accumulation to residence in the bulk of the film. Interestingly, we find that the hydrodynamic swimmer-type has little effect on this crossover. This is an important observation as it indicates that hydrodynamic interactions are not a dominant factor when run-and-tumble dynamics are present, as in *E. coli*.

Neutral drifters (swimmers subject to enhanced Brownian noise) can also escape from the surfaces with ease. However, drifters with hydrodynamic interactions remain attached to the surfaces at much lower HI Péclet numbers (**Fig. 5.6**b). Moreover, the escape crossover is much sharper. This difference arises because the slowly accumulating Brownian noise is continuously countered by hydrodynamic and steric interactions, and therefore a certain threshold must be exceeded before swimmers can escape from a surface. The level of critical noise is $\text{Pé}_r^{\text{HI}*} \approx 8$ for pusher drifters and ≈ 2 for puller drifters. Also notice that the attraction towards the bottom wall is a factor of 3/2 larger for pushers (see **Eq. 4.11**), and therefore the fraction of pushers at the bottom wall peaks before decaying with decreasing HI Péclet number.

This crossover from boundary accumulation to detachment is particularly relevant in many typical micro-environments. For *E. coli*-like with $\tau_r \approx 0.9$s ($\text{Pé}_r^{\text{HI}} \approx 8$), the total fraction at both surfaces is $f_s = f_w + f_i \approx 0.3$. However, for longer run times near surfaces[59], $\tau_r \approx 2$s ($\text{Pé}_r^{\text{HI}} \approx 20$), the fraction almost doubles to $f_s \approx 0.55$.

In summary, the tumbling mechanism is more effective in preventing surface accumulation than Brownian noise of equivalent strength, particularly at the HI Péclet numbers relevant in nature. Flagellated organisms like *E. coli* bacteria could employ this to their advantage, using hydrodynamic interactions to get close to surfaces (§**5.3**) and then tumbling to escape them. We have demonstrated that hydrodynamic interactions with confining walls break the equivalence between active Brownian motion and run-tumble dynamics. While it is commonly true that active Brownian motion and run-tumble dynamics are equivalent this is

Symbol	Definition	Name
λ	$a^3 v_{\max}/\kappa H$	Detachment number
$\mathrm{Pé}^{\mathrm{HI}}$	$3a\kappa/8b^2 D$	Translational HI Péclet number
$\mathrm{Pé}_{\mathrm{r}}^{\mathrm{HI}}$	$3\kappa/16b^3 D_{\mathrm{r}}$	Rotational HI Péclet number

Table 5.1: Summary of dimensionless number definitions.

not always the case[305]. Recent research that did not account for hydrodynamic interactions has shown that run-and-tumble dynamics lead to different density distributions near surfaces than simple active Brownian particles[263]. Our results support this previous finding and further demonstrate that run-tumble dynamics dominate over hydrodynamic interactions that can likely be safely neglected in future studies of bacteria.

5.5 Conclusions and discussion

In this chapter we have presented a comprehensive description of the dynamics and statistics of swimming cells in flowing films, demonstrating that swimmer trajectories show distinct behaviours depending on the swimming mechanism of the organism. We focus on two classes of model organisms, flagellated (*E. coli*-like) and ciliated (*Volvox*-like) swimmers, with parameters tuned to experiments. Flagellated swimmers accumulate at surfaces due to hydrodynamic interactions, whereas ciliated organisms can avoid surfaces.

We have shown that swimmers can be detached from the bottom wall above a critical flow strength, which we predict analytically and obtain numerically for dipolar and higher-order hydrodynamic interactions. Conversely, we see that steric interactions with the surfaces and background film flow favours wall (interface) accumulation above (below) a critical flow speed, due to a vorticity-trapping mechanism. Therefore, boundary accumulation is not always prevented by imposing stronger flows. Instead, there is a finite range of intermediate flows for which microbes do not accumulate at the bottom wall. Our work predicts the extent of this range for both pusher and puller swimmers in terms of three dimensionless numbers (**Table 5.1**). The flow-controlled crossover from surface accumulation to interface accumulation may have important implications for biofouling.

In addition, we demonstrate that run-and-tumble dynamics can act as a mechanism that organisms, such as *E. coli*, could employ to prevent boundary accumulation at surfaces, whereas enhanced Brownian noise requires much smaller Péclet numbers (greater noise)

to achieve this goal. Whereas hydrodynamic interactions are important for systems with enhanced Brownian noise, we find that they have little impact on the swimmer distributions for the run-tumble dynamics expected for micro-organisms such as *E. coli*. This conclusion has ramifications for future theoretical and computational investigations as it implies that computationally expensive and theoretically cumbersome hydrodynamic interactions may be neglected in biologically relevant scenarios if experimentally significant run-tumble noise is accounted for.

Our results provide a number of testable predictions with implications for biofilm initiation. Genetic modification of *E. coli* can alter run-and-tumble dynamics[55]. *E. coli* modified in this way is predicted to have markedly different distributions within flowing films compared to unmutated samples. Likewise, different motile microbes, such as *Volvox*, are expected to reside at different points in the flowing film due to their different swimming strategies. The fraction of swimmers at the no-slip wall compared to the number at the no-shear interface could be measured. Measuring such fractions as a function of flow rate would provide direct experimental verification of the predictions made here. The rate of biofilm initiation at the solid surface is expected to correlate with the fraction of swimmers at the wall and so our work suggests a non-monotonic dependence of the initiation rate on the film flow velocity, with a maximum at moderate flow strengths.

CHAPTER 6

Lattice-Boltzmann Simulations of Anisotropic Microswimmers

"The children grew but you don't see them grow."

Voice of Hope soprano Pumeza Matshikiza (1979–)

6.1 Introduction

In chapters §2–§5 we have developed a mathematical framework to model micro-swimmers and used this to predict swimmer dynamics and distributions in micro-channels and liquid films. In order to test the theoretical predictions made, we seek to perform more detailed computer simulations and resolve swimmer flows and hydrodynamic interactions (HI).

A wide range of techniques is available to study the behaviour of active particles using simulations. The most common model is active Brownian model (ABM), which does not take HI into account. It has been applied to simulate shape-anisotropic particles, in bulk[378], under confinement[274], and in capturing geometries[379]. Hydrodynamics can be incorporated to first order, by introducing a point-like dipole interaction, either using lattice-Boltzmann (LB) simulations[380,381], or using a Stokesian description[382–385]. Universal aspects of swimmer dynamics are known to arise from these long-range hydrodynamics. Therefore, having models that can effectively simulate the correct long-range HI, without concern for specific short-range interactions is very valuable.

Thus far, there have been very few studies of highly shape-anisotropic particles, where HI have been taken into account[261,386–389]. The models that have been considered are typically highly system specific, or too computationally expensive to simulate a large number of particles. An intermediate form is therefore required that takes into account HI and strikes a balance between the accurate simulation of shape-anisotropic particles and computational efficiency. The LB algorithm has been shown to efficiently simulate HI and is therefore considered ideally suited to this task. In particular, the simulations of Nash *et al.*[381] demonstrate that LB can readily simulate thousands of swimmers.

In this chapter, we introduce a model with the aforementioned features. We simulate active colloids of arbitrary shape by approximating them as clusters of spheres, see **Fig. 6.1**. These clusters are coupled to an LB fluid using the viscous coupling scheme introduced by Ahlrichs and Dünweg[390], in which the friction depends on the relative velocity of particle and fluid. The effect of this coupling is the formation of a hydrodynamic hull around the points, which thus gain an effective hydrodynamic size[390]. Thereby, a solid particle can be modelled, which resembles a raspberry[391] for a sufficient density of coupling points[392,393]. Self-propulsion is introduced by following the principles of Refs.[380,382,383]: We assign a direction (unit) vector to the raspberry particle and apply a persistent force along this direction and an equal and opposite (counter) force to the fluid (see **Fig. 6.1**a). The location of the counter force determines the nature of the leading dipole moment and distinguishes pusher (extensile) from puller (contractile) swimmers.

Using our model, we demonstrate that the anisotropy of the particle induces higher order multipole moments, in addition to the dipole moment that we impose. These multipole moments account for the flow of fluid around the object. We introduce a method to determine the magnitude of these multipole moments by means of a Legendre-Fourier analysis – we limit ourselves to axisymmetric anisotropic swimmers here. This characterisation technique is applicable beyond our raspberry swimmers, and may be of use in establishing the hydrodynamic nature of complex swimmers, for which the flow field has only been determined numerically[144,145,394,395]. We confirm that we obtain the correct leading-order dipole moment by considering the displacement of a tracer particle in the flow field caused by the swimmer. This also serves as a proof of principle that our raspberry-swimmer model has applications in more complex settings than single-particle bulk simulations.

The raspberry swimmers introduced in this chapter present a facile method, by which

anisotropic swimmers can be modelled. It allows us to incorporate HI that go beyond the principal dipole and are essential to the accurate description of shape-anisotropic swimmers. The raspberry swimmers can be utilised to gain new insights into the behaviour of anisotropic swimmers in various geometries, as we will further demonstrate in the next Chapter §**6**.

6.2 Methods

In this section, we give an overview of the approaches followed to obtain the results presented in §**6.3**. We first outline the principles of the raspberry model and the construction of the raspberry swimmers. Next, we specify the Molecular Dynamics (MD) and LB parameters used in our work. We subsequently provide details of the simulations used to characterise the shape of the swimmers. This is followed by a discussion on the determination of the hydrodynamic moments via a Legendre-Fourier decomposition method, as well as by considering the displacement of a tracer particle.

6.2.1 The Raspberry Model

Ahlrichs and Dünweg[390] introduced a simple coupling scheme to simulate moving particles in an LB fluid without using Ladd (grid-based) bounce-back boundary conditions[396]. In this approach, the particles are described as points that couple to the fluid through a frictional force, acting both on the solvent and on the solute, which depends on the relative velocity. A hydrodynamic hull forms around the points, which thus gain a finite hydrodynamic extent (effective hydrodynamic radius)[390], due to this coupling and the interpolation of the force onto the LB grid. This method is particularly suited to simulate a monodisperse system of colloids where the far-field hydrodynamics dominate over the near-field contributions, which are typically not accurately captured.

Lobaskin and Dünweg[391] utilised the point coupling to simulate extended objects moving through a fluid by introducing the "raspberry" model. A larger particle – compared to a single coupling point – is modelled by discretising the surface (and interior[392]) of the particle. The method derives its name from this discretised nature of the surface, which resembles a raspberry, when represented by molecular-dynamics (MD) beads. When a sufficient number of points is used to couple to the fluid, the LB fluid inside the particle co-moves with the coupling points, thus modelling a hydrodynamically solid object. This raspberry coupling

typically leads to an effective hydrodynamic extent of the object, that is larger than that of outmost coupling points[392]. Despite the introduction of other methods of describing extended particles in a LB fluid, the raspberry method has remained popular, due to its simplicity.

6.2.2 Raspberry Swimmers

We study four different particle shapes. These are a point-particle, a sphere (**Fig. 6.1**b), a rod (**Fig. 6.1**a,c), and a cylinder (**Fig. 6.1**d). The details of the construction of generic raspberry particles are given in Ref.[392]. We will only remark on several important construction differences and features of our models in the following.

The point-particle is similar to the system of Nash *et al.*[380,381] and will serve as a reference to which we compare our anisotropic particles. It should be noted that the Ahlrichs and Dünweg coupling scheme[390] does not lead to rotational motion in a quiescent LB fluid (without an external torque), because there is no rotational coupling to the vorticity of the fluid flow. Nash *et al.* have suggested a simple model to introduce such rotations, which we find to be sensitive to lattice artifacts without external flow, even when a 3-point interpolation scheme is used. We therefore prefer to introduce rotational coupling by utilising the properties of an extended raspberry model, which is known to accurately reproduce the desired rotational coupling[391–393].

We chose an axisymmetric distribution of 269 coupling points for the sphere raspberry with two concentric shells to introduce internal coupling points. The shells contain 134 points each, split up over 12 semi-circles with 11 equidistantly spread points and 2 points at the pole; the central bead makes for 269. This is different from the construction recipe provided in Ref.[392], where a random distribution of coupling points was used. We favored an axisymmetric distribution here, since the swimmer has a preferred direction, namely its direction of motion. An asymmetric (random) distribution leads to undesirable deviations from rectilinear motion in the absence of external torques.

The rod and cylinder raspberry models simulate oblong particles. The rod is built up of 9 coupling points spaced 0.5σ apart over a line, with σ the LB grid spacing (σ is also the MD unit length). The cylinder consists of 161 coupling points spread over 23 groups of hexagonal disks (7 particles with distance σ), stacked alternatingly with a separation of 0.5σ along the axis. The rod is a simplified version of the cylinder, because the rod cannot experience fluid-flow induced rotation about its short axis in the standard coupling scheme for the same

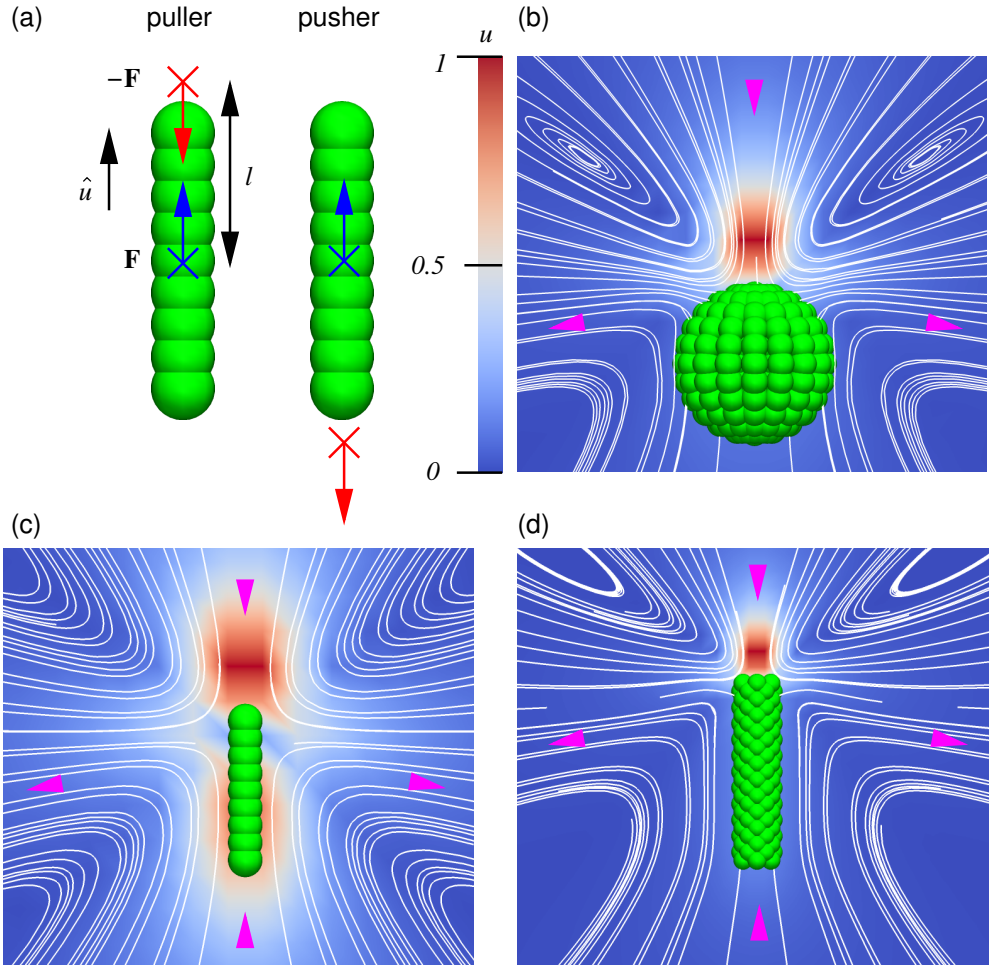

Figure 6.1: The construction of raspberry swimmers. (a) A sketch of the construction of pusher and puller raspberry swimmers, in this case rods. The viscous coupling leads to an effective hydrodynamic radius, as indicated by the use of green spheres with a radius comparable to the effective one ($\sim 0.5\sigma$). A force $\boldsymbol{F}$ (blue arrow) is applied to the central bead (blue cross) in the direction of the symmetry axis $\boldsymbol{p}_\mathrm{s}$ (black arrow). A counter force $-\boldsymbol{F}$ (red arrow) is applied to the fluid at a point $l\boldsymbol{p}_\mathrm{s}$ (red cross), with l the dipole length. For $l > 0$ the particle is a puller and for $l < 0$ it is a pusher. (c-d) The flow field around puller raspberry swimmers. The normalised magnitude of the flow velocity in the lab frame is indicated by the coloring (red $\max|\boldsymbol{u}(\boldsymbol{r})| = 1$, dark blue $|\boldsymbol{u}(\boldsymbol{r})| = 0$) in a plane through the symmetry axis that is parallel to one of the box faces; only a part of the box is shown. The location of the counter-force point is clearly visible as a red region. The white curves are stream lines to the flow field and the magenta arrow heads indicate the direction of flow. We show three of our models: (b) the rod, (c) the sphere, and (d) the cylinder.

reasons that the point particle cannot rotate[390]. Moreover, the hydrodynamic coupling of the rod is substantially reduced with respect to that of the cylinder, such that the quality of the cylindrical surface that it approximates is limited, due to the low coupling-point density[392]. Finally, it should be noted that the cylinder model has been constructed to be approximately axisymmetric about the direction of motion. Technically the symmetry group is discrete, C_n for an given n, but if n is large enough it will approximate axisymmetry with good accuracy.

All particles are made into swimmers by assigning a unit (direction) vector $\hat{u} = \boldsymbol{p}_\mathrm{s}$ to the particle, along its symmetry axis and originating from its center of mass (CM), see **Fig. 6.1**a. This $\boldsymbol{p}_\mathrm{s}$ is updated according to the particle's orientation and its position (it co-moves). We apply a force $\boldsymbol{F}$ to the CM in the direction of $\boldsymbol{p}_\mathrm{s}$ ($\boldsymbol{F} = F\boldsymbol{p}_\mathrm{s}$) to cause the raspberry particle to move. We follow the approach of Nash *et al.* and apply a counter force $-\boldsymbol{F}$ to the fluid at a position $l\boldsymbol{p}_\mathrm{s}$, with l the dipole length that can be positive or negative, see **Fig. 6.1**a. Thereby, the swimmer reaches a terminal (swimming) velocity U and its flow field is force free. For positive values of l the swimmer is a puller and for negative values it is a pusher, see **Fig. 6.1**a. Our choice of the force coupling causes the dipole moment to be off center with respect to the CM. For the swimmer to obtain a reasonable U, we require $l > \sigma$.

6.2.3 Simulation Parameters

We used a graphics processing unit (GPU) based LB solver,[397] that is attached to the MD software ESPResSo[398,399]. The GPU variant of LB implemented in ESPResSo utilises a D3Q19 lattice and a fluctuating multi-relaxation time (MRT) collision operator[400]. All of our simulations were performed in a quiescent (unthermalised) a LB fluid with periodic boundary conditions. We employed the LB viscous coupling of Ref.[390], with a 3-point interpolation stencil[396]. We found the 2-point interpolation to give rise to lattice artifacts, *e.g.*, oscillations in U of over 20% for the point particle.

Here, we employ the same LB parameters as in Refs.[392,393], since these lead to faithful reproduction of the Stokesian mobility tensor – both in bulk and under confinement. We set the fluid density to $\rho = 1.0 m_0 \sigma^{-3}$, the lattice spacing to 1.0σ, the time step to $\Delta t = 0.005\tau$ (τ is the MD time unit), the (kinematic) viscosity to $\nu = 1.0\sigma^2\tau^{-1}$, and the bare particle-fluid friction to $\zeta_0 = 25 m_0 \tau^{-1}$, with m_0 the MD mass unit. We refer the reader to Ref.[392] for a detailed description of the dimensionless numbers that specify the fluid properties to which these choices correspond.

shape	R/σ	H/σ	M/m_0	$I_\parallel$	$I_\perp$	R_h/σ	H_h/σ
point	-	-	4.8	4.8	4.8	0.56	-
sphere	2.5	-	66.	160	160	3.1	-
rod	-	2.0	7.1	1.5	17	0.87	2.9
cylinder	1.0	5.5	85.	95.	1100	1.6	6.1

Table 6.1: List of the properties of our raspberry swimmers. From left to right, the particle shape, the imposed radius R and half length H, the mass of the particle M, the moment of inertia parallel to the axis of symmetry $I_\parallel$ (with unit $m_0\sigma^2$), the moment perpendicular to this axis $I_\perp$ (with unit $m_0\sigma^2$), and the measured effective hydrodynamic radius R_h and half length H_h. We used the MD units σ (unit length) and m_0 (unit mass) to non-dimensionalise our parameters.

On the MD level, the raspberry particles are allowed to freely move and rotate, unless otherwise specified. All the forces acting on the MD beads are transferred to the central bead *via* the virtual sites (rigid bonds). To stabilise the simulation for the bare friction coefficients used, we set the (bare) mass and rotational inertia of the raspberry; these quantities should not be confused with the virtual mass of the body in a fluid, see, *e.g.*, Ref.[401] for the definition. The mass and rotational inertia tensor are based on the particle's dimensions and the fluid mass density, and must be chosen reasonably to ensure the stability of the algorithm. The values of the imposed physical quantities are listed in **Table 6.1**.

6.2.4 Raspberry Characterisation

We employed the methods of Refs.[392,393] to characterise the hydrodynamic properties of the raspberry particles. For the point and sphere swimmer, the methods of Refs.[392,393] could be applied directly to determine the effective hydrodynamic radius R_h. For the rod and cylinder swimmer, we used the formalism developed in Ref.[392] for a dumbbell. The theoretical expressions for the hydrodynamic mobility tensor (HMT) of a cylinder segment[402] were used to extract the effective hydrodynamic radius R_h and half length H_h of the rod and cylinder.

There are two fit parameters for a rod-shaped particle (R_h and H_h) that can be extracted from the measurements, to which the extrapolated bulk HMT must be fit. In order to determine these two parameters simultaneously, we minimised the following functional

$$f(H,R) = \big((\mu_\parallel^m - \mu_\parallel(H,R))^2 + (\mu_\perp^m - \mu_\perp(H,R))^2 + (\mu_r^m - \mu_r(H,R))^2\big), \tag{6.1}$$

where the superscript 'm' signifies the measured quantity, $\mu_{\parallel}$ is the translational mobility parallel to the symmetry axis, $\mu_{\perp}$ the translational mobility perpendicular to this axis, and μ_r the mobility associated with reorientation of the symmetry axis. To minimise internal inconsistency we use a single fit parameter for both $H_h = H + \Delta$ and $R_h = R + \Delta$. That is, we minimise $f(H + \Delta, R + \Delta)$, with H and R the imposed half-length and radius. This also ensures a well-definedness of the result for $R = 0$ (the rod), since we have $\Delta > 0$ which eliminates the divergences in the logarithmic terms of Ref.[402]. The value of Δ found for the rod is then its effective hydrodynamic radius and should be comparable to the effective radius of a point. This is indeed the case, as can be inferred from the measured parameters listed in **Table 6.1**.

6.2.5 Moment Characterisation

The hydrodynamic properties of the raspberry swimmers are assessed by placing a single swimmer in the center of a cubic box with side length $L = 150\sigma$ and periodic boundary conditions, that is centered on the origin and axis aligned. This length L is a trade-off between simulation speed and minimisation of periodicity effects. We let the swimmer move along the z-axis in the positive direction and allow a steady-state flow field to set in and take a snapshot, see **Fig. 6.1**b-d. We determine the distance d travelled by the swimmer and we shift the measured flow field by this distance, such that the swimmer's CM is located in the origin.

The flow fields display a clear hydrodynamic dipole. The near-field curvature of the flow-lines is due to the finite separation of the force and counter-force point. Note that the flow lines mostly pass around the extended raspberries (sphere and cylinder), indicating that the viscous coupling indeed causes a hydrodynamic hull to form around the raspberry. Those that pass through the object are mostly due to the result being shown in the laboratory frame, although the extended raspberries can have a slight porosity[392]. It is the flow around the object, coupled to the shape-anisotropy, that is responsible for the presence of higher-order moments in the swimmer's flow field. Finally, far away from the swimmer (not visible on the scale of **Fig. 6.1**b-d) the flow lines are closed due to the periodic boundary conditions.

The flow field is Legendre-Fourier (LF) decomposed into modes to determine these hydrodynamic moments. First, we transform the fluid velocity field $\boldsymbol{u}(\boldsymbol{r})$ from Cartesian coordinates to spherical polar coordinates, with ϕ the azimuthal and θ the polar angle. The

azimuthal $\hat{\phi}$ component is zero due to symmetry and can be ignored, leaving the radial $\hat{r}$ and polar (tangential) $\hat{\theta}$ components. This flow field is then cylindrically averaged around the z-axis to arrive at expressions of the form $u_r(r,\theta)$ and $u_\theta(r,\theta)$ for the radial and tangential components of the flow field, respectively. Finally, we project out the θ dependence using LF decomposition

$$u_{x,n}(r) = \frac{2n+1}{2}\int_0^\pi \sin(\theta) L_n(\cos(\theta)) u_x(r,\theta)\mathrm{d}\theta, \tag{6.2}$$

with n the index of the mode, L_n the Legendre polynomial of order n, and $x = r$ or $x = \theta$ depending on the component. For the series of mode functions $u_{r,n}(r)$ and $u_{\theta,n}(r)$, we fit the long-range decay using a power-law, see, *e.g.*, **Fig. 6.2**. Note that for u_θ it might be more convenient to perform the decomposition using the associated Legendre polynomials, but either method works.

We compare the power-law decay obtained in our modes to the expected decay of the monopole (S, Stokeslet), dipole (D), source-doublet (SD), quadrupole (Q), octupole (O), and source-octupole (SO) moments. We found that there are no monopole and source terms[1] ($\boldsymbol{u}^{\mathrm{S}}$, $\boldsymbol{u}^{\mathrm{SD}}$, and $\boldsymbol{u}^{\mathrm{SO}} = \boldsymbol{0}$). Thus the expressions for the flow fields generated by a swimmer that is centered at the origin and pointing along the $\hat{z}$ direction are given by a sum of

$$\boldsymbol{u}^{\mathrm{D}}(r,\theta) = \frac{A}{r^2}\left(\frac{1+3\cos(2\theta)}{2}, 0\right); \tag{6.3}$$

$$\boldsymbol{u}^{\mathrm{Q}}(r,\theta) = \frac{B}{r^3}\left(-\frac{\cos(\theta)+3\cos(3\theta)}{2}, \frac{\sin(\theta)-3\sin(3\theta)}{8}\right); \tag{6.4}$$

$$\boldsymbol{u}^{\mathrm{O}}(r,\theta) = \frac{C}{r^4}\left(\frac{3+4\cos(2\theta)+25\cos(4\theta)}{16}, \frac{-2\sin(2\theta)+5\sin(4\theta)}{8}\right), \tag{6.5}$$

up to fourth order. Here, the coefficients A, B, and C give the strength and we list the components $\hat{r}$ (first entry) and $\hat{\theta}$ (second entry). When the first four hydrodynamic moments are LF decomposed, we obtain a series of power-law decays.

Table 6.2 shows the mode decomposition and the following observations can be made. (i) Every moment has a 'unique' power-law decay: $\boldsymbol{u}^{\mathrm{S}}$ r^{-1}, $\boldsymbol{u}^{\mathrm{D}}$ r^{-2}, $\boldsymbol{u}^{\mathrm{Q}}$ r^{-3}, $\boldsymbol{u}^{\mathrm{O}}$ r^{-4}, *etc.*; provided that the source terms can be ignored. (ii) It is sufficient to consider $u_{\theta,0}$ and check for r^{-1} decay to determine if the system is force free. (iii) The dipole is the only moment that

[1]The absence of source terms is specific to the LB force/counter-force raspberry swimmer. That is, there are no sources or sinks of the LB fluid. However, other models such as the squirmer[98,99] can have source-dipole contributions that must be considered in fitting the data.

name		$\boldsymbol{u}^{\mathrm{S}}$	$\boldsymbol{u}^{\mathrm{D}}$	$\boldsymbol{u}^{\mathrm{SD}}$	$\boldsymbol{u}^{\mathrm{Q}}$	$\boldsymbol{u}^{\mathrm{O}}$	$\boldsymbol{u}^{\mathrm{SO}}$
decay		r^{-1}	r^{-2}	r^{-3}	r^{-3}	r^{-4}	r^{-4}
n	comp	pref	pref	pref	pref	pref	pref
0	$\hat{r}$	0	0	0	0	0	0
	$\hat{\theta}$	$-\pi/2^2$	0	$\pi/2^2$	$\pi/2^5$	0	0
1	$\hat{r}$	2	0	2	2/5	0	0
	$\hat{\theta}$	0	0	0	0	$-3\pi/2^5$	$-3\pi/2^3$
2	$\hat{r}$	0	2	0	0	$-6/7$	-2
	$\hat{\theta}$	$5\pi/2^5$	0	$-5\pi/2^5$	$-25\pi/2^7$	0	0
3	$\hat{r}$	0	0	0	$-12/5$	0	0
	$\hat{\theta}$	0	0	0	0	$203\pi/2^9$	$7\pi/2^5$
4	$\hat{r}$	0	0	0	0	20/7	0
	$\hat{\theta}$	$9\pi/2^8$	0	$-9\pi/2^8$	$387\pi/2^{12}$	0	0

Table 6.2: The Legendre-Fourier (LF) mode decomposition of the first hydrodynamic moments for a swimmer that can have an arbitrarily complex flow field. The first row lists the moments: monopole (S, Stokeslet), dipole (D, Stresslet), source-dipole (SD), quadrupole (Q), octupole (O), and source-octupole (SO). The second row provides the decay. The third row labels the content of the rest of the table, from left to right: the mode, the radial/tangential component, and the prefactors. We only specify modes up to $n = 4$ here. The table is used to determine a specific LF mode by combining the prefactor with the decay and relevant strength coefficient. For example, the 2nd mode of the tangential component of the quadrupole is given by $u^{\mathrm{qu}}_{\theta,2}(r) = -25\pi B/(2^7 r^3)$, where B is the quadrupole coefficient.

has exactly one nonzero entry in its LF spectrum. Thus A can be extracted by fitting r^{-2} to the $u_{r,2}$ mode. (iv) For the quadrupole moment, the $u_{r,3}$ mode is ideally suited to determine the factor B, as there is no $n = 3$ component to the source-dipole. (v) If we subtract the measured quadrupole moment from the $u_{\theta,2}$ mode then we find no remaining r^{-3} decay, proving the absence of the source dipole moment. (vi) The strength B of the quadruple moment can be double checked by using any of the other nonzero entries, provided that the source-dipole term can be excluded. (v) Finally, a similar approach can be followed to establish the value of C for the octupole moment (by fitting r^{-4} to $u_{r,4}$) and the higher-order moments.

It should be noted that there are short-ranged monopolar signatures, because point forces are used in the raspberry force/counter-force scheme. However, there is no long-range ($r \gg \max(H, R)$) decay that is proportional to r^{-1}. In fact, all the decays must be measured sufficiently far away from the swimmer, as the 3-point interpolation and finite size of the object will significantly modify the near-field shape of the decay, as we will see. Another source of error, when fitting, is the periodicity of the LB simulation domain. Care must be taken to only use the decay sufficiently far from the edge of the periodic simulation box. In

practice, this limits the regime over which the decay can be fitted but these limitations are apparent from the data.

Finally, it is possible to use the LF mode decomposition to extract moments in other swimmer bases. We have used this method to extract a series of coefficients for the squirmer model[98,99]. The result is a set of coefficients that is analogous to the above moment decomposition and may be used to map our models onto LB simulations of squirmers – we do not provide these coefficients here. Interestingly, the near-field correspondence between the raspberry flow field and that of the matched squirmer is not substantially improved, even for a spherical particle. We attribute this to the difference in method of achieving self-propulsion. That is, squirmers have a predefined surface slip velocity, which inadequately captures the presence of the counter-force point in the near field.

6.2.6 Tracer Displacement Matching

We confirmed that our LF decomposition gives reasonable values for the strength of the dipole moment, by considering the displacement of a tracer particle in the flow field of the swimmer. Again, we performed our simulations in a cubic box with edge length $L = 150\sigma$, with periodic boundary conditions. The swimmer is initially positioned at $(0, 0, -L/2)$ pointing in the $\hat{z}$ direction, and the tracer is placed at $(15\sigma, 0, 0)$. The minimum swimmer-tracer separation of 15σ gives reasonable results that are not too strongly affected by periodicity. As the swimmer moves from one edge of the box to the other, the tracer is advected (displaced) by the swimmer's flow field. A sketch of this situation is provided in **Fig. 6.3**.

The expression for the dipole moment can be used to numerically solve for the trajectory of a tracer using the form

$$\frac{\partial \boldsymbol{r}_\mathrm{t}}{\partial t} = \boldsymbol{u}^\mathrm{D}(\boldsymbol{r}_\mathrm{t} - \boldsymbol{r}_\mathrm{s}), \tag{6.6}$$

where $\boldsymbol{r}_\mathrm{t}$ is the position of the tracer, $\boldsymbol{r}_\mathrm{s}$ the position of the swimmer, and $\boldsymbol{u}^\mathrm{D}$ the dipole flow field generated by the tracer (see **Eq. 2.2**). Since the trajectory of the swimmer is a straight line and it moves at a constant speed, **Eq. 6.6** becomes a differential equation in terms of the tracer position only, which can be numerically evaluated. The theoretically predicted trajectory can then be fitted to the trajectory observed in the LB simulations for strength of the dipole moment, which we denote by A^* to differentiate it from the value obtained from

the mode decomposition.

The trajectory of the tracer has a characteristic concave triangular shape (see **Fig. 2.3**); an example is shown in **Fig. 6.3** for a puller. This shape is formed as follows (in the case of a puller). First, the tracer is pulled towards the swimmer, as the tracer is in front of the swimmer (i in **Fig. 6.3**). Then the tracer is pushed away from the swimmer, when it is alongside the swimmer (ii). Finally, when the swimmer moves away from the tracer, the tracer is again pulled towards the swimmer (iii). Here, we have accounted for the effects of periodic boundary conditions on the displacement trajectories, which are minor.

6.3 Results

In this section we present our results. We first discuss the reasons for choosing specific values for the force/counter-force point separation l. This is followed by an analysis of our LF-mode decomposition applied to the raspberry particles that we constructed. Finally, we provide results for the displacement experiment that we performed to verify our mode decomposition.

6.3.1 Swimming Speed and the Counter-Force Point

We first measured the hydrodynamic mobility of our particles to determine their shape and size using the procedures outlined in §**6.2.4**, see **Table 6.1**. Please refer to Refs.[391,392] for additional details on the way in which the effective size and shape of the raspberry particles can be established. Using our fitted shape parameters, the mass and rotational inertia can be determined using the standard expressions for cylindrical and spherical objects, assuming a mass density that is the same of that of the fluid, see **Table 6.1**. This ensures the stability of the simulation[392]. To verify that our anisotropic distribution of coupling points did not give the sphere an anisotropic hydrodynamic mobility tensor, we measured the sphere's mobility around different axes. We found the mobility to be isotropic to within an acceptable tolerance: all measurements gave mobilities that differed by at most 2%.

We varied the dipole lengths and force values to study their impact on the velocity and dipole strength. Provided the counter-force point is sufficiently far from the swimmer, one would expect the velocity of the swimmer to be dominated by the force applied to it directly and its hydrodynamic mobility, with the counter-force point having almost no effect. However, when the counter-force point is close to the swimmer, it starts to influence the measured

shape ×	l/σ 1	F 1	U 10^{-3}	U_{pr} 10^{-3}	A 10^{-2}	A^* 10^{-2}	B 10^{-2}	C 1
point	1.0 −1.0	0.37	20. 20.	35.	−1.4 1.4	−1.4 1.4	N/A N/A	N/A N/A
sphere	3.5 −3.5	3.8	3.5 3.3	67.	−10. 10.	−10. 10.	N/A N/A	−3.1 3.1
rod	2.7 −2.7	0.21	2.5 2.5	3.4	−1.3 1.3	−1.4 1.4	3.7 3.7	−0.11 0.11
cylinder	6.5 −6.5	0.60	0.99 1.0	4.8	−2.7 2.7	−3.2 3.2	23. 23.	−2.1 2.1

Table 6.3: The imposed and measured properties of our LB raspberry swimmers. The table provides the shape, the position l at which the counter force is applied (positive for a puller and negative for a pusher), the force F in units of $m_0\sigma/\tau^2$, the measured velocity U of the swimmer in units of (σ/τ), the velocity U_{pr} in units of (σ/τ) that is predicted on the basis of force and mobility, the dipole strength A from the LF decomposition in units of (σ^3/τ), the dipole strength A^* as measured in the displacement experiment, and B and C the quadrupole and octupole strength from the LF decomposition in units of $(\sigma^4/\tau$ and $\sigma^5/\tau)$, respectively. The entries N/A indicate that a certain moment was not found.

velocity. In all cases, the velocity decreases with respect to that of a swimmer where the counter force is applied far away. When the counter-force point is too close, the effective swimming speed is negligible. This is also partially due to the 3-point interpolation applying the counter-force directly inside the volume occupied by the raspberry particle. Fortunately, when the counter-force is applied more than 1 grid spacing away from the closest coupling point, we found that the velocity U of the swimmer is dominated by the mobility $\mu_{\parallel}$ and the value of F, i.e., $U = \mu_{\parallel}F$, and reasonable swimming speeds can be obtained. **Table 6.3** provides the swimming parameters (specifically the value of l) that we used for the remainder of our investigation. Our choice is based on a trade-off between stability and speed of the swimmer (or equivalently, overall run time of the simulation).

The values of the measured and predicted speed ($U_{\mathrm{pr}} = \mu_{\parallel}F$) in **Table 6.3** illustrate the speed reduction due to the counter-force being applied relatively close to the swimmer. For a sphere the effect is most pronounced, since we have $U_{\mathrm{pr}} = F/(6\pi\eta R_h) \approx 6.7\ 10^{-2}\ \sigma/\tau$, where R_h is the effective hydrodynamic radius (as discussed in §6.2), and we observe $U = 3.5\ 10^{-3}\ \sigma/\tau$. For the point, rod, and cylinder, on the other hand, U_{pr} is comparable to U, as these shapes experience less of an effect of the counter force. Also note that there can be a measurable difference between the speed of a pusher and a puller for the same raspberry particle, see the sphere entry in **Table 6.3**. This difference is caused by the asymmetry in the way the forces are applied for the two types of swimming, as shown in **Fig. 6.1**a, and

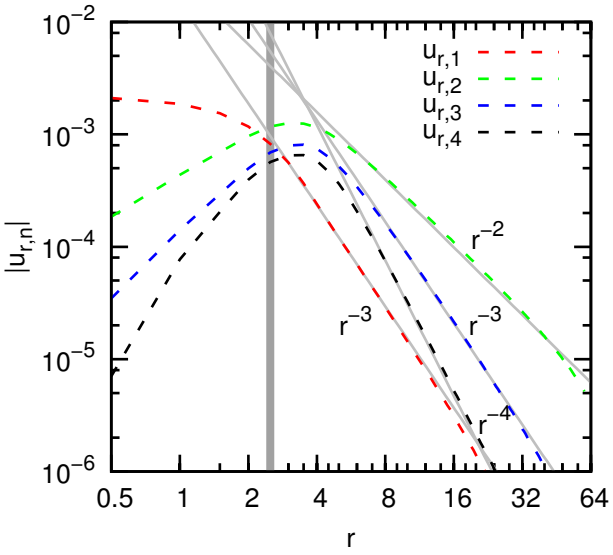

Figure 6.2: Legendre-Fourier mode decomposition of the flow field around a puller-type rod-shaped raspberry swimmer. Log-log plot of the first four radial modes obtained by our averaging and decomposition procedure: $u_{r,1}$ (red), $u_{r,2}$ (green), $u_{r,3}$ (blue), and $u_{r,4}$ (black). The dashed curves show the LB data, while the gray curves show the power-law fits to this data. The thick gray vertical line indicates $r = l$.

is most strongly revealed for the simulations where the counter-force point is close to the swimmer. Finally, it should be pointed out that we averaged U over several periods of the oscillations resulting from the lattice interpolation, see Ref.[392] for a discussion. The deviation from this average was found to be limited to less than 5%.

6.3.2 The Legendre-Fourier Decomposition

Fig. 6.2 shows a representative example of the LF decomposition of the flow fields for the specific case of the rod-shaped puller. There are several points of interest. (i) The long-range decay of each mode follows a power law. These decays are fitted using r^{-2}, r^{-3}, and r^{-4}, respectively, showing that the flow field can be well approximated by a dipole, quadrupole, and octupole moment, to fourth order. (ii) For $u_{r,1}$ **Table 6.2** predicts a sum of r^{-n} terms, with $n = 1, 3$. However, there is clearly no r^{-1} term, signifying that there is no long-range monopole moment, and the remaining decay is well captured using the r^{-3} term only. (iii) Deviations far from the particle can be attributed to the periodicity of the simulation domain, but are limited, as can be seen. (iv) The small r deviations from the expected power laws mark the onset of the near-field region in the immediate vicinity of the swimmers. For $r < l$, as indicated using the thick dark-gray line in **Fig. 6.2**, the projection onto LF modes

integrates over parts of the fluid where the particle is present. For $r \approx l$ the maximum is achieved, due to the counter-force point being included in the projection. (v) As explained in §**6.2.5** the $u_{r,1}$ and $u_{r,3}$ curves can be fitted to determine the value of B independently. (vi) The value of C was extracted from $u_{r,4}$ and verified against other modes that decay as r^{-4}. **Table 6.3** lists the moments that were obtained using the decomposition. The error on the fit is very small, but there are numerous sources of systematic error (interpolation, averaging, etc.). From our analysis, we consider an estimated 15% error to be justified, which we arrive at by considering the value obtained for the various modes.

We found quadrupole moments for both the rod and the cylinder using our LF decomposition. For the point swimmer, there was no sign of a quadrupole moment, since the viscous coupling and application of the counter force lead to a symmetric (albeit off-center from the bead) force configuration. Surprisingly, for the sphere we could not establish a quadrupole moment. The extent of the sphere, coupled with the off-center force/counter-force scheme that we used, should result in a quadrupole moment. However, it is likely that it was too small to be measured, despite the application of high forces for this swimmer. This leads us to conclude that the shape anisotropy of the rod and cylinder is the primary reason behind the large quadrupole moment. Spagnolie and Lauga[238] relate the appearance of the quadrupole moment to a length asymmetry between the body and flagellum in a mechanically propelled swimmer. This interpretation lends itself to our data, as the shape anisotropic particle applies force to the fluid over a much greater length than the counter-force point does. However, Spagnolie and Lauga also claim that the size of the body induces a source dipole, which we do not observe in our results. Finally, we found an octupole moment for all particles, save the point swimmer (as expected). This implies that our model swimmers can be described by a series of force multipoles only, rather than a combination of force and source multipoles.

6.3.3 Tracer Displacement by a Raspberry Swimmer

To verify our mode decomposition and demonstrate the utility of the raspberry-swimmer model, we considered the displacement of a tracer particle in the fluid flow field generated by a swimmer, as explained in §**6.2.6**. **Fig. 6.3** shows a representative example of such an displacement curve, in this case for the rod-shaped puller with a fitted coefficient A^*. The value of A^* could be fitted with an estimated error of 15%, due to the asymmetry in the curve. The curve is far less sensitive to the value of the quadrupole and octupole moment,

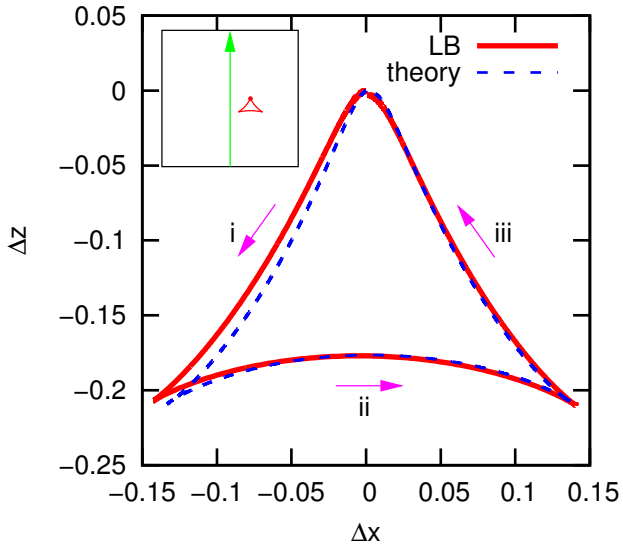

Figure 6.3: Displacement curve for a tracer in the flow field of a rod-shaped raspberry swimmer. The parameters Δx and Δz show the amount of deviation from the tracer's original position as the swimmer, in this case a puller, moves through the box. The red curve shows the result of our LB simulations, while the blue dashed curve shows the fitted theoretical result. The numbers and magenta arrows indicate the way in which this curve is traversed by the tracer. The inset shows a sketch of the trajectory of a puller-type swimmer (green arrow) and the displacement of the tracer (red dot) that this effects.

because of their faster decay, which made it difficult to establish these moments from the curve with any accuracy. A much smaller tracer-swimmer separation would be required to measure the quadrupole moment and an even smaller separation for the octupole moment. However, this too introduces difficulties due to the near-field deviations from the power-law decay, as shown in **Fig. 6.2**.

Retardation effects cause the deviation observed on the left-hand side of **Fig. 6.3**; part (i) of the trajectory. This is the part of the trajectory for which the swimmer moves towards the particle. However, as the swimmer starts off in a quiescent fluid, it takes a finite simulation time for the steady-state flow field to be established, which is reflected in that part of the trajectory. Nevertheless, the fact that we can reproduce far-field tracer trajectories with a high level of accuracy indicates that our method can be successfully applied to more complex situations.

6.4 Conclusion and Outlook

Summarising, we have introduced a new model to simulate anisotropic self-propelled colloids with hydrodynamic interactions utilising the lattice Boltzmann method. Our LB model is based on the raspberry-type viscous coupling method introduced in Refs.[390,391] and recently re-examined in detail in Refs.[392,393]. The raspberry particles are made to move by applying a force along a unit vector that describes their orientation. The correct force-free flow field is achieved by applying an opposing counter force to the fluid, see **Fig. 6.1**a. This force/counter-force formalism is similar to the ones introduced in Refs.[380,382,383]. However, we go beyond the level of description presented there to introduce the particle shape and size.

We verified that our raspberry swimmers model self-propelled colloids, by considering four basic shapes: a point, a sphere, a rod, and a cylinder, see **Fig. 6.1**. We discussed the creation of these swimmers, as well as the limitations of our method in detail. We introduce and carefully detail a Legendre-Fourier mode decomposition of the steady-state flow field (in bulk). This LF decomposition allowed us to determine the hydrodynamic moments of our swimmers, by fitting the mode-space decays with characteristic power-laws. The exponent of the decay for a specific mode is characteristic of a certain hydrodynamic moment. Using this formalism, we found that there is no monopole moment, as physically required for a force-free swimmer. The strengths for the series of higher-order moments were determined up to the octupole term. Our LF decomposition formalism is sufficiently generic to be applied to other swimmer bases as well and, for example, can be used to obtain the coefficient list for a squirmer.

To validate our LF decomposition result, as well as providing a proof-of-concept application of our simulation method, we considered the displacement of a tracer particle in the flow field of a passing swimmer. The displacement curve allowed us to verify the dipole moment predicted by the decomposition. The quadrupole and octupole moments could not be verified in this fashion, due to their faster decay as well as near-field discretisation artifacts. Fortunately, using the LF modes allows for internal verification of their strength. We observed that anisotropy introduces a strong quadrupole moment into the flow field surrounding the swimmer, as is expected.

The advantage of our raspberry-swimmer description over previously introduced models[380,382,383] is that we obtain the hydrodynamic mobility tensor of our swimmers directly from

the LB coupling, which ensures that the raspberry swimmers display the correct translational and rotational behaviour in flow. In addition, our raspberries have a finite extent, which leads to a more physical description of particle-particle collisions than can currently be achieved by LB sub-lattice methods[380,381]. The coupling to the LB fluid makes it difficult to accurately describe the near-field HI, which is also a limiting factor for other methods. However, our raspberry method ensures that fluid flows around the body, provided that a sufficient number of coupling points is used[392]. This allows us to capture the higher-order sub-dominant HI terms, which can be of importance for the long-range flow field.

In chapter §**7** we continue this work by considering the effect of the shape anisotropy and the quadrupole moment on the motion of self-propelled particles in confining geometries. The presence of such modes will prove crucial to the behaviour of such particles, despite their much stronger decay compared to that of the dipole moment. Further extensions of the formalism could include incorporating rotational contributions to the flow field, in a similar spirit the work of Nash *et al.*[380], as well as verification of the method for non-axisymmetric shapes. Finally, the characterisation method of LF decomposition, as described here, can be applied to determine the HI of complex swimmers, for which only numerical solutions to the flow field exist. We therefore expect that raspberry swimmers and the methods developed in this chapter will open the way for new directions in the study of active anisotropic particles.

CHAPTER 7

Understanding the Onset of Oscillatory Swimming in Micro-channels

> "The instruction we find in books is like fire. We fetch it from our neighbours, kindle it at home, communicate it to others, and it becomes the property of all."
>
> Voltaire (1694–1778)

7.1 Introduction

We extend the Raspberry model swimmer of chapter §6 by including boundaries, as the locomotion of self-propelled particles typically occurs under confinement. Accurately describing the effect of confinement on swimmers is of significant interest to understanding the behaviour of micro-organisms and artificial micro-robots. In modelling these systems, hydrodynamic interactions (HIs) are often ignored, which is a valid approximation in some cases, such as when microbial swimmers' run-and-tumble dynamics dominate (see §5). However, HIs can play an important role, e.g., see Refs.[205,253,362,403,404], and therefore cannot be *a priori* ignored in modelling. Recent experiments on self-phoretic colloidal swimmers have shown that their orientation is strongly influenced by HIs due to the presence of a wall[405]. However, there is ongoing debate on the importance of near-wall effects and the level at which to truncate the hydrodynamic moment expansion[238].

A specific example of this are the helical and oscillatory trajectories of single swimmers in confining geometries as observed experimentally by Jana *et al.*[403] and in simulations[221,389,406].

Such oscillatory trajectories appear to be common place, having been reproduced by many models, and independent of specific swimmer type. However, a physical understanding of these oscillations remains wanting. It is indisputable that the oscillations do not arise simply from the lowest order hydrodynamics, which result in direct attraction to surfaces[246], while the inclusion of higher-order modes can lead to more complex behaviour[238,407]. Although observed in confined quiescent fluids, these oscillatory trajectories are reminiscent of those observed in the rheotaxis of swimmers subjected to external flows[214], which result primarily from the interplay between the flow and persistent particle motion due to self-propulsion. Zöttl and Stark[219,239] indicate that near-field lubrication theory can be used when there is no externally applied flow to describe such trajectories. Yet, the observations of Zhu *et al.* demonstrate that oscillatory trajectories arise in a channel that is three times as wide as the self-propelled particle. Additionally, the trajectories of squirmers close to single walls in quiescent fluid show oscillations[216], which have been explained by the competition between far-field HIs and short-ranged wall-swimmer potentials[217]. Thus, there is a clear need to establish to what extent the observation of oscillatory trajectories in systems with confinement originate from a near- or far-field effect and, in conjunction, to assess the importance of higher-order hydrodynamic modes.

In this chapter, we demonstrate that the onset of time-varying oscillatory trajectories in systems confined within a channel and without external flow can be well-understood using far-field theory, as discussed in §4. We investigate the specific case of two parallel infinite plates that enclose the fluid and a single rod-shaped swimmer, using our lattice-Boltzmann (LB) 'raspberry' force/counter-force formalism (see §6 and **Fig. 7.1**; insets). We have previously shown that the rod-shaped LB swimmers have well-defined higher-order hydrodynamic moments; see **Table 7.1** for representations of the first five moments. These simulations conclusively show that a puller-type rod that starts far from the wall but off-centre follows a damped oscillatory trajectory towards the middle of the channel, whereas a pusher-type rod moves between the walls along a sinusoidal path with increasing amplitude. Surprisingly, the oscillations are observable even for plate separations as great as ten times the length of the rod. We explain these observations within the framework of our far-field hydrodynamic theory: the dipole and octupole moments induce hydrodynamic forces towards the centre (puller) or towards the walls (pusher), while the quadrupole moment causes pure oscillatory motion. The oscillatory trajectories within plate confinement thus provides an

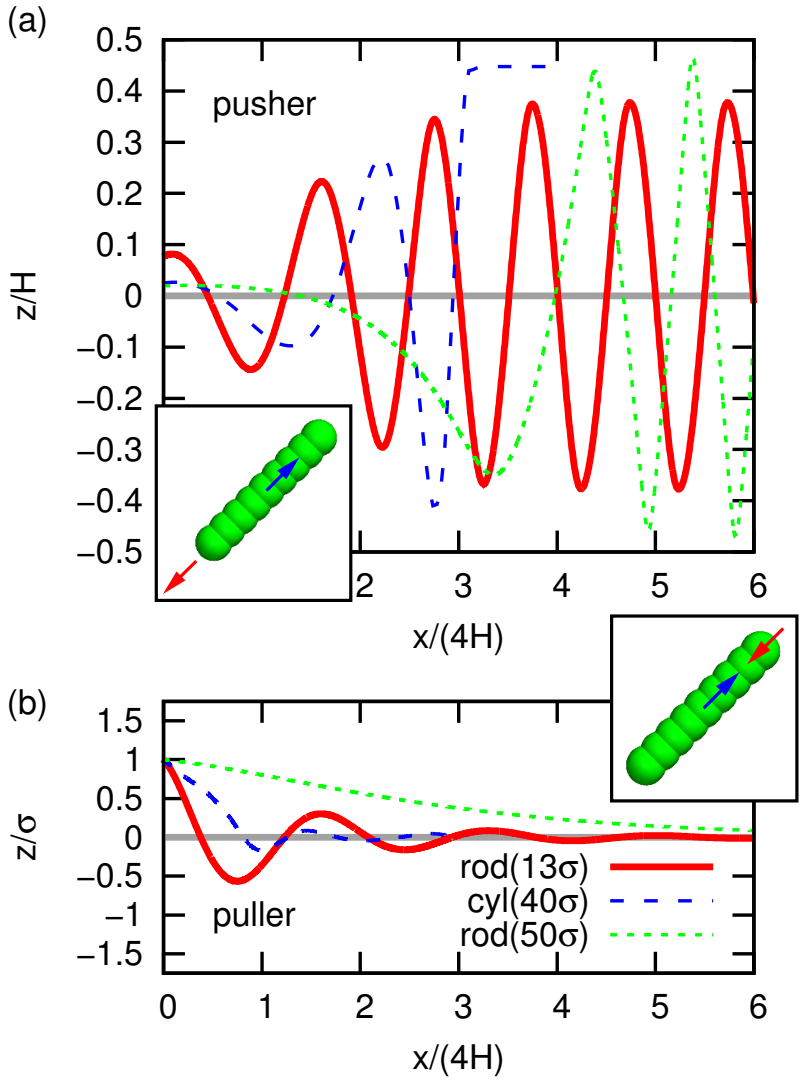

Figure 7.1: The trajectory of swimmers between two parallel plates with separation H. The horizontal displacement x and vertical position z are given for a swimmer that is initially oriented parallel to the walls and at $z = 1\sigma$, with σ the MD unit of length (LB lattice size) and $z = 0$ the centre of the channel. (a) The results for pushers: rod for $H = 13\sigma$ (red, solid), cylinder for $H = 40\sigma$ (blue, dashed), and rod for $H = 50\sigma$ (green, dots). The inset shows a schematic representation of the raspberry rod-swimmer (scaled for $H = 13\sigma$), the force is indicated in red and counter force in blue. (b) The results for pullers, otherwise the systems are the same. The ESI contains a companion figure showing the evolution of the angle ϕ for these swimmers.

indirect means to characterise the hydrodynamic properties of swimmers, which would grant access to moments beyond those that can be obtained from lattice swimming[408] or tracer paths (see §6). This chapter is accompanied by an Electronic Supplementary Information (ESI) file at URL[409].

7.2 LB simulations

We consider two raspberry swimmers (rod and cylinder) to study the movement of shape-anisotropic swimmers under confinement using the ESPResSo LB implementation (see insets in **Fig. 7.1** and model details in §6). These raspberry particles are placed in a fluid between two parallel (no-slip) bounce-back plates, with normals in the $\hat{\boldsymbol{e}}_z$ direction, separated by a distance H. The fluid domain is periodic in the other two (xy) directions. The vertical position of the swimmer's centre of mass (CM) is indicated using $z \in [-H/2, H/2]$, with $z = 0$ the middle of the channel. Lateral displacement is given by x and measured from the swimmer's initial position ($x = 0$) — our trajectories are straight in the xz-plane. Finally, the angle of the swimmer's director $\boldsymbol{p}_s$ with the plate normal $\hat{\boldsymbol{e}}_z$ is given by $\phi \in [-\pi/2, \pi/2]$, with $\phi = 0$ swimming parallel to the plates. To prevent the swimmers from penetrating the wall, a short-ranged (almost hard) Weeks-Chandler-Anderson (WCA) interaction is imposed between the raspberry swimmers and the walls (ESI). This wall-swimmer interaction is necessary as our LB algorithm does not explicitly account for near-wall lubrication corrections[392]. All of the results shown in the main text employ a WCA diameter $d = \sigma$, with σ the LB lattice spacing. We limit the swimming speed to ensure the low Reynolds number regime, $Re < 0.01$.

Fig. 7.1 and the supplemental movies (ESI) demonstrate the onset of oscillatory trajectories. These are representative sample swimmer trajectories, where the swimmers start off-centre and oriented parallel to the plates. Both the rod and cylinder models of pushers and pullers display time-varying oscillatory behaviour. In the specific case of our rods, the wavelength of the oscillations is $\lambda \approx 4H$. All pushers move towards the wall and the pullers move towards the centre of the plates. After only a few periods, the pullers move along the centre line of the channel whereas pushers arrive in the near-wall region, where swimmer-specific details and lubrication corrections are required to accurately predict dynamics. Oscillations are observed for all cylinder and rod swimmers in plate separations that we could simulate ($5\sigma \leq H \leq 50\sigma$). The rod is $\sim 5\sigma$ in length, thus the oscillatory trajectories arise in systems with a channel height to particle size ratio up to at least 10.

To verify the generality of the initial oscillations, we considered several initial positions z and orientations ϕ for rod pusher and puller swimmers. We found that depending on the type of swimmer and its initial position/orientation, several oscillations in the physical regime can be observed, before near-wall effects cannot be ignored. We further showed that oscillations

	Rod		Cylinder	
⇓ Coefficient	LB	theory	LB	Theory
κ	± 0.013	± 0.0153	± 0.027	± 0.0312
ν	0.038	0.0294	0.21	0.194
μ	0.0	0.0	0.0	0.0
o_1	0.0	0.0	0.0	0.0
o_2	± 0.113	± 0.1256	± 2.11	± 2.176
v_s	0.0025	0.0025	0.0010	0.0010

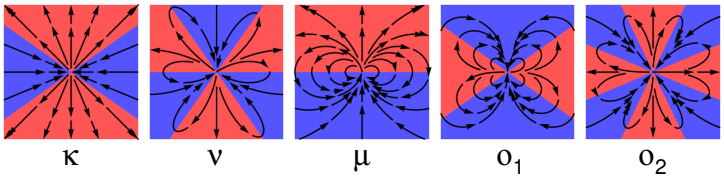

Table 7.1: Multipole moments of the swimmer-generated flow field for the two swimmer types: the rod and the cylinder. The columns labelled 'LB' provide the values measured in Chapter §**6** by means of Legendre-Fourier decomposition in a close-to-bulk system with periodic boundary conditions. The columns labelled 'theory' provide the moments fitted from the trajectory in our confining geometry by using the theoretical model (**Eq. 1.45**). Values are given in LB simulation units, and the positive/negative signs correspond to puller and pusher swimmers, respectively. The bottom row shows representations of the flow field of the first five hydrodynamic moments in bulk: dipole κ, quadrupole ν, source dipole μ, source octupole o_1, and octupole o_2. The arrows are stream lines and the colors indicate flow away from (red) or towards (blue) the swimmer.

for rod-like swimmers appear for a large range in rod aspect ratios (ESI). At long times the LB pusher rods display a limit cycle, whereas the pusher cylinder does not. To what extent such a limit cycle (**Fig. 7.1**a; solid red curve) or sliding dynamics (**Fig. 7.1**a; dashed blue curve) might be physical is not considered here, as algorithmic artifacts close to the walls impact the near-wall dynamics. The ESI provides a discussion of these limitations and this work does not confirm their physical nature[406]. However, our results establish that the initial oscillations before the rod comes close to the wall (a proximity of $\sim 2\sigma$) are physical. It is this onset of oscillatory trajectories that we concern ourselves with here and subject to theoretical analysis in the following.

We study the raspberry particles theoretically using our multipole swimmers (§**1.3.1**). The shapes of its multipole flows (**Eq. 1.32**) in bulk are shown in **Table 7.1**. The effect of the confining walls (two parallel no-slip plates) is accounted for by the method of images, where we truncate the approximation after four image systems on each side of the micro-channel. Subsequently, the hydrodynamic interactions with the surfaces are calculated (§**4**).

7.3 Results

To predict the swimmer dynamics of **Fig. 7.1** theoretically, we integrate the equations of motion **(1.45–1.46)**. Here, we use the same swimming speed and initial conditions as in the LB simulations, but we allow the multipole coefficients to vary about their measured values. We can thus fit the multipole coefficients via a least-squares method. To obtain the best agreement with the measured trajectory, we used the four initial oscillations (ESI). The 3$^{\text{rd}}$ and 5$^{\text{th}}$ columns of **Table 7.1** show the multipole coefficients found in this manner for swimmers of the rod and cylinder type, respectively. Using only a single oscillation leads to a change in the fitted values of $\sim 20\%$, showing our method to be robust and requiring only fragments of a trajectory to be effective. In addition, we verified that the result of the fitting was independent of the height H of the channel, eliminating the possibility of boundary artifacts. In chapter §**6** we obtained the multipole coefficients directly from the flow field of the swimmers in our LB simulations by means of projection via a Legendre-Fourier decomposition. These values are listed in the 2$^{\text{nd}}$ and 4$^{\text{th}}$ columns of **Table 7.1**, respectively. The projection was carried out in the absence of confinement, using a large simulation box with periodic boundary conditions, for which the finite-size effects differ strongly from those of the confining geometry. There is excellent correspondence between the two measurements of the hydrodynamic moments for both swimmer shapes. This demonstrates the applicability of far-field theory to describe the onset of the observed oscillatory trajectories. The far-field result is accurate until the swimmer-wall distance becomes too small.

Let us now focus on the general features of the theoretical model and analyze the impact of the various hydrodynamic moments on the motion of the swimmer. Firstly, our calculations confirm that the pusher swimmer ($\kappa > 0$) undergoes oscillatory trajectories that move away from the centre of the channel, and pullers ($\kappa < 0$) converge towards the centre line. However, oscillations about the centre only occur if the quadrupolar terms are included, and the oscillation wavelength decreases with the associated quadrupolar coefficients ν and μ. A spherical swimmer with $\nu = \mu = 0$ (§**6**) does not display such oscillations. The octupolar contributions further control the damping and growth of the trajectories, where the positive signs of o_1 and o_2 correspond to motion towards the boundaries. The aspect ratio γ leads only to a second-order correction in the theory. That is, the hydrodynamic moments dominate the dynamics of the swimmer, therefore rods with different aspect ratios still show similar

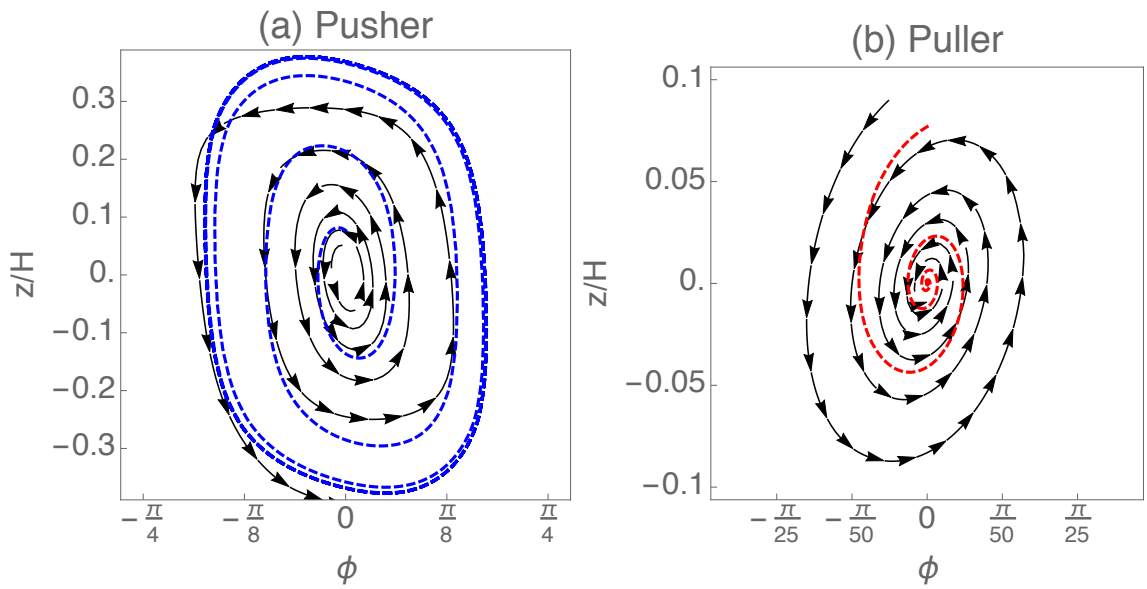

Figure 7.2: Trajectories of swimmers in (ϕ,z) phase space, for a rod-type pusher (a) and puller (b) with a wall separation of $H = 13\sigma$. The LB simulation data are shown as thick, dashed, blue and red lines. The theoretical predictions are superimposed as black arrows.

oscillations (ESI).

The dynamical system can be understood further by considering the motion of the swimmer in phase space. Due to the translational invariance in the x and y coordinates, the equations of motion can be reduced to two coupled first-order PDEs in (ϕ,z) space, next to the uncoupled equation for the x coordinate. **Fig. 7.2** shows the LB swimmer trajectories in phase space, superimposed with the theoretical model, where the fitted multipole moments in **Table 7.1** have been used. The dipolar term leads to a star-type fixed point (curves radiating from a point) at the origin, that is stable for pullers and unstable for pushers. The oscillatory motion due to the quadrupolar contributions corresponds to a circle-type phase-space trajectory (closed loops around a point) centred on the origin. Together the dipole and quadrupole produce a spiral. For pushers, the trajectories spiral outwards (**Fig. 7.2**a), and inwards for pullers (**Fig. 7.2**b). The theoretical predictions do not show a limit cycle in **Fig. 7.2**. Both the far-field framework and the LB method are unable to adequately capture hydrodynamic interactions in the near-wall region and further study of this region, where both lubrication corrections[219] and short-ranged potentials[217] can play a role, is required.

Our result shows that movement of a swimmer under confinement can in principle be used to quantitatively determine the hydrodynamic moments, even up to the octupolar moment as shown here. Specifically, about one period is the minimum path length required to fit these modes to the theory with discrepancy less than $\sim$ 20%. This suggests that

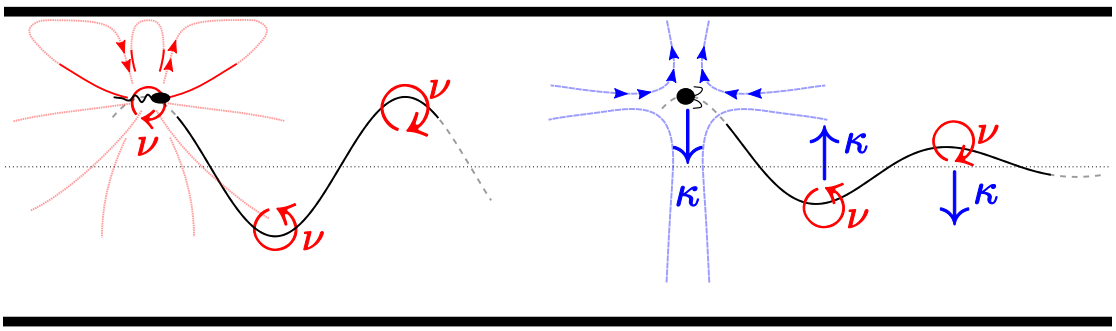

Figure 7.3: Illustration of the mechanisms of oscillatory swimmer motion in micro-channels. (a) Quadrupolar moment only. The HI rotates the swimmer away from the nearest wall resulting in an oscillatory trajectory. (b) Quadrupole and puller-type dipole. The dipole pushes the swimmer away from the nearest wall, decreasing the oscillation amplitude.

our method has applicability to experimental systems where thermal noise and tumbling can effect the trajectory. The presence of these sources of noise would require ensemble averaging trajectories in (ϕ, z) space, which can then be fitted using our procedure. Noise also implies that parts of the trajectory will occur many times during measurements, meaning the near-wall dynamics in which we observed a limit cycle, does not play an important role. One simply averages many different trajectories away from the wall to improve the fitting statistics.

7.4 Physical intuition

A physical intuition for the onset of oscillatory swimming can be distilled from the LB simulations and far-field hydrodynamic description by considering the trajectory of a swimmer initially set at z_0 near the centre line and oriented parallel to the walls (**Fig. 7.3**). Since our raspberry swimmers have large quadrupolar moments ($\nu \sim 10^{-1}$), we first consider only the flow fields generated by the positive quadrupole. This flow serves to rotate the swimmer away from the nearest wall, as shown schematically in **Fig. 7.3**a. The continual rotation away from the nearest wall establishes the oscillations. By linearly expanding the equations of motion about the centre line, the micro-swimmer dynamics can be captured by a linear system of coupled differential equations (ESI). Whenever there is only a quadrupolar flow field, the trajectory is approximated to be simple oscillatory motion $z\,(t) \approx z_0 \cos(\omega t)$ with angular frequency $\omega = 4\left(3\nu v_s/H^5\right)^{1/2}$ and wavelength $\lambda \approx 2\pi v_s/\omega$. Although $\mu = 0$ in this study, a source dipole moment also leads to simple oscillations (ESI). This also theoretically explains the observations of persistent oscillations for neutral squirmers made by Zhu *et*

al.[221], even though there are differences in the confining geometry.

Next we add the dipolar term to the expansion, which yields

$$z(t) \approx z_0 e^{\alpha t} \cos(\omega t) \tag{7.1}$$

where $\alpha = 3\kappa/H^3$, which is negative for pullers. The dipolar term also modifies the frequency ω due the wall-induced rotation $\mathbf{\Omega}_{\mathrm{HI}}$, but this effect is negligible if $\nu \gg 81\kappa^2/(48Hv_s)$, which is the case here. A pusher also obeys **Eq. 7.1** but with $\alpha > 0$ and exponentially growing amplitudes, which leads to a rapid breakdown of the near-centre line assumption. The sensitivity of oscillations to channel height is unmistakable in the $\exp\left(H^{-3}\right)$-dependence of **Eq. 7.1** reflecting the fact that the essential hydrodynamic moments are high order. Whereas higher order moments are required to predict the oscillation wavelength and damping factor quantitatively, the dipolar and quadrupolar moments can be fit from the dynamics using (7.1) with a error margin of $\sim 40\%$ compared to the LB-measured values. Hence, **Eqs. 1.32, 7.1** allow for characterisation of the swimmer's hydrodynamic properties based on experimental trajectories and can be readily transferred to the observations made by Zhu *et al.*[221]. Likewise, LB raspberry simulations can be extended to more complex 3D geometries such as square channels and round tubes, in which we observed helical motion (ESI).

7.5 Conclusion

In conclusion, we have studied the onset of oscillatory motion of swimmers in micro-channels without externally applied flow and in an otherwise quiescent medium using both LB simulations and hydrodynamic theory. The pusher-type swimmers follow a sinusoidal trajectory with increasing amplitude, whereas pullers perform a damped oscillation towards the centre of the channel. Our results and previous observations of such phenomena[221] can be explained by our theoretical model, which uses far-field hydrodynamics only. We conclude that the onset of oscillations can be described without taking into account near-wall lubrication effects as has been previously presumed[219] provided that a quadrupole moment (or source-dipole) is accounted for in addition to the primary dipole moment. To fully characterise particle trajectories in relatively wide channels, many hydrodynamic moments are required, as high as the octupole in our case. However, the excellent match of our trajectory-fitted moments to those measured in bulk suggests that similar experimental measurements can be used to

determine the hydrodynamic moment decomposition of micro-organisms or artificial swimmers. Our work stresses the relevance of far-field hydrodynamics in confining geometries and thus opens the way for new studies that aim to exploit these insights in microfluidic environments[408]. Future work will focus on the analysis of more complex force/counter-force swimmers to model the richness in shape and hydrodynamic moments of experimentally available swimmers.

CHAPTER 8

Discussion

"Words are but pictures of our thoughts."

John Dryden (1631–1700)

Multiple aspects of 'Hydrodynamics of Micro-swimmers in Complex Fluids and Environments' are considered in this thesis. In §8.1 the main conclusions of these considerations are summarised, and their potential impacts on biologically or industrially relevant situations are discussed. Finally, §8.2 provides an outlook for research that I am currently working on or propose to do in future.

8.1 Summary of conclusions

8.1.1 Chapter 2

In this chapter we consider tracer particle transport due to the flows created by a self-propelled micro-swimmer, such as a swimming bacterium, alga or a microscopic artificial swimmer. Recent theoretical work has shown that, as a swimmer moves in the fluid bulk along an infinite straight path, tracer particles far from its path perform closed loops, whereas those close to the swimmer are entrained by its motion. However in biologically and technologically important cases tracer transport is significantly altered for swimmers that move in a run-and-tumble fashion with a finite persistence length, or/and in the presence of a free surface or a solid boundary. Here we present a systematic analytical and numerical study exploring the

resultant regimes and their crossovers. Our focus is on describing qualitative features of the tracer particle transport and developing quantitative tools for its analysis. Our work is a step towards understanding the ecological effects of flows created by swimming organisms, such as enhanced fluid mixing and biofilm formation.

8.1.2 Chapter 3

Interactions between microorganisms and their complex flowing environments are essential in many biological systems. In this chapter we develop a model for micro-swimmer dynamics in non-Newtonian Poiseuille flows. We predict that swimmers in shear-thickening (-thinning) fluids migrate upstream more (less) quickly than in Newtonian fluids and demonstrate that viscoelastic normal stress differences reorient swimmers causing them to migrate upstream at the centreline, in contrast to well-known boundary accumulation in quiescent Newtonian fluids. Based on these observations, we suggest a sorting mechanism to select microbes by swimming speed.

8.1.3 Chapter 4

One of the principle mechanisms by which surfaces and interfaces affect microbial life is by perturbing the hydrodynamic flows generated by swimming. By summing a recursive series of image systems we derive a numerically tractable approximation to the three-dimensional flow field of a Stokeslet within a viscous film between a parallel no-slip surface and a no-shear interface and, from this Green's function, we compute the flows produced by a force- and torque-free micro-swimmer. We also extend the exact solution of Liron & Mochon (1976) to the film geometry, which demonstrates that the image series gives a satisfactory approximation to the swimmer flow fields if the film is sufficiently thick compared to the swimmer size. Concentrating on the thick film case, we find that the dipole moment always induces a bias towards swimmer accumulation at the no-slip wall rather than the water-air interface, but that higher-order multipole moments can oppose this. Based on the analytic predictions we propose an experimental method to find the multipole coefficient that induces circular swimming trajectories, allowing one to analytically determine the swimmer's three-dimensional position under a microscope.

8.1.4 Chapter 5

Biological flows over surfaces and interfaces can result in accumulation hotspots or depleted voids of micro-organisms in natural environments. Apprehending the mechanisms that lead to such distributions is essential for understanding biofilm initiation. Using the formalism developed in Chapter 4 we resolve the dynamics and statistics of swimming microbes within flowing films, considering the impact of confinement through steric and hydrodynamic interactions, flow, and motility, along with Brownian and run-and-tumble fluctuations. Microswimmers can be peeled off the solid wall above a critical flow strength. However, the interplay of flow and fluctuations causes organisms to migrate back towards the wall above a secondary critical value. Hence, faster flows may not always be the most efficacious strategy to discourage biofilm initiation. Moreover, we find the run-and-tumble dynamics commonly used by flagellated microbes to be an intrinsically more successful strategy to escape from boundaries than equivalent levels of enhanced Brownian noise in ciliated organisms.

8.1.5 Chapter 6

There are a plethora of active matter models that describe the behaviour of self-propelled particles (or swimmers), both with and without hydrodynamics. However, there are few studies that consider shape-anisotropic swimmers and include hydrodynamic interactions. Here, we introduce a simple method to simulate self-propelled colloids interacting hydrodynamically in a viscous medium using the lattice-Boltzmann technique. Our model is based on raspberry-type viscous coupling and a force/counter-force formalism which ensures that the system is force free. We consider several anisotropic shapes and characterise their hydrodynamic multipolar flow field. We demonstrate that shape-anisotropy can lead to the presence of strong quadrupole and octupole moments, in addition to the principal dipole moment. The ability to simulate and characterise these higher-order moments will prove crucial for understanding the behaviour of model swimmers in confining geometries.

8.1.6 Chapter 7

Self-propelled colloids (swimmers) in confining geometries follow trajectories determined by hydrodynamic interactions with the bounding surfaces. However, typically these interactions are ignored or truncated to lowest order. We demonstrate that higher-order hydrodynamic

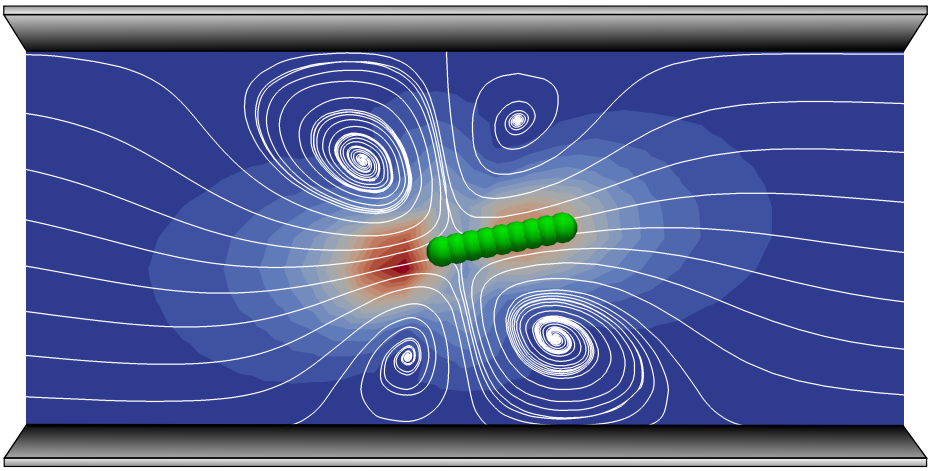

Figure 8.1: The flow field produced by a Raspberry swimmer oscillating in a micro-channel. Streamlines are shown in white and the magnitude of the velocity field ranges between zero (blue) and unity (red). This is a pusher-type swimmer with a force applied to the liquid behind the swimmer body made of green drupelets.

moments cause rod-like swimmers to follow oscillatory trajectories in a quiescent fluid between two parallel plates (**Fig. 8.1**), using a combination of far-field calculations and Lattice-Boltzmann simulations of the raspberry swimmers developed in Chapter 6. This behaviour occurs even far from the confining walls and does not require lubrication results. We show that a swimmer's hydrodynamic quadrupole moment is crucial to the onset of the oscillatory trajectories. This insight allows us to develop a simple model for the dynamics near the channel centre based on the higher hydrodynamic moments, and suggests opportunities for trajectory-based experimental characterisation of swimmers' hydrodynamic properties.

8.2 Outlook

It could be argued that the structure of the research presented in this thesis is based on a 'bottom-up' approach. We started by looking at micro-swimmers with imposed swimming trajectories, and afterwards the dynamics were allowed to vary. We then considered the effects on the swimming dynamics of adding more and more terms; steric interactions with the walls, hydrodynamics interactions, externally imposed flow fields, the inclusion of thermal and biological fluctuations, and viscoelasticity. The advantage of this approach is that each term in the model can be tuned and compared to individual experiments or simulations. The hydrodynamic effects, for example, could be matched with simulations of Raspberry swimmers. This way, the model parameters can be determined for a particular micro-swimmer, so that

its behaviour in different circumstances can be predicted.

During the last year of the PhD more and more contacts were established with collaborators: In particular with Joost de Graaf (University of Edinburgh), Anke Lindner (ESPCI Paris) and Marco Polin (University of Warwick). I am very thankful for the experimental and computational data they share, the valuable discussions we have, and for inviting me to their labs in order to get closer to reality. Consequently a number of diverse projects emerged, some of which are completed and some are work in progress:

With Anke we are trying to understand experiments on micro-swimmers in corners. Microbial life is known to be connected tightly with surfaces, and in particular to cavities and crevices where organisms are protected from harsh environmental conditions such as externally imposed flows. With a new experimental technique of 3D tracking of individual cells, we study the influence of different imposed flow speeds on corner accumulation and the ability to swim upstream.

With Joost we have already published two papers, discussed in this thesis, on raspberry swimmers. Since the LB algorithm allows to construct arbitrarily shaped swimmers and swimmer environments, the next natural step to take in this study is to look at different more complicated swimmer shapes and different geometries such as swimmers in a water droplet or in a porous medium. Another interesting line of thought would be to include swimmer-swimmer interactions and look at dense suspensions of organisms, for which very non-trivial phenomena such as swarming have been observed.

With Marco we continue to investigate tracer displacement by *Chlamydomonas* algae. The multipole expansion model we have used until now gives a good prediction of the flow fields far away from the swimmer, but the model breaks down nearby. Therefore we have constructed a new model that accounts for the finite size of the swimmer and its no-slip surface. By matching the model parameters with experiments we aim to explain and quantify the long entrainments of tracer particles close to the swimmer body.

CHAPTER 9

References

"The devil can cite Scripture for his purpose."

William Shakespeare (1564–1616)

Bibliography

[1] A. J. T. M. Mathijssen, D. O. Pushkin, and J. M. Yeomans. Tracer trajectories and displacement due to a micro-swimmer near a surface. J. Fluid Mech., 773:498 – 519, June 2015. doi:10.1017/jfm.2015.269.

[2] A. J. T. M. Mathijssen, T. N. Shendruk, J. M. Yeomans, and A. Doostmohammadi. Upstream swimming in microbiological flows. Phys. Rev. Lett., 116:028104, Jan 2016. doi:10.1103/PhysRevLett.116.028104.

[3] A. J. T. M. Mathijssen, A. Doostmohammadi, J. M. Yeomans, and T. N. Shendruk. Hydrodynamics of microswimmers in films. J. Fluid Mech. accepted; preprint arXiv:1511.01859, 2015. URL http://arxiv.org/abs/1511.01859.

[4] A. J. T. M. Mathijssen, A. Doostmohammadi, J. M. Yeomans, and T. N. Shendruk. Hotspots of boundary accumulation: dynamics and statistics of micro-swimmers in flowing films. J. R. Soc. Interface, 13:20150936, 2016. doi:10.1098/rsif.2015.0936.

[5] J. de Graaf, H. Menke, A. J. T. M. Mathijssen, M. Fabritius, C. Holm, and T. Shendruk. Lattice-boltzmann hydrodynamics of anisotropic active matter. J. Chem. Phys., 144:134106, 2016. doi:10.1063/1.4944962.

[6] J. de Graaf, A. J. T. M. Mathijssen, M. Fabritius, H. Menke, C. Holm, and T. N. Shendruk. Understanding the onset of oscillatory swimming in microchannels. Soft Matter, 12:4704–4708, 2016. doi:10.1039/C6SM00939E.

[7] M. Youle, F. Rohwer, A. Stacy, M. Whiteley, B. C. Steel, N. J. Delalez, A. L. Nord, R. M. Berry, J. P. Armitage, S. Kamoun, et al. The microbial olympics. Nat. Rev. Microbiol., 10(8):583–588, 2012. doi:10.1038/nrmicro2837.

[8] J. Elgeti, R. G. Winkler, and G. Gompper. Physics of microswimmers—single particle motion and collective behavior: A review. Rep. Progr. Phys., 78(5):056601, 2015. doi:10.1088/0034-4885/78/5/056601.

[9] M. Marchetti, J. Joanny, S. Ramaswamy, T. Liverpool, J. Prost, M. Rao, and R. Simha. Hydrodynamics of soft active matter. Rev. Mod. Phys., 85:1143, 2013. doi:10.1103/RevModPhys.85.1143.

[10] E. Lauga and T. R. Powers. The hydrodynamics of swimming microorganisms. Rep. Progr. Phys., 72(9):096601, 2009. doi:10.1088/0034-4885/72/9/096601.

[11] E. M. Purcell. Life at low Reynolds number. Am. J. Phys, 45(1):3–11, 1977. URL http://www.damtp.cam.ac.uk/user/gold/pdfs/purcell.pdf.

[12] M. Cates. Diffusive transport without detailed balance in motile bacteria: does microbiology need statistical physics? Rep. Progr. Phys., 75:042601, 2012. doi:10.1088/0034-4885/75/4/042601.

[13] M. Cates and J. Tailleur. Motility-induced phase separation. Annu. Rev. Cond. Mat. Phys., 6: 219, 2015. doi:10.1209/0295-5075/108/56004.

[14] S. Ramaswamy. The mechanics and statistics of active matter. Annu. Rev. Cond. Mat. Phys., 1:323–345, 2010. doi:10.1146/annurev-conmatphys-070909-104101.

[15] Y. Hong, D. Velegol, N. Chaturvedi, and A. Sen. Biomimetic behavior of synthetic particles: from microscopic randomness to macroscopic control. Phys. Chem. Chem. Phys., 12(7):1423–1435, 2010. doi:10.1039/B917741H.

[16] A. Pohorille and D. Deamer. Self-assembly and function of primitive cell membranes. Res. Microbiol., 160:449—456, 2009. doi:10.1016/j.resmic.2009.06.004.

[17] W. E. Collins. *Plasmodium knowlesi*: A malaria parasite of monkeys and humans. Annu. Rev. Entomology, 57:107–121, 2012. doi:10.1146/annurev-ento-121510-133540.

[18] J. L. Bargul, J. Jung, F. A. McOdimba, C. O. Omogo, V. O. Adunga, T. Krüger, D. K. Masiga, and M. Engstler. Species-specific adaptations of Trypanosome morphology and motility to the Mammalian host. PloS Pathog., 12(2):e1005448, 2016. doi:10.1371/journal.ppat.1005448.

[19] C. Combes. The art of being a parasite. University of Chicago Press, 2005. ISBN 0226114384.

[20] E. W. Hook III. *Trichomonas vaginalis*: No longer a minor STD. Sexually Transm. Dis., 26(7): 388–389, 1999. doi:10.1097/00007435-199908000-00004.

[21] World Health Organisation. Schistosomiasis fact sheet. URL http://www.who.int/mediacentre/factsheets/fs115/en/.

[22] M. J. van der Werf, S. J. de Vlas, S. Brooker, C. W. Looman, N. J. Nagelkerke, J. D. F. Habbema, and D. Engels. Quantification of clinical morbidity associated with *Schistosome* infection in sub-Saharan Africa. Acta Tropica, 86(2):125–139, 2003. doi:10.1016/S0001-706X(03)00029-9.

[23] M. Prakash and D. Krishnamurthy. The deadly swimming of *Cercariae*: an unusual Stokesian swimmer. Bull. Amer. Phys. Soc., 59, 2014. doi:10.1103/APS.DFD.2014.GFM.V0049.

[24] A. Zöttl and H. Stark. Emergent behavior in active colloids. J. Phys. Cond. Mat., accepted:–, 2016. URL http://arxiv.org/abs/1601.06643.

[25] G. A. Ozin, I. Manners, S. Fournier-Bidoz, and A. Arsenault. Dream nanomachines. Adv. Mat., 17(24):3011–3018, 2005. doi:10.1002/adma.200501767.

[26] H.-L. Lien and W.-x. Zhang. Transformation of chlorinated methanes by nanoscale iron particles. J. Environ. Eng., 125(11):1042–1047, 1999. doi:10.1061/(asce)0733-9372(1999)125:11(1042).

[27] B. J. Nelson, I. K. Kaliakatsos, and J. J. Abbott. Microrobots for minimally invasive medicine. Annu. Rev. Biomed. Eng., 12:55–85, 2010. doi:10.1146/annurev-bioeng-010510-103409.

[28] W. Wang, S. Li, L. Mair, S. Ahmed, T. J. Huang, and T. E. Mallouk. Acoustic propulsion of nanorod motors inside living cells. Angew. Chem. Int. Ed., 53(12):3201–3204, 2014. doi:10.1002/ange.201309629.

[29] G. F. Paciotti, L. Myer, D. Weinreich, D. Goia, N. Pavel, R. E. McLaughlin, and L. Tamarkin. Colloidal gold: a novel nanoparticle vector for tumor directed drug delivery. Drug Delivery, 11 (3):169–183, 2004. doi:10.1080/10717540490433895.

[30] N. Koumakis, A. Lepore, C. Maggi, and R. Di Leonardo. Targeted delivery of colloids by swimming bacteria. Nature Comm., 4, 2013. doi:10.1038/ncomms3588.

[31] Y. Katz, K. Tunstrøm, C. Ioannou, C. Huepe, and I. Couzin. Inferring the structure and dynamics of interactions in schooling fish. Proc. Nat. Acad. Sci., 108(46):18720, 2011. doi:10.1073/pnas.1107583108.

[32] M. Ballerini, N. Cabibbo, R. Candelier, A. Cavagna, E. Cisbani, I. Giardina, V. Lecomte, A. Orlandi, G. Parisi, A. Procaccini, M. Viale, and V. Zdravkovic. Interaction ruling animal collective behavior depends on topological rather than metric distance: Evidence from a field study. Proc. Nat. Acad. Sci., 105:1232, 2008. doi:10.1073/pnas.0711437105.

[33] J. Buhl, D. J. T. Sumpter, I. D. Couzin, J. J. Hale, E. Despland, E. R. Miller, and S. J. Simpson. From disorder to order in marching locusts. Science, 312:1402, 2006. doi:10.1126/science.1125142.

[34] D. Helbing, I. Farkas, and T. Vicsek. Simulating dynamical features of escape panic. Nature, 407:487, 2000. doi:10.1038/35035023.

[35] S. M. Burrows, W. Elbert, M. G. Lawrence, and U. Pöschl. Bacteria in the global atmosphere–

part 1: Review and synthesis of literature data for different ecosystems. Atmosph. Chem. Phys., 9(23):9263–9280, 2009. doi:10.5194/acp-9-9263-2009.

[36] I. J. Bear and R. G. Thomas. Nature of argillaceous odour. Nature, 1964. doi:10.1038/201993a0.

[37] N. N. Gerber. Three highly odorous metabolites from an actinomycete: 2-isopropyl-3-methoxy-pyrazine, methylisoborneol, and geosmin. J. Chem. Ecol., 3(4):475–482, 1977. doi:10.1007/bf00988190.

[38] D. Powell. Rain-making bacteria control the weather from the ground. New Scientist, 201(2690): 11, 2009. doi:10.1016/S0262-4079(09)60073-7.

[39] E. Bianconi, A. Piovesan, F. Facchin, A. Beraudi, R. Casadei, F. Frabetti, L. Vitale, M. C. Pelleri, S. Tassani, F. Piva, et al. An estimation of the number of cells in the human body. Ann. Hum. Biol., 40(6):463–471, 2013. doi:10.3109/03014460.2013.807878.

[40] F. Bäckhed, R. E. Ley, J. L. Sonnenburg, D. A. Peterson, and J. I. Gordon. Host-bacterial mutualism in the human intestine. Science, 307(5717):1915–1920, 2005. doi:10.1126/science.1104816.

[41] R. Sender, S. Fuchs, and R. Milo. Revised estimates for the number of human and bacteria cells in the body. bioRxiv, page 036103, 2016. doi:10.1101/036103.

[42] W. B. Whitman, D. C. Coleman, and W. J. Wiebe. Prokaryotes: the unseen majority. Proc. Nat. Acad. Sci., 95(12):6578–6583, 1998. doi:10.1073/pnas.95.12.6578.

[43] J. Breton, N. Tennoune, N. Lucas, M. Francois, R. Legrand, J. Jacquemot, A. Goichon, C. Guérin, J. Peltier, M. Pestel-Caron, et al. Gut commensal *E. coli* proteins activate host satiety pathways following nutrient-induced bacterial growth. Cell Metabol., 2015. doi:10.1016/j.cmet.2015.10.017.

[44] R. Vallery-Radot. The life of Pasteur. BiblioLife, 1902. ISBN 112416393X.

[45] G. S. Wilson. The Pasteurization of milk. British Med. J., 1(4286):261, 1943. URL `http://www.ncbi.nlm.nih.gov/pmc/articles/PMC2282302/`.

[46] S. Namdeo, S. Khaderi, and P. Onck. Numerical modelling of chirality-induced bi-directional swimming of artificial flagella. Proc. R. Soc. A, 470(2162):20130547, 2014. doi:10.1098/rspa.2013.0547.

[47] S. Tamm and G. Horridge. The relation between the orientation of the central fibrils and the direction of beat in cilia of *Opalina*. Proc. R. Soc. B, 175(1040):219–233, 1970. doi:10.1098/rspb.1970.0020.

[48] H. P. Sørensen and K. K. Mortensen. Advanced genetic strategies for recombinant protein expression in *Escherichia coli*. J. Biotech., 115(2):113–128, 2005. doi:10.1016/j.jbiotec.2004.08.004.

[49] B. M. Carpenter, T. K. McDaniel, J. M. Whitmire, H. Gancz, S. Guidotti, S. Censini, and D. S. Merrell. Expanding the *Helicobacter pylori* genetic toolbox: modification of an endogenous plasmid for use as a transcriptional reporter and complementation vector. Appl. Envir. Microbiol., 73(23):7506–7514, 2007. doi:10.1128/AEM.01084-07.

[50] Y. Sowa and R. M. Berry. Bacterial flagellar motor. Quart. Rev. Biophys., 41(02):103–132, 2008. doi:10.1017/S0033583508004691.

[51] R. M. Macnab. Bacterial flagella rotating in bundles: A study in helical geometry. Proc. Nat. Acad. Sci., 74(1):221–225, 1977. doi:10.1073/pnas.74.1.221.

[52] G. Lowe, M. Meister, and H. C. Berg. Rapid rotation of flagellar bundles in swimming bacteria. Nature, 325:637–640, 1987. doi:10.1038/325637a0.

[53] S. Chattopadhyay, R. Moldovan, C. Yeung, and X. Wu. Swimming efficiency of bacterium *Escherichia coli*. Proc. Nat. Acad. Sci., 103(37):13712–13717, 2006. doi:10.1073/pnas.0602043103.

[54] E. M. Purcell. The efficiency of propulsion by a rotating flagellum. Proc. Nat. Acad. Sci., 94 (21):11307–11311, 1997. URL `http://www.pnas.org/content/94/21/11307`.

[55] H. C. Berg and D. A. Brown. Chemotaxis in *Escherichia coli* analysed by three-dimensional tracking. Nature, 239(5374):500–504, 1972. doi:10.1038/239500a0.

[56] D. V. Nicolau Jr, J. P. Armitage, and P. K. Maini. Directional persistence and the optimality of *run-and-tumble* chemotaxis. Comp. Biol. Chem., 33(4):269–274, 2009. doi:10.1016/j.compbiolchem.2009.06.003.

[57] K. Son, J. S. Guasto, and R. Stocker. Bacteria can exploit a flagellar buckling instability to change direction. Nat. Phys., 9(8):494–498, 2013. doi:10.1038/nphys2676.

[58] H. C. Berg. *E. coli* in motion. Springer Media, 2004. ISBN 0387008888.

[59] M. Molaei, M. Barry, R. Stocker, and J. Sheng. Failed escape: Solid surfaces prevent tumbling of *Escherichia coli*. Phys. Rev. Lett., 113(6):068103, 2014. doi:10.1103/PhysRevLett.113.068103.

[60] University of Austin, Texas. Products, utex 90, *Chlamydomonas reinhardtii*. URL `http:`

//utex.org/products/utex-0090.

[61] E. H. Harris, D. B. Stern, and G. Witman. The *Chlamydomonas* sourcebook. Academic Press, Oxford, 2009. ISBN 0123708737.

[62] R. E. Goldstein. Green algae as model organisms for biological fluid dynamics. Annu. Rev. Fluid Mech., 47:343, 2015. doi:10.1146/annurev-fluid-010313-141426.

[63] T. Pedley and J. Kessler. Hydrodynamic phenomena in suspensions of swimming microorganisms. Annu. Rev. Fluid Mech., 24(1):313–358, 1992. doi:10.1146/annurev.fl.24.010192.001525.

[64] S. S. Merchant, S. E. Prochnik, O. Vallon, E. H. Harris, S. J. Karpowicz, G. B. Witman, A. Terry, A. Salamov, L. K. Fritz-Laylin, L. Maréchal-Drouard, et al. The *Chlamydomonas* genome reveals the evolution of key animal and plant functions. Science, 318(5848):245–250, 2007. doi:10.1126/science.1143609.

[65] K. W. Foster and R. D. Smyth. Light antennas in phototactic algae. Microbiol. Rev., 44(4):572, 1980. URL http://mmbr.asm.org/content/44/4/572.

[66] R. R. Bennett and R. Golestanian. A steering mechanism for phototaxis in *Chlamydomonas*. J. R. Soc. Interface, 12(104):20141164, 2015. doi:10.1098/rsif.2014.1164.

[67] W. M. Durham, E. Climent, and R. Stocker. Gyrotaxis in a steady vortical flow. Phys. Rev. Lett., 106(23):238102, 2011. doi:10.1103/PhysRevLett.106.238102.

[68] G. J. Pazour, N. Agrin, J. Leszyk, and G. B. Witman. Proteomic analysis of a Eukaryotic cilium. J. Cell Biol., 170(1):103–113, 2005. doi:10.1083/jcb.200504008.

[69] L. Vincensini, T. Blisnick, and P. Bastin. 1001 model organisms to study cilia and flagella. Biol. Cell, 103(3):109–130, 2011. doi:10.1042/BC20100104.

[70] I. Ibañez-Tallon, N. Heintz, and H. Omran. To beat or not to beat: roles of cilia in development and disease. Human Mol. Genet., 12(suppl 1):R27–R35, 2003. doi:10.1093/hmg/ddg061.

[71] D. R. Mitchell. *Chlamydomonas* flagella. J. Phycol., 36(2):261–273, 2000. doi:10.1046/j.1529-8817.2000.99218.x.

[72] M. Schliwa and G. Woehlke. Molecular motors. Nature, 422(6933):759–765, 2003. doi:10.1038/nature01601.

[73] T. Mitchison and H. Mitchison. Cell biology: how cilia beat. Nature, 463(7279):308–309, 2010. doi:10.1038/463308a.

[74] M. Polin, I. Tuval, K. Drescher, J. Gollub, and R. E. Goldstein. *Chlamydomonas* swims with two "gears" in a Eukaryotic version of run-and-tumble locomotion. Science, 325(5939):487–490, 2009. doi:10.1126/science.1172667.

[75] J. S. Guasto, K. A. Johnson, and J. P. Gollub. Oscillatory flows induced by microorganisms swimming in two dimensions. Phys. Rev. Lett., 105(16):168102, 2010. doi:10.1103/PhysRevLett.105.168102.

[76] U. Rüffer and W. Nultsch. Flagellar coordination in *Chlamydomonas* cells held on micropipettes. Cell Motil. Cytoskel., 41(4):297–307, 1998. doi:10.1002/(SICI)1097-0169(1998)41:4<297::AID-CM3>3.0.CO;2-Y.

[77] Q. Wang, J. Pan, and W. J. Snell. Intraflagellar transport particles participate directly in cilium-generated signaling in *Chlamydomonas*. Cell, 125(3):549–562, 2006. doi:10.1016/j.cell.2006.02.044.

[78] B. A. Afzelius. A human syndrome caused by immotile cilia. Science, 193(4250):317–319, 1976. doi:10.1126/science.1084576.

[79] M. A. Sleigh. The Biology of Cilia and Flagella, volume 12 of International Series of Monographs on Pure and Applied Biology: Zoology. Pergamon Press, Oxford, 1962. ISBN 1175766704.

[80] C. A. Solari, S. Ganguly, J. O. Kessler, R. E. Michod, and R. E. Goldstein. Multicellularity and the functional interdependence of motility and molecular transport. Proc. Nat. Acad. Sci., 103 (5):1353–1358, 2006. doi:10.1073/pnas.0503810103.

[81] C. Ainsworth. Cilia: tails of the unexpected. Nature, 448(7154):638–641, 2007. doi:10.1038/448638a.

[82] R. Golestanian, J. M. Yeomans, and N. Uchida. Hydrodynamic synchronization at low Reynolds number. Soft Matter, 7(7):3074–3082, 2011. doi:10.1039/C0SM01121E.

[83] N. Uchida and R. Golestanian. Generic conditions for hydrodynamic synchronization. Phys. Rev. Lett., 106(5):058104, 2011. doi:10.1103/PhysRevLett.106.058104.

[84] R. Stocker and W. M. Durham. Tumbling for stealth? Science, 325(5939):400–402, 2009. doi:10.1126/science.1177269.

[85] K. Y. Wan and R. E. Goldstein. Rhythmicity, recurrence, and recovery of flagellar beating. Phys. Rev. Lett., 113(23):238103, 2014. doi:10.1103/PhysRevLett.113.238103.

[86] R. R. Bennett and R. Golestanian. Phase-dependent forcing and synchronization in the three-sphere model of *Chlamydomonas*. New J. Phys., 15(7):075028, 2013. doi:10.1088/1367-2630/15/7/075028.

[87] R. R. Bennett and R. Golestanian. Emergent run-and-tumble behavior in a simple model of *Chlamydomonas* with intrinsic noise. Phys. Rev. Lett., 110(14):148102, 2013. doi:10.1103/PhysRevLett.110.148102.

[88] C. Brennen and H. Winet. Fluid mechanics of propulsion by cilia and flagella. Annu. Rev. Fluid Mech., 9(1):339–398, 1977. doi:10.1146/annurev.fl.09.010177.002011.

[89] H. Machemer. Ciliary activity and the origin of metachrony in *Paramecium*: effects of increased viscosity. J. Exp. Biol., 57(1):239–259, 1972. URL `http://jeb.biologists.org/content/57/1/239.long`.

[90] K. Okamoto and Y. Nakaoka. Reconstitution of metachronal waves in ciliated cortical sheets of paramecium-wave stabilities. J. Exp. Biol., 192(1):61–72, 1994. URL `http://jeb.biologists.org/content/192/1/61`.

[91] K. Drescher, K. C. Leptos, I. Tuval, T. Ishikawa, T. J. Pedley, and R. E. Goldstein. Dancing *Volvox*: Hydrodynamic bound states of swimming algae. Phys. Rev. Lett., 102:168101, Apr 2009. doi:10.1103/PhysRevLett.102.168101.

[92] J. Lighthill. Flagellar hydrodynamics. SIAM Rev., 18(2):161–230, 1976. doi:10.1137/1018040.

[93] N. Bruot and P. Cicuta. Realizing the physics of motile cilia synchronization with driven colloids. Annu. Rev. Cond. Mat. Phys., 7:1–26, 2016. doi:10.1146/annurev-conmatphys-031115-011451.

[94] R. Ma, G. S. Klindt, I. H. Riedel-Kruse, F. Jülicher, and B. M. Friedrich. Active phase and amplitude fluctuations of flagellar beating. Phys. Rev. Lett., 113(4):048101, 2014. doi:10.1103/PhysRevLett.113.048101.

[95] J. Kotar, M. Leoni, B. Bassetti, M. C. Lagomarsino, and P. Cicuta. Hydrodynamic synchronization of colloidal oscillators. Proc. Nat. Acad. Sci., 107(17):7669–7673, 2010. URL `http://www.pnas.org/content/107/17/7669.short`.

[96] N. Uchida and R. Golestanian. Synchronization and collective dynamics in a carpet of microfluidic rotors. Phys. Rev. Lett., 104(17):178103, 2010. doi:10.1103/PhysRevLett.106.058104.

[97] M. Fliegauf, T. Benzing, and H. Omran. When cilia go bad: cilia defects and ciliopathies. Nat. Rev. Mol. Cell Biol., 8(11):880–893, 2007. doi:10.1038/nrm2278.

[98] M. J. Lighthill. On the squirming motion of nearly spherical deformable bodies through liquids at very small Reynolds numbers. Comm. Pure Appl. Math., 5(2):109–118, 1952. doi:10.1002/cpa.3160050201.

[99] J. R. Blake. A spherical envelope approach to ciliary propulsion. J. Fluid Mech., 46(01):199–208, 1971. doi:10.1017/S002211207100048X.

[100] M. Eisenbach and L. C. Giojalas. Sperm guidance in mammals—an unpaved road to the egg. Nat. Rev. Mol. Cell Biol., 7(4):276–285, 2006. doi:10.1038/nrm1893.

[101] C. R. Austin and R. V. Short. Reproduction of Mammals. Cambridge University Press, 1982. ISBN 0521246288. doi:10.1002/mrd.1120240115.

[102] G. S. Fraenkel and D. L. Gunn. The orientation of animals: Kineses, taxes and compass reactions. Dover Publications, 1961. doi:10.1126/science.136.3517.707-b.

[103] A. Bahat, I. Tur-Kaspa, A. Gakamsky, L. C. Giojalas, H. Breitbart, and M. Eisenbach. Thermotaxis of mammalian sperm cells: a potential navigation mechanism in the female genital tract. Nat. Med., 9(2):149–150, 2003. doi:10.1038/nm0203-149.

[104] A. Bahat, S. R. Caplan, and M. Eisenbach. Thermotaxis of human sperm cells in extraordinarily shallow temperature gradients over a wide range. PloS one, 7(7):e41915, 2012. doi:10.1371/journal.pone.0041915.

[105] S. Boryshpolets, S. Pérez-Cerezales, and M. Eisenbach. Behavioral mechanism of human sperm in thermotaxis: a role for hyperactivation. Hum. Repr., 30(4):884–892, 2015. doi:10.1093/humrep/dev002.

[106] M. Eisenbach. Sperm chemotaxis. Rev. Reprod., 4(1):56–66, 1999. doi:10.1530/ror.0.0040056.

[107] L. Armon and M. Eisenbach. Behavioral mechanism during human sperm chemotaxis: involvement of hyperactivation. PloS one, 6(12):e28359, 2011. doi:10.1371/journal.pone.0028359.

[108] F. P. Bretherton and L. Rothschild. Rheotaxis of spermatozoa. Proc. R. Soc. B, 153(953):

490–502, 1961. doi:10.1098/rspb.1961.0014.

[109] J. A. Riffell and R. K. Zimmer. Sex and flow: The consequences of fluid shear for sperm–egg interactions. J. Exp. Biol., 210(20):3644–3660, 2007. doi:10.1242/jeb.008516.

[110] K. Miki and D. E. Clapham. Rheotaxis guides mammalian sperm. Curr. Biol., 23(6):443 – 452, 2013. doi:10.1016/j.cub.2013.02.007.

[111] V. Kantsler, J. Dunkel, M. Blayney, and R. E. Goldstein. Rheotaxis facilitates upstream navigation of mammalian sperm cells. eLife, 3:e02403, 2014. doi:10.7554/eLife.02403.

[112] K. Shiba, S. A. Baba, T. Inoue, and M. Yoshida. $Ca.^{2+}$ bursts occur around a local minimal concentration of attractant and trigger sperm chemotactic response. Proc. Nat. Acad. Sci., 105 (49):19312–19317, 2008. doi:10.1073/pnas.0808580105.

[113] U. B. Kaupp, N. D. Kashikar, and I. Weyand. Mechanisms of sperm chemotaxis. Annu. Rev. Physiol., 70:93–117, 2008. doi:10.1146/annurev.physiol.70.113006.100654.

[114] D. F. Katz, J. W. Overstreet, S. J. Samuels, P. W. Niswander, T. D. Bloom, and E. L. Lewis. Morphometric analysis of spermatozoa in the assessment of human male fertility. J. Andrology, 7(4):203–210, 1986. doi:10.1002/j.1939-4640.1986.tb00913.x.

[115] S. Pitnick, G. S. Spicer, T. A. Markow, et al. How long is a giant sperm. Nature, 375(6527): 109–109, 1995. doi:10.1038/375109a0.

[116] S. Lüpold, M. K. Manier, N. Puniamoorthy, C. Schoff, W. T. Starmer, S. H. B. Luepold, J. M. Belote, and S. Pitnick. How sexual selection can drive the evolution of costly sperm ornamentation. Nature, 533(7604):535–538, 2016. doi:10.1038/nature18005.

[117] J. Gray and G. Hancock. The propulsion of sea-urchin spermatozoa. J. Exp. Biol., 32(4): 802–814, 1955. URL http://jeb.biologists.org/content/32/4/802.

[118] B. Friedrich, I. Riedel-Kruse, J. Howard, and F. Jülicher. High-precision tracking of sperm swimming fine structure provides strong test of resistive force theory. J. Exp. Biol., 213(8): 1226–1234, 2010. doi:10.1242/jeb.039800.

[119] D. Woolley. Motility of spermatozoa at surfaces. Reprod., 126:259, 2003. doi:10.1530/rep.0.1260259.

[120] L. Alvarez, B. M. Friedrich, G. Gompper, and U. B. Kaupp. The computational sperm cell. Trends Cell Biol., 24(3):198–207, 2014. doi:10.1016/j.tcb.2013.10.004.

[121] J. F. Jikeli, L. Alvarez, B. M. Friedrich, L. G. Wilson, R. Pascal, R. Colin, M. Pichlo, A. Rennhack, C. Brenker, and U. B. Kaupp. Sperm navigation along helical paths in 3D chemoattractant landscapes. Nat. Comm., 6, 2015. doi:10.1038/ncomms8985.

[122] R. Golestanian, T. B. Liverpool, and A. Ajdari. Designing phoretic micro- and nano-swimmers. New J. Phys., 9(5):126, 2007. doi:10.1088/1367-2630/9/5/126.

[123] S. J. Ebbens and J. R. Howse. In pursuit of propulsion at the nanoscale. Soft Matter, 6(4): 726–738, 2010. doi:10.1039/B918598D.

[124] W. Gao and J. Wang. Synthetic micro/nanomotors in drug delivery. Nanoscale, 6(18):10486–10494, 2014. doi:10.1039/C4NR03124E.

[125] S. Sánchez, L. Soler, and J. Katuri. Chemically powered micro-and nanomotors. Angew. Chem. Int. Ed., 54(5):1414–1444, 2015. doi:10.1002/anie.201406096.

[126] S. Thutupalli. Towards Autonomous Soft Matter Systems. Springer, 2014. ISBN 3319007343.

[127] W. F. Paxton, K. C. Kistler, C. C. Olmeda, A. Sen, S. K. St. Angelo, Y. Cao, T. E. Mallouk, P. E. Lammert, and V. H. Crespi. Catalytic nanomotors: Autonomous movement of striped nanorods. J. Am. Chem. Soc., 126(41):13424–13431, 2004. doi:10.1021/ja047697z.

[128] A. A. Solovev, W. Xi, D. H. Gracias, S. M. Harazim, C. Deneke, S. Sanchez, and O. G. Schmidt. Self-propelled nanotools. ACS Nano, 6(2):1751–1756, 2012. doi:10.1021/nn204762w.

[129] S. Herminghaus, C. C. Maass, C. Krüger, S. Thutupalli, L. Goehring, and C. Bahr. Interfacial mechanisms in active emulsions. Soft Matter, 10(36):7008–7022, 2014. doi:10.1039/C4SM00550C.

[130] L. Zhang, J. J. Abbott, L. Dong, K. E. Peyer, B. E. Kratochvil, H. Zhang, C. Bergeles, and B. J. Nelson. Characterizing the swimming properties of artificial bacterial flagella. Nano Lett., 9(10):3663–3667, 2009. doi:10.1021/nl901869j.

[131] P.-G. de Gennes. Soft matter (nobel lecture). Angew. Chem., 31(7):842–845, 1992. doi:10.1002/anie.199208421.

[132] C. Casagrande and M. Veyssie. Janus beads-realization and 1st observation of interfacial properties. C. R. Acad. Sci. II (Paris), 306(20):1423–1425, 1988. URL http://gallica.bnf.fr/ark:/12148/cb34394200t/.

[133] S. Fournier-Bidoz, A. C. Arsenault, I. Manners, and G. A. Ozin. Synthetic self-propelled nanorotors. Chem. Comm., 4:441–443, 2005. doi:10.1039/B414896G.

[134] R. Golestanian, T. B. Liverpool, and A. Ajdari. Propulsion of a molecular machine by asymmetric distribution of reaction products. Phys. Rev. Lett., 94(22):220801, 2005. doi:10.1103/PhysRevLett.94.220801.

[135] G. Rückner and R. Kapral. Chemically powered nanodimers. Phys. Rev. Lett., 98(15):150603, 2007. doi:10.1103/physrevlett.98.150603.

[136] R. Golestanian. Anomalous diffusion of symmetric and asymmetric active colloids. Phys. Rev. Lett., 102(18):188305, 2009. doi:10.1103/PhysRevLett.102.188305.

[137] M. Popescu, S. Dietrich, M. Tasinkevych, and J. Ralston. Phoretic motion of spheroidal particles due to self-generated solute gradients. Eur. Phys. J. E, 31(4):351–367, 2010. doi:10.1140/epje/i2010-10593-3.

[138] B. Sabass and U. Seifert. Dynamics and efficiency of a self-propelled, diffusiophoretic swimmer. J. Chem. Phys., 136(6):064508, 2012. doi:10.1063/1.3681143.

[139] A. Brown and W. Poon. Ionic effects in self-propelled pt-coated Janus swimmers. Soft Matter, 10(22):4016–4027, 2014. doi:10.1039/C4SM00340C.

[140] W. E. Uspal, M. N. Popescu, S. Dietrich, and M. Tasinkevych. Self-propulsion of a catalytically active particle near a planar wall: from reflection to sliding and hovering. Soft Matter, 11(3): 434–438, 2015. doi:10.1039/c4sm02317j.

[141] A. Erbe, M. Zientara, L. Baraban, C. Kreidler, and P. Leiderer. Various driving mechanisms for generating motion of colloidal particles. J. Phys. Cond. Mat., 20(40):404215, 2008. doi:10.1088/0953-8984/20/40/404215.

[142] J. R. Howse, R. A. Jones, A. J. Ryan, T. Gough, R. Vafabakhsh, and R. Golestanian. Self-motile colloidal particles: From directed propulsion to random walk. Phys. Rev. Lett., 99(4):048102, 2007. doi:10.1103/PhysRevLett.99.048102.

[143] J. Palacci, S. Sacanna, A. P. Steinberg, D. J. Pine, and P. M. Chaikin. Living crystals of light-activated colloidal surfers. Science, 339(6122):936–940, 2013. doi:10.1126/science.1230020.

[144] H.-R. Jiang, N. Yoshinaga, and M. Sano. Active motion of a Janus particle by self-thermophoresis in a defocused laser beam. Phys. Rev. Lett., 105:268302, 2010. doi:10.1103/physrevlett.105.268302.

[145] T. Bickel, A. Majee, and A. Würger. Flow pattern in the vicinity of self-propelling hot Janus particles. Phys. Rev. E, 88:012301, 2013. doi:10.1103/physreve.88.012301.

[146] M. Braun and F. Cichos. Optically controlled thermophoretic trapping of single nano-objects. ACS Nano, 7(12):11200–11208, 2013. doi:10.1021/nn404980k.

[147] P. de Buyl and R. Kapral. Phoretic self-propulsion: a mesoscopic description of reaction dynamics that powers motion. Nanoscale, 5(4):1337–1344, 2013. doi:10.1039/C2NR33711H.

[148] G. Volpe, I. Buttinoni, D. Vogt, H.-J. Kümmerer, and C. Bechinger. Microswimmers in patterned environments. Soft Matter, 7(19):8810–8815, 2011. doi:10.1039/C1SM05960B.

[149] J. R. Gomez-Solano, A. Blokhuis, and C. Bechinger. Dynamics of self-propelled Janus particles in viscoelastic fluids. Phys. Rev. Lett., 116(13):138301, 2016. doi:10.1103/PhysRevLett.116.138301.

[150] A. A. Solovev, S. Sanchez, M. Pumera, Y. F. Mei, and O. G. Schmidt. Magnetic control of tubular catalytic microbots for the transport, assembly, and delivery of micro-objects. Adv. Funct. Mater., 20(15):2430–2435, 2010. doi:10.1002/adfm.200902376.

[151] S. Sanchez, A. A. Solovev, S. M. Harazim, C. Deneke, Y. Feng Mei, and O. G. Schmidt. The smallest man-made jet engine. Chem. Rec., 11(6):367–370, 2011. doi:10.1002/tcr.201100010.

[152] S. Thutupalli, R. Seemann, and S. Herminghaus. Swarming behavior of simple model squirmers. New J. Phys., 13(7):073021, 2011. doi:10.1088/1367-2630/13/7/073021.

[153] H. Ebata and M. Sano. Swimming droplets driven by a surface wave. Scient. Rep., 5, 2015. doi:10.1038/srep08546.

[154] A. A. Darhuber and S. M. Troian. Principles of microfluidic actuation by modulation of surface stresses. Annu. Rev. Fluid Mech., 37:425–455, 2005. doi:10.1146/annurev.fluid.36.050802.122052.

[155] J. Zhang, Y. Yao, L. Sheng, and J. Liu. Self-fueled biomimetic liquid metal mollusk. Adv. Mat., 27(16):2648–2655, 2015. doi:10.1002/adma.201405438.

[156] K. E. Peyer, S. Tottori, F. Qiu, L. Zhang, and B. J. Nelson. Magnetic helical micromachines. Chem. Eur. J., 19(1):28–38, 2013. doi:10.1002/chem.201203364.

[157] H. Gadêlha. On the optimal shape of magnetic swimmers. Reg. Chaot. Dyn., 18(1-2):75–84,

2013. doi:10.1134/S156035471301005X.

[158] P. Katsamba and E. Lauga. Micro-tug-of-war: A selective control mechanism for magnetic swimmers. Phys. Rev. Appl., in press, 2016. URL https://journals.aps.org/prapplied/accepted/9e07aA5dAaf1c700501d45e8cb6abdde54b13eef3.

[159] B. A. Grzybowski, H. A. Stone, and G. M. Whitesides. Dynamic self-assembly of magnetized, millimetre-sized objects rotating at a liquid–air interface. Nature, 405(6790):1033–1036, 2000. doi:10.1038/35016528.

[160] P. Tierno, R. Golestanian, I. Pagonabarraga, and F. Sagués. Controlled swimming in confined fluids of magnetically actuated colloidal rotors. Phys. Rev. Lett., 101(21):218304, 2008. doi:10.1103/PhysRevLett.101.218304.

[161] R. Dreyfus, J. Baudry, M. L. Roper, M. Fermigier, H. A. Stone, and J. Bibette. Microscopic artificial swimmers. Nature, 437(7060):862–865, 2005. doi:10.1038/nature04090.

[162] G. Katsikis, J. S. Cybulski, and M. Prakash. Synchronous universal droplet logic and control. Nat. Phys., 2015. doi:10.1038/nphys3341.

[163] S. Kim and S. Karilla. Microhydrodynamics: principles and selected applications. Dover Publications, ed. Howard Brenner, 1991. ISBN 978-0-7506-9173-4.

[164] L. D. Landau and E. M. Lifshitz. Fluid Mechanics, volume 6 of A Course of Theoretical Physics. Pergamon Press, London, 1959. ISBN 0750627670.

[165] C. L. M. H. Navier. Memoir on the laws of fluid motion. Mem. Acad. Sci. (Paris), 6:389–416, 1827.

[166] G. Orwell. Animal Farm: A Fairy Story. Secker and Warburg, London, 1945. ISBN 0452284244.

[167] C.-C. Huang, G. Gompper, and R. G. Winkler. Hydrodynamic correlations in multiparticle collision dynamics fluids. Phys. Rev. E, 86(5):056711, 2012. doi:10.1103/PhysRevE.86.056711.

[168] G. I. Taylor. Film notes for: Low Reynolds-number Flows. National Committee for Fluid Mechanics Films, 1967. URL http://web.mit.edu/hml/ncfmf/07LRNF.pdf.

[169] Olivier Dauchot. Chaotic mixing. URL http://iramis.cea.fr/Phocea/Vie_des_labos/Ast/ast_visu.php?id_ast=993.

[170] E. Lauga. Life around the scallop theorem. Soft Matter, 7(7):3060–3065, 2011. doi:10.1039/C0SM00953A.

[171] G. Mathew, I. Mezić, S. Grivopoulos, U. Vaidya, and L. Petzold. Optimal control of mixing in stokes fluid flows. J. Fluid Mech., 580:261–281, 2007. doi:10.1017/S0022112007005332.

[172] National Committee for Fluid Mechanics Films. Illustrated experiments in fluid mechanics. URL http://web.mit.edu/hml/ncfmf.html.

[173] E. Gouillart, N. Kuncio, O. Dauchot, B. Dubrulle, S. Roux, and J.-L. Thiffeault. Walls inhibit chaotic mixing. Phys. Rev. Lett., 99:114501, Sep 2007. doi:10.1103/PhysRevLett.99.114501.

[174] E. Gouillart, O. Dauchot, J.-L. Thiffeault, and S. Roux. Open-flow mixing: Experimental evidence for strange eigenmodes. Phys. Fluids, 21(2):023603, 2009. doi:10.1063/1.3080680.

[175] E. Gouillart, J.-L. Thiffeault, and O. Dauchot. Rotation shields chaotic mixing regions from no-slip walls. Phys. Rev. Lett., 104:204502, May 2010. doi:10.1103/PhysRevLett.104.204502.

[176] A. D. Stroock, S. K. Dertinger, A. Ajdari, I. Mezić, H. A. Stone, and G. M. Whitesides. Chaotic mixer for microchannels. Science, 295(5555):647–651, 2002. doi:10.1126/science.1066238.

[177] H. A. Stone, A. D. Stroock, and A. Ajdari. Engineering flows in small devices: microfluidics toward a lab-on-a-chip. Annu. Rev. Fluid Mech., 36:381–411, 2004. doi:10.1146/annurev.fluid.36.050802.122124.

[178] D. Link, S. L. Anna, D. Weitz, and H. Stone. Geometrically mediated breakup of drops in microfluidic devices. Phys. Rev. Lett., 92(5):054503, 2004. doi:10.1103/PhysRevLett.92.054503.

[179] P. L. Boyland, H. Aref, and M. A. Stremler. Topological fluid mechanics of stirring. J. Fluid Mech., 403:277–304, 2000. doi:10.1017/S0022112099007107.

[180] J. M. Yeomans, D. O. Pushkin, and H. Shum. An introduction to the hydrodynamics of swimming microorganisms. Eur. Phys. J. Spec. Top., 223(9), 2014. doi:10.1140/epjst/e2014-02225-8.

[181] J. Lighthill. Reinterpreting the basic theorem of flagellar hydrodynamics. J. Eng. Math., pages 25–34, 1996. doi:10.1007/bf00118822.

[182] J. Lighthill. Helical distributions of Stokeslets. J. Eng. Math., 30(1-2):35–78, 1996. doi:10.1007/BF00118823.

[183] J. R. Blake. A note on the image system for a Stokeslet in a no-slip boundary. Math. Proc. Camb. Phil. Soc, 70:303 – 310, 1971. doi:10.1017/S0305004100049902.

[184] N. Liron and S. Mochon. Stokes flow for a Stokeslet between two parallel flat plates. J. Eng. Math., 10(4):287–303, 1976. doi:10.1007/BF01535565.

[185] M. E. Staben, A. Z. Zinchenko, and R. H. Davis. Motion of a particle between two parallel plane walls in low-Reynolds-number Poiseuille flow. Phys. Fluids, 15(6):1711–1733, 2003. doi:10.1063/1.1568341.

[186] D. Crowdy, S. Lee, O. Samson, E. Lauga, and A. E. Hosoi. A two-dimensional model of low-Reynolds number swimming beneath a free surface. J. Fluid Mech., 681:24–47, 2011. doi:10.1017/jfm.2011.223.

[187] A. Doostmohammadi, R. Stocker, and A. Ardekani. Low-Reynolds-number swimming at pycnoclines. Proc. Nat. Ac. Sci., 109:3856, 2012. doi:10.1073/pnas.1116210109.

[188] N. V. Bukoreshtliev, K. Haase, and A. E. Pelling. Mechanical cues in cellular signalling and communication. Cell Tiss. Res., 352(1):77–94, 2013. ISSN 0302-766X. doi:10.1007/s00441-012-1531-4.

[189] T. Ishikawa and T. Pedley. The rheology of a semi-dilute suspension of swimming model micro-organisms. J. Fluid Mech., 588:399–435, 2007. doi:10.1017/S0022112007007835.

[190] J. Gachelin, G. Miño, H. Berthet, A. Lindner, A. Rousselet, and É. Clément. Non-Newtonian viscosity of *Escherichia coli* suspensions. Phys. Rev. Lett., 110(26):268103, 2013. doi:10.1103/PhysRevLett.110.268103.

[191] H. M. López, J. Gachelin, C. Douarche, H. Auradou, and E. Clément. Turning bacteria suspensions into superfluids. Phys. Rev. Lett., 115:028301, Jul 2015. doi:10.1103/PhysRevLett.115.028301.

[192] M. J. Kim and K. S. Breuer. Controlled mixing in microfluidic systems using bacterial chemotaxis. Anal. Chem., 79(3):955–959, 2007. doi:10.1021/ac0614691.

[193] K. C. Leptos, J. S. Guasto, J. Gollub, A. I. Pesci, and R. E. Goldstein. Dynamics of enhanced tracer diffusion in suspensions of swimming eukaryotic microorganisms. Phys. Rev. Lett., 103 (19):198103, 2009. doi:10.1103/PhysRevLett.103.198103.

[194] T. Ishikawa, J. Locsei, and T. Pedley. Fluid particle diffusion in a semidilute suspension of model micro-organisms. Phys. Rev. E, 82(2):021408, 2010. doi:10.1103/PhysRevE.82.021408.

[195] H. Kurtuldu, J. S. Guasto, K. A. Johnson, and J. Gollub. Enhancement of biomixing by swimming algal cells in two-dimensional films. Proc. Nat. Acad. Sci., 108(26):10391–10395, 2011. doi:10.1073/pnas.1107046108.

[196] G. Mino, T. E. Mallouk, T. Darnige, M. Hoyos, J. Dauchet, J. Dunstan, R. Soto, Y. Wang, A. Rousselet, and E. Clement. Enhanced diffusion due to active swimmers at a solid surface. Phys. Rev. Lett., 106(4):048102, 2011. doi:10.1103/PhysRevLett.106.048102.

[197] A. Karimi and A. Ardekani. Gyrotactic bioconvection at pycnoclines. J. Fluid Mech., 733: 245–267, 2013. doi:10.1017/jfm.2013.415.

[198] D. O. Pushkin and J. M. Yeomans. Stirring by swimmers in confined microenvironments. J. Stat. Mech., 2014(4):P04030, 2014. doi:10.1088/1742-5468/2014/04/P04030.

[199] V. Magar, T. Goto, and T. J. Pedley. Nutrient uptake by a self-propelled steady squirmer. Quart. J. Mech. App. Math., 56(1):65–91, 2003. doi:10.1093/qjmam/56.1.65.

[200] K. Katija. Biogenic inputs to ocean mixing. J. Exp. Biol., 215(6):1040–1049, 2012. doi:10.1242/jeb.059279.

[201] A. Jepson, V. A. Martinez, J. Schwarz-Linek, A. Morozov, and W. C. Poon. Enhanced diffusion of nonswimmers in a three-dimensional bath of motile bacteria. Phys. Rev. E, 88(4):041002, 2013. doi:10.1103/PhysRevE.88.041002.

[202] J. D. Jackson. Classical electrodynamics. John Wiley and sons, New York etc., 3 edition, 1998. ISBN 047130932X.

[203] D. J. Jeffrey and Y. Onishi. Calculation of the resistance and mobility functions for two unequal rigid spheres in low-Reynolds-number flow. J. Fluid Mech., 139:261–290, 2 1984. ISSN 1469-7645. doi:10.1017/S0022112084000355.

[204] T. Ishikawa, M. Simmonds, and T. Pedley. Hydrodynamic interaction of two swimming model micro-organisms. J. Fluid Mech., 568:119–160, 2006. doi:10.1017/S0022112006002631.

[205] K. Drescher, J. Dunkel, L. H. Cisneros, S. Ganguly, and R. E. Goldstein. Fluid dynamics and noise in bacterial cell–cell and cell–surface scattering. Proc. Nat. Acad. Sci., 108(27): 10940–10945, 2011. doi:10.1073/pnas.1019079108.

[206] I. Grant. Particle image velocimetry: A review. Proc. Inst. Mech. Eng. C, 211(1):55–76, 1997.

doi:10.1243/0954406971521665.

[207] K. Y. Wan and R. E. Goldstein. Coordinated beating of algal flagella is mediated by basal coupling. Proc. Nat. Acad. Sci., 113(20):E2784–E2793, 2016. doi:10.1073/pnas.1518527113.

[208] K. Drescher, R. E. Goldstein, N. Michel, M. Polin, and I. Tuval. Direct measurement of the flow field around swimming microorganisms. Phys. Rev. Lett., 105(168101), 2010. doi:10.1103/PhysRevLett.105.168101.

[209] L. Turner, W. S. Ryu, and H. C. Berg. Real-time imaging of fluorescent flagellar filaments. J. Bacteriol., 182(10):2793–2801, 2000. doi:10.1128/JB.182.10.2793-2801.2000.

[210] R. Kamiya and E. Hasegawa. Intrinsic difference in beat frequency between the two flagella of *C*hlamydomonas reinhardtii. Exp. Cell Res., 173(1):299–304, 1987. doi:10.1016/0014-4827(87)90357-0.

[211] T. Ishikawa, G. Sekiya, Y. Imai, and T. Yamaguchi. Hydrodynamic interactions between two swimming bacteria. Biophys. J., 93(6):2217–2225, 2007. doi:10.1529/biophysj.107.110254.

[212] I. O. Götze and G. Gompper. Mesoscale simulations of hydrodynamic squirmer interactions. Phys. Rev. E, 82(4):041921, 2010. doi:10.1103/PhysRevE.82.041921.

[213] T. Ishikawa, J. Locsei, and T. Pedley. Development of coherent structures in concentrated suspensions of swimming model micro-organisms. J. Fluid Mech., 615:401, 2008. doi:10.1017/S0022112008003807.

[214] A. Zöttl and H. Stark. Nonlinear dynamics of a microswimmer in Poiseuille flow. Phys. Rev. Lett., 108(21):218104, 2012. doi:10.1103/PhysRevLett.108.218104.

[215] I. Pagonabarraga and I. Llopis. The structure and rheology of sheared model swimmer suspensions. Soft Matter, 9:7174, 2013. doi:10.1039/C3SM51258D.

[216] G.-J. Li and A. M. Ardekani. Hydrodynamic interaction of microswimmers near a wall. Phys. Rev. E, 90:013010, Jul 2014. doi:10.1103/PhysRevE.90.013010.

[217] J. Lintuvuori, A. Brown, K. Stratford, and D. Marenduzzo. Hydrodynamic oscillations and tunable swimming speed in squirmers close to repulsive walls. arxiv, 1508.04255:1, 2015. URL `http://arxiv.org/abs/1508.04255`.

[218] M. Downton and H. Stark. Simulation of a model microswimmer. J. Phys. Cond. Mat., 21: 204101, 2009. doi:10.1088/0953-8984/21/20/204101.

[219] A. Zöttl and H. Stark. Hydrodynamics determines collective motion and phase behavior of active colloids in quasi-two-dimensional confinement. Phys. Rev. Lett., 112:118101, 2014. doi:10.1103/physrevlett.112.118101.

[220] K. Schaar, A. Zöttl, and H. Stark. Detention times of microswimmers close to surfaces: Influence of hydrodynamic interactions and noise. Phys. Rev. Lett., 115:038101, 2015. doi:10.1103/PhysRevLett.115.038101.

[221] L. Zhu, E. Lauga, and L. Brandt. Low-Reynolds-number swimming in a capillary tube. J. Fluid Mech., 726:285, 2013. doi:10.1017/jfm.2013.225.

[222] J. Molina, Y. Nakayama, and R. Yamamoto. Hydrodynamic interactions of self-propelled swimmers. Soft Matter, 9:4923–4936, 2013. doi:10.1039/c3sm00140g.

[223] R. Matas-Navarro, R. Golestanian, T. Liverpool, and S. M. Fielding. Hydrodynamic suppression of phase separation in active suspensions. Phys. Rev. E, 90:032304, 2014. doi:10.1103/physreve.90.032304.

[224] B. Delmotte, E. Keaveny, F. Plouraboué, and E. Climent. Large-scale simulation of steady and time-dependent active suspensions with the force-coupling method. J. Comp. Phys., 302:524, 2015. doi:10.1016/j.jcp.2015.09.020.

[225] A. Najafi and R. Golestanian. Simple swimmer at low Reynolds number: Three linked spheres. Phys. Rev. E, 69(6):062901, 2004. doi:10.1103/PhysRevE.69.062901.

[226] J. Dunkel, V. B. Putz, I. M. Zaid, and J. M. Yeomans. Swimmer-tracer scattering at low Reynolds number. Soft Matter, 6(17):4268–4276, 2010. doi:10.1039/c0sm00164c.

[227] J. Avron, O. Kenneth, and D. Oaknin. Pushmepullyou: An efficient micro-swimmer. New J. Phys., 7(1):234, 2005. doi:10.1088/1367-2630/7/1/234.

[228] G. P. Alexander and J. M. Yeomans. Dumb-bell swimmers. Europhys. Lett., 83(3):34006, 2008. doi:10.1209/0295-5075/83/34006.

[229] E. Lauga and D. Bartolo. No many-scallop theorem: Collective locomotion of reciprocal swimmers. Phys. Rev. E, 78(3):030901, 2008. doi:10.1103/PhysRevE.78.030901.

[230] R. Golestanian and A. Ajdari. Analytic results for the three-sphere swimmer at low Reynolds

number. Phys. Rev. E, 77(3):036308, 2008. doi:10.1103/PhysRevE.77.036308.

[231] R. Golestanian and A. Ajdari. Mechanical response of a small swimmer driven by conformational transitions. Phys. Rev. Lett., 100(3):038101, 2008. doi:10.1103/PhysRevLett.100.038101.

[232] R. Golestanian. Three-sphere low-Reynolds-number swimmer with a cargo container. Eur. Phys. J. E, 25(1):1–4, 2008. doi:10.1140/epje/i2007-10276-2.

[233] D. J. Earl, C. Pooley, J. Ryder, I. Bredberg, and J. M. Yeomans. Modeling microscopic swimmers at low Reynolds number. J. Chem. Phys., 126(6):064703, 2007. doi:10.1063/1.2434160.

[234] C. Pooley, G. Alexander, and J. Yeomans. Hydrodynamic interaction between two swimmers at low Reynolds number. Phys. Rev. Lett., 99(22):228103, 2007. doi:10.1103/physrevlett.99.228103.

[235] G. P. Alexander, C. Pooley, and J. M. Yeomans. Scattering of low-Reynolds-number swimmers. Phys. Rev. E, 78(4):045302, 2008. doi:10.1103/PhysRevE.78.045302.

[236] G. P. Alexander, C. M. Pooley, and J. M. Yeomans. Hydrodynamics of linked sphere model swimmers. J. Phys. Cond. Mat., 21(20):204108, 2009. doi:10.1088/0953-8984/21/20/204108.

[237] G. P. Alexander and J. M. Yeomans. Hydrodynamic interactions at low Reynolds number. Exp. Mech., 50(9):1283–1292, 2010. doi:10.1007/s11340-010-9387-6.

[238] S. E. Spagnolie and E. Lauga. Hydrodynamics of self-propulsion near a boundary: Predictions and accuracy of far-field approximations. J. Fluid Mech., 700:105–147, 2012. doi:10.1017/jfm.2012.101.

[239] R. Rusconi, J. S. Guasto, and R. Stocker. Bacterial transport suppressed by fluid shear. Nat. Phys., 10(3):212–217, 2014. doi:10.1038/nphys2883.

[240] H. C. Crenshaw. A new look at locomotion in microorganisms: rotating and translating. Amer. Zool., 36(6):608–618, 1996. doi:10.1093/icb/36.6.608.

[241] R. Ledesma-Aguilar, H. Löwen, and J. M. Yeomans. A circle swimmer at low Reynolds number. Eur. Phys. J. E, 35(8):1–9, 2012. doi:10.1140/epje/i2012-12070-5.

[242] F. Kümmel, B. ten Hagen, R. Wittkowski, I. Buttinoni, R. Eichhorn, G. Volpe, H. Löwen, and C. Bechinger. Circular motion of asymmetric self-propelling particles. Phys. Rev. Lett., 110: 198302, 2013. doi:10.1103/physrevlett.110.198302.

[243] R. M. Harshey. Bacterial motility on a surface: Many ways to a common goal. Annu. Rev. Microbiol., 57(1):249–273, 2003. doi:10.1146/annurev.micro.57.030502.091014.

[244] L. Rothschild. Non-random distribution of bull spermatozoa in a drop of sperm suspension. Nature, 198(488):1221, 1963. doi:10.1038/1981221a0.

[245] P. D. Frymier, R. M. Ford, H. C. Berg, and P. T. Cummings. Three-dimensional tracking of motile bacteria near a solid planar surface. Proc. Nat. Acad. Sci., 92(13):6195–6199, 1995. URL http://www.pnas.org/content/92/13/6195.short.

[246] A. P. Berke, L. Turner, H. C. Berg, and E. Lauga. Hydrodynamic attraction of swimming microorganisms by surfaces. Phys. Rev. Lett., 101(3):038102, 2008. doi:10.1103/PhysRevLett.101.038102.

[247] G. Li and J. X. Tang. Accumulation of microswimmers near a surface mediated by collision and rotational brownian motion. Phys. Rev. Lett., 103:078101, Aug 2009. doi:10.1103/PhysRevLett.103.078101.

[248] G. Li, J. Bensson, L. Nisimova, D. Munger, P. Mahautmr, J. X. Tang, M. R. Maxey, and Y. V. Brun. Accumulation of swimming bacteria near a solid surface. Phys. Rev. E, 84(4):041932, 2011. doi:10.1103/PhysRevE.84.041932.

[249] J. Leach, H. Mushfique, S. Keen, R. Di Leonardo, G. Ruocco, J. M. Cooper, and M. J. Padgett. Comparison of Faxén's correction for a microsphere translating or rotating near a surface. Phys. Rev. E, 79:026301, Feb 2009. doi:10.1103/PhysRevE.79.026301.

[250] V. Kantsler, J. Dunkel, M. Polin, and R. E. Goldstein. Ciliary contact interactions dominate surface scattering of swimming eukaryotes. Proc. Nat. Acad. Sci., 110(4):1187–1192, 2013. doi:10.1073/pnas.1210548110.

[251] I. Vladescu, E. Marsden, J. Schwarz-Linek, V. Martinez, J. Arlt, A. Morozov, D. Marenduzzo, M. Cates, and W. Poon. Filling an emulsion drop with motile bacteria. Phys. Rev. Lett., 113 (26):268101, 2014. doi:10.1103/physrevlett.113.268101.

[252] T. J. Pedley and J. O. Kessler. The orientation of spheroidal microorganisms swimming in a flow field. Proc. R. Soc. B, 231(1262):47–70, 1987. ISSN 0080-4649. doi:10.1098/rspb.1987.0035.

[253] E. Lauga, W. R. DiLuzio, G. M. Whitesides, and H. A. Stone. Swimming in circles: Motion of bacteria near solid boundaries. Biophys. J., 90(2):400–412, 2006. doi:10.1529/biophysj.105.069401.

[254] Y. Or and R. M. Murray. Dynamics and stability of a class of low Reynolds number swimmers near a wall. Phys. Rev. E, 79:045302, Apr 2009. doi:10.1103/PhysRevE.79.045302.

[255] D. G. Crowdy and Y. Or. Two-dimensional point singularity model of a low-Reynolds-number swimmer near a wall. Phys. Rev. E, 81:036313, Mar 2010. doi:10.1103/PhysRevE.81.036313.

[256] J. Elgeti and G. Gompper. Self-propelled rods near surfaces. Eur. Phys. Lett., 85(3):38002, 2009. doi:10.1209/0295-5075/85/38002.

[257] H. Shum, E. A. Gaffney, and D. J. Smith. Modelling bacterial behaviour close to a no-slip plane boundary: The influence of bacterial geometry. Proc. R. Soc. A, 2010. doi:10.1098/rspa.2009.0520.

[258] J. Elgeti and G. Gompper. Wall accumulation of self-propelled spheres. Europhys. Lett., 101 (4):48003, 2013. doi:10.1209/0295-5075/101/48003.

[259] G.-J. Li, A. Karimi, and A. Ardekani. Effect of solid boundaries on swimming dynamics of microorganisms in a viscoelastic fluid. Rheol. Acta, 53(12):911–926, 2014. doi:10.1007/s00397-014-0796-9.

[260] K. Martens, L. Angelani, R. Di Leonardo, and L. Bocquet. Probability distributions for the run-and-tumble bacterial dynamics: An analogy to the Lorentz model. Eur. Phys. J. E, 35(9): 84, 2012. ISSN 1292-8941. doi:10.1140/epje/i2012-12084-y.

[261] J. Elgeti, U. B. Kaupp, and G. Gompper. Hydrodynamics of sperm cells near surfaces. Biophys. J., 99(4):1018 – 1026, 2010. ISSN 0006-3495. doi:10.1016/j.bpj.2010.05.015.

[262] A. Costanzo, J. Elgeti, T. Auth, G. Gompper, and M. Ripoll. Motility-sorting of self-propelled particles in microchannels. Eur. Phys. Lett., 107(3):36003, 2014. doi:10.1209/0295-5075/107/36003.

[263] J. Elgeti and G. Gompper. Run-and-tumble dynamics of self-propelled particles in confinement. Eur. Phys. Lett., 109(5):58003, 2015. doi:10.1209/0295-5075/109/58003.

[264] M. Van Loosdrecht, J. Lyklema, W. Norde, and A. Zehnder. Influence of interfaces on microbial activity. Microbiol. Rev., 54(1):75–87, 1990. URL http://mmbr.asm.org/content/54/1/75.

[265] J. W. Costerton, Z. Lewandowski, D. E. Caldwell, D. R. Korber, and H. M. Lappin-Scott. Microbial biofilms. Annu. Rev. Microbiol., 49(1):711–745, 1995. doi:10.1146/annurev.mi.49.100195.003431.

[266] A. Kaiser, H. H. Wensink, and H. Löwen. How to capture active particles. Phys. Rev. Lett., 108:268307, Jun 2012. doi:10.1103/PhysRevLett.108.268307.

[267] D. Papavassiliou and G. P. Alexander. Orbits of swimmers around obstacles. arXiv:1407.1337, 2014. URL http://arxiv.org/abs/1407.1337.

[268] D. Takagi, J. Palacci, A. B. Braunschweig, M. J. Shelley, and J. Zhang. Hydrodynamic capture of microswimmers into sphere-bound orbits. Soft matter, 10(11):1784–1789, 2014. doi:10.1039/c3sm52815d.

[269] S. E. Spagnolie, G. R. Moreno-Flores, D. Bartolo, and E. Lauga. Geometric capture and escape of a microswimmer colliding with an obstacle. Soft Matter, 11(17):3396–3411, 2015. doi:10.1039/C4SM02785J.

[270] O. Sipos, K. Nagy, R. Di Leonardo, and P. Galajda. Hydrodynamic trapping of swimming bacteria by convex walls. Phys. Rev. Lett., 114:258104, Jun 2015. doi:10.1103/PhysRevLett.114.258104.

[271] L. Angelani, R. Di Leonardo, and G. Ruocco. Self-starting micromotors in a bacterial bath. Phys. Rev. Lett., 102:048104, Jan 2009. doi:10.1103/PhysRevLett.102.048104.

[272] L. Angelani, A. Costanzo, and R. Di Leonardo. Active ratchets. Europhys. Lett., 96(6):68002, 2011. doi:10.1209/0295-5075/96/68002.

[273] A. Doostmohammadi, M. F. Adamer, S. P. Thampi, and J. M. Yeomans. Stabilization of active matter by flow-vortex lattices and defect ordering. Nature Comm., 7, 2016. doi:10.1038/ncomms10557.

[274] H. H. Wensink and H. Löwen. Aggregation of self-propelled colloidal rods near confining walls. Phys. Rev. E, 78:031409, 2008. doi:10.1103/physreve.78.031409.

[275] A. Costanzo, R. Di Leonardo, G. Ruocco, and L. Angelani. Transport of self-propelling bacteria in micro-channel flow. J. Phys. Cond. Mat., 24(6):065101, 2012. doi:10.1088/0953-8984/24/6/065101.

[276] F. Peruani, A. Deutsch, and M. Bär. A mean-field theory for self-propelled particles interacting by velocity alignment mechanisms. Eur. Phys. J. Spec. Top., 157(1):111–122, 2008. ISSN 1951-6355. doi:10.1140/epjst/e2008-00634-x.

[277] R. Stocker. Marine microbes see a sea of gradients. Science, 338(6107):628–633, 2012.

doi:10.1126/science.1208929.

[278] W. M. Durham, J. O. Kessler, and R. Stocker. Disruption of vertical motility by shear triggers formation of thin phytoplankton layers. Science, 323(5917):1067–1070, 2009. doi:10.1126/science.1167334.

[279] R. Rusconi and R. Stocker. Microbes in flow. Curr. Op. Microbiol., 25:1–8, 2015. doi:10.1016/j.mib.2015.03.003.

[280] N. Figueroa-Morales, G. Miño, A. Rivera, R. Caballero, E. Clément, E. Altshuler, and A. Lindner. Living on the edge: Transfer and traffic of *E. coli* in a confined flow. Soft Matter, 11:6284–6293, 2015. doi:10.1039/C5SM00939A.

[281] H. C. F. Marcos, T. R. Powers, and R. Stocker. Bacterial rheotaxis. Proc. Nat. Acad. Sci., 109 (13):4780–4785, 2012. doi:10.1073/pnas.1120955109.

[282] E. Altshuler, G. Mino, C. Perez-Penichet, L. d. Rio, A. Lindner, A. Rousselet, and E. Clément. Flow-controlled densification and anomalous dispersion of *E. coli* through a constriction. Soft Matter, 9:1864–1870, 2013. doi:10.1039/C2SM26460A.

[283] A. Zöttl and H. Stark. Periodic and quasiperiodic motion of an elongated microswimmer in Poiseuille flow. Eur. Phys. J. E, 36(1):4, 2013. doi:10.1140/epje/i2013-13004-5.

[284] H. Masoud and H. A. Stone. A reciprocal theorem for marangoni propulsion. J. Fluid Mech., 741:R4, 2014. doi:10.1017/jfm.2014.8.

[285] H. Masoud, H. A. Stone, and M. J. Shelley. On the rotation of porous ellipsoids in simple shear flows. J. Fluid Mech., 733:R6, 2013. doi:10.1017/jfm.2013.476.

[286] M. Cloitre, R. Borrega, and L. Leibler. Rheological aging and rejuvenation in microgel pastes. Phys. Rev. Lett., 85:4819–4822, Nov 2000. doi:10.1103/PhysRevLett.85.4819.

[287] S. P. Sutera and R. Skalak. The history of Poiseuille's law. Annu. Rev. Fluid Mech., 25(1):1–20, 1993. doi:10.1146/annurev.fl.25.010193.000245.

[288] A. M. Ardekani and E. Gore. Emergence of a limit cycle for swimming microorganisms in a vortical flow of a viscoelastic fluid. Phys. Rev. E, 85(5):056309, 2012. doi:10.1103/PhysRevE.85.056309.

[289] A. Karimi, S. Yazdi, and A. M. Ardekani. Hydrodynamic mechanisms of cell and particle trapping in microfluidics. Biomicrofluidics, 7(2):021501, 2013. doi:10.1063/1.4799787.

[290] C. Montecucco and R. Rappuoli. Living dangerously: how *Helicobacter pylori* survives in the human stomach. Nat. Rev. Mol. Cell Biol., 2(6):457–466, 2001. doi:10.1038/35073084.

[291] J. P. Celli, B. S. Turner, N. H. Afdhal, S. Keates, I. Ghiran, C. P. Kelly, R. H. Ewoldt, G. H. McKinley, P. So, S. Erramilli, et al. *Helicobacter pylori* moves through mucus by reducing mucin viscoelasticity. Proc. Nat. Acad. Sci., 106(34):14321–14326, 2009. doi:10.1073/pnas.0903438106.

[292] S. A. Mirbagheri and H. C. Fu. *Helicobacter pylori* couples motility and diffusion to actively create a heterogeneous complex medium in gastric mucus. Phys. Rev. Lett., 116:198101, May 2016. doi:10.1103/PhysRevLett.116.198101.

[293] R. B. Kimsey and A. Spielman. Motility of lyme disease spirochetes in fluids as viscous as the extracellular matrix. J. Infect. Dis., 162(5):1205–1208, 1990. doi:10.1093/infdis/162.5.1205.

[294] B. Liu, T. R. Powers, and K. S. Breuer. Force-free swimming of a model helical flagellum in viscoelastic fluids. Proc. Nat. Acad. Sci., 108(49):19516–19520, 2011. doi:10.1073/pnas.1113082108.

[295] D. Gagnon, N. Keim, and P. Arratia. Undulatory swimming in shear-thinning fluids: Experiments with caenorhabditis elegans. J. Fluid Mech., 758:R3, 2014. doi:10.1017/jfm.2014.539.

[296] Y. Gao, M. Neubauer, A. Yang, N. Johnson, M. Morse, G. Li, and J. X. Tang. Altered motility of *Caulobacter crescentus* in viscous and viscoelastic media. BMC Microbiol., 14(1):322, 2014. doi:10.1186/s12866-014-0322-3.

[297] V. A. Martinez, J. Schwarz-Linek, M. Reufer, L. G. Wilson, A. N. Morozov, and W. C. Poon. Flagellated bacterial motility in polymer solutions. Proc. Nat. Acad. Sci., 111(50):17771–17776, 2014. doi:10.1073/pnas.1415460111.

[298] B. Thomases and R. D. Guy. Mechanisms of elastic enhancement and hindrance for finite-length undulatory swimmers in viscoelastic fluids. Phys. Rev. Lett., 113:098102, Aug 2014. doi:10.1103/PhysRevLett.113.098102.

[299] E. Lauga. Propulsion in a viscoelastic fluid. Phys. Fluids, 19(8):083104, 2007. doi:10.1063/1.2751388.

[300] H. C. Fu, V. B. Shenoy, and T. R. Powers. Low-Reynolds-number swimming in gels. Europhys. Lett., 91(2):24002, 2010. doi:10.1209/0295-5075/91/24002.

[301] J. Teran, L. Fauci, and M. Shelley. Viscoelastic fluid response can increase the speed and efficiency of a free swimmer. Phys. Rev. Lett., 104(3):038101, 2010. doi:10.1103/PhysRevLett.104.038101.

[302] S. E. Spagnolie, B. Liu, and T. R. Powers. Locomotion of helical bodies in viscoelastic fluids: Enhanced swimming at large helical amplitudes. Phys. Rev. Lett., 111(6):068101, 2013. doi:10.1103/PhysRevLett.111.068101.

[303] T. D. Montenegro-Johnson, D. J. Smith, and D. Loghin. Physics of rheologically enhanced propulsion: Different strokes in generalized Stokes. Phys. Fluids, 25(8):081903, 2013. doi:10.1063/1.4818640.

[304] R. Ledesma-Aguilar and J. M. Yeomans. Enhanced motility of a microswimmer in rigid and elastic confinement. Phys. Rev. Lett., 111(13):138101, 2013. doi:10.1103/PhysRevLett.111.138101.

[305] M. E. Cates and J. Tailleur. When are active Brownian particles and run-and-tumble particles equivalent? Consequences for motility-induced phase separation. Eur. Phys. Lett., 101(2):20010, 2013. doi:10.1209/0295-5075/101/20010.

[306] J. Saragosti, V. Calvez, N. Bournaveas, B. Perthame, A. Buguin, and P. Silberzan. Directional persistence of chemotactic bacteria in a traveling concentration wave. Proc. Nat. Acad. Sci., 108(39):16235–16240, 2011. doi:10.1073/pnas.1101996108.

[307] J. Saragosti, P. Silberzan, and A. Buguin. Modeling *E. coli* tumbles by rotational diffusion. Implications for chemotaxis. PloS one, 7(4):e35412, 2012. doi:10.1371/journal.pone.0035412.

[308] S. Tavaddod, M. Charsooghi, F. Abdi, H. Khalesifard, and R. Golestanian. Probing passive diffusion of flagellated and deflagellated *Escherichia coli*. Eur. Phys. J. E, 34(2):16, 2011. ISSN 1292-8941. doi:10.1140/epje/i2011-11016-9.

[309] M. Jabbarzadeh, Y. Hyon, and H. C. Fu. Swimming fluctuations of micro-organisms due to heterogeneous microstructure. Phys. Rev. E, 90(4):043021, 2014. doi:10.1103/PhysRevE.90.043021.

[310] A. Sokolov, R. E. Goldstein, F. I. Feldchtein, and I. S. Aranson. Enhanced mixing and spatial instability in concentrated bacterial suspensions. Phys. Rev. E, 80(3), 2009. doi:10.1103/PhysRevE.80.031903.

[311] X.-L. Wu and A. Libchaber. Particle diffusion in a quasi-two-dimensional bacterial bath. Phys. Rev. Lett., 84(13):3017, 2000. doi:10.1103/physrevlett.84.3017.

[312] P. T. Underhill, J. P. Hernandez-Ortiz, and M. D. Graham. Diffusion and spatial correlations in suspensions of swimming particles. Phys. Rev. Lett., 100(24):248101, 2008. doi:10.1103/PhysRevLett.100.248101.

[313] J.-L. Thiffeault and S. Childress. Stirring by swimming bodies. Phys. Lett. A, 374(34):3487–3490, 2010. doi:10.1016/j.physleta.2010.06.043.

[314] Z. Lin, J.-L. Thiffeault, and S. Childress. Stirring by squirmers. J. Fluid Mech., 669:167–177, 2011. doi:10.1017/s002211201000563x.

[315] J.-L. Thiffeault. Short-time distribution of particle displacements due to swimming microorganisms. Phys. Rev. E, 92:023023, 2015. doi:10.1103/PhysRevE.92.023023.

[316] C. Darwin. Note on hydrodynamics. In Math. Proc. Camb. Phil. Soc., volume 49 of 2, pages 342–354. Cambridge Univ Press, 1953. doi:10.1017/s0305004100028449.

[317] D. O. Pushkin, H. Shum, and J. M. Yeomans. Fluid transport by individual microswimmers. J. Fluid Mech., 726:5–25, 2013. doi:10.1017/jfm.2013.208.

[318] G. Miño, J. Dunstan, A. Rousselet, E. Clément, and R. Soto. Induced diffusion of tracers in a bacterial suspension: theory and experiments. J. Fluid Mech., 729:423–444, 2013. doi:10.1017/jfm.2013.304.

[319] D. O. Pushkin and J. M. Yeomans. Fluid mixing by curved trajectories of microswimmers. Phys. Rev. Lett., 111(18):188101, 2013. doi:10.1103/PhysRevLett.111.188101.

[320] A. Morozov and D. Marenduzzo. Enhanced diffusion of tracer particles in dilute bacterial suspensions. Soft Matter, 10(16):2748–2758, 2014. doi:10.1039/c3sm52201f.

[321] Please see the Supplementary Information. URL http://doi.org/10.1017/jfm.2015.269.

[322] R. Di Leonardo, D. Dell'Arciprete, L. Angelani, and V. Iebba. Swimming with an image. Phys. Rev. Lett., 106(3):038101, 2011. doi:10.1103/physrevlett.106.038101.

[323] E. A. Simone, T. D. Dziubla, and V. R. Muzykantov. Polymeric carriers: Role of geometry in drug delivery. Expert Opin. Drug Deliv., 2008. doi:10.1517/17425240802567846.

[324] M. Brown and C. Wittwer. Flow cytometry: principles and clinical applications in hematology. Clin. Chem., 46(8):1221–1229, 2000. URL http://www.clinchem.org/content/46/8/1221.full.

[325] S. Berger and L. Jou. Flows in stenotic vessels. Annu. Rev. Fluid Mech., 32(1):347–382, 2000. doi:10.1146/annurev.fluid.32.1.347.

[326] S. Hwang, M. Litt, and W. Forsman. Rheological properties of mucus. Rheol. Acta, 8(4): 438–448, 1969. doi:10.1007/bf01976227.

[327] A. Gilboa and A. Silberberg. In situ rheological characterization of epithelial mucus. Biorheol., 13(1):59–65, 1976. URL http://www.ncbi.nlm.nih.gov/pubmed/938741.

[328] T. J. Moriarty, M. U. Norman, P. Colarusso, T. Bankhead, P. Kubes, and G. Chaconas. Real-time high resolution 3d imaging of the lyme disease spirochete adhering to and escaping from the vasculature of a living host. PloS Pathog., 4(6):e1000090, 2008. doi:10.1371/journal.ppat.1000090.

[329] M. J. Hickey and P. Kubes. Intravascular immunity: the host–pathogen encounter in blood vessels. Nat. Rev. Immunol., 9(5):364–375, 2009. doi:10.1038/nri2532.

[330] J. D. Radolf, M. J. Caimano, B. Stevenson, and L. T. Hu. Of ticks, mice and men: understanding the dual-host lifestyle of lyme disease spirochaetes. Nat. Rev. Microbiol., 10(2):87–99, 2012. doi:10.1038/nrmicro2714.

[331] S. Uppaluri, N. Heddergott, E. Stellamanns, S. Herminghaus, A. Zöttl, H. Stark, M. Engstler, and T. Pfohl. Flow loading induces oscillatory trajectories in a bloodstream parasite. Biophys. J., 103(6):1162–1169, 2012. doi:10.1016/j.bpj.2012.08.020.

[332] R. Chacón. Chaotic dynamics of a microswimmer in Poiseuille flow. Phys. Rev. E, 88(5):052905, 2013. doi:10.1103/PhysRevE.88.052905.

[333] S. Chilukuri, C. H. Collins, and P. T. Underhill. Impact of external flow on the dynamics of swimming microorganisms near surfaces. J. Phys. Cond. Mat., 26(11):115101–115101, 2014. doi:10.1088/0953-8984/26/11/115101.

[334] C. K. Tung, F. Ardon, A. Roy, D. L. Koch, S. S. Suarez, and M. Wu. Emergence of upstream swimming via a hydrodynamic transition. Phys. Rev. Lett., 114(10):108102, 2015. doi:10.1103/PhysRevLett.114.108102.

[335] O. S. Pak, L. Zhu, L. Brandt, and E. Lauga. Micropropulsion and microrheology in complex fluids via symmetry breaking. Phys. Fluids, 24(10):103102, 2012. doi:10.1063/1.4758811.

[336] L. Zhu, E. Lauga, and L. Brandt. Self-propulsion in viscoelastic fluids: Pushers vs. pullers. Phys. Fluids, 24(5):051902, 2012. doi:10.1063/1.4718446.

[337] A. Acharya, R. Mashelkar, and J. Ulbrecht. Flow of inelastic and viscoelastic fluids past a sphere. Rheol. Acta, 15(9):454–470, 1976. ISSN 0035-4511. doi:10.1007/BF01530348.

[338] R. J. Phillips and L. Talini. Chaining of weakly interacting particles suspended in viscoelastic fluids. J. Non-Newt. Fluid Mech., 147(3):175 – 188, 2007. ISSN 0377-0257. doi:10.1016/j.jnnfm.2007.08.007.

[339] Please see the Supplemental Material for movies. URL http://journals.aps.org/prl/supplemental/10.1103/PhysRevLett.116.028104.

[340] K. G. Wahlund. Flow field-flow fractionation: Critical overview. J. Chromatogr. A, 1287(0):97 – 112, 2013. doi:10.1016/j.chroma.2013.02.028.

[341] N. Sato, S. Kawano, S. Tsuji, T. Ogihara, and S. Yamada. Gastric blood flow in ulcer diseases. Scand. J. Gastroentero., 30(S208):14–20, 1995. doi:10.3109/00365529509107756.

[342] A. Rösler, G. W. Vandermeulen, and H. M. Klok. Advanced drug delivery devices via self-assembly of amphiphilic block copolymers. Adv. Drug Deliver. Rev., 64:270–279, 2012. doi:10.1016/j.addr.2012.09.026.

[343] R. B. Bird, R. C. Armstrong, O. Hassager, and C. F. Curtiss. Dynamics of polymeric liquids. Vol. 1: Fluid mechanics, volume 1. Wiley, 1977. ISBN 047180245X.

[344] B. Ho and L. Leal. Migration of rigid spheres in a two-dimensional unidirectional shear flow of a second-order fluid. J. Fluid Mech., 76(04):783–799, 1976. doi:10.1017/S002211207600089X.

[345] P.-H. Chan and L. Leal. A note on the motion of a spherical particle in a general quadratic flow of a second-order fluid. J. Fluid Mech., 82(03):549–559, 1977. doi:10.1017/s0022112077000834.

[346] L. Leal. Particle motions in a viscous fluid. Annu. Rev. Fluid Mech., 12(1):435–476, 1980. doi:10.1146/annurev.fl.12.010180.002251.

[347] A. M. Leshansky, A. Bransky, N. Korin, and U. Dinnar. Tunable nonlinear viscoelastic "focusing" in a microfluidic device. Phys. Rev. Lett., 98:234501, Jun 2007. doi:10.1103/PhysRevLett.98.234501.

[348] G. d'Avino, P. L. Maffettone, F. Greco, and M. Hulsen. Viscoelasticity-induced migration of a rigid sphere in confined shear flow. J. Non-Newt. Fluid Mech., 165(9):466–474, 2010.

doi:10.1016/j.jnnfm.2010.01.024.

[349] M. M. Villone, G. D'Avino, M. A. Hulsen, F. Greco, and P. L. Maffettone. Numerical simulations of particle migration in a viscoelastic fluid subjected to Poiseuille flow. Comp. & Fluids, 42(1): 82–91, 2011. doi:10.1016/j.compfluid.2010.11.009.

[350] M. Villone, G. D'Avino, M. Hulsen, F. Greco, and P. L. Maffettone. Simulations of viscoelasticity-induced focusing of particles in pressure-driven micro-slit flow. J. Non-Newt. Fluid Mech., 166 (23):1396–1405, 2011. doi:10.1016/j.jnnfm.2011.09.003.

[351] G. D'Avino and P. Maffettone. Particle dynamics in viscoelastic liquids. J. Non-Newt. Fluid Mech., 215:80–104, 2015. doi:10.1016/j.jnnfm.2014.09.014.

[352] L. H. Cisneros, R. Cortez, C. Dombrowski, R. E. Goldstein, and J. O. Kessler. Fluid dynamics of self-propelled microorganisms, from individuals to concentrated populations. Experim. Fluids, 43(5):737–753, 2007. doi:10.1007/978-3-642-11633-9_10.

[353] I. S. Aranson, A. Sokolov, J. O. Kessler, and R. E. Goldstein. Model for dynamical coherence in thin films of self-propelled microorganisms. Phys. Rev. E, 75(4):040901, 2007. doi:10.1103/PhysRevE.75.040901.

[354] L. Hall-Stoodley, J. W. Costerton, and P. Stoodley. Bacterial biofilms: From the natural environment to infectious diseases. Nat. Rev. Microbiol., 2(2):95–108, 2004. doi:10.1038/nrmicro821.

[355] J. C. Conrad. Physics of bacterial near-surface motility using flagella and type *IV* pili: Implications for biofilm formation. Res. Microbiol., 163(9–10):619 – 629, 2012. ISSN 0923-2508. doi:10.1016/j.resmic.2012.10.016.

[356] M. Givskov, L. Eberl, and S. Molin. Control of exoenzyme production, motility and cell differentiation in *Serratia liquefaciens*. FEMS Microbiol. Lett., 148(2):115–122, 1997. doi:10.1016/S0378-1097(96)00530-7.

[357] M. A. Bees, P. Andresen, E. Mosekilde, and M. Givskov. The interaction of thin-film flow, bacterial swarming and cell differentiation in colonies of *Serratia liquefaciens*. J. Math. Biol., 40 (1):27–63, 2000. doi:10.1007/s002850050004.

[358] R. M. Harshey and T. Matsuyama. Dimorphic transition in *Escherichia coli* and *Salmonella typhimurium*: Surface-induced differentiation into hyperflagellate swarmer cells. Proc. Nat. Acad. Sci., 91(18):8631–8635, 1994. doi:10.1073/pnas.91.18.8631.

[359] A. Karimi, D. Karig, A. Kumar, and A. Ardekani. Interplay of physical mechanisms and biofilm processes: Review of microfluidic methods. Lab Chip, 15(1):23–42, 2015. doi:10.1039/c4lc01095g.

[360] L. Vaccari, D. Allan, N. Sharifi-Mood, A. Singh, R. Leheny, and K. Stebe. Films of bacteria at interfaces: Three stages of behaviour. Soft Matter, 11:6062–6074, 2015. doi:10.1039/C5SM00696A.

[361] H. A. Stone and H. Masoud. Mobility of membrane-trapped particles. J. Fluid Mech., 781: 494–505, 2015. doi:10.1017/jfm.2015.486.

[362] R. Di Leonardo, D. Dell'Arciprete, L. Angelani, and V. Iebba. Swimming with an image. Phys. Rev. Lett., 106:038101, Jan 2011. doi:10.1103/physrevlett.106.038101.

[363] S. Wang and A. M. Ardekani. Swimming of a model ciliate near an air-liquid interface. Phys. Rev. E, 87:063010, Jun 2013. doi:10.1103/PhysRevE.87.063010.

[364] D. Lopez and E. Lauga. Dynamics of swimming bacteria at complex interfaces. Phys. Fluids, 26(7):071902, 2014. doi:10.1063/1.4887255.

[365] R. A. Lambert, F. Picano, W.-P. Breugem, and L. Brandt. Active suspensions in thin films: Nutrient uptake and swimmer motion. J. Fluid Mech., 733:528–557, 10 2013. doi:10.1017/jfm.2013.459.

[366] Please see the Electronic Supplementary Information. URL `http://arxiv.org/abs/1511.01859`.

[367] S. S. Ozarkar and A. S. Sangani. A method for determining Stokes flow around particles near a wall or in a thin film bounded by a wall and a gas-liquid interface. Phys. Fluids, 20(6):063301, 2008. doi:10.1063/1.2930667.

[368] H. C. Berg and L. Turner. Chemotaxis of bacteria in glass capillary arrays. *Escherichia coli*, motility, microchannel plate, and light scattering. Biophys. J., 58(4):919–930, 1990. doi:10.1016/S0006-3495(90)82436-X.

[369] W. R. DiLuzio, L. Turner, M. Mayer, P. Garstecki, D. B. Weibel, H. C. Berg, and G. M. Whitesides. *Escherichia coli* swim on the right-hand side. Nature, 435(7046):1271–1274, 2005. doi:10.1038/nature03660.

[370] H. A. Guidobaldi, Y. Jeyaram, C. A. Condat, M. Oviedo, I. Berdakin, V. V. Moshchalkov, L. C. Giojalas, A. V. Silhanek, and V. I. Marconi. Disrupting the wall accumulation of human sperm

cells by artificial corrugation. Biomicrofluidics, 9(2):024122, 2015. doi:10.1063/1.4918979.

[371] B. Ezhilan, R. Alonso-Matilla, and D. Saintillan. On the distribution and swim pressure of run-and-tumble particles in confinement. J. Fluid Mech., 781:R4, 2015. doi:10.1017/jfm.2015.520.

[372] S. J. Weinstein and K. J. Ruschak. Coating flows. Annu. Rev. Fluid Mech., 36:29–53, 2004. doi:10.1146/annurev.fluid.36.050802.122049.

[373] A. S. Utada, R. R. Bennett, J. C. Fong, M. L. Gibiansky, F. H. Yildiz, R. Golestanian, and G. C. Wong. *Vibrio cholerae* use pili and flagella synergistically to effect motility switching and conditional surface attachment. Nat. Comm., 5, 2014. doi:10.1038/ncomms5913.

[374] K. A. Wemmer and W. F. Marshall. Flagellar motility: All pull together. Curr. Biol., 14(23): R992–R993, 2004. doi:10.1016/j.cub.2004.11.019.

[375] V. F. Geyer, F. Jülicher, J. Howard, and B. M. Friedrich. Cell-body rocking is a dominant mechanism for flagellar synchronization in a swimming alga. Proc. Nat. Acad. Sci., 110(45): 18058–18063, 2013. doi:10.1073/pnas.1300895110.

[376] K. Y. Wan, K. C. Leptos, and R. E. Goldstein. Lag, lock, sync, slip: the many 'phases' of coupled flagella. J. R. Soc. Interface, 11(94):20131160, 2014. doi:10.1098/rsif.2013.1160.

[377] A. Hamel, C. Fisch, L. Combettes, P. Dupuis-Williams, and C. N. Baroud. Transitions between three swimming gaits in *Paramecium* escape. Proc. Nat. Acad. Sci., 108(18):7290–7295, 2011. doi:10.1073/pnas.1016687108.

[378] H. Wensink and H. Löwen. Emergent states in dense systems of active rods: from swarming to turbulence. J. Phys. Cond. Mat., 24:464130, 2012. doi:10.1088/0953-8984/24/46/464130.

[379] A. Kaiser, K. Popowa, H. H. Wensink, and H. Löwen. Capturing self-propelled particles in a moving microwedge. Phys. Rev. E, 88:022311, 2013. doi:10.1103/physreve.88.022311.

[380] R. Nash, R. Adhikari, and M. Cates. Singular forces and pointlike colloids in Lattice Boltzmann hydrodynamics. Phys. Rev. E, 77:026709, 2008. doi:10.1103/physreve.77.026709.

[381] R. Nash, R. Adhikari, J. Tailleur, and M. Cates. Run-and-tumble particles with hydrodynamics: Sedimentation, trapping, and upstream swimming. Phys. Rev. Lett., 104:258101, 2010. doi:10.1103/physrevlett.104.258101.

[382] J. P. Hernandez-Ortiz, C. G. Stoltz, and M. D. Graham. Transport and collective dynamics in suspensions of confined swimming particles. Phys. Rev. Lett., 95(20):204501, 2005. doi:10.1103/physrevlett.95.204501.

[383] D. Saintillan and M. Shelley. Orientational order and instabilities in suspensions of self-locomoting rods. Phys. Rev. Lett., 99:058102, 2007. doi:10.1103/physrevlett.99.058102.

[384] J. Swan, J. Brady, R. Moore, and C. 174. Modeling hydrodynamic self-propulsion with Stokesian dynamics. or teaching Stokesian dynamics to swim. Phys. Fluids, 23:071901, 2011. doi:10.1063/1.3594790.

[385] R. Singh, S. Ghose, and R. Adhikari. Many-body microhydrodynamics of colloidal particles with active boundary layers. J. Stat. Mech., 2015:P06017, 2015. doi:10.1088/1742-5468/2015/06/p06017.

[386] Y.-G. Tao and R. Kapral. Design of chemically propelled nanodimer motors. J. Chem. Phys., 128(16):164518, 2008. doi:10.1063/1.2908078.

[387] F. Lugli, E. Brini, and F. Zerbetto. Shape governs the motion of chemically propelled Janus swimmers. J. Phys. Chem. C, 116:592, 2012. doi:10.1021/jp205018u.

[388] J. Hu, M. Yang, G. Gompper, and R. Winkler. Modelling the mechanics and hydrodynamics of swimming *E. coli*. Soft Matter, 11:7867, 2015. doi:10.1039/c5sm01678a.

[389] H. Wu, M. Thiébaud, W.-F. Hu, A. Farutin, S. Rafai, M.-C. Lai, P. Peyla, and C. Misbah. Amoeboid motion in confined geometry. Phys. Rev. E, 92:050701, 2015. doi:10.1103/physreve.92.050701.

[390] P. Ahlrichs and B. Dünweg. Simulation of a single polymer chain in solution by combining Lattice Boltzmann and molecular dynamics. J. Chem. Phys., 111:8225, 1999. doi:10.1063/1.480156.

[391] V. Lobaskin and B. Dünweg. A new model of simulating colloidal dynamics. New J. Phys., 6: 54, 2004. doi:10.1088/1367-2630/6/1/054.

[392] L. Fischer, T. Peter, C. Holm, and J. de Graaf. The raspberry model for hydrodynamic interactions revisited, part i: Periodic arrays of spheres and dumbbells. J. Chem. Phys., 143: 084107, 2015. doi:10.1063/1.4928502.

[393] J. de Graaf, T. Peter, L. Fischer, and C. Holm. The raspberry model for hydrodynamic interactions revisited, part ii: The effect of confinement. J. Chem. Phys., 143:084108, 2015.

doi:10.1063/1.4928503.

[394] J. de Graaf, G. Rempfer, and C. Holm. Diffusiophoretic self-propulsion for partially catalytic spherical colloids. NanoBioScience, 14(3), 2015. doi:10.1109/tnb.2015.2403255.

[395] S. Samin and R. van Roij. Self-propulsion mechanism of active Janus particles in near-critical binary mixtures. Phys. Rev. Lett., 115:188305, 2015. doi:10.1103/physrevlett.115.188305.

[396] A. Ladd. Numerical simulations of particulate suspensions via a discretized boltzmann equation. part 1. theoretical foundation. J. Fluid Mech., 271:285, 1994. doi:10.1017/s0022112094001771.

[397] D. Roehm and A. Arnold. Lattice Boltzmann simulations on GPUs with ESPResSo. Eur. Phys. J. ST, 210:73, 2012. doi:10.1140/epjst/e2012-01639-6.

[398] H. J. Limbach, A. Arnold, B. A. Mann, and C. Holm. ESPResSo – an extensible simulation package for research on soft matter systems. Comp. Phys. Comm., 174:704, 2006. doi:10.1016/j.cpc.2005.10.005.

[399] A. Arnold, O. Lenz, S. Kesselheim, R. Weeber, F. Fahrenberger, D. Roehm, P. Košovan, and C. Holm. ESPResSo 3.1 — Molecular Dynamics Software for Coarse-Grained Models. In M. Griebel and M. A. Schweitzer, editors, Meshfree Methods for Partial Differential Equations VI, volume 89 of Lecture Notes in Computational Science and Engineering, page 1. Springer, 2013. doi:10.1007/978-3-642-32979-1_1.

[400] D. d'Humières, I. Ginzburg, M. Krafczyk, P. Lallemand, and L.-S. Luo. Multiple-relaxation-time Lattice Boltzmann models in three dimensions. Philos. Trans. A Math. Phys. Eng. Sci., 360: 437, 2002. doi:10.1098/rsta.2001.0955.

[401] R. Zwanzig and M. Bixon. Compressibility effects in the hydrodynamic theory of brownian motion. J. Fluid Mech., 69:21, 5 1975. doi:10.1017/s0022112075001280.

[402] M. Tirado, C. Martinez, and J. de la Torre. Comparison of theories for the translational and rotational diffusion coefficients of rodâlike macromolecules. application to short dna fragments. J. Chem. Phys., 81:2047, 1984. doi:10.1063/1.447827.

[403] S. Jana, S. Um, and S. Jung. Paramecium swimming in capillary tube. Phys. Fluids, 24:041901, 2012. doi:10.1063/1.4704792.

[404] E. Lushi, H. Wioland, and R. Goldstein. Fluid flows created by swimming bacteria drive self-organization in confined suspensions. Proc. Nat. Acad. Sci., 111:9733, 2014. doi:10.1073/pnas.1405698111.

[405] S. Das, A. Garg, A. Campbell, J. Howse, A. Sen, D. Velegol, R. Golestanian, and S. Ebbens. Boundaries can steer active Janus spheres. Nat. Comm., 6:8999, 2015. doi:10.1038/ncomms9999.

[406] H. Shum and E. Gaffney. Hydrodynamic analysis of flagellated bacteria swimming near one and between two no-slip plane boundaries. Phys. Rev. E, 91:033012, 2015. doi:10.1103/physreve.91.033012.

[407] K. Ishimoto and E. Gaffney. Squirmer dynamics near a boundary. Phys. Rev. E, 88:062702, 2013. doi:10.1103/physreve.88.062702.

[408] A. Brown, I. Vladescu, A. Dawson, T. Vissers, J. Schwarz-Linek, J. Lintuvuori, and W. Poon. Swimming in a crystal. Soft Matter, 12:131, 2016. doi:10.1039/c5sm01831e.

[409] Please see the Electronic Supplementary Information. URL `http://doi.org/10.1039/C6SM00939E`.